Identification of long-range solid-like correlations in liquids and role of the interaction fluid-substrate

Philipp Kahl

▶ To cite this version:

HAL Id: tel-01317455

https://tel.archives-ouvertes.fr/tel-01317455

Submitted on 18 May 2016

Thèse de Doctorat

Philipp KAHL

Mémoire présenté en vue de l'obtention du
grade de Docteur de l'Université du Maine
sous le label de L'Université Nantes Angers Le Mans

École doctorale : *3MPL, ED500*

Discipline : *Milieux denses et matériaux, CNU Groupe 6, Section 28*
Spécialité : *Physique*
Unité de recherche *: Laboratoire Léon Brillouin (LLB, CEA-Saclay) – UMR n° 12*
Institut des Molécules et de Matériaux du Mans (IMMM) – UMR n° 6283

Soutenance le 11.01.16

Identification of long-range solid-like correlations in liquids and role of the interaction fluid-substrate

JURY

Rapporteurs : **Günter REITER**, Professeur, Albert-Ludwigs-Universität Freiburg
Alessio ZACCONE, Professeur, University of Cambridge

Examinateurs : **Elie RAPHAEL**, Directeur de recherche, Gulliver UMR 7083
Jean-François TASSIN, Professeur, Université du Maine

Directeurs de Thèse : **Jean-François BARDEAU**, Chargé de recherche, Université du Maine
Laurence NOIREZ, Directeur de recherche, Laboratoire Léon Brillouin, CEA-Saclay

"Und es wurde fertig, das Leidenswerk.
Es wurde vielleicht nicht gut, aber es wurde fertig.
Und als es fertig war, siehe, da war es auch gut."

Thomas Mann

Acknowledgements

Contents

General Introduction

Collective effects play a significant role in nature and the systems they appear in, may differ strongly ranging from soft matter physics (gelation, glass formation, phase transition)[1, 2] over electronic circuits (flash converter) [3] to living processes (ligand-enzyme reactions, beating cilia, yeast cells) [4–8]. Being at the origin of collective events the propagation and the synchronization of the signals remain the centre of intensive research.

For systems found in a liquid medium fluid mechanics become a fundamental key-parameter. While liquids exhibit longitudinal collective signal propagation the transversal modes are supposed to only show dissipative flow [9]. Of the three states of matter the liquid state is by far the least understood. It seems to be more and more obvious that the dynamic processes at the nano-, micro and even submillimeter scale are different from those at the macroscopic scale and rather demand a multi-scale approach. Flow properties close to a wall/surface are not identical to those observed at the macroscopic scale. In particularly this deviation can be found for flow under confined conditions [10] or in a porous medium [11]. Further it has been shown that the transportation/diffusion of water in carbon nanotubes is faster than predicted by conventional models [12]. By modifying the surface properties the nature of the interactions with the wall can affect the flow behaviour in a spectacular way. Recently it has been shown that it is possible to electrically switch the wetting behaviour in order to modulate the adhesion or slip, and thus the flow, of a liquid on a surface [13].

Despite the relevance of these questions on the flow that is a process out of thermodynamic equilibrium, only few studies consider the possibility that the dynamic response close to equilibrium (the liquid is solicited at a low frequency) may also show a dependency on the boundary conditions. From 1992 on Granick [14–20], Reiter [21] and Israelachvili [22–24] have identified, at the nanoscale, a low frequency solid-like response of polymer solutions which they attributed to a surface effect. The Russian group of Derjaguin observed a solid-like response for various liquids at the micrometer scale at frequencies of several kHz which they attributed to a physical property [25, 26]. Some years later Martinoty and Collin have shown that the low frequency response of molten polymer films of several tens of micrometers thickness does not show a terminal flow but a gel-like behaviour [27]. This low

frequency shear elasticity was then evidenced at the Laboratoire Leon Brillouin [28–34] by improving the transmission of the stress to the liquid [35]. This permitted the observation of a solid-like response at sample thicknesses of several to hundreds of micrometer for molten polymers, super-cooled liquids (glycerol, polypropylene glycol, o-Terphenyl)[36–38], alkanes (heptadecane), ionic liquids [39, 40] and even liquid water [41]. The delicate property mostly observable at low thickness geometry is hardly experimentally measurable and is hidden in conventional mechanical measurements. The existence of a terminal elasticity shows that the liquid state is a state correlated elastically at long distance. This property opposes the definition of a liquid state constituted by dynamically free molecules and introduces the concept of long-range elastic correlations. This is a strong claim that puts the dynamic interpretation, in terms of molecular dynamics, at question.

The identification of the terminal shear elasticity is here extended to the isotropic phase of liquid crystals [42] that is from a thermodynamic, crystallographic and conventional rheological point of view considered as a simple liquid. A further intention consists in inventing an approach to visualize the elastic response by using birefringent properties of pretransitional fluctuations present in the isotropic phase as optical and dynamical tracers. The premise hereby is that the pretransititional swarms are embedded in the shear elastic network and respond to a low frequency mechanical stimulation by a collective orientation of the anisotropic molecules. We report here on the emergence of a harmonic birefringent signal in the isotopic phase [43] whose appearance is neither predictable on the basis of the standard viscous or visco-elastic behaviour, nor on the basis of the lifetimes of the pretransitional fluctuations which are from far too fast [44, 45]. The low frequency birefringence is related to the shear elasticity.

Further, the emergence of the low frequency birefringence is evidenced on a molecular scale by X-ray and neutron scattering techniques. The results indicate a weak orientation of the pretransitional swarms upon the application of a strain and are able to explain the observation of the optic signal.

Finally, though the low frequency shear elasticity and birefringence are properties of the bulk, their experimental evidence demands a control of the fluid-substrate interaction. The total wetting condition achieved in the stress measurements is further investigated by surface techniques as atomic force microscopy, contact angle and Zeta-potential measurements.

The manuscript is divided into 5 chapters.

Chapter 1 State of the art: The description of the dynamic stress relaxation of soft matter is based on an interpretation of visco-elastic measurements. The conventional molecular approaches stand on the developments of the Rouse and reptation models and predict the absence of a shear elasticity at low frequencies in fluids. However several phenomena like shear-thinning are not satisfactorily treated. Seldom alternative molecular approaches consider intermolecular interactions and even predict a low frequency shear elasticity. In the past two decades such a solid-like behaviour was experimentally identified at very small length-scales by various authors. Notably the improvement of the wetting condition lead to a recent identification of a low frequency shear elasticity in liquids up to the sub-millimeter scale.

Chapter 2 Shear elasticity in the isotropic phase of liquid crystals: This identification of a terminal shear elasticity in liquids using wetting improved dynamic mechanical analysis by Noirez et. al presents the very basis of this chapter. For the first time a low frequency solid-like response is revealed by a careful stress/strain signal analysis in the isotropic phase of three representative liquid crystal molecules at the sub-millimeter scale: the 8CB (low molecular weight, $M_{8CB} = 292g/mol$), the LCP95 ($12 \times M_{8CB}$) and the PACN ($187 \times M_{8CB}$), a non-entangled side-chain liquid crystal polymer. Being measured close to equilibrium it is demonstrated that the solid-like behaviour is the fundamental response of the isotropic phase of the liquid crystal. The influence of several parameters including the temperature, strain amplitude, frequency, wetting condition and sample thickness are considered. The results contradict any interpretation of the shear elasticity in terms of pretransitional effects or experimental artefacts and indicate a generic property of the liquid state.

Chapter 3 Visualization of the shear elasticity: This chapter proposes an alternative technique that gains insight into the shear elastic properties of liquids. The principle of dynamic mechanical analysis is transferred to optical measurements. For this the birefringent properties of the orientational pretransitional fluctuations present in the isotropic phase of liquid crystals are used. We show that a low frequency mechanical solicitation gives rise to a strong, defect free and reversible birefringence. The analysis of the birefringence/strain signals reveals a strain dependent behaviour of the bulk that can neither be explained by pretransitional dynamics nor by a viscous approach. The influence of temperature and strain amplitude is studied. The emergence of this birefringent signal at low frequency indicates that a long-range order of the isotropic phase is established (i.a. a loss of entropy while the strain increases the energy). The conclusion points out the similarity between the stress and the optical behaviour versus the strain amplitude.

Chapter 4 Structure X-ray / neutron scattering: The emergence of macroscopic birefringent signal in the isotropic phase is the result of an anisotropy at the molecular level. This chapter presents the results of X-ray and small angle neutron scattering carried

out to analyse the structure of the isotropic phase submitted to a low frequency strain amplitude at macroscopic sample sizes. The results indicate a weak orientation of the pretransitional swarms and are able to explain the observation of the birefringent signal from chapter 3.

Chapter 5 Role of the surface interaction: The last chapter is dedicated to the liquid-substrate interactions. In the first part the influence of the surface condition in the optic birefringent experiments from chapter 3 is evaluated. Several surface treatments are applied to the transparent quartz fixtures in order to play with the anchoring conditions of the liquid crystal. It is shown that an increase of the contact angle (de-wetting) between the isotropic phase and the surface reduces the strain induced birefringent signal and vice versa. The second part elaborates on the wetting performance of the α-alumina. The re-initialized ceramic shows total wetting boundary conditions for many liquids. Fixtures of this material are used for the identification of the shear elasticity in chapter 2. We present the influence of the surface conditions on the contact angle (wetting behaviour) and discuss the interaction with liquids by atomic force microscopy, Zeta-potential measurements and neutron scattering.

Chapter 1

State of the art: From polymer visco-elasticity to hidden elastic properties in liquids

The description of the dynamic stress relaxation of soft matter is based on a molecular interpretation of visco-elastic (VE) measurements and therefore assumes that the validity of the experiments is fulfilled. Visco-elastic measurements are essentially carried out by transmission of an oscillatory shear strain or stress from a substrate to the sample. The no-slip boundary condition is certainly one of the strongest assumptions together with the causality-linearity condition. The experimental VE protocol is discussed more in detail in Chapter 2. Theoretical approaches consider the materials (usually polymers in solution or bulk phase, entangled or not) to be constituted of dynamically individual molecules showing no long-range dynamic correlations i.e. the absence of shear elasticity. The VE properties are attributed to the dynamic properties of a single molecular chain [46, 47]. While the Rouse model convincingly describes the conventional visco-elastic data of dilute solutions of short chain polymers, the treatment of high mass entangled polymers by the reptation theory [48] has not been fully satisfying. New mechanisms as the contour length fluctuations and convective constraint release have been added in order to coincide with experimental results [49, 50]. Despite its success relatively simple rheological observations as shear-thinning and stick-slip do not always find a general consensus. The molecular models are not able to predict the dynamic behaviour of polymers at nano/micro scale conditions. Here, being neglected in the models, the molecular interactions between the chains and in particular between the substrate and the polymer become of most importance and the dynamics may change surprisingly not only in the case of visco-elastic materials but also for simple liquids. This first chapter gives a brief introduction to the molecular description by the Rouse and reptation models, some of their adjustments, open questions

and alternative theoretical approaches. Further we will discuss the experiments that lead to a successive identification of a terminal solid-like behaviour from several nanometers up to hundreds of micrometers for polymers and later simple liquids. This includes in particular the surface force measurements of Granick, Reiter [14–21] and Israelachvili [22–24], piezo-rheometric measurements by Collin, Martinoty [27] and Derjaguin [25, 26] and experiments by Mendil and Noirez [28–30, 32–34, 36, 38–41]. Despite different approaches of the results these experiments share the observation of a non-vanishing shear elasticity at low frequencies that cannot be predicted on the basis of the usually addressed molecular models.

Contents

1.1 Conventional polymer dynamics - Single chain description

1.1.1 Molecular models: From Rouse to reptation

The visco-elastic dynamic behaviour of molten polymers was first proposed by the Rouse model [46]. Initially developed for a single polymeric chain in free space or dissolved in a solvent it was extended to a chain surrounded by other chains. Zimm [47] later improved the statistical approach by hydrodynamic interactions taking the cooperativity of chain segments into consideration. The model idealizes a polymeric molecule as a succession of N harmonic springs of a length l that connect $N + 1$ beads. Every spring is long enough to be described by a Gaussian conformation. (The individual entities show no hydrodynamic interactions between each other.) The description of a dynamic force applied to the chains considers the elastic force between two neighbouring springs, a viscous friction and a random force due to the Brownian motion in a solvent. Other forces and interactions in particular between polymeric chains are neglected, e.g. an excluded volume interaction and the back-flowing forces induced by the movement of neighbouring chains. The average force vector of the individual forces of the springs is perpendicular to the chain and thus the molecule diffuses laterally. The sum of the applied forces to the molecules leads to an equation obeying to a generalized Maxwell equation at small deformations with a distribution of relaxation times. Its solution gives N cooperative modes each possessing their own relaxation time. The slowest mode, the Rouse time τ_{Rouse} is the time needed for the chain to cover a distance equal to its gyration radius and also the time needed to renew its conformation:

$$\tau_{Rouse} = \frac{\zeta_0 l^2}{3\pi^2 k_b T} N^2 \text{ and thus } \tau_{Rouse} \sim N^2. \tag{1}$$

With the friction coefficient ζ_0, the Boltzmann constant k_b and the temperature T. The only constraint on the chain from its neighbours (polymer or solvent) results from a friction parameter.
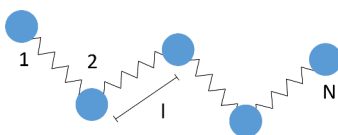
Figure 1.1: The Rouse Model: Beads connected by springs in free space.

Experimental relaxation times are i.a. accessible by dynamic mechanical analysis. Figure 1.2 presents a spectrum of a short chain polymer calculated with the Rouse model. The elastic modulus G' and the loss modulus G'' describe the visco-elastic behaviour due to

an applied oscillatory deformation. At low frequencies or times longer than any relaxation mode the characteristic evolution of the moduli can be modelled by the Maxwell approximation where G' is proportional to ω^2 and G'' to ω. This zone where G'' dominates the dynamic response and G' vanishes at long times is identified as the low frequency flow behaviour. The zone at shorter times where $G' = G'' \sim \omega^{\frac{1}{2}}$ is called transition zone, where we find the relaxation time of modes of several monomers, segmental relaxations. The Rouse time is determined by the intersection of G' and G''. The viscosity at zero frequency η_0 is found to be proportional to the molecular mass M of the chain.
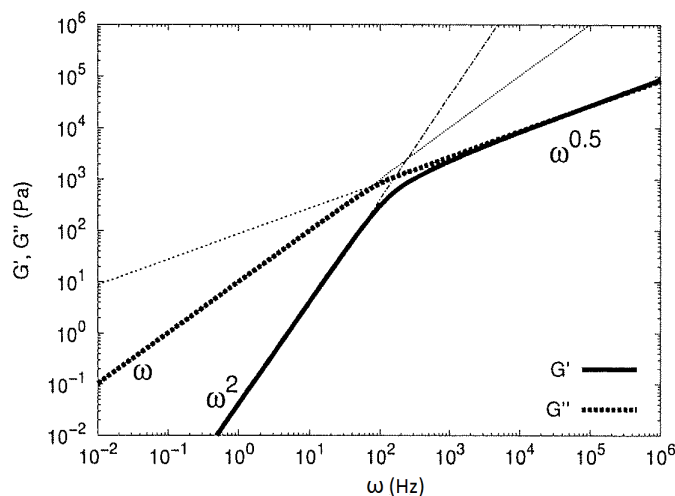
Figure 1.2: Rouse model: Evolution of the visco-elastic moduli as a function of frequency for a short chain polymer. Reproduced from [51]. Calculated for $\tau_{Rouse} = 10^{-3}$ and $N = 1000$.

This description is considered to match dynamic relaxation data as long as the polymer chains are short. For longer molecules (monomer repetition $N > 100$) the dynamics differ by an elastic regime at shorter times: the rubbery plateau. In contrast to the chemical cross-linking that is responsible for the elasticity of "real rubbers" the origin of the observed plateau was attributed to temporary entanglements between individual chains [52, 53]. Early models treated temporary cross-links [54–58] or introduced an entanglement friction [59]. Still used for the description of associating polymers [60, 61] this theoretical approach of a transient network was then modified and overthrown by the development of new outstanding concepts. First proposed for the diffusion of polymeric molecules at rest by de Gennes in 1971 [48] the reptation theory was later extended to the description of chain dynamics under external stress by Doi and Edwards [62–64] who developed a method to calculate the stress relaxation function. For linear polymers the model considers free chains (defined by N elements of length l) confined in a tube in an array of topological

constraints (figure 1.3). The tube size is determined by the neighbouring molecules. Due to their presence the polymer is unlikely to diffuse tangentially to the tube but is preferably moving along the tube - it reptates. Practically one dimensionally, reptation describes a Rouse type diffusion of the chain along the tube. As it is unhindered by topological constraints no further interactions are considered. When the chain reaches an extremity of its tube it can randomly choose a new path, creating a new tube. According to the model the macroscopic diffusion coefficient D of this process is proportional to N^{-2}. The longest or characteristic event is thus the time for a molecular chain to diffuse out of its initial tube. It is represented by the reptation time τ_{rept}:

$$\tau_{rept} = \frac{Nl^2}{\pi^2 D} \text{ and thus } \tau_{rept} \sim N^3. \tag{2}$$
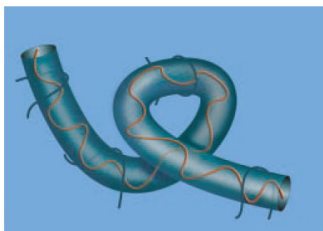
Figure 1.3: Tube model: The neighbouring chains confine a given test chain inside a virtual tube. Reproduced from [65].

The dynamic relaxation spectrum of entangled polymers is identical to the dynamical behaviour of short chains at high and low frequencies (Figure 1.4). In the transition zone the Rouse model applies $G' = G'' \sim \omega^{\frac{1}{2}}$ whereas in the terminal region the Maxwell model describes the flow comportment $G' \sim \omega^2$ and $G'' \sim \omega$. The viscosity at zero frequency η_0 is proportional to M^3. At intermediate frequency the spectrum shows a zone with no apparent relaxation process. This is the rubbery plateau where G' is invariant to the frequency and G'' descends indicating an absence of dissipation. The value of the plateau where $G' = G_N^0$ is used as a measure of the distance between entanglements. The rubbery plateau is still a relatively badly understood phenomenon and subject to high research interest.

The reptation or simply tube model simplifies the complex, many-body effects of chain interpenetration in terms of a smooth tube-like confinement on an ideal test chain and assumes that this test chain undergoes Rouse dynamics inside the tube. Conclusively the reptation theory is addressed to explain the origin of shear thinning due to alignment in flow of the tubes, the origin of a plateau region in the dynamic elastic modulus $G'(\omega)$ above the terminal time (rubbery plateau), and the approximate scaling of this reptation time τ_{rept} with chain length N.
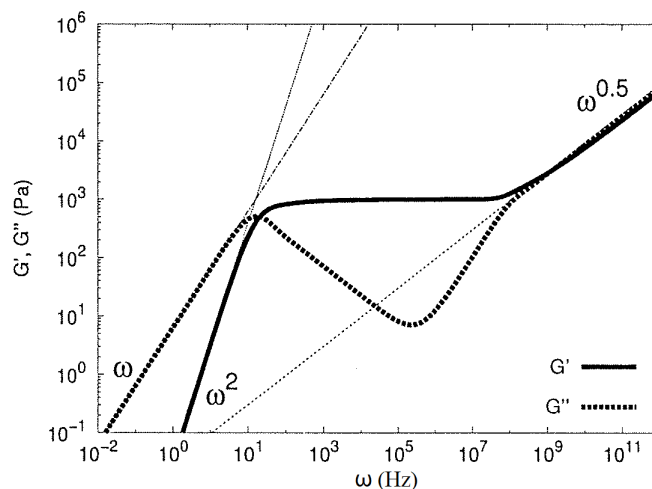
Figure 1.4: Reptation model: Evolution of the visco-elastic moduli as a function of frequency for a long chain polymer. Reproduced from [51]. Calculated for $\tau_{Rouse} = 10^{-10}s$ with $N = 1000$ and $\tau_{rept} = 10^{-3}s$ with 1000 modes.

1.1.2 Extensions and development of additional chain relaxation mechanisms

Though the visco-elastic data of entangled polymers is qualitatively well described, the simplification of the many-chain problem to a single chain moving in a tube of permanent obstacles was rapidly shown to be oversimplified. While the difference between experimental $D \sim M^{-2.3}$ and theoretical $D \sim M^{-2}$ diffusion times of long chain polymers seems to be resolved [66] other salient properties rest to be only qualitatively in agreement with the reptation theory. The characteristic time τ_{rept} is predicted to vary as $\tau_{rept} \sim M^3$ but experiments showed a variation as $\tau_{rept} \sim M^{3.4}$ [50]. Another discrepancy was found for the behaviour of the dynamic loss modulus $G''(\omega)$ at frequencies above τ_{rept}^{-1}. Instead of going as $\omega^{-\frac{1}{2}}$ experiments found a much weaker power law, between zero and -1/4 depending on chain length [67]. To overcome these problems additional molecular mechanisms were included [68]. The most prominent among them are the contour length fluctuations that describes a chain stretching assumed to occur on scales of the Rouse time and constraint release, the relaxation of chain orientation which occurs on scales of the reptation time.

Contour length fluctuations

A major shortcoming was i.a. addressed to the fact that the original theory did not consider the finite lifetimes of the tube determining constraints. The physical origin of the

3.4 scaling has been addressed to the relaxation of some portion of the stress by a faster process than reptation, which would decrease the viscosity [69]. The fast process becomes less important as N becomes large. Doi identified this faster process with contour-length fluctuations, (CLF) i.e., the fluctuation-driven stretchings and contractions of the chain along the tube [70]. When the chain contracts within the tube and then stretches out again, the orientation of the ends of the tube is forgotten, and stress associated with alignment of those portions of the tube is relaxed. Doi argued that the fraction of tube relaxed in this way should scale as $N^{-\frac{1}{2}}$. Simulations by O'Connor and Ball [71] and Rubinstein [72] of the combined reptation and contour-length dynamics of a single chain within a tube, give a result for $\eta(N)$ consistent with the experimental 3.4 scaling. Rubinstein, Helfand, and Pearson [73] proposed the Rouse-like path-length fluctuations at the chain ends as the source for the near $\omega^{-\frac{1}{4}}$ form of $G''(\omega)$ at high frequencies. However, they were unable to treat the crossover quantitatively [28]. The importance of the contour length fluctuations decreases with N and is neglectable for infinite long chains. According to Richter et al. [65] a direct molecular proof of the CLF has been evidenced in 2005 although their Spin Echo experiments assume the premise of the validity of reptation.
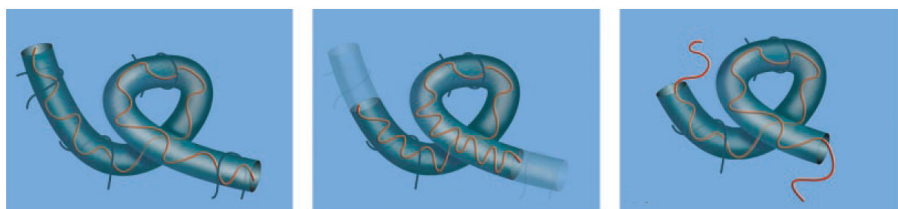
Figure 1.5: Mechanism of contour length fluctuations: (left) The test chain is confined into a tube by the surrounding chains. (middle) The chain ends fluctuate retracting into the original tube, thus "forgetting" the initial confinement of the vacated tube parts. (right) The chain ends may then explore the surroundings. Reproduced from [65].

Constraint releases

The correct modelling of the dynamic behaviour of entangled chains has been found to be more complicated in the intermediate frequency zone. In actual polymer melts the lifetime of obstacles (surrounding chains) is finite which leads to constraint releases (CR) on the test chain also known as tube reorganisation. First proposed by de Gennes and later refined by Klein [74] the tube itself was treated as a Rouse chain with elementary segments adjusted to the tubes dimensions. In this approach relaxation of a single test chain results from two independent and concurrent processes: Reptation inside the tube and tube reorganization, the latter being the slower one and thus usually has little effect on diffusion properties in the case of homopolymer melts. A most important problem of

the reptation up to today is the excessive shear thinning which is predicted in steady flows and the correct modelling of the rubbery plateau. Eventually Marrucci and Ianniruberto [75] incorporated the concept of convective constraint releases (CCR) in order to predict the stress plateau in steady shear experiments. They have discussed the fact that at shear rates above the rate of reptation, the shear stress is predicted to go through a maximum and decrease indefinitely thereafter.

The additions of CLF, CR and CCR to the reptation theory were seen as breakthrough in the understanding of the complex dynamics of polymers and are subject to a vast number of research papers. Nevertheless phenomena like shear-thinning, stress overshoot, shear-banding and reptation are still discussed intensively. A long list of experiments is not in agreement with the single molecular approach. The dynamic behaviour at small scales is badly covered or cannot be explained at all by conventional models despite their strongly growing scientific interest.

1.2 Alternative theoretical approaches: Importance of collective properties

In the conventional VE theory the properties of polymers are dominated by intramolecular forces which are due to the chain connectivity [36, 49]. The tube model attributes the properties of the melt to the dynamics of a single chain surrounded by other chains which create a topological constraint. This constraint can be modelled by a mean-field approach [76] and determines the chain conformation. The dynamics of the melt are described by the conformation of a single chain surrounded by other chains as a function of time.

This approach, which is eventually based on the Rouse model, leads to the prediction of an absence of shear elasticity at long time-scales for small, simple molecules and the presence of a Maxwell flow curve for polymeric chains entangled or not.

Conventional visco-elasticity is certainly the by far dominating approach to the dynamic description of polymers. However different theoretical models have been proposed which show a fairly different behaviour of polymers and liquids at slow time-scales. These theoretical approaches may even allow for a terminal shear elastic behaviour. More recent and remarkable results that abandon the dynamic description on the basis of single molecules and introduce collective interacting systems will be presented in the following.

1.2.1 Can liquids be seen as crystals containing defects?

Granato developed a model for the treatment of mechanical properties of simple condensed matter based interstitialcies, a concept usually used for the description of crystal properties [77]. Consequently his "Interstitialcy Theory of Condensed Matter" (ITCM) views liquids as a solid-like continuum containing few percent of intersticials, e.g. discontinuities or defects, in its otherwise crystalline configuration. The model was developed around the changes of thermodynamic key-parameters shear modulus and entropy, yielding simple mechanical models. With setting the correlation between molecules as crucial the ITCM is able to predict an initial elastic behaviour for the stress relaxation in molten metal alloys. Within the model the elastic modulus above the glass transition decreases rapidly as the concentration of defects increases. The latter indicates a transition from a solid to a dissipative liquid behaviour. Though the model has not yet been applied to many liquid systems it has been successfully verified for some cases [78, 79] and may explain low frequency elastic properties in liquids.

1.2.2   Intra and Intermolecular interactions: Cooperative dynamics

The dynamic description by the Rouse model neglects any intermolecular (inter-chain) interactions. To overcome this deficit Guenza developed a generalized Langevin equation for the cooperative dynamics of interacting, flexible polymer fluids where intramolecular and intermolecular forces are explicitly included [80–82]. Though the model does not explicitly predict an elastic behaviour of the polymer melts at long times, it introduces long-range dynamics and for the first time sets the intermolecular interactions as crucial even for non-entangled polymers (It correctly describes the dynamic behaviour at short-times where the Rouse-model has short-comings).

Ibar sees the need for a "New theory in Polymer physics" and proposes a cooperative coupling nature of the interactions between the polymer macromolecules which form a network, the Energetic Kinetic Network [83, 84]. The model consists in cohesive heterogeneous dynamics for the interactions of polymers. Within this formalism he is able to explain the effect of shear-thinning for entangled polymers.

Finally, Volino elaborated a couple of years ago (1997), a new formalism called the "non-extensive visco-elastic theory" that predicts for fluids that any finite volume of liquid possesses a non-zero static shear elasticity [85]. This theory can be considered as an extension of the elastic modes of nematic phases to the isotropic liquids. To our knowledge, this is the only theoretical approach predicting the shear elasticity and its dependence on the scale at which it is measured. Independently, a low frequency shear elasticity plateau was first identified in the isotropic phase of liquid crystal polymers by Martinoty, then by Noirez et al. at several tens of microns and then at larger thicknesses on various liquids. These early experimental measurements might credit the validity of Volino's prediction. Finally, it should be pointed out that the mechanical dynamic analysis is crucial in this approach and is very likely the only method able to access to this shear elasticity.

1.3   Confrontation with experimental results

1.3.1   Shear-thinning as a troubling phenomenon: Unresolved challenges in VE theory

We have seen that the reptation model is able to describe the presence of the rubbery plateau in linear rheology. Considerable effort was being made to explain the viscosity decrease with the applied shear rate in non-linear experiments as shown in figure 1.6. This phenomenon, referred to as shear-thinning, presents the most common form of non-Newtonian behaviour. Considered to be a result of entangled chains it is seen in suspensions, emulsions, polymer solutions and gels. Complementary to figure 1.6, three zones can be distinguished. In the terminal (low shear rates) and the transition zone (high shear rates) the polymer shows Newtonian behaviour with a difference in viscosity of several decades. This decrease that is modelled by a power law is mediated by the non-Newtonian behaviour in the intermediate zone.
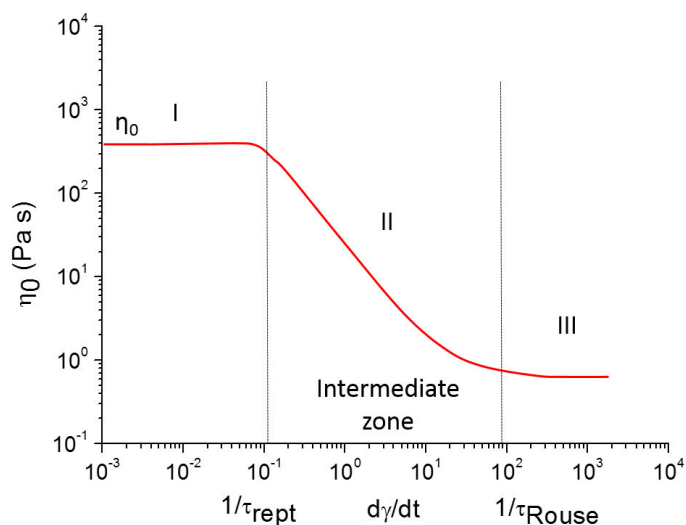
Figure 1.6: Behaviour of the viscosity versus shear rate for an entangled polymer.

The shear thinning zone is delimited by the inverse of the reptation (a low shear rates) and the Rouse time (high shear rates). Theoretical models predict that once the applied shear rate $\dot{\gamma}$ becomes competitive with the chain dynamics, i.e. $\dot{\gamma} > \tau_{rept}^{-1}$ the flow is supposed to rearrange the tubes along the velocity direction. When the reciprocal rate of an applied force becomes comparable to the characteristic time of a molecular event its relaxation is
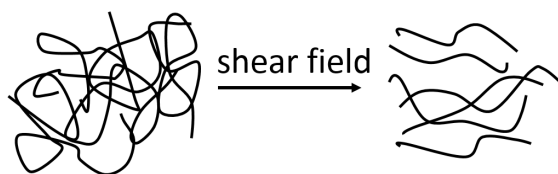
Figure 1.7: Proposed scheme of the mechanism of shear thinning on the molecular level: Disentanglement and shear alignment of the chains due to the flow.

probed. This circumstance is described by the Deborah number D:

$$D = \frac{\tau_{rept}}{\dot{\gamma}^{-1}} \tag{3}$$

Where τ_{rept} presents the characteristic time of the chain and the inverse of the applied shear rate $\dot{\gamma}$. For values of D close to unity the relaxation of the corresponding molecular event is probed. The supposed origin of the shear thinning is thus attributed to, on a molecular scale, the coupling of the flow to the chain which is supposed to induce an entanglement-disentanglement transition (figure 1.7). This interpretation may be too simple to explain the phenomenological curve as seen in figure 1.6. The mentioned power law modelling was the first used to describe the shear rate dependence of the viscosity and applies well at higher shear rates (the intermediate zone). However the values predicted at low shear rates are too high and the Newtonian value η_0 is not provided. It has been attempted to replace this empirical description by structural models as the Cross [86] or Carreau [87] equations as well as by theoretical models, notably the Krieger-Dougherty equation [88]. Since then these models were further modified. However, complications arise from the circumstance that viscosities obtained from the linear and non-linear experiments are not always comparable. Though their relation is postulated by the empirical Cox-Merz law [89]; The flow viscosity $\eta(\dot{\gamma})$ equals the complex viscosity in dynamical measurements $|\eta^*|(\omega, 0)$ when the applied strain equals the frequency. It is not completely verified.

In terms of the reptation model, it has been tried to solve the problem of excessive shear thinning by including the relaxation mechanism of convective constraint release (CCR) [90–92]. In contrast to the original reptation model where the topological constraint of the surrounding chains is fixed they are now free to move by a non-thermal motion. This motion can be induced either directly by a velocity gradient, or indirectly by chain retraction following a "very fast" deformation (i.e., with a rate larger than the reciprocal Rouse time). Incorporated into the reptation model for the stress plateau, the CCR mechanism was able to predict the appearance of shear thinning. However the description of the phenomenon might be to simplified.

1.3.2   Shear thinning and the question of the molecular orientation

Another interesting rheological phenomenon related to the shear thinning in entangled polymers is the stress overshoot during start-up shear at sufficiently high shear rates. In the intermediate regime the stress is supposed to display an overshoot before reaching a steady value at shear rates between τ_{rept}^{-1} and τ_{Rouse}^{-1}. While a stretching of the chain (CLF becomes important close to τ_{Rouse}^{-1}) is usually neglected, the stress is merely addressed to a chain orientation (CR). Yet reptation models accounting for chain orientation alone do not predict a steady state for the viscosity at high shear rates. An additional mechanism, termed convective constraint release (CCR), was invoked to predict the steady-state and shear-thinning behaviour of the viscosity in fast shear flows [90]. Molecularly the stress overshoot is attributed to chain alignment in the confining tube by the shear deformation. In spite of its apparent success in describing stress overshoot during start-up shear there has never been direct validation of the molecular mechanism (apart from molecular dynamics simulations i.e. in [93]). In velocimetry measurements a wall slip regime has been used to explain the stress overshoot that finally leads to shear banding in micro-gels [94]. Furthermore, there has been considerable controversy regarding the theoretical implications of a number of particle-tracking velocimetric observations of shear banding in polymer melts under flow from S.-Q. Wangs group [95, 96] and Rheo-SANS experiments by Noirez et al. [97].

1.3.3   When experiments reveal that the chains are not stretched under shear flow

The shear-thinning under non-linear flow can be modelled by modified reptation theories with certain constraints. However there has never been any proof of its origin on a molecular scale. Indeed experiments probing the molecular structure indicate that the admitted claim that the shear-thinning of entangled polymer chains is due to an orientation of entanglement segments under shear flow holds not true in the molten state. Watanabe et al. [98] and Noirez et. al [97] have independently determined the radius of gyration of linear entangled polymer melts as a function of the applied shear rate in Couette geometry using small angle neutron scattering (Rheo-SANS, figure 1.8(a)). This technique is the only method to access directly the chain dimensions. Two components of the radius of gyration, along and perpendicular to the direction of the velocity are measured. The radius of gyration R_g which describes the dimensions of a polymeric coil showed no dependence on the shear rate[1] (figure 1.8(b)). The supposed disentanglement and alignment of the chain resulting in an increase of R_g above the reptation time (the onset of shear-thinning) is not observed (figure 1.8(b)). In fact the chain dimension keeps its value under shear flow. The authors

---

[1]The present results cannot be generalized to polymer solutions [99] or to micellar solutions [100] where a chain elongation is observed using Rheo-SANS or Rheo-SAXS.

(a) Rheo-SANS setup

(b) Radius of gyration vs the shear rate
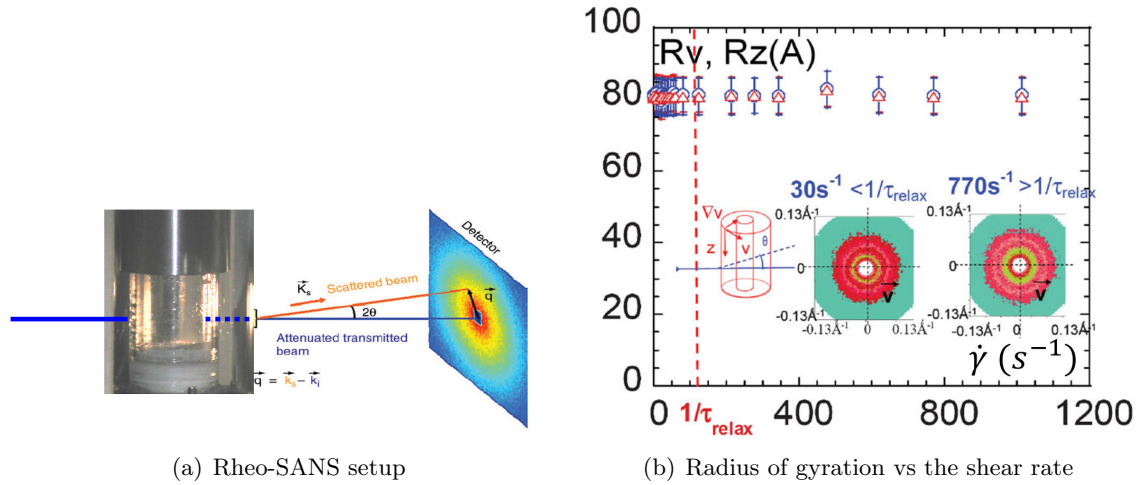
Figure 1.8: Rheo-SANS: (a) The experimental setup with the shear cell in Couette geometry filled with a polybutadien melt with a relaxation time $\tau_{relax} = 10^{-2} sec$. (b) The radius of gyration (R_v of the polymer chain in the velocity direction and R_z in the neutral direction perpendicular to the velocity direction of the spinning Couette) as a function of the shear rate. No change of the coil size is observed above the repatation time (denoted as τ_{relax}). Reproduced from [97]

interpreted this as the result of partial wall slip as well as a formation of shear bands as soon as the lowest shear rates in the Couette geometry. Both effects participate in the dissipation of the transmitted stress leading to a hindrance of chain disentanglement in the major part of the melt. As the transmission of stress is the key event in a rheological experiment dissipative effects could serve as an explanation for the decrease in stress (stress plateau) under non-linear conditions in entangled polymer melts.

1.4 Shear elasticity at low frequencies: A question of scale and surface

Non-linear phenomenon as shear-thinning, shear-banding and stress overshoot are fascinating but puzzling observations when it comes to results that cannot be explained satisfactorily by existing molecular models. Indeed modifications of the original reptation theory have established a seemingly convenient description of the visco-elastic behaviour for linear and branched polymers. However a disagreement between the Rouse equation and computer-simulated data of short-time non-entangled [101, 102] and entangled [103, 104] linear polymer dynamics, both in the molten state and in concentrated solutions is well known. Experimentally, another polymeric class, non-concatenated rings do not trap themselves as suggested by Obukhov [105] but instead relax as self-similar power law without any rubbery plateau [106]. Wang et al. observed reptation times under linear (oscillatory) conditions that were not compatible to the ones from non-linear experiments [107]. Martins even concludes in his theoretical works that the interaction energies between chains are not sufficiently high for any properties assigned to entanglements [108]. The claim that the reptation time presents the slowest mode in the relaxation spectrum is questioned by the shear induced isotropic to nematic transition in liquid crystal polymers as its appearance takes place at time-scales much lower than any predicted visco-elastic relaxation time [109]. Further discrepancies between theoretically predicted and experimentally evidenced results have been observed in dynamic experiments on the nano and micro-scale that have shown a pronounced dependency on the boundary conditions, e.g. the interaction between the sample and the surface. This section will present some of the experiments and discoveries that are seemingly in contradiction to existing molecular models but may give a new insight in fluid dynamics at slow time-scales.

1.4.1 Elasticity of thin films: Surface force measurements at the nanoscale

Deviations from the theoretical predictions are not only found in non-linear experiments and entangled polymers. The linear dynamics of thin liquid films can differ remarkably from the ones observed under conventional bulk conditions. There is an extensive amount of measurements on the dynamics of fluids that have been carried out in the Surface Force Apparatus, a technique pioneered by Israelachvili and co-workers [22–24] and Granick and co-workers [14–20]. A Surface Force Apparatus is a ultra-sensitive piezoelectric device that can resolve distances within $0.1nm$ and forces down to $10^{-8}N$. This technique can be used to measure electrostatic forces, van der Waals forces, and even hydration or solvation forces. While early measurements focused on forces between mica surfaces in air or vacuum and later liquids and aqueous solutions it was extended to perform dynamic measurements,
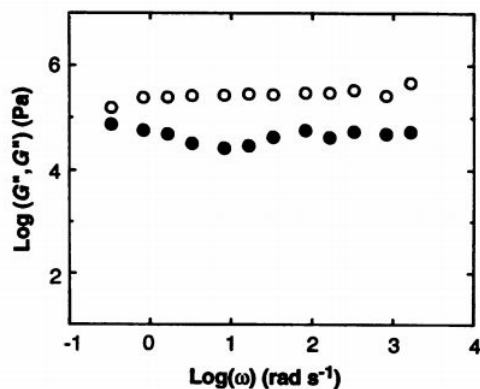
Figure 1.9: Dynamic relaxation spectrum obtained by Surface Force Apparatus measurements of thin films (4.2 nm) of low molecular weight polyphenylmethylsiloxane melts (4620 g/mol) $44°C$ above the glass transition: Instead of the expected Rouse-type flow behaviour the elastic (G' and viscous G'' modulus show no apparent dependence on the frequency, indicating a solid-like response. Reproduced from [14].

in order to determine viscous and visco-elastic properties of fluids. Granick has shown that the viscoleastic behaviour of thin nano-metric films (ca. 4x the gyration radius) of low molecular weight, non-entangled polyphenylmethylsiloxane melts do not obey a Rouse-type flow at long times-scales but show no relaxation at the probed low frequency range [14]. This terminal solid-like behaviour qualitatively resembles the conventional rubbery plateau of entangled polymers at the transition zone. As the films get thinner the elastic response gets stronger with G' exceeding G'' by an order of magnitude. Interestingly the elastic response is enhanced by strong adhesion forces and is weakened by less interacting surfaces. The same group reproduced their results for smaller molecules and observed a transition from an elastic response to a dissipative state as a function of the deformation [21]. The signal analysis revealed a stick to slip response of the liquids - usually a property addressed to describe the movement between solid materials. The elastically stored energies were found to be low and the transition could be reproduced in repetitive cycles with a pronounced hysteresis. The low values of G' indicate that the molecules are not in a crystalline order as this would result in a higher modulus and therefore behave like soft solids.

Comparable observations have been made by Schoen et al. using Monte-Carlo simulations. They studied the shearing of monolayer and bilayer mono-atomic films confined between planar solid surfaces. When such ordered films are subjected to a shear strain , they respond initially as an elastic solid at small strains and the stress depends linearly on the strain. As the shear strain increases, the response becomes highly nonlinear.

1.4.2 Dynamics at the micrometer-scale: Piezorheometer

In the late 1980ies the Russian group of Derjaguin published remarkable papers on the complex shear modulus of polymeric and small-molecule liquids [25, 26]. Using the atomic vibration of a piezoelectric membrane to study the dynamic response of thin films of several micrometer thickness, they identified a shear elasticity for non-entangled polymeric melts and "simple" liquids as liquid water, glycols, small alcohols and alkanes. Improved wetting conditions were established by cleaning the surfaces with a hydrogen-flame. Initially having studied the mechanical properties of boundary layers of liquids they attributed the elastic moduli found at larger thickness to a bulk property. Experimentally they observed a shear elastic response at small deformation angles with values of G' in the order of $10^5 Pa$ depending on the film thickness. At larger deformations the response (they measured the real part of the piezo-quartz frequency shift which is proportional to the shear modulus) strongly decreases (figure 1.10). The given frequency of their apparatus was 73.5 kHz which can be considered to be a low when compared to frequencies needed to access the classical relaxation time of liquids found by the Einstein formula or the Maxwell model. These values lie around $\tau_{relax}^{-1} = 10^{11} Hz$. The authors claim that the presence of the shear elasticity at low frequency proves that a so far neglected visco-elastic relaxation process takes place in liquids and attributed the processes involved to collective interactions of molecules. Upon the different types of samples tested, a "property possessed by all liquids without exception, independently of their viscosity and polarity" was postulated. Only
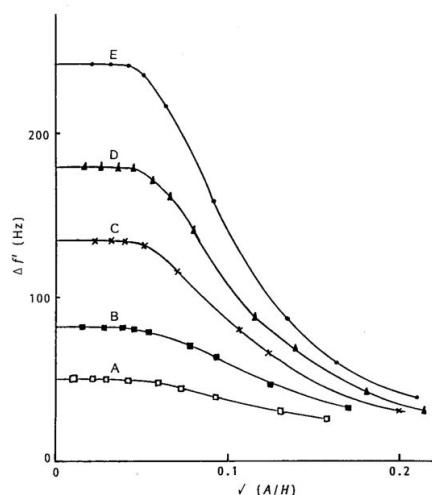
Figure 1.10: Real part of the frequency shift $\Delta f'(Hz)$ of Derjaguin's piezorheometric experiments for diethylene glycol films of different thicknesses (A: $4.75\mu m$, B: $3.05\mu m$, C: $1.173\mu m$, D: $1.37\mu m$, E: $1.05\mu m$) vs deformation angle A divided by the film thickness H. Reproduced from [25].

few years later in 1994, the French group of Martinoty carried out piezoelectric dynamic measurements of liquid crystal polymers in the isotropic phase [110]. Qualitatively similar to Derjaguin they observed an elastic plateau at small film thickness smaller than $100\mu m$) which increases as the sample thickness gets smaller. The elastic modulus showed values of up to 10^6 Pa in a frequency range where the isotropic phase is supposed to show a flow behaviour (figure 1.11). They emphasized the necessity of strong anchoring conditions of the liquid to the piezoelectric slides for their observations and explained the results by the existence of a transient network created by the dynamic association of mesogenic groups belonging to different chains. These elastic clusters of various sizes are supposed to be separated by viscous regions. The formation of elastic clusters by the mesogenic
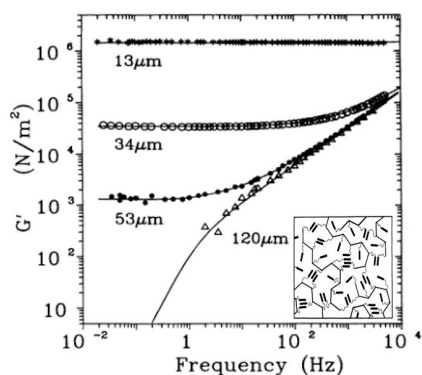
Figure 1.11: The elastic moduli G' of the isotropic phase of a side-chain liquid crystal polymer at low frequencies for various sample thickness and strong anchoring. The insert shows the proposed model of long-living clusters formed by the liquid crystal mesogens resulting in a intermolecular network. Reproduced from [110].

groups held not true as the same authors presented analogues experiments carried out for low molecular weight linear flexible polymer melts almost ten years later [27]. Again they observed a low frequency shear modulus where the overall comportment progressively shifted from a liquid-type behaviour to a solid-type one as the sample-thickness decreased from $100\mu m$ to $15\mu m$. Interestingly they showed that for a strong anchoring the response is found to be elastic while for a weak adhesion the sample shows conventional visco-elastic behaviour, a circumstance they addressed to slip (figure 1.12). Here, in the absence of liquid crystal moieties (and thus pretransitional effects) the authors attributed their results to dynamic clusters associated to the glass transition and suggested that they were due to long-range density-fluctuations which are frozen as a result of their ultra-slow relaxation times and thus display an elastic response.
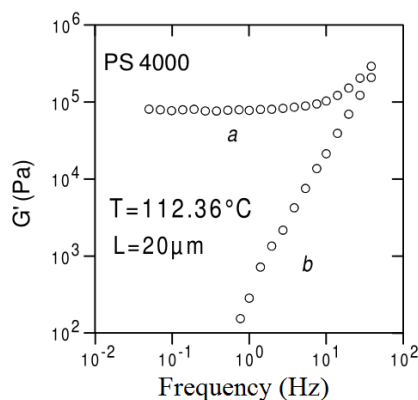
Figure 1.12: The elastic G' and viscous modulus G'' of a low molecular weight linear polystyrene melt ($4000g/mol$) at low frequencies for various sample thicknesses and strong anchoring at $40°C$ above the glass transition. Reproduced from [27].

1.4.3   Solid-like properties at the submillimeter-scale

In 2001 Noirez et al. have identified a shear induced phase transition in the isotropic phase of side-chain liquid crystal polymers [109]. Since no known characteristic times (pretransitionnal fluctuation life times, viscoelastic relaxation time) could be addressed to explain the collective orientation of molecules in the isotropic phase at the observed time-scales, the authors assumed the existence of longer relaxation times [32–34]. They carried out dynamic relaxation experiments using a conventional rheometer and conventional Aluminium fixtures in order to identify a relaxation mode at low frequencies. They noticed that the low frequency data did not scale with the expected ω, ω^2 flow behaviour. By repeating and improving the measurement, they noticed that the spread low frequency data collapses and forms a well-defined low frequency plateau pointing out a non or weak dependence of the moduli with respect to the frequency; i.e. a terminal elastic behaviour. The elastic plateau persists at low strain amplitude and far in the isotropic phase but lowers by increasing the strain (Figure 1.13). The low frequency plateau indicates that the liquid does not flow at these frequencies but still keeps an elastic nature that might explain the origin of the shear induced transitions [32]. It was also concluded that the elastic behaviour might be observable because of the excellent anchoring properties of the liquid crystal moieties [29, 31].

A systematic search was then carried out at the LLB to identify surfaces exhibiting high energy in order to reinforce the anchoring of the molecules on the surface. The wetting ability was selected as a quality criterion. Several surfaces were identified among them the zero porosity alumina that procures a total wetting at a macroscopic scale and for its ease of
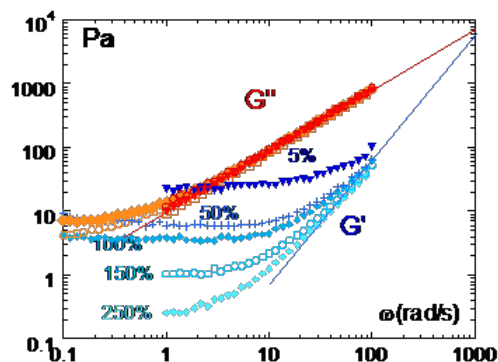
Figure 1.13: The elastic G' and viscous G'' modulus versus the frequency at different strain amplitudes of a side-chain liquid crystal polymer $+5°C$ above the isotropic transition. The solid lines correspond to the conventional Maxwell behaviour (ω^2 and ω). Substrate: aluminium, cone-plate geometry, $1mm$ thickness at the edge. Reproduced from [32].

cleaning and regeneration via heating. By improving the liquid-surface interaction e.g. the wetting conditions using non-conventional surfaces, a terminal solid-like response was then first identified in the low frequency range for a series of ordinary polymer melts (PBuA, Poylbutadiene, Polystyrene) even at $100°C$ above the glass transition. The optimisation of the boundary conditions produces a spectacular increase of the elastic modulus for polymeric liquids (by two to four orders of magnitude compared to the conventional VE response) and makes it apparent for small molecules in the first place at several tenths of millimeter.

This shear elasticity implies long range intermolecular interactions. Since the first fluids were Van der Waals polymer melts, it was important to detect the same elastic property in hydrogen-bond polymers. The polypropylene glycol (PPG-4000) was then successfully examined [36]. PPG has a glass transtion at $T_g = -75°C$ and is supercooled until the melting temperature $T_m = 53°C$. PPG does not crystallize in its liquid state below T_g. Interestingly solid type correlations were identified by photon correlation on the same fluid [111].

The low frequency shear elasticity was then identified in molecular glass formers as glycerol [37] and ortho-terphenyl (OTP) above the melting point. The elastic response is unambiguous (figure 1.14(a)) and is invisible when the measurement is performed on conventional surfaces (figure 1.14(b)). The ortho-terphenyl (OTP) is a typical molecule model of the literature of glasses. This van der Waals liquid ($T_g = -33°C$ and $T_m = 56°C$) exhibits also a terminal shear elasticity when it is probed under total wetting conditions above its melting point (figure 1.15). The figure shows that the shear elasticity vanishes at high strain rate (1000%) being replaced by the viscous behavior ($G'' = \eta\omega$) as already observed for other

(a) Glycerol on alumina (Al_2O_3).   (b) Glycerol on aluminium (Al).
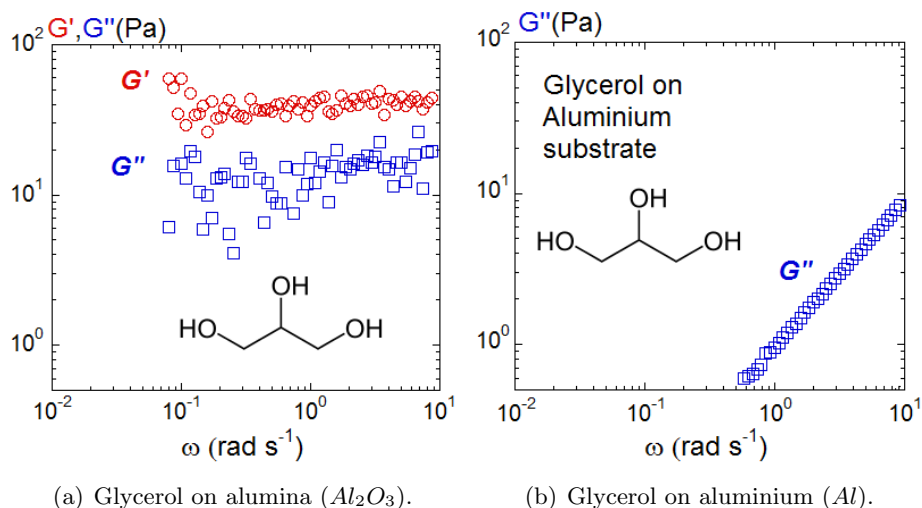
Figure 1.14: (a) Elastic G' (red dots) and viscous modulus G'' (blue emtpy boxes) of Glycerol at $T = 24°C$ at a sample thickness of $0.040mm$ measured under total wetting conditions (under nitrogen flow due to the hygroscopic properties) [37]. (b) The same measurement performed on conventional aluminium surfaces. The viscosity derived from the slope of G'' as a function of the frequency is in agreement with the tabulated data ($\eta = 1.1Pa.s$)

.

studied molecules. Other liquids as alkanes (heptadecane), ionic liquids [39, 40] or even liquid water [41] have been studied to establish the generic feature of the low frequency elasticity.
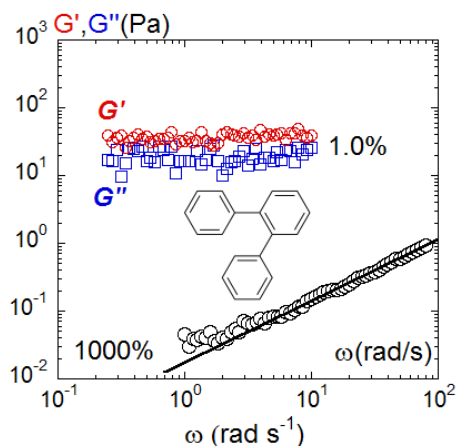
Figure 1.15: Dynamic relaxation of o-terphenyl at $+7.5°C$ above T_m measured for total wetting conditions G', red dots: G'', blue filled boxes (thickness: $0.045mm$). The black line represents the conventional viscosity curve ($G = \eta\omega$). It is superimposed on the data (black circles) obtained at very large strain amplitudes.

1.5   Conclusions

The conventional theoretical description of the dynamic stress relaxation of soft matter is based on the interpretation of visco-elastic measurements. The models stand on the Rouse and Reptation models that consider materials to be constituted of dynamically individual molecules with no long-range dynamic correlations, e.g. a vanishing shear elasticity at low frequencies. Alternative approaches that consider intra and intermolecular interactions, e.g. cooperative dynamics are scarce.

From an experimental point of view, this chapter has shown the identification a of low frequency shear elasticity in various liquids: The observation of a strain invariant elastic modulus at small strains that declines at larger deformations and larger sample sizes. This has been obtained by different groups using various techniques as e.g. the surface force apparatus measurements by Granick and Israelachvili and their co-workers at the nano-meter scale or the piezorheometric experiments of several micrometer thicknesses by Martinoty et al. and Derjaguin et al. Although the latter was the first to publish a low frequency elasticity in simple liquids his experiments somehow seem to having been forgotten. Finally the group of Noirez at the LLB has identified this very same terminal elastic behaviour since 2005 using a conventional TA-Instrument rheometer (ARES II), first for molten polymers and in the isotropic phase of liquid crystal polymers [29, 31, 32] and then, at a sub-millimeter scale in various liquids. Certainly this list is not complete; other groups that did not explicitly appear in this chapter have made similar discoveries.

In 2007, S.Q. Wang (Akron Univ. US) reproduced the results of the LLB using the same wetting protocol with a conventional Anton-Paar rheometer [112]. In 2008 Orrit et al. reported that it is possible to reveal in the supercooled state of glycerol and ortho-terphenyl (OTP), a solid-like response by applying very low stress [113]. It was however, not possible to state that crystallization or ageing was contributing.

What are the similarities between these experiments? The measurements are mostly carried out at sub-millimeter thicknesses or include an improvement of the liquid/substrate boundary conditions or a strong anchoring of the molecules (liquid crystals). In the case of the piezorheometer, the applied stress is transmitted from the molecular vibration. Its amplitude is extremely low. In the case of measurements with a conventional rheometer, low thicknesses, low strains and high energy surfaces (mostly high-density ceramics) are used. The common point is the minimization of the dissipation of the stress at the surface. As observed by several authors, the elastic response disappears above a critical strain, giving way to the usual visco-elastic spectrum. The shear elastic response must therefore be seen as a first linear regime prior to the VE response which presents a second linear regime.

In the following chapter we will continue the path of the experimental identification of a terminal elasticity in a liquid usually devoid of interest: the isotropic phase of liquid

crystals.

Chapter 2

Terminal shear elasticity in the isotropic phase of liquid crystals: Identification of a generic property
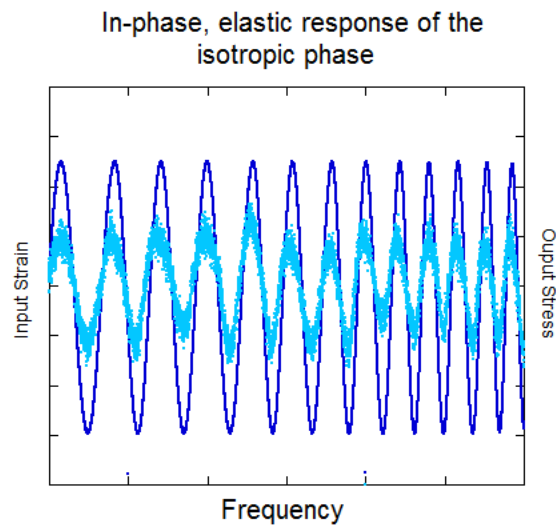
In the previous chapters we have seen that it is possible to reveal at the sub-millimeter scale a terminal shear elasticity when the liquid-substrate interactions are enhanced. This has been established for substances as molten polymers, glass formers, H-bond polar, ionic and vdW-liquids [28–30, 33, 34, 38–41].

In a first step, we will show the identification of shear elasticity in the liquid (isotropic

phase) of liquid crystals (LC). The isotropic phase is conventionally considered as an ordinary liquid in a rheological, symmetrical and thermodynamic sense. Identifying a shear-elasticity in the isotropic phase is not only challenging from a dynamic mechanical point of view it presents an additional interest: the pretransitional fluctuations coexisting in the liquid phase can be used as an optical tracker to probe the strain field. This will be demonstrated in chapter 3.

This chapter presents for the first time a low frequency solid-like response at the sub-millimeter scale in the isotropic phase of representative low and higher molecular weight liquid crystals. We will see that long range correlations are preserved when the LC order is lost. The following will discuss the experimental procedure in the detection of a low frequency shear elastic regime via wetting-improved dynamic mechanical analysis. We will see its dependence on the frequency and strain, the molecular mass, sample thickness and temperature.

Contents

2.1 Experimental: The isotropic phase of liquid crystal molecules

To probe the dynamic response of the isotropic phase of liquid crystals we chose three representative molecules:

- The first one, the 4,4-n-octylcyanobiphenyl (8CB), is one of the most intensively studied liquid crystals and may be considered a model of small liquid crystals [114, 115]. The 8CB presents a crystalline phase at low temperatures that enables to rule on the question of pretransitional glass transition effects. It exhibits the following phase sequence: Crystalline , smectic A, nematic and isotropic phase.
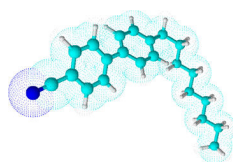
Figure 2.1: 3D-structure of 8CB

- The second molecule (LCP95) is commercially available and used in liquid crystal displays [116]. It consists of a 12 repetitive units acrylate backbone crafted with cyanobiphenyl ended side chains linked by a propyl spacer. The LCP95 presents a smectic A phase between the liquid and crystalline/glassy state. Its hydrodynamic radius determined by light scattering is 1.4 nm.
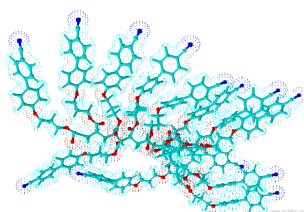
Figure 2.2: 3D-structure of LCP95

- The last sample (PACN) is a Side-Chain Liquid Crystal Polymer (SCLCP) and resembles the LCP95 from a structural point of view. As its lower molecular weight counterpart it is constituted of a 80 repetitive units acrylate backbone. The crafted cyanobiphenyl ended side chains are here linked by a butyl spacer. The molecular mass is far below the critical mass of entanglement [28] and it shows a glassy-nematic and nematic-isotropic transition.
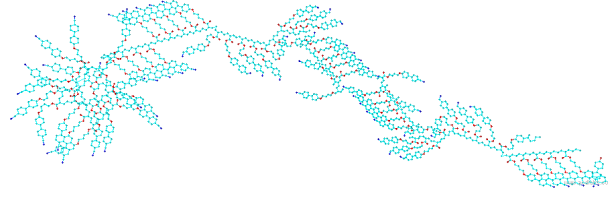
Figure 2.3: 3D-structure of PACN

The molecular structures along with the transition temperatures, molecular masses, degree of polymerization and polydispersity for the substances are summarized in table 1. The 8CB and LCP95 were purchased from Merck. The PACN monomer was synthesized at the LLB and a polymerization was carried out by PolymerExpert Inc. The transition temperatures were verified optically using a polarization microscope and by thermal analysis via Dynamic Scanning Calorimetry (DSC) and are in accordance with the literature data if available [116, 117].
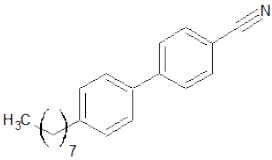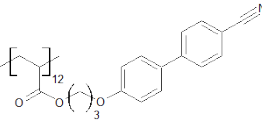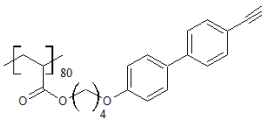
Sample	8CB	LCP95	PACN
Provided by	Merck	Merck	Home-made + Polymer-Expert
Molecular mass (g/mol)	292.4	3790	26800
Degree of Polymerization	1	12	80
Polydispersity	1.0	1.58	1.3
Radius of gyration (nm)	/	12.6	/
Phase sequence	$C < 21.5°C - S_A < 33°C - N < 40.5°C - I$	$T_g < 54°C - S_A < 79.8°C - I$	$T_g < 54°C - S_A < 124°C - I$
Structure			

Table 1: The molecular masses, phase sequences, polydispersities and structures of the 8CB, LCP95 and PACN.

2.1.1 First order transitions in liquid crystals

Both transitions, SA-I and N-I are first order transitions forbidding the miscibility between the isotropic and the liquid crystal phases. The liquid crystal acquires in the isotropic liquid all symmetries, making the transition similar to the process of fusion [118]. Due to the relatively low energies involved the transition is referred to as being of weakly first order which is why pretransitional fluctuations persist over a wider temperature range. These swarms in the isotropic phase are optically and dynamically uncorrelated at equilibrium for the SA-I or N-I transition. They coexist with the isotropic phase. Consequently from a thermodynamically and crystallographic point of view the isotropic phase fulfils the definition of a liquid.

The transition order can be determined by thermal analysis and in this respect the 8CB has been extensively studied [117]. The thermal analysis of the 8CB is presented in figure 2.4 and shows a sharp nematic to isotropic transition at $40°C$.
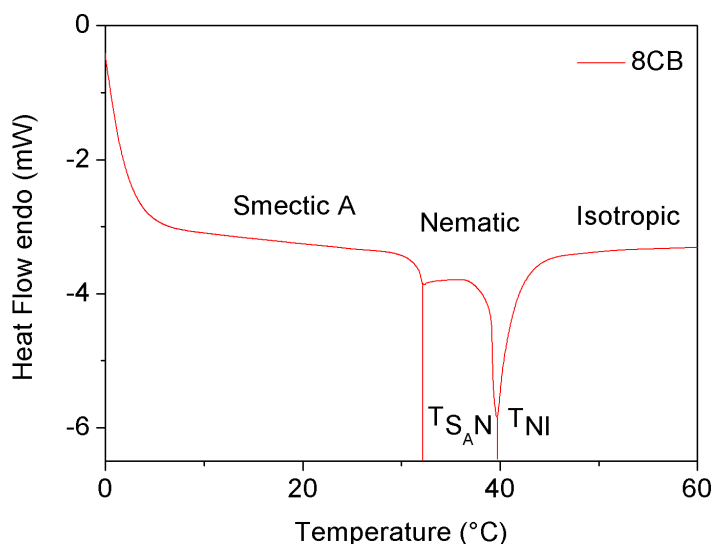
Figure 2.4: DSC data of the 8CB. The molecule shows two transitions: From the smectic A to the nematic phase T_{SAN} and from the nematic to the isotropic phase T_{NI}. The thermal analysis was carried out using a TA instruments Q100 DSC with a temperature gradient of $10C°/min$. The expected crystallization peak only appears at slower temperature gradients. The first order transition from the nematic to the isotropic phase is characterized by sharp peak similar to the process of melting and corresponds to a large amount of energy involved.

Figure 2.5 shows the thermal analysis of the LCP95 and the PACN. The LCP95 presents a smectic A to isotropic(SA-I) transition at $T_{SAI} = 79.80°C$ and a glass / crystalline transition (depending on the cooling conditions) at $T_g = 54°C$. The PACN exhibits a nematic-isotropic (N-I) transition at $T_g = 124°C$ and a glass transition at $T_g = 54°C$.
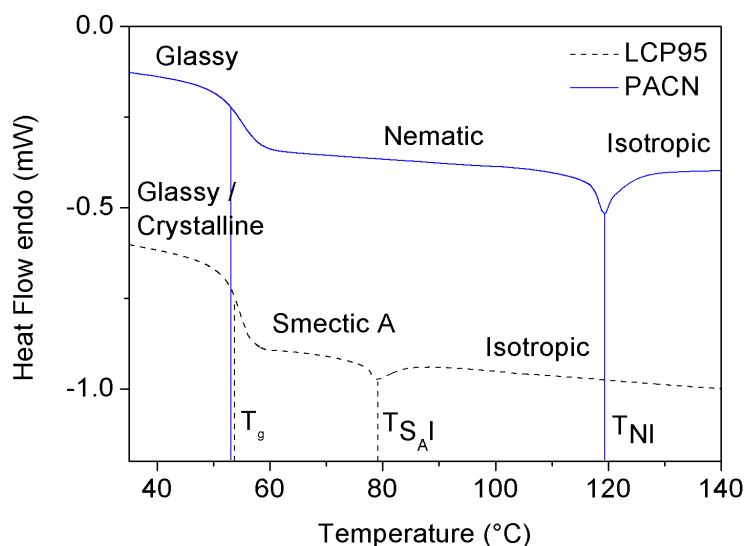
Figure 2.5: DSC data of the LCP95 and PACN. Both molecules show a first order transition from the smectic A (LCP95) or the nematic (PACN) to isotropic phase though by a around a factor 8 weaker than in the case of the 8CB. Additionally the PACN and the LCP95 show a glassy transition whereas the latter does crystallize for very long cooling times (several days). The thermal analysis was carried out using a TA instruments Q100 DSC with a temperature gradient of $10C°/min$.

2.1.2 Conventional rheology of the isotropic phase

We first present the results of VE measurements obtained with the conventional procedure which consists in using aluminium surfaces and probing sample thickness larger than $0.5mm$. Figures 2.6(a) and (b) show the dynamic behaviour of the 8CB and the LCP95 in the isotropic phase. For both cases we observe a viscous modulus G'' going with ω yielding the dynamic viscosity. From a conventional, macroscopic rheological point of view the isotropic phase of low molecular weight liquid crystals behaves as a Newtonian liquid showing no shear elastic properties at low frequencies.

Due to its polymeric character the PACN presents visco-elastic properties with a flow behaviour at low frequencies (Maxwell behaviour) as presented in figures 2.6(c). In the literature, the early standard studies of Side-Chain Liquid Crystal Polymers have shown that they behave essentially like ordinary flexible polymer melts 2.6(d). The terminal low frequency dynamic behaviour reveals a conventional visco-elastic liquid. The viscous modulus G'' obeys to a ω - scale and the elastic modulus G' obeys a ω^2 - scale indicating an apparent terminal flow behaviour. This comportment persists even until higher molecular masses than ordinary polymers, where usually chain entanglements emerge [119]. The liquid crystalline nature does not lead to any particular dynamics above the isotropic transition [119–122]. The characteristic terminal relaxation times are of the same order as those reported in conventional visco-elastic liquids and lie around $\tau_{relax} = 10^{-3} - 10^{-2}s$.

Assimilated to ordinary viscous liquids, the isotropic phase is not supposed to exhibit solid-like properties. In the following sections, we will show that these visco-elastic curves correspond to the second linear regime and that the primary response of the isotropic phase is the solid-like regime.

(a) 8CB

(b) LCP95

(c) PACN

(d) PMAM
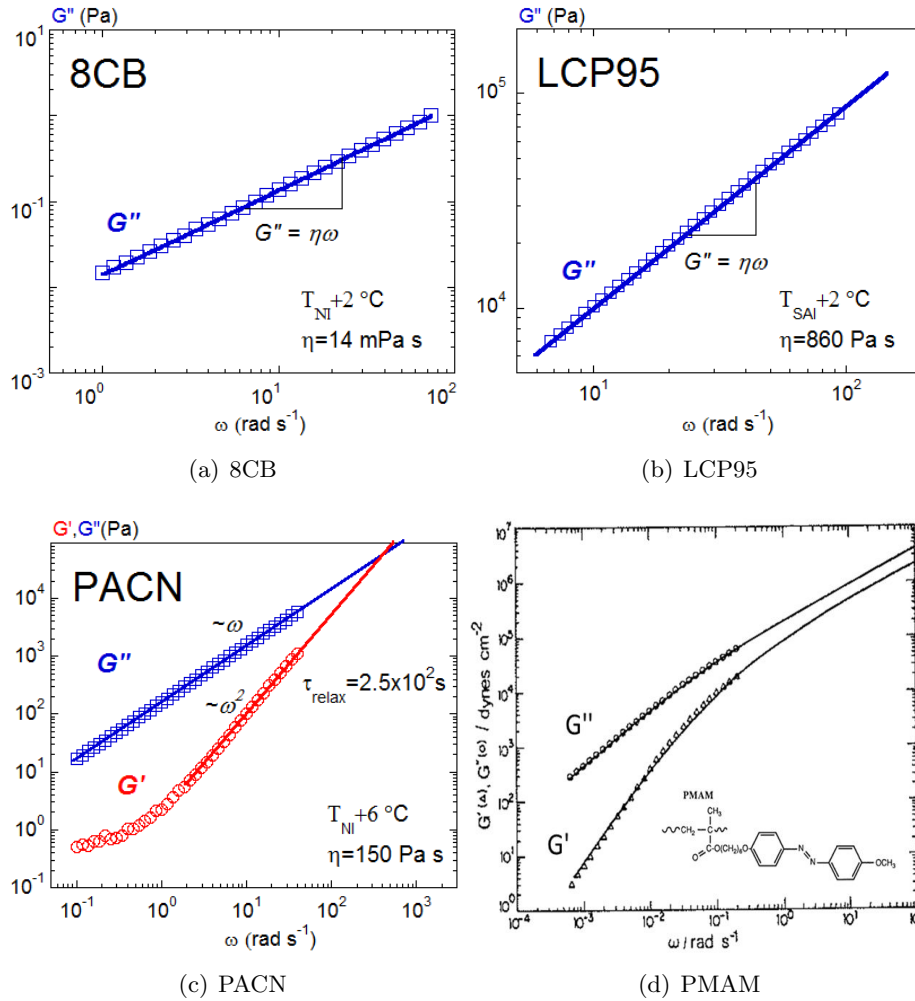
Figure 2.6: Visco-elastic spectra of the 8CB (low molecular weight LC), LCP95 (12 repetitive units LC) and PACN (80 repetitive units LC) obtained by an ARES II Rheometer under conventional, macroscopic conditions. (a),(b) The viscous modulus G'' versus the frequency for the 8CB (a) and the LCP95 (b) $2°C$ above the isotropic transition. The dynamic comportment reveals a ω scaling of the viscous modulus indicating a Newtonian behaviour yielding the respective viscosities (c) Dynamic behaviour the PACN. The isotropic phase at $6°C$ above the transition exhibits a visco-elastic behaviour with G'' scaling with ω and G' going with $\sim \omega^2$ (flow behaviour). (d) The dynamic behaviour of the isotropic phase of a SCLCP (PMAM) as reported in the literature [119].

2.2   Signal analysis in wetting improved Dynamic Mechanical Analysis: Identification of a low frequency elasticity

The evidence of a low frequency (=at long times) shear elasticity in liquids is an experimental challenge. Dynamic relaxation is one of the few techniques that gives access to long relaxation times. Experimentally the initial molecular equilibrium is disturbed by an applied stress which may be mechanical, either shear or compression, or in the case of polar molecules it may be applied magnetically/electrically [9]. The attainment of a new equilibrium state following the stress application is not instantaneous but takes a finite time which depends on the ability of molecules to move relative to their neighbours. In the case of a mechanical analysis, the yielding stress in the sample must result from the applied force (causality) but it must not change the mechanical properties of the material (linearity). This combined principle (causality-linearity) guarantees that the real and imaginary part of the time-dependant measurement are related (Kramers-Kronig relation). In principle, any form of time dependent stress function may be used and the dynamic properties evaluated from the ratio of the resulting strain to applied stress. For practical reasons and for ease of analysis, two types of stress variation are used, either a step function (Heaviside) or a harmonic variation at a specified frequency (oscillatory). While the sample is placed between to surfaces, one mobile the other static, the excitation can be an external stress (stress-controlled) or a deformation (strain-controlled), depending on the apparatus. For a strain controlled oscillatory deformation with amplitude γ_0 and a frequency ω we can write:

$$\gamma(t) = \gamma_0 sin(\omega t) \tag{4}$$

The strain amplitude γ_0 presents the applied deformation l in simple shear geometry divided by the sample thickness e. Since the deformation and sample thickness have the dimension of a length the strain is dimensionless and is most often given in percent. The resulting stress σ is measured by a sensor attached to the static surface:

$$\sigma(t) = \sigma_0 sin(\omega t + \phi) \tag{5}$$

Where ϕ is the phase shift or loss angle. It presents the loss of energy associated to the viscous character of the sample.

2.2.1   Causality-linearity conditions: definition of the visco-elastic moduli

In order to guarantee that the material is not distorted and that intrinsic properties are probed it has to be ensured that the relation $\frac{\sigma(t,\gamma)}{\gamma}$ yields a constant (linear domain) in the concerned frequency domain. This proportionality coefficient defines the complex visco-elastic modulus G^* of the material:

$$G^*(\omega) = \frac{\sigma(t)}{\gamma} = \frac{\sigma}{\gamma}(cos(\phi)sin(\omega t) + sin(\phi)cos(\omega t)) \tag{6}$$

Which can be written in its complex form:

$$G^*(\omega) = G'sin(\omega t) + G''cos(\omega t) = G'(\omega) + iG''(\omega) \tag{7}$$

Where:

- G', the real part of the complex modulus is called the storage or (shear) elastic modulus. It is in-phase in respect to the applied deformation.

- G'', the imaginary part of the complex modulus is called the loss or viscous modulus. It is phase shifted by $\frac{\pi}{2}$ in respect to the applied deformation.

The moduli are macroscopic quantities and their unit is the Pascal.

In an dynamic relaxation experiment the initial input (strain) and output (stress) signals as shown in figure 2.7(a) are converted to the visco-elastic moduli depicted as a function of the frequency. While the signals intensities define the magnitude of G^* their phase shift attributes this magnitude to either G' or G'' which are interpreted in terms of solid-like and liquid-like behaviour. A liquid-like character is identifiable by a vanishing response at low frequencies whereas a solid-like behaviour (elastic) exhibits a finite response independent of the frequency (Figure 2.7(b)). A perfect solid-like response exhibits no phase shift. Experimentally, solid-like materials exhibit always a short delay due to internal freedom degrees and thus exhibits a non-zero G''. When the phase shift is lower than $\Delta\phi < \frac{pi}{4}$, the elastic component G dominates the viscous component G'' (Figure 1 right). If the output response of the material presents a phase shift larger than $\frac{\pi}{4}$, then the viscous component G'' dominates the elastic component G (Figure 2.7(c)). The sample behaves liquid-like. If the phase shift reaches $\frac{\pi}{2}$ (G vanishes), the sample is defined as purely viscous. A (Maxwell) liquid-like behaviour displays typically a vanishing response characterised by a ω-scaling of the viscous modulus and a ω^2-scaling dependence of the elastic modulus.
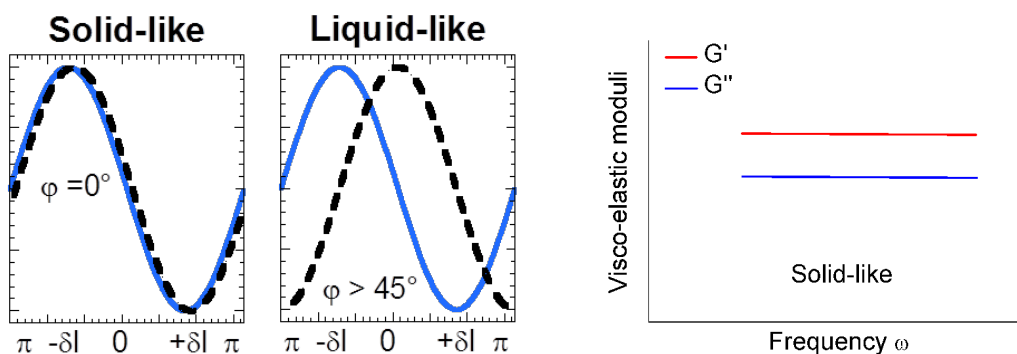
(a) The initial input (strain, black dashed) and output (blue, continuous) signals.

(b) Solid-like behaviour
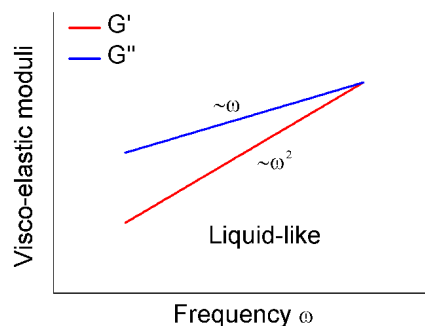
(c) Flow behaviour

Figure 2.7: Analysis of a dynamic relaxation experiment. (a) The phase shift between input and output signal permits the determination of a solid-like (no or very small phase shift) or liquid-like (phase shift larger than $\frac{\pi}{2n}$) behaviour at a given frequency. (b) The solid-like or elastic-like comportment presents an elastic modulus indifferent in respect to the frequency or superior to the viscous modulus. (c) A liquid-like or flow behaviour is characterized by an dominating viscous modulus going with ω^2 while the weaker elastic modulus goes with ω

.

The conversion of the strain / stress to the visco-elastic moduli is usually carried out automatically by the apparatus and up-to-date only few attention is given to the initial signals. Additionally since the moduli can be calculated by knowing one of the two via the Kramer-Kronigs relation rheometers consistently measure the in-phase component and
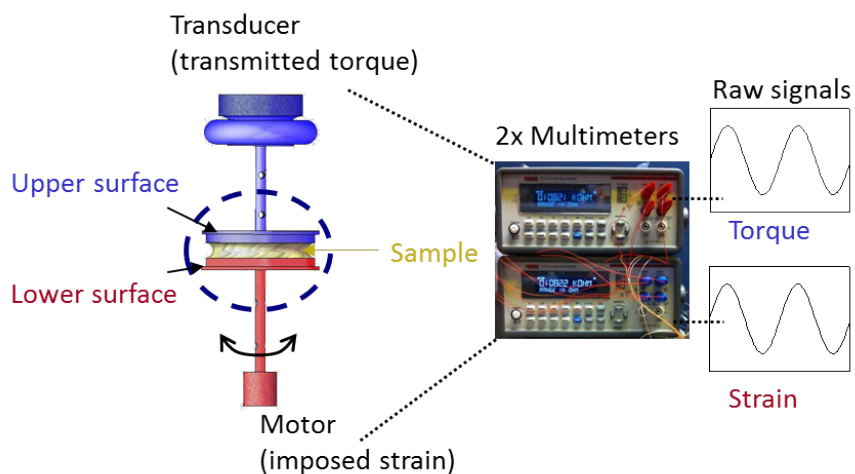
Figure 2.8: Scheme of the dynamic mechanical analysis. The sample is initially at rest between a mobile and a static surface. The oscillatory movement of the lower surface provokes a stress in the sample that is transmitted by the molecules to the sensor attached to the static surface. Analysis of input (strain) and output (stress) signals permits to deduce the phase shift between them.

calculate the loss modulus. In conventional experiments the experimentalist does not access to the raw signals. We have implemented the rheometer with two multi-meters: one connected to the motor that applied the strain and one to the sensor that measures the torque, to access to the input strain and output transmitted stress signals. Experimentally the key point is the transmission of the applied stress to the sample by the surface and from there its communication to the sensor. Figure 2.8 shows the line of transmission in a dynamic relaxation experiment. The stronger the transmission in the very first step the higher the measured signals. In conventional experiments the optimum transmission is supposed to be guaranteed by the postulated no-slip condition. In the following section we will show that this condition is not fulfilled for common surfaces and a most effective transmission is thus not automatically ensured.

2.2.2 Role of the boundary conditions: Surface effects, wetting and slippage

How is it possible that a terminal elastic plateau in liquids we have seen in section (*1.4*) has been observed by certain groups while in conventional experiments this comportment is not detected? As the sample thickness e decreases the interactions between the surface and the liquid molecules become more important and at a certain point when approaching the scale of the molecules itself surface effects become predominant. While this interpretation might hold true for measurements with the Surface Force Apparatus (e ca. 4x the molecular size) and maybe but less likely the Piezorheometric measurements (e at least 100x the molecular size) the conventional experiments by Noirez et al. (e at least 1000x the molecular size) exclude an interpretation in terms of a surface induced effect. The surface condition is however a central parameter in detecting the under conventional conditions hidden elastic properties:

Being of most importance in a rheological experiment, the possible influence of the surface roughness, the wettability properties on the dynamic measurement and the presence of gas and (nano,micro)bubbles in the fluid have to be considered. Often it is not differentiated between rough and smooth surfaces, gas polluted liquids and homogeneous liquids, hydrophilic and hydrophobic surfaces. However, surface roughness, presence of gas and wettability are known to favour the violation of the no-slip boundary condition [123, 124]. The "Tolstoi formula" [125, 126] has been an attempt to relate the wetting property which is determined by measurements of the equilibrium contact angle θ to the slippage ability.

$$b \sim exp(\frac{\delta^2 \gamma_{lg}(1 - cos\theta)}{kT} - 1) \text{ Total wetting is given for } \theta = 0 \qquad (8)$$

Where δ is parameter related to the molecular size, γ_{lg} is the liquid surface tension and b is the slippage length. The latter is defined as the distance from the surface corresponding to the origin of the velocity gradient as depicted in figure 2.9. This equation considers the case of an ideal smooth surface and thus neglects any influence of surface roughness. The later can, if its magnitude is larger than the slip length b, mask slip [127, 128]. As it
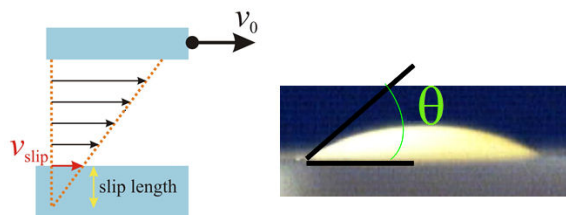
Figure 2.9: Definition of the slippage length b under simple shear (left) and the contact angle θ (Photograph of a polymer droplet on a flat substrate) (right).

is the origin of the motion of transfer, the surface plays an important role in rheological experiments. If the dynamic transfer is incomplete which can be the case for partial slippage, the measurement may underestimate the material's response. The dynamic transfer is improved and a movement/slip of the liquid on the surface is avoided for total wetting conditions. Total wetting acts an anchorage for the molecules and their interaction with the surface may be seen as an activated process:

$$t \sim exp(-\frac{U}{k_b T}) \tag{9}$$

Where t is a dynamic parameter (e.g. the life time) of the contact and U the energy of interaction of the molecules with the surface. For total wetting conditions U is large and t is small. Short life time contacts are less disturbed under shear strain than long life time contacts. This mechanism might preserve the no-slip boundary condition. The degree of wetting can be determined via the contact angle method [124, 125]. The evolution of the profile of a liquid drop on a given surface is measured versus the time. The contact angle θ is the angle of the drop tangent in respect to the surface. In the case of total wetting the drop spreads uniformly on the entire surface. The liquid is progressing via a thin layer called molecular part in front of the drop which is typical of complete wetting. While moving this layer avoids to trap air between the liquid and the substrate. Figure 2.10 shows that the metallic substrates conventionally used for the rheological measurements (Aluminium, stainless steel, glass) do not provide a total wetting interaction. The molecular
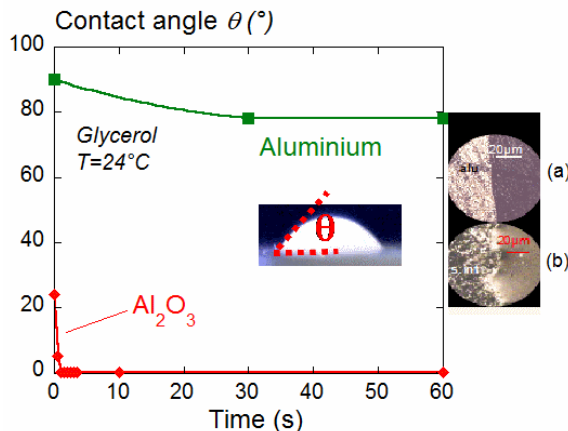
Figure 2.10: Evolution of the contact angle versus time for glycerol at $24°C$ deposited on aluminium (green filled boxes)and alumina (red filled diamonds). The contact angle reaches a finite stationary value of $80°$ the case of aluminium (partial wetting), whereas it vanishes in the case of alumina (total wetting).

part is absent and a stationary contact angle $\theta = 80°$ is observed. In contrast, other substrates as alumina exhibit a rapid propagation of the liquid via a molecular part and at a macroscopical scale a final total wetting state ($\theta \equiv 0$). The boundary conditions are known to have significant quantitative impact on the interpretation of experimental results ref.

2.3 Identification of a low frequency shear elasticity in the isotropic phase of 8CB

An improvement of the transfer of the motion to the liquid is achieved by ensuring total wetting boundary conditions between the liquid and the substrate using alumina plates of $40mm$ diameter and by probing small gaps. The oscillatory motion and the shear stress measurement are provided using a dynamic force apparatus (ARES2). A 7-digits voltmeter (Keitley, Data rate: one signal each $3/100s$ with a dead time of $3/1000s$) measures the voltage of the motor imposing the oscillation (input wave), while another 7-digits voltmeter measures the voltage associated to the sensor (output wave). This setup enables the simultaneous access to the strain/stress signals and to the dynamic profile versus frequency and strain amplitude. The applied wetting improved protocol gives access to long relaxation times. It consists in applying an as weak as possible oscillatory strain to the sample to probe its equilibrium properties (at rest). The equilibrium state properties are described as a function of the frequency (ω), typically from $0.1rad/s$ up to $100rad/s$.

2.3.1 Signal analysis of the terminal response

Our fundamental result is presented in figure 2.11. It shows the raw wave signals of the applied strain and the transmitted stress in the terminal frequency zone ($5 - 15rad/s$) of the isotropic phase of the 8CB ($T = T_{NI} + 1°C$) at a sub-millimeter sample thickness $0.050mm$. For a small strain amplitude (1.5%) wave signals superpose which indicates a solid-like or gel-like response. Instead of the usually expected phase shifted stress response we observe an elastic behaviour of the isotropic phase.

The in-phase stress response is delicate and influenced by several parameters. In the following we examine the wave signals and their phase behaviour as a function of the applied strain amplitudes and the frequency. Figure 2.12 illustrates the input sinusoidal wave and the output shear stress over one period transmitted by a layer of $0.050mm$ in the isotropic phase of 8CB for low, intermediate and large strain amplitudes. The liquid crystal is solicited at $T = 41.5°C, (\pm 0.05°C)$, i.e. at $T = T_{NI} + 1°C$ above the N-I transition temperature (in situ optically verified).

At low strain amplitude ($\gamma_0 = 6\%$,(a)) the input and output waves show almost superposition with a phase shift $\Delta\phi$ of $12°$. This indicates a nearly instantaneous sample response i.e. a solid-like response. A similar in-phase signal is observed for a wide range of frequencies from 1 up to $40rad/s$. Since the low frequency output shear stress is sinusoidal (linear regime), it can be described in terms of elastic G' and viscous G'' moduli. On the right side of figure 2.12(a) the evolution of G' and G'' is presented as a function of the frequency at low strain amplitude. Being at least three times as large as G'', the elastic shear modulus
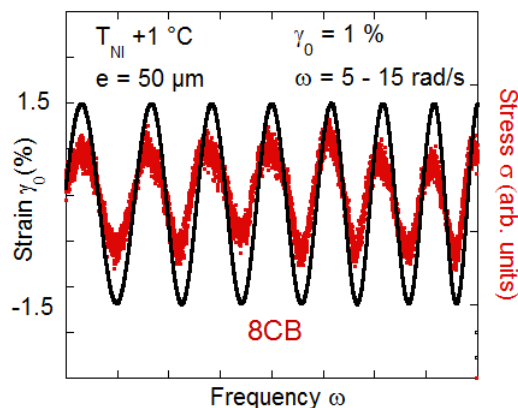
Figure 2.11: Superposition of the input strain and output stress signals indicating an elastic-like response for total wetting conditions. The result shown is observed at low frequencies ($5 - 15 rad/s$) and a constant small strain amplitude (1.5%) in the isotropic phase of the 8CB ($T = T_{NI} + 1°C$) of $0.050mm$ thickness.

G' dominates its viscous counterpart. The elastic modulus G' shows no apparent dependencies on the frequency. The viscous modulus G'' is also nearly constant at low frequency and does not obey a ω-scale as it is expected for a liquid behaviour. Therefore both moduli indicate a non-flowing state.

For intermediate strain amplitudes ($\gamma_0 = 100\%$, figure 2.12(b)), the output signal becomes slightly distorted and its phase is shifted with respected to the input signal. The insets in the strain/stress diagrams in figure 2.12 show the discrepancy ($\Delta\sigma$) between the sine function model and the experimental points. For small ($\gamma_0 = 6\%$) and for large ($\gamma_0 = 8000\%$) deformations a straight line is obtained indicating a convenient fit while for intermediate ($\gamma_0 = 100\%$) strain amplitude the subtraction yields a pronounced periodical deviation. The latter displays two harmonics over one period (inset in the intermediate figure 2.12). The appearance of these harmonics can be interpreted as the entrance into the non-linear regime where the moduli G' and G'' become strongly strain and frequency dependent. A modelling of the signals in terms of G' and G'' is questionable. The occurrence of a slip mechanism might be addressed to illustrate the sin wave distortion in this regime.

At large strains (figure 2.12(c)), the output wave recovers its sinusoidal shape enabling a modelling in terms of G'' and G'. The phase shift is nearly $\frac{\pi}{2}$ indicating a viscous behaviour. The corresponding relaxation spectrum displayed on the right side of (figure 2.12(c)) confirms the liquid-like response; G'' obeys a ω-scaling with a slope of $14mPas$, yielding a dynamic viscosity in agreement with the literature data [129].

Figure 2.12: Input shear strain sine wave (black squares) and output shear stress wave (red dots,) of 8CB in the isotropic phase ($41.5°C$) at $0.050mm$ gap thickness for low ($\gamma_0 = 6\%$, (a)), intermediate ($\gamma_0 = 100\%$, (b)) and high ($\gamma_0 = 8000\%$, (c)) strain amplitudes. The dashed black and continuous red lines correspond to a sine modelling of the input (- - -) and the output waves (—) of the data points. Insets: Data resulting from the subtraction of the model sine function from the data points ($\sigma_{experimental} - \sigma_0 = \Delta\sigma$, green boxes). Dynamic relaxation spectra (G: red dots; (G'' blue squares) are shown for (a) and (c)[42].

2.3.2 Elastic "pre-regime" - Dependence on the strain amplitude

We have seen that the in-phase (solid-like) response is easily lost upon increasing the perturbation of the sample being progressively replaced by a completely out-of-phase (viscous) response. Figure 2.13 presents the evolution of the dynamic moduli in the isotropic phase on increasing the strain amplitude from 0.3% up to $10^4\%$. The experiment was carried out at a given frequency of $\omega = 5rad/s$ and a gap thickness of $0.050mm$.
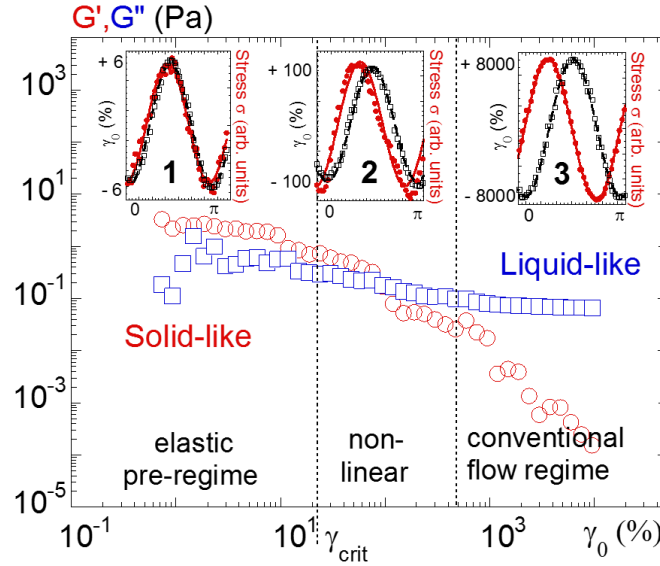
Figure 2.13: Strain dependence of the visco-elastic moduli (G'': red circles; G'' blue squares) of 8CB in the isotropic phase ($41.5°C$) at $0.050mm$ gap thickness at a frequency of $\omega = 5rad/s$ (γ_0 evolves from 2.8 up to $10^4\%$). The vertical dashed bars delimit the zone where the output signal exhibits periodic distortions from a pre-elastic regime at small strains (signals in phase) and the conventional flow regime (signals phase shifted by $\frac{\pi}{2}$) Insets: Periodic stress/strain signals at small (1), intermediate (2) and large (3) strain amplitudes ($\gamma_0 = 6\%$, $\gamma_0 = 100\%$ and at $\gamma_0 = 8000\%$ respectively).

At low strain amplitude, the elastic modulus G' dominates the viscous modulus G'' which contributes in average only to about 4% of the total modulus ($\sqrt{(G'^2 + G''^2)}$). Upon increasing the strain amplitude both, the elastic and viscous moduli decrease, with a more pronounced fall of G' leading to a transition from solid-like to liquid-like behaviour. At high strain amplitude, the viscous modulus dominates the elastic modulus, the latter becoming negligible with respect to the total modulus (less than 1%). The usual and generally expected viscous behaviour of the liquid crystal in the isotropic phase is recovered by

applying high strain amplitudes, thus away from mechanical equilibrium conditions. This is very conveniently evidenced as one examines the input and output wave signals. Whereas in the solid-like zone, the pre-elastic regime, the signals superpose they become phase shifted by $\frac{\pi}{2}$ in the liquid-like, conventional flow regime. The intermediate regime or transition zone from solid-like to a liquid-like behaviour is delimited by a critical strain threshold γ_{crit} (here $\gamma_{crit,8CB} = 24\%$)above which the wave signals become distorted confirming the results from figure 2.12. This critical value may be interpreted as the maximum strain the liquid, or more precisely the elastic network can withstand before it collapses upon entering the flow regime. As a major result for applying the wetting improved protocol a linear solid-like regime is found to precede the conventional flow regime. The solid-like response collapses upon entering the viscous regime.

2.3.3   Shear elasticity vs temperature in the isotropic phase of 8CB

For a better understanding of the origin of the elastic response, the experiments were also carried out for $T < T_{NI}$ in the nematic and smectic phases. Figure 2.14 shows the values of the shear elasticity measured at low thickness versus temperature. Both nematic and isotropic phases exhibit values of G of around $0.81 Pa$ with no significant temperature dependency upon crossing the N-I transition temperature. This result indicates that neither pretransitional dynamics nor the nematic phase have an influence on the elastic response. Similar observations were reported for liquid crystal polymers [29, 110]. The situation is different regarding below the SmA-N transition. Due to the presence of a positional order of the smectic phase, the values of the shear elasticity obtained in this phase exceed at least by two decades the ones found for the nematic and isotropic phases.
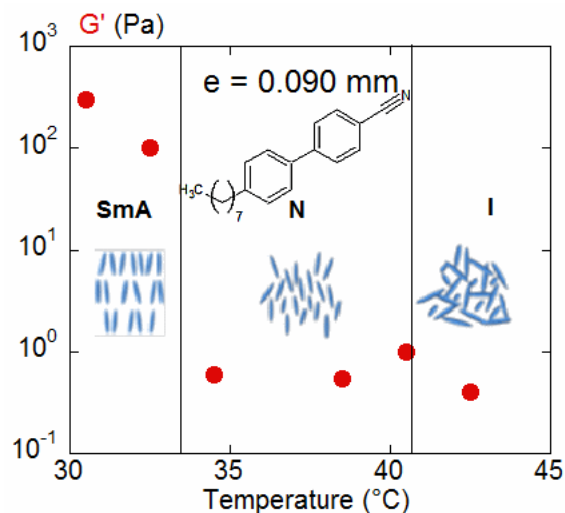
Figure 2.14: Shear modulus G' of 8CB versus temperature at $0.090 mm$ gap thickness. The vertical lines indicate the transition temperatures of the smectic (SmA) - nematic transition (N) and the nematic - isotropic (I) transition.

2.3.4 Sample thickness dependence of the elastic modulus

The thickness of the sample has also a significant influence on the elastic response. Figure 2.15 presents the evolution of the elastic modulus of 8CB in the isotropic phase as a function of the gap thickness. The average values of G' increase upon decreasing the gap thickness from 0.100 down to $0.050mm$ following an exponential law:

$$G' = (G'_0 - G'_\infty exp - (\frac{e - e_{crossover}}{e_0})^{\frac{1}{2}} + G'_\infty \qquad (10)$$

up to around $e_{crossover} = 70\mu m$, thickness value at the onset of the saturation with $G'_0 = 1.7Pa$ the saturated shear modulus, $e_0 = 7.3\mu m$ a constant length scale and $G_\infty = 0.12Pa$ the shear modulus at infinite thickness which is negligible. The rapid lowering of the shear modulus might result from multiple effects as increased voids, degree of freedom or loss of the shear stress transmission from and to the surfaces. In contrast, wall or capillary effects cannot explain the reinforcement of the moduli at low thickness. The probed gap distances far exceed coherence lengths that lie in the order of several nanometres by at least a factor of 1000 [117, 118, 130, 131]. An interpretation in terms of Franks elasticity [118] is also irrelevant since the elasticity is transmitted in the isotropic phase. The nematic and isotropic phases yield similar shear moduli indicating that neither pretransitional dynamics nor the symmetry of the phase have an influence on the elastic response.
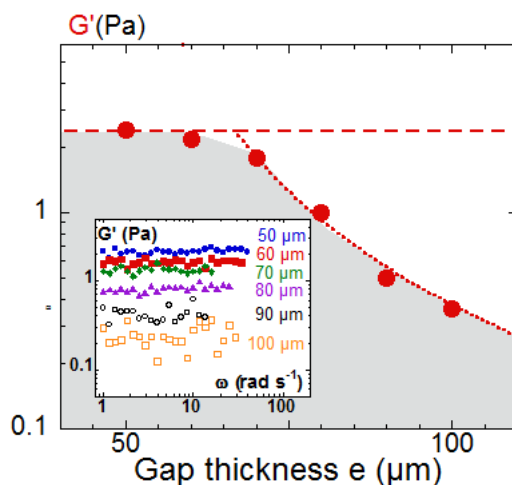
Figure 2.15: Evolution of the shear modulus G' of 8CB versus gap thickness measured in the isotropic phase at $(T = T_{NI} + 1°)$. Above $70\mu m$, the values fall rapidly following an exponential decrease (small dashed points). The inset displays the shear modulus from 1 up to $40rad/s$ at different gap thickness. the elastic behaviour is no more measurable above $100\mu m$.

2.4 Identification of a low frequency shear elasticity in the isotropic phase of LCP95

Experimentally the identification of a low frequency shear elasticity for the LCP95 was carried out under similar conditions to the 8CB. Additionally to the total wetting alumina plates conventionally used glass plates both of $20mm$ diameter were used to discuss the influence of wetting. Again and for both substrates the applied protocol consists in applying an as weak as possible oscillatory strain to the sample to probe its equilibrium properties.

2.4.1 Signal analysis of the terminal response

As for the 8CB we an improved wetting enables us to observe an elastic, in-phase behaviour of the raw stress and strain signals in the isotropic phase of LCP95, here at $T = T_{SAI} + 25°C$ and at $0.170mm$ sample thickness. Figure 2.16 shows the raw wave signals recorded for at a low frequency $(0.5rad/s)$ and a constant strain amplitude (1.0%).
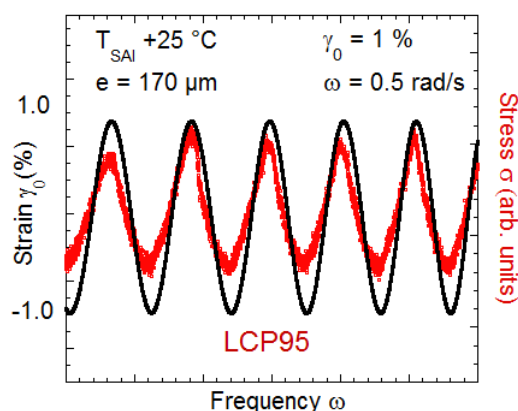
Figure 2.16: In-phase behaviour of the input strain and output stress signals for the isotropic phase of the LCP95 $(T = T_{SAI} + 25°C)$ at a thickness of $0.170mm$. The raw signals were recorded shown at a low frequency $(0.5rad/s)$ and a constant small strain amplitude (1.0%).

The careful examination of the raw signals as a function of the strain amplitude and the frequency reveal the evolution of the elastic property with the strain and frequency: Figure 2.17 illustrates the input sinusoidal wave and the output shear stress wave over one period transmitted by a layer of $0.170mm$ in the isotropic phase of LCP95 for low, intermediate and large strain amplitudes. The liquid crystal is here solicited at $T = 105°C, (\pm 0.05°C)$, i.e. at $T = T_{SAI} + 25°C$ above the SA-I transition temperature.

Identically the input and output waves show almost superposition with a phase shift $\Delta\phi$ of $10°$ at low strain amplitude ($\gamma_0 = 1\%$,(a)). Again the sample response is nearly instantaneous, it presents a solid-like response. The in-phase signal is observed for a wide range of frequencies from 1 up to $40 rad/s$. Since the low frequency output shear stress wave is sinusoidal (linear regime) the description in terms of G' and G'' is justified. On the right side of figure 2.17(a) the evolution of G' and G'' is presented as a function of the frequency at low strain amplitude and as for the 8CB the elastic shear modulus G' dominates its viscous counterpart G'' by a factor around three. Due to the higher molecular mass and the strong adhesion properties of the LCP95 the elastic modulus G' is strongly enhanced by a factor of around 100 in comparison to the 8CB while its molecular weight is only 12 times higher. The viscous modulus G'' is also frequency independent at low frequency and does not obey a ω-scale.

For intermediate strain amplitudes ($\gamma_0 = 50\%$, figure 2.17(b)), the output signal becomes slightly distorted and its phase is shifted with respected to the input signal. The insets in the strain/stress diagrams in figure 2.17 show the discrepancy ($\Delta\sigma$) between the sine function model and the experimental points. For small ($\gamma_0 = 1\%$) and for large ($\gamma_0 = 800\%$) deformations a relatively straight line is obtained indicating a convenient fit while for intermediate ($\gamma_0 = 50\%$) strain amplitude the subtraction yields a pronounced periodical deviation. The appearance of these distortions can again be interpreted as the entrance into the non-linear regime where the moduli G' and G'' become strongly strain and frequency dependent. A modelling of the signals in terms of G' and G'' is not justified sin wave distortion in this regime may be addressed to slip.

At large strains (figure 2.17(c)), the output wave recovers its sinusoidal shape justifying a modelling in terms of G'' and G'. The analysis of the signal indicates that phase shift is nearly $\frac{\pi}{2}$ and that actually the in-phase component G' cannot be determined. The corresponding relaxation spectrum displayed on the right side of (figure 2.12(c)) confirms the liquid-like response; G'' obeys a ω-scaling with a slope of $160 Pas$, yielding the dynamic viscosity.
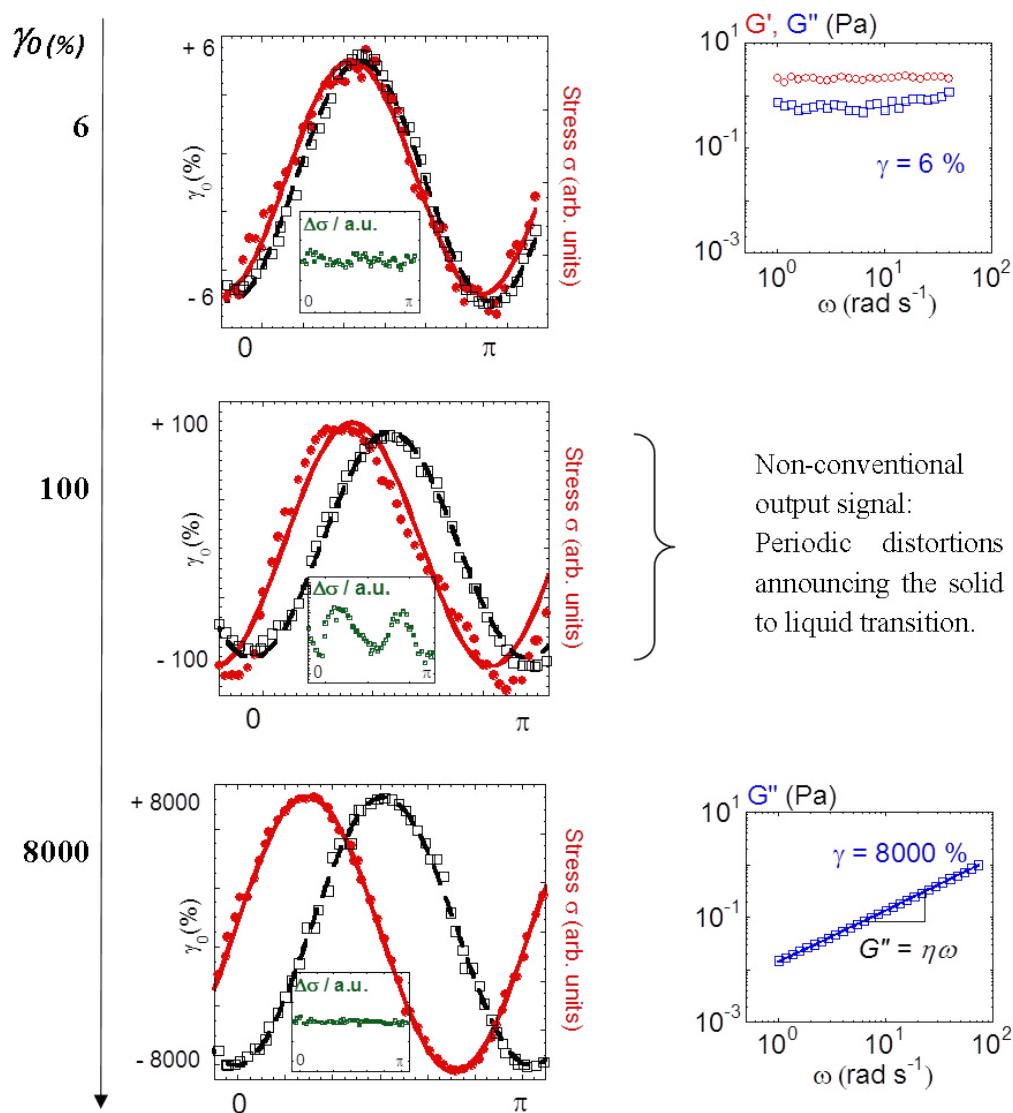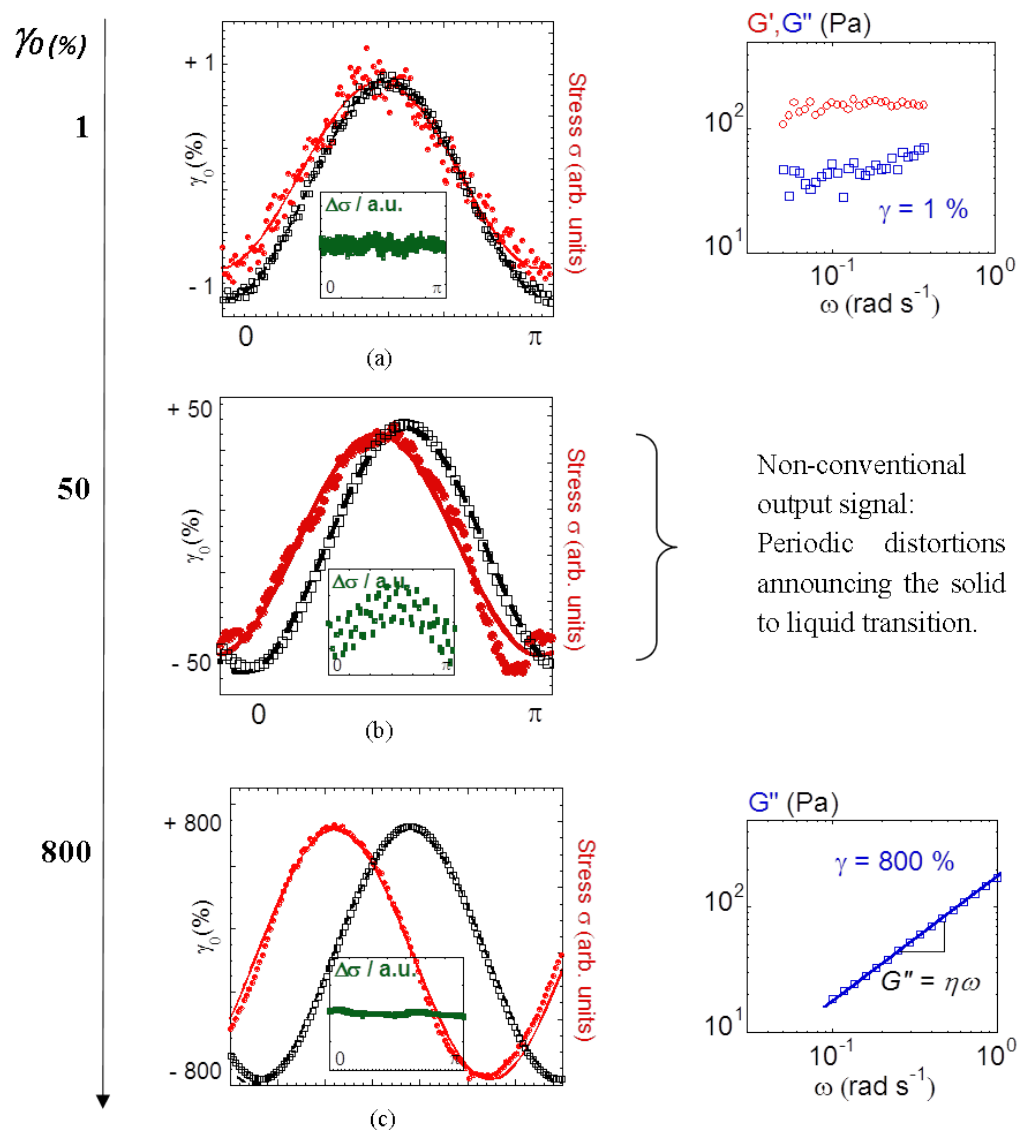
Figure 2.17: Input shear strain sine wave (black squares) and output shear stress wave (red dots,) of LCP95 in the isotropic phase ($105°C$) at $0.170mm$ gap thickness for low ($\gamma_0 = 1\%$, (a)), intermediate ($\gamma_0 = 50\%$, (b)) and high ($\gamma_0 = 800\%$, (c)) strain amplitudes. The dashed black and continuous red lines correspond to a sine modelling of the input (- - -) and the output waves (—) of the data points. Insets: Data resulting from the subtraction of the model sine function from the data points ($\sigma_{experimental} - \sigma_0 = \Delta\sigma$, green boxes). Dynamic relaxation spectra (G: red dots; (G blue squares) are shown for (a) and (c).

2.4.2   Elastic "pre-regime" - Dependence on the strain amplitude

Increasing the strain amplitude at a constant frequency revealed the existence of an elastic pre-regime in the isotropic phase of the 8CB. Above a critical strain value the solid-like response was lost and the dynamic response entered the conventional flow-regime. The strain dependence of the dynamic moduli for the LCP95 shows a similar behaviour.Figure 2.18 presents the evolution of the dynamic moduli in the isotropic phase on increasing the strain amplitude from 0.05% up to $3 \times 10^3\%$. The frequency was constant $\omega = 5rad/s$ and the gap thickness was $0.170mm$.
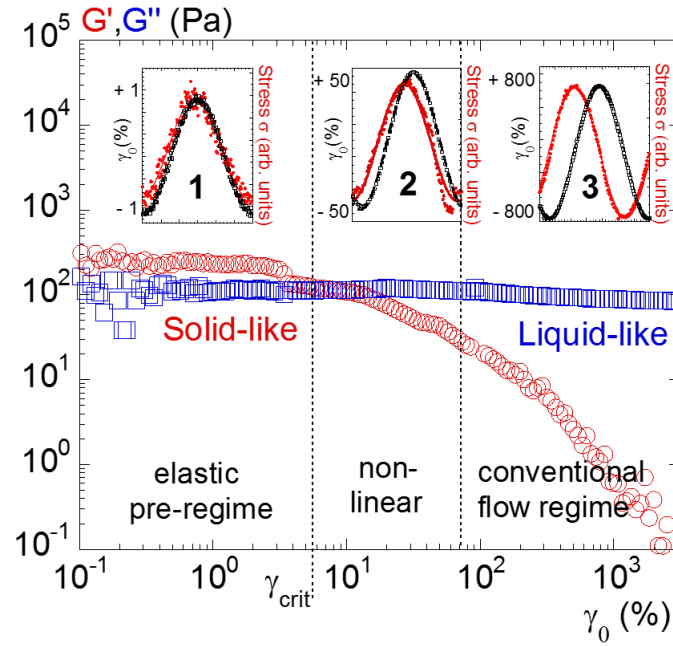
Figure 2.18: Evolution of the strain dependence of the visco-elastic moduli (G'': red circles; G'' blue squares) of LCP95 in the isotropic phase ($105°C$) at $0.170mm$ gap thickness at a frequency of $\omega = 0.5rad/s$ (γ_0 evolves from 0.05 up to $3x10^3\%$). The vertical dashed bars delimit the zone where the output signal exhibits periodic distortions from a pre-elastic regime at small strains (signals in phase) and the conventional flow regime (signals phase shifted by $\frac{\pi}{2}$) Insets: Periodic stress/strain signals at small (1), intermediate (2) and large (3) strain amplitudes ($\gamma_0 = 1\%$, $\gamma_0 = 50\%$ and at $\gamma_0 = 800\%$ respectively).

We can identify a solid-like regime at low strain amplitude where the elastic modulus G' dominates the viscous modulus G''. Due to the higher molecular mass the moduli are strongly enhanced ($G' = 300Pa$)in comparison to the 8CB ($G' = 3Pa$) and yield an elastic

plateau of a 100 times higher. Upon increasing the strain amplitude both, the elastic and viscous moduli decrease as seen for the 8CB. While we observe a comparable fall of G', the viscous modulus decreases less intense as in the case of the 8CB. Nevertheless the consequences are equal: We observe a transition from solid-like to liquid-like behaviour. At high strain amplitude, the viscous modulus dominates the elastic modulus, the latter becoming negligible with respect to the total modulus. The usual and generally expected viscous behaviour of the liquid crystal in the isotropic phase is recovered by applying high strain amplitudes. Again this is confirmed by the input and output wave signals. They are in-phase at small strain amplitudes and phase shifted by $\frac{\pi}{2}$ in the conventional flow regime. One enters the intermediate regime and loses the elastic dominated response above the critical strain threshold $\gamma_{crit} = 6\%$ which yields a fourth of the value of the 8CB in the case of the LCP95. This means that the elastic network of the isotropic phase of the LCP95 collapses at smaller strains than in case of the 8CB. The isotropic phase of the LCP95 may thus be seen as less gel-like and more solid-like. However the experiments have not been carried out at the same sample thickness and due to a pronounced fall of the moduli with e (2.15)the critical thresholds γ_{crit} may also change and this interpretation is precarious.

The decrease of the elastic modulus with the strain amplitude can be observed at a larger low frequency range. Figure 2.19 shows the terminal elastic plateau vs the frequency for small strain amplitudes between 1 and $5rad/s$. An increase of γ_0 results in a lowering of the plateau with no apparent dependence on the frequency. This validates the usage of any low frequency in the strain sweep experiment in figure 2.18.
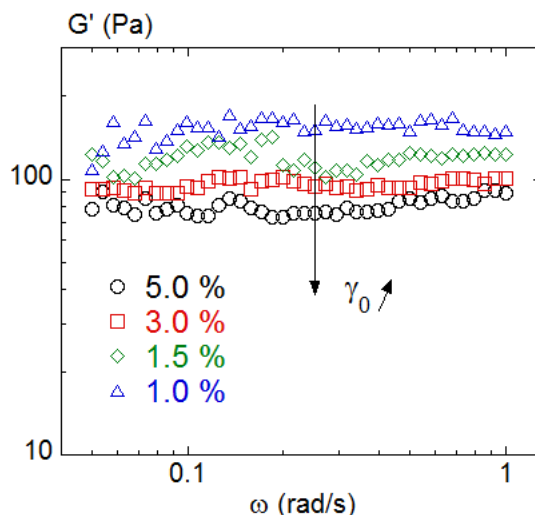
Figure 2.19: Shear modulus G' of LCP95 versus the frequency at $0.110mm$ gap thickness for different strain amplitudes at $T = T_{SA} + 25°C$.

2.4.3 Temperature dependence of the elastic response

The terminal elastic plateau was measured for several temperatures above the smectic - isotropic transition ($T_{SA} = 79.8°C$). Figure 2.19 shows its values at a thickness of $0.170mm$ versus temperature. Above T_{SA} the values of G' of around $170 - 190Pa$ behave indifferent in respect to the temperature from $82 - 112°C$. This result indicates that the pretransitional swarms present in the isotropic phase have no influence on the elastic response as for the 8CB. No usable values could be measured in the smectic phase. Below the smectic - isotropic transition and close to the glass transition the sample becomes very stiff making it difficult for the apparatus to give reliable data.
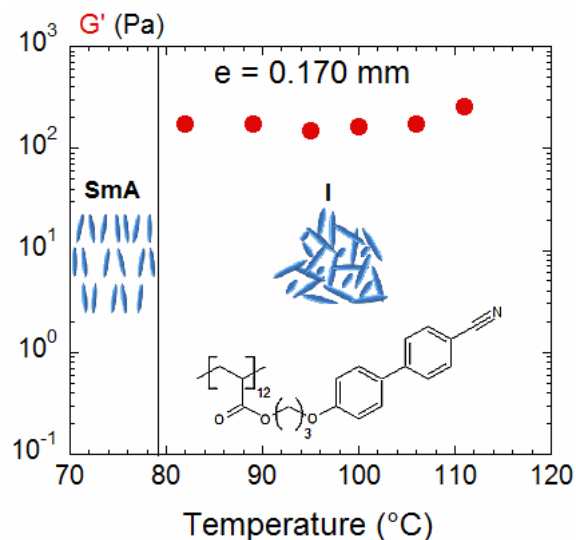
Figure 2.20: Shear modulus G' of LCP95 versus temperature at $0.170mm$ gap thickness. The vertical line indicates the transition temperatures of the smectic (SmA) - isotropic (I) transition.

2.4.4 Role of the surface: Partial vs Total wetting substrates

Magnitude of the strain amplitudes

The low frequency elastic property is usually not detected in standard measurements since this delicate signal is hardly experimentally measurable and mostly observable at low thickness geometry (sub-millimetre scale). It might be that in conventional experiments the flow regime is accessed for small strain amplitudes while for the usage of total wetting substrates e.g. alumina one observes first an elastic regime as soon as the smallest strain amplitudes and the conventional response only at very large strain amplitudes. This is probably due to the strong anchoring of the liquid molecules to the surface. When the molecules are strongly anchored it seems convenient that it takes more energy (e.g. a larger strain) to overcome the elastic network and enter the viscous flow regime. A similar behaviour has been observed for other total wetting substrates e.g. zirconium dioxide ZrO_2, and silicon carbide SiC.

Low frequency behaviour on glass and alumina substrates

Until so far we have compared the in-phase, elastic signals at low strain amplitudes with the out-of-phase, viscous signals at larger strains. In order to deduce the important role of the wetting condition we have applied the same protocol (low frequencies and small strain amplitudes) to the isotropic phase of the LCP95 on a wetting substrate and a conventional glass surface. Figure 2.21 shows the raw stress and strain signals (at a single frequency value, $\omega = 0.1 rad/s$) and the corresponding dynamic relaxation spectrum for the alumina (a) and the glass (b) surface. The experiments have a part from the surface been carried out under the same conditions at a sample thickness of $0.170mm$ and $T = T_{SAI} + 25°C$. Only the strain amplitude of differed slightly: $\gamma_0 = 1\%$ (a) and $\gamma_0 = 51\%$ (b). We observe that under the otherwise same conditions, the improvement of the anchoring has an enormous influence on the dynamic property of the isotropic phase. While on the conventional surface the out-of-phase contribution of the stress transmission is dominating and so large (phase shift $= \frac{\pi}{2}$) that the rheometer is not able to calculate reasonable values of the in-phase component G' and its values do not appear in the shown spectrum (figure 2.21(b)). On the alumina the stress is almost in-phase with the strain resulting in the appearance of both, the elastic and viscous moduli in the spectrum (figure 2.21(a)). Due to the in-phase behaviour the elastic modulus G' characterizes the sample as solid-like.

Figure 2.22 shows the dynamic spectra figure 2.21 combined in one plot. First we observe that at low frequencies both, the frequency independent elastic and viscous moduli obtained under total wetting conditions give larger values that the viscous modulus (going with ω) on the glass substrate. This confirms that the elastic response is the genuine response of
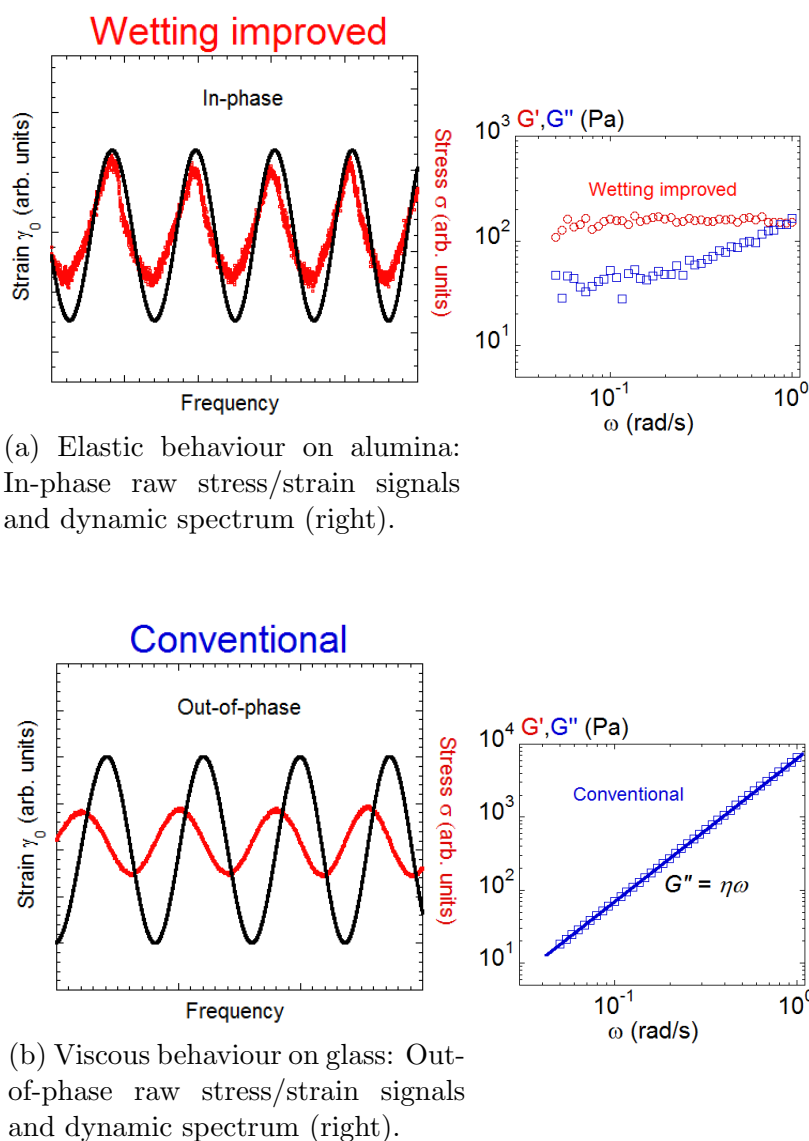
(a) Elastic behaviour on alumina: In-phase raw stress/strain signals and dynamic spectrum (right).

(b) Viscous behaviour on glass: Out-of-phase raw stress/strain signals and dynamic spectrum (right).

Figure 2.21: Influence of the wetting condition. The raw stress and strain signals as well the corresponding dynamic relaxation spectra are shown for a alumina (a) and glass (b) substrates. The measurements were otherwise carried out under the same conditions in the isotropic phase of the LCP95 $T = T_{SAI} + 25°C$, $e = 0.170mm$, small strain amplitude $(1.0\%(a),5.0\%(b)$, respectively) at low frequency $(0.1rad/s)$.

the sample as it is the dominating one. Second, at frequencies above $0.3 rad/s$ the both viscous moduli superpose. This result may indicate that at larger frequencies the close to equilibrium condition is no longer fulfilled and the response on the alumina enters a dissipative regime. It certainly shows that the experiments have been carried out under the same conditions as the slopes are equal (G'' goes with ω) which yields the same viscosity value in the conventional interpretation.
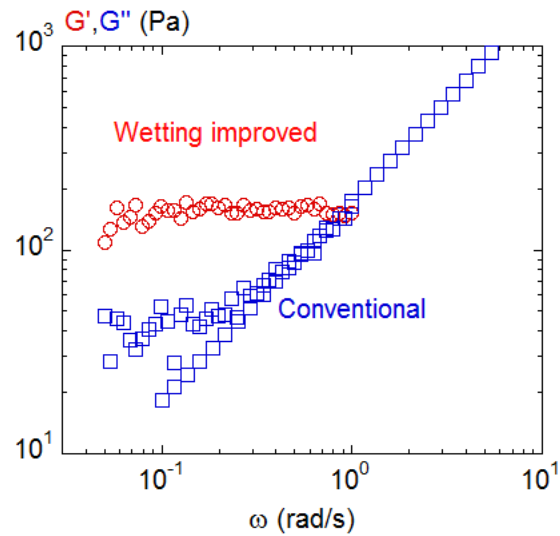
Figure 2.22: Dynamic relaxation spectra from 2.21(a) and (b) in one plot. The values of G'' obtained on two different surfaces, alumina and glass superpose at higher frequencies which shows that the same experimental conditions were conserved.

2.5 Low frequency shear elasticity in the isotropic phase of PACN

We have seen in sections (ref) and (ref) that the improvement of the liquid / substrate interactions e.g. wetting condition permits to observe an elastic behaviour in conventional dynamic measurements. Side-chain liquid crystal polyacrylates naturally exhibit excellent adhesion properties that persist in the isotropic phase and were to no surprise among the first molecules for which a terminal elastic plateau was observed. The low frequency shear elastic properties of the isotropic phase of different SCLCPs have been identified by Martinoty et al. [110] using a Piezorheometer and by Mendil et al. by applying the total wetting protocol to conventional dynamic measurements [28, 29]. The latter were motivated by the identification of a shear induced phase transition in same class of material that could not be explained by any known characteristic time [109]. As we make use of this effect to establish a connection between the mechanical and optical (birefringent) elastic properties at low frequencies in chapter 3 we will here briefly recall the identification of a terminal shear elasticity for a SCLCP, the PACN.

2.5.1 Low frequency behaviour

Figure 2.23 illustrates the dynamic low frequency behaviour of the isotropic phase of the PACN at $T = T_{NI} + 6°C$ above the nematic to isotropic transition for small (1%,(a)) and large (100%,(b)) strain amplitude. The applied strain was transmitted by layer of $0.200mm$ using total wetting conditions.

The observation of a low frequency elastic plateau at small strain amplitude in figure 2.23(a) is consistent with the terminal elastic response identified in the isotropic phase of the 8CB and LCP95. G' is superior to G'' both showing no dependence on the applied frequency between $0.1 - 1Hz$. The elastic modulus yields a value of around $1000Pa$, higher than for the LCP95 and the 8CB due to its larger molecular structure and polymeric properties.

At higher frequencies $1 - 10^2 Hz$ the dynamic moduli begin to establish a pronounced dependence on the frequencies. This happens first for G'' which is bypassing G' at $10Hz$. Here the isotropic phase is disturbed so fast that the response enters a dissipative regime eventually resulting in the conventional flow behaviour at very large frequencies (which are not accessible with the apparatus.)

This flow behaviour at larger frequencies becomes possibly accessible by being shifted to lower frequencies when increasing the strain amplitude. Figure 2.23(b) shows the dynamic moduli of the isotropic phase for a large strain amplitude of (100%. We observe the conventionally expected flow behaviour for the isotropic phase of an SCLCP where G'' scales with ω and dominates G' which is going with ω^2. Consequently and in contrast to

(a) Low strain amplitude (1%). (b) Higher strain amplitude (100%).
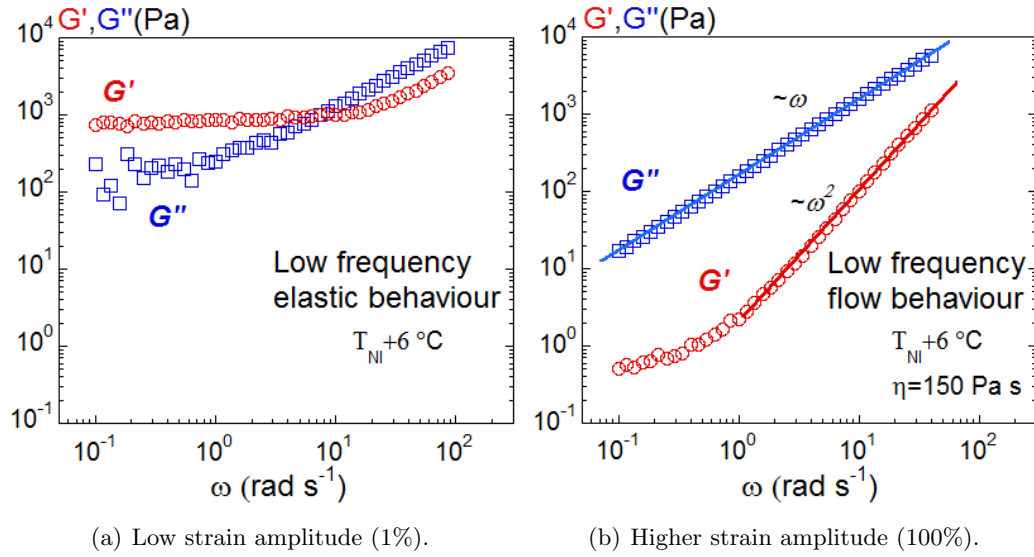
Figure 2.23: The visco-elastic moduli vs the frequency for a low strain amplitude of 1%(a) and higher strain amplitude of 100%(b) for the PACN at 6°C above the nematic - isotropic transition temperature. The spectra were acquired for total wetting conditions at a sample thickness of 0.200mm.

the 8CB and the LCP95 we observe a visco-elastic behaviour at large strain amplitude (and complementary under conventional conditions) instead of a purely viscous response. The visco-elastic relaxation time determined by the intersection of G' and G'', scaling with ω^2 and ω, lies approximately around $\tau_{relax} = 2 \times 10^{-2} s$.

2.5.2 Elastic "pre-regime" - Dependence on the strain amplitude

As for the isotropic phases of the 8CB and LCP95 the strain dependence of the low frequency elastic response for the PACN reveals a solid-like regime at small strain amplitudes that transits into a flow regime for large values of γ_0. Figure 2.24(a) presents the evolution of the dynamic moduli in the isotropic phase at $T = T_{NI}+6°C$ for smaller and larger strain amplitudes ranging from 0.3% up to 100%. The frequency was constant $\omega = 5rad/s$ and the gap thickness was $0.200mm$. Again we observe a pronounced fall of the dominating elastic modulus G' with the strain amplitude while the viscous modulus G'' stays almost constant. Due to the higher molecular mass and the influence of the polymeric chain both
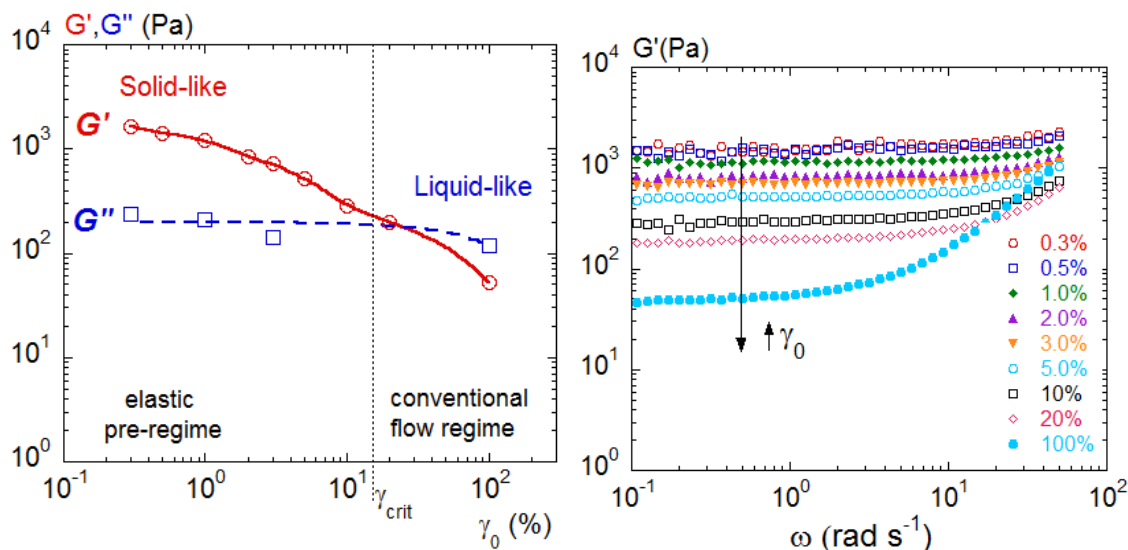
(a) Dynamic moduli vs the strain amplitude.

(b) Terminal elastic plateau for various strain amplitudes.

Figure 2.24: Strain dependence of the dynamic moduli of PACN at $(6°C)$ above the isotropic transition: (a) The visco-elastic moduli (G': red circles; G'' blue squares) at $0.200mm$ gap thickness at a frequency of $\omega = 5rad/s$ for several strain amplitudes. The vertical dashed bar indicates the critical strain amplitude below which the elastic modulus dominates the viscous modulus. Below γ_{crit} the conventional liquid-like behaviour is recovered. (b) The elastic modulus G' vs the frequency of the isotropic phase for various strain amplitudes. The terminal elastic plateau decreases with increasing γ_0. For large strain amplitudes (100%) G' begins to recover the conventional ω behaviour at higher frequencies.

moduli naturally exceed the values in comparison to their small molecular weight counterparts. The transition between the solid-like and liquid-like regime takes place above the

critical strain threshold $\gamma_{crit} = 10\%$ which is comparable to the LCP95. The experiments were not carried out at the same sample thickness and thus the values are only qualitatively comparable. Figure 2.24(b) shows the terminal elastic plateau under the same conditions as above as a function of the frequency for various applied strain amplitudes ranging from $0.3 - 100\%$. The augmentation of γ_0 results in a descend of the plateau with no apparent dependence on the frequency. Consequently the veritable elastic modulus is obtained for the smallest strain amplitudes, e.g. closer to equilibrium conditions.

2.5.3 Elastic response in the nematic and isotropic phase.

The PACN shows a nematic to isotropic transition similar to the 8CB and just alike the behaviour of the elastic response in the nematic and isotropic phase is expected to be similar. Figure 2.25 shows the plateau value at small strain amplitude of G' versus the temperature transmitted by a film of $0.200mm$. Above and below T_{NI} the values of G' of around $1000Pa$ behave indifferent in respect to the temperature from $110 - 135°C$. Pretransitional swarms persisting in the isotropic phase have no influence on the elastic response as does the glass transition at $54°C$. The symmetry of the phase does not have any influence on the solid-like behaviour be it for small or large molecules.
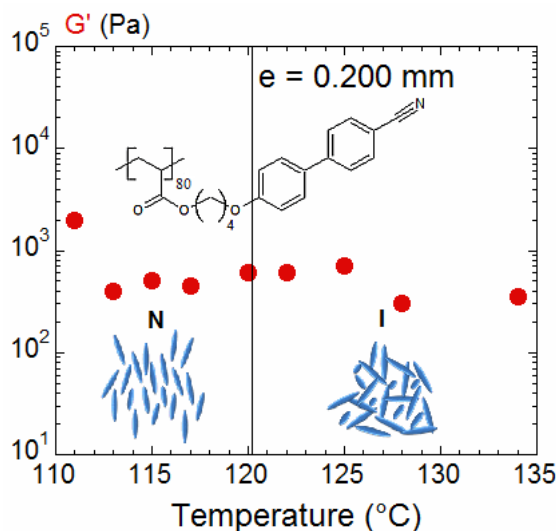
Figure 2.25: Shear modulus G' of PACN versus temperature at $0.200mm$ gap thickness. The vertical line indicates the transition temperature of the nematic (N) - isotropic (I) transition. Reproduced from [28].

2.5.4 Role of the molecular weight. Comparison between 8CB, LCP95 and PACN.

In the last three sections we have reported on the successive identification of a low frequency shear elastic behaviour of the 8CB, LCP95 and PACN and it is time for a comparison of the dynamic behaviour of the three molecules. Table 2 gathers the elastic moduli at the lowest strain amplitude $G'_{\gamma \to 0}$ and the critical strain amplitude γ_{crit} from the strain dependence measurements (see figure 2.13, 2.18, 2.24(a)). The 8CB exhibits the lowest shear elasticity ($G = 3Pa$) while the larger LCP95 ($G = 300Pa$) exceeds its value by a factor of 100. The highest measured shear elasticity was obtained for the PACN ($G = 1400Pa$). The molecular weight has a significant influence on the terminal elastic behaviour which becomes less important as the molecules become large. Figure 2.26 compares the shear moduli displayed by the 8CB, LCP95, PACN and a low molecular weight polybutylacrylate chain (pBuA). It shows that the regular grafting of liquid crystal moieties on a polymer chain reinforces the elastic character with respect to the low molecular weight liquid crystal but also with respect to the chain alone (though to a much lesser extent), pointing out the key role of the intermolecular interactions.

Sample	8CB	LCP95	PACN
$G'_{\gamma \to 0}$ (Pa s)	3.0	300	1400
γ_{crit} (%)	24	5	10

Table 2: The critical strain amplitudes and the low frequency elasticity plateau values of 8CB, LCP95 and PACN deduced from at the strain sweep experiments at the lowest strain amplitudes in pre-elastic regime.

Table 2 further recalls the critical strain amplitude γ_{crit} above which the solid-like response transits into a liquid-like response. This quantity which is not a critical value but rather defines a range for the strain amplitude and may be interpreted as the resistance of the sample the applied to stress. Below it, the initial response is solid-like while it shear-melts at larger strain amplitudes entering the viscous flow. We observed a higher value of γ_{crit} for the 8CB (24%) than for the LCP95 (5%) and the PACN (10%). This means that though the elastic moduli of the 8CB is weaker as for the other two materials it supports more applied stress before it begins to flow an effect comparable to the behaviour of real solids. The isotropic phases of the LCP95 and PACN thus behave more solid-like than the 8CB. This is in accord with the values of G' which are much weaker for the 8CB. The stiffer a solid material the less strain it supports before it breaks. We also have to consider that the strain dependence experiments from which we have drawn our critical values have not been carried out at the very same sample thickness (the elastic response is thickness dependent, see figure 2.15) and are thus only quantitatively comparable.
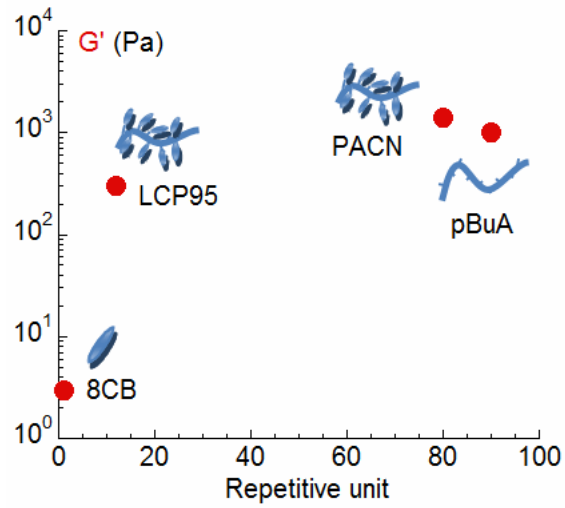
Figure 2.26: Comparison of the shear modulus G' in the isotropic phase, versus degree of polymerisation (repetitive unit) from low to high molecular weight: 8CB, LCP95, PANC and a polybutylacrylate chain (PBuA).

2.6 Sample preparation and establishment of the elastic signal

The identification of a shear elastic response is challenging. In order to establish strong signals a careful preparation of sample and substrate is necessary to achieve optimum boundary conditions.

2.6.1 Sample and surface preparation

Concerning the preparation of the samples, gas bubbles dispersed in the liquids are undesirable but almost inevitable. They may hinder the establishment of an equilibrium at the liquid-substrate interface, reduce the wetting performance by adsorbing on the surface and most importantly present a source of dissipation of stress during the measurements. Gas bubbles have varying sizes from the milimeter to the nano-scale. Larger bubbles can be eliminated relative easily by centrifugation, gently heating, shearing the liquid, an application of ultra-sound vibration or submission to vacuum. The more viscous the liquid the harder it is to get rid of this disturbing factor.

Nano-bubbles are more difficult to get rid of. These long-living, gas containing cavities [132, 133] are smaller than the wavelength of light and therefore too small to be visible to the naked eye or standard microscope. A way to reduce the number of bubbles can be by cooling the liquid to the more dense solid state (crystalline or glassy state, strongly ordered liquid crystal phase for example) which will then squeeze out the gas. When
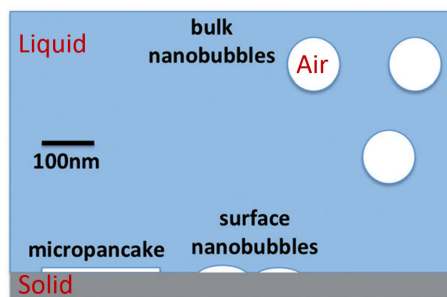
Figure 2.27: A liquid containing nano-bubbles in contact with a surface. The nano-bubbles migrate to the surface forming a surface-air-liquid interface, a "air-pancake". Reproduced from [134, 135].

a liquid containing nano-bubbles comes in contact with a surface the bubbles migrate to the surface and may coagulate to form a "micro-pancake" [134, 135], a surface-air-liquid interface (figure 2.27). The stability of this interface depends largely on the surface

condition of the substrate [124]. Depending on the amount of air trapped in the liquid this may lead to a lowering of transmission of stress and in the worst case to an appearance of slip by serving as a lubricating layer [124, 136, 137]. Either way it is strongly advisable to reduce the amount of bubbles.

A further crucial experimental factor is presented by the boundary condition of the substrate. In our wetting improved dynamic mechanical analysis we used α-alumina fixtures. In order to guarantee an improved wetting performance the fixtures are reinitialized and cleaned of organic pollutions by heating them to $450°$ for several hours. The substrate is used immediately after it has cooled down to avoid any re-pollution. A more detailed treatment on the subject of the interactions between liquids and the α-alumina e.g. its wetting behaviour can be found in chapter 5.

2.6.2   Establishment of the elastic signal

Once the sample and substrate preparations are finished, the liquid is placed between the fixtures. In most cases the identification of a low frequency shear elastic signal is not possible right after setting the gap thickness and thermal stabilization. At small strain amplitudes the signal is noisy (left side of figure 2.28). Given a sufficient equilibration time (hours to days depending on the nature of the sample) the (nano)-bubbles migrate to the surface where they collapse because of the high surface energy of the α-alumina avoiding the formation of a stable surface-air-liquid interface. As a result the resolution of the spectra improves and the visco-elastic moduli approach the shear elastic plateau with a pronounced separation of the elastic and viscous modulus as identified in this chapter (center and right side of figure 2.28). A similar observation is made for the raw strain/stress signals as they transit from distorted, weak waves to well defined sine waves.

2.7   Discussion of Artefacts and role of the surface tension

The possibility to reveal an elastic response in liquids arises from improving the liquid-substrate interactions by using total wetting surfaces, a careful sample and substrate preparation and by probing small sample thicknesses, low frequencies and strain amplitudes. Naturally such an important result raises questions on the origin of the measured signals. In this final section we confront our results with possible experimental artefacts and in particular we discuss the role of the surface tension as an origin of the shear elasticity.
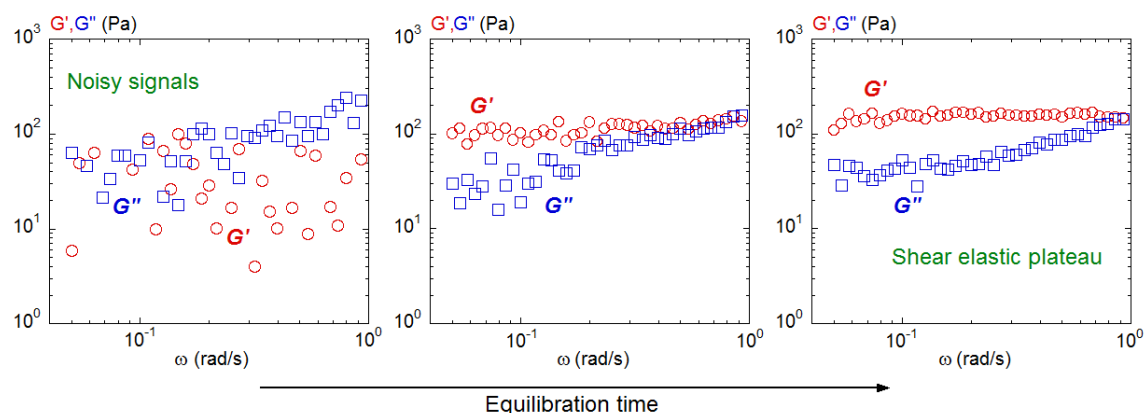
Figure 2.28: The importance of equilibration of the liquid is here shown for the LCP95 measured under the same experimental conditions ($T = T_{SAI} + 25°C$, a thickness of $0.170mm$, $\gamma_0 = 1.0\%$). A sufficient equilibration time (hours to days) improves the spectra from completely noisy signals to te identification of a well defined elastic plateau at low frequencies.

2.7.1   The terminal shear elasticity is not an artefact

A part of the discussion on artefacts is taken from the commentaries of McKenna on the identification of terminal shear elasticity in molten polymers in a focus point of Eur. Phys. J. E and can be found in [28] and [138].

Nanocavitation

When the system is heated or cooled, a temperature difference between fixtures and sample and thus a local difference in the thermal expansion coefficient might arise. This difference may provoke a variation of volume creating the nanocavitation phenomenon. Internal cavities create high surface tensions which may correspond to a hydrodynamic stress in the order of up to $10^6 Pa$ which could be responsible for the elastic response [138].

The ARES II rheometer is equipped with an air-pulsed oven to homogenize the temperature and two thermal sensors. Additionally it has two mechanical sensors, one is measuring the torque (which solely measures the visco-elastic properties) while the other one measures the vertical (normal) force. First, if any effect of nano-cavitation is present (hydrodynamic pressure is equally affecting all directions of space), the apparatus would detect a variation of the normal force (at rest or under strain) which it does not. Second, a terminal shear elastic plateau was obtained for room temperature liquids excluding any heating related effects [39, 41].

Poker chip effect

A weak default in parallelism between the fixtures may give rise to the so called "poker chip" effect [138, 139]. The "poker chip" geometry is a geometry where the thickness is by far smaller than the diameter. If the sample is restraint by one of the surfaces, any axial component of the stress may contribute to the measured moduli. Even at small deformations this effect may contribute significantly and increase with decreasing sample thickness.

This type of artefact can be excluded by the stress relaxation behaviour of the sample. Stress relaxation consists in applying a deformation (in the order of $30 - 50\mu m$) and measuring the evolution of the stress function $(G(t))$ versus time. In the case of a solid, the sample stays restraint. For a (visco-elastic) liquid the stress decreases rapidly with the time, the sample flows (left side of figure 2.29). The right side of figure 2.29 shows the stress relaxation of the LCP95 for a gap thickness of $200\mu m$ at $T = T_{SAI} + 20°C$. $G(t)$ does not relax versus time and thus presents a solid-like behaviour. Moreover this means the shear elasticity is intrinsic and does not only exist dynamically. This basically rules out any involvement of geometrical artefacts like the "poker chip" effect. Additionally figure 2.30

(a) Stress relaxation ideal behaviour

(b) Stress relaxation Isotropic phase LCP95
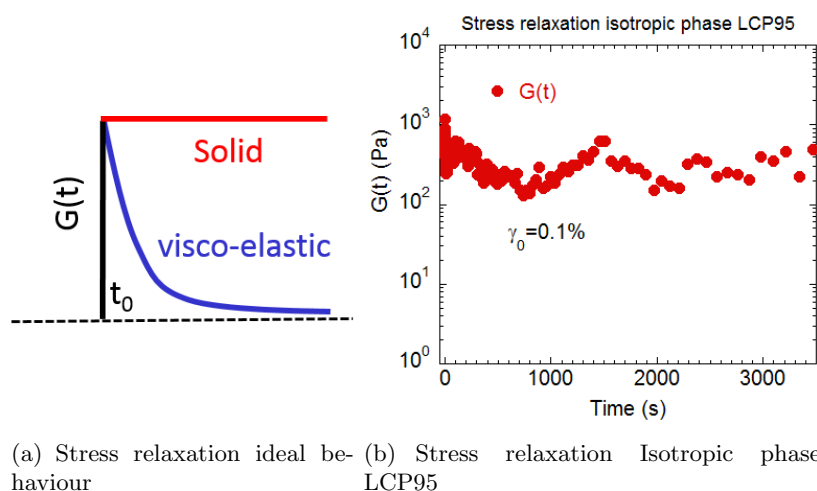
Figure 2.29: Stress relaxation experiment. (left) Ideal behaviour of the stress versus time for a deformation: In the case of a visco-elastic liquid the stress relaxes rapidly while for solid the stress remains constant. (right) Solid-like stress relaxation of the LCP95 for a $\gamma_0 = 0.1\%$ at a gap thickness of $200\mu m$ at $T = T_{SAI} + 20°C$.

shows that the parallelism of the fixtures is inferior to the wavelength of light. Larger air bubbles would be visible and would create a normal force. The surfaces are open towards the sides excluding excess pressure in the system.
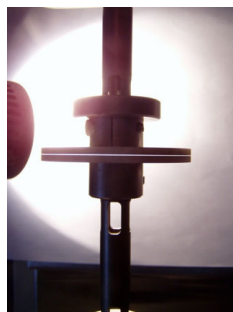
Figure 2.30: Photograph of a liquid between the alumina fixtures. The gap thickness is $200\mu m$ and the precision of the parallelism is inferior to the wavelength of light.

Low torque limit effects

All the measurements displayed in the manuscript have been carried out over the torque limits imposed by the manufacturer which is $0.02g \times cm$. Figure 2.31 presents the shear elastic modulus versus the frequency of the isotropic phase of the LCP95 together with the torque. At the lowest frequencies the measured torque lies a factor 3 above the low torque limit.

Frequency (rad/s)	G' (Pa)	Torque (g x cm)
0.05	78	0.064
0.07	74	0.063
0.08	75	0.064
0.09	81	0.069
0.11	74	0.065
0.13	81	0.071
0.15	83	0.074
0.17	76	0.069
0.20	73	0.068
0.23	75	0.071
0.27	76	0.076
0.32	79	0.079
0.37	76	0.082
0.43	78	0.087
0.50	85	0.096
0.58	85	0.102
0.68	83	0.111
0.79	85	0.119
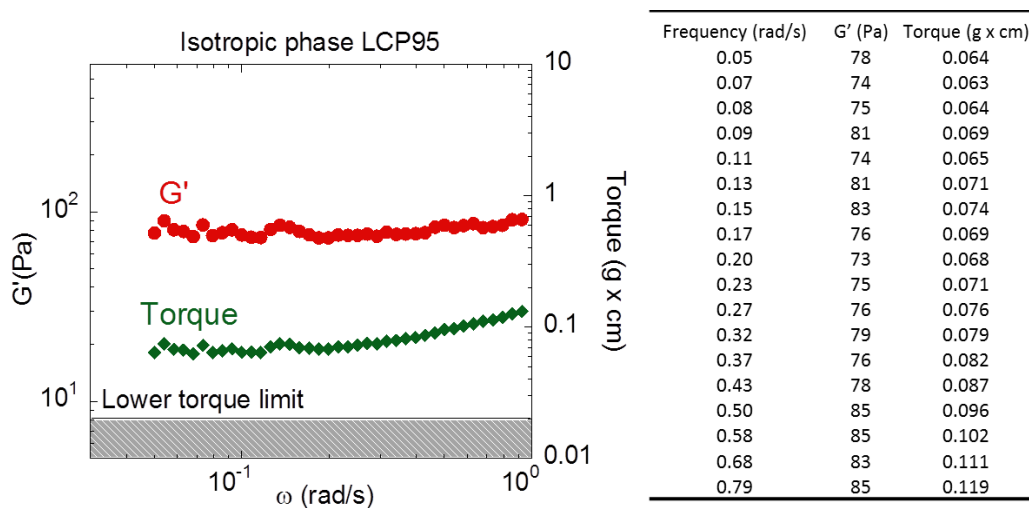
Figure 2.31: Low frequency shear elastic modulus of the isotropic phase of the LCP95 versus frequency together with torque. Experimental conditions: $T = T_{SAI} + 25°C$, $\gamma_0 = 5.0\%$, $110\mu m$, diameter fixtures $20mm$.

2.7.2   The surface tension and the shear elasticity

Figure 2.32 shows the situation of a liquid between two fixtures. The surface tension of the liquid sample gives rise to a capillary force at small gap sizes which essentially holds the liquid in place. In contrast to piezorheometry (translation), the present dynamic mechanical analysis is carried out in rotational symmetry at small strain amplitudes (for the elastic response). The same values of the shear elastic response at small sample thicknesses are obtained for different fixtures including cone-plate, plate-plate with and without recovery duct (which destroys the meniscus, figure 2.32) and for various diameters ($10 - 40mm$). The response is thus independent of the geometry [29]. The measurement gives access to
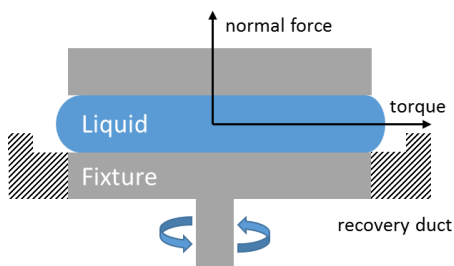
Figure 2.32: The liquid forms a meniscus between the fixtures which can be destroyed by using surface with a recovery duct. A sensor measures torque and normal force independently.

the normal force and to the torque at rest and under oscillatory strain via two independent transducers. The interfacial forces between the two surfaces are related to the normal force. The normal force is unchanged while the torque transducer measures the shear elastic behaviour during the dynamic measurement. Figure 2.33 shows that, under rotation, the sum of tangential forces that result from the deformation, disappear due to symmetry reasons (rotational symmetry), which is the case in any careful visco-elastic measurement. Finally, the shear elasticity is measured at small strain amplitude and at low frequency (i.e. in close to equilibrium conditions) while the VE behaviour is recovered at large strain amplitudes.
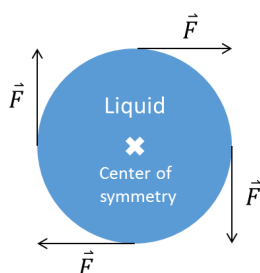
Figure 2.33: The tangential forces that arise due to a deformation in rotational geometry are eliminating each other.

These are strong indications that permit to rule out the surface tension as the origin of the elastic response. In fact the surface tension would only play a role when the surface of the sample changes during the oscillation, which is here not the case because of symmetry

reasons and the application of very small amplitudes to access the shear elasticity. If there is no variation of the surface, there is no change in surface energy and thus no capillary force. The capillary forces and the shear elasticity share the same origin - the intermolecular interactions. If there were no cohesive forces in the liquid there would be no capillary tension and no shear elasticity.

As a complementary information, we will see in the chapter 3, that the birefringence induced at small strain amplitude is a bulk property and is homogeneous in the very same plane as shown in figure 2.32 which excludes artefacts as inertial effects due to a partial filling or a parallelism effect.

2.8   Summary and Conclusions

In this chapter we have for the first time identified a low frequency shear elasticity in the isotropic phase of diverse liquid crystals. As representative samples we picked three liquid crystals, the 8CB (low molecular weight, $M_{8CB} = 292 g/mol$), the LCP95 ($12 \times M_{8CB}$) and the PACN ($80 \times M_{8CB}$), a non-entangled side-chain liquid crystal polymer.

- The transitions from the liquid crystal phases (smectic A (LCP95) and nematic (8CB, PACN)) to the isotropic phase are of first order. Above the transition the liquid crystal loses any long range order and fulfils, from a thermodynamic and crystallographic point of view, the definition of an isotropic liquid.

- We probed the low frequency dynamic properties of the isotropic phase using wetting improved dynamic mechanical analysis. Total wetting boundary conditions were achieved by applying cleaned α-alumina fixtures and a careful liquid-sample preparation (reduction of gas bubbles). Two external multimeters permit to directly access the raw stress/strain signals of the ARES II rheometer in addition to the dynamic visco-elastic moduli.

- At small strain amplitudes, an in-phase behaviour of the strain/stress signals brings the evidence for the existence of terminal shear elasticity of the liquids.
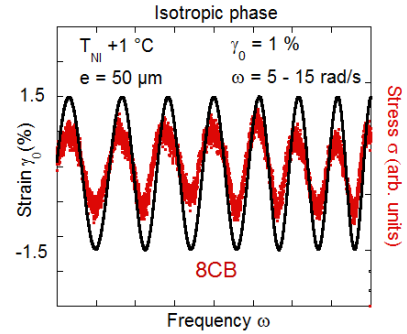
- This solid-like behaviour persists over a large range of frequencies and in terms of visco-elastic moduli reveals a terminal elastic plateau $G' > G'' \neq fct(\omega)$. The strength of the elastic moduli depends strongly on the molecular architecture and ranges from $G' = 1 Pa$, in the case of the 8CB to $G' = 10^3 Pa$, in the case of the PACN.
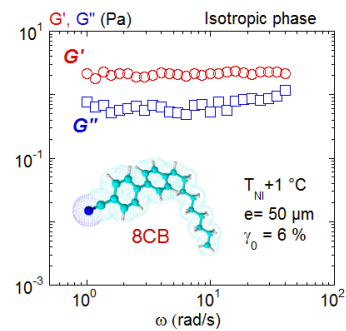
The shear elastic response is strain dependent:

- By increasing the strain amplitude the initially in-phase stress/strain signals become phase shifted and distorted. The response is no longer harmonic at intermediate strain amplitudes above a critical strain γ_{crit}. At large strain amplitudes the stress/strain signals recover their wave form and are phase-shifted by $\frac{\pi}{2}$.
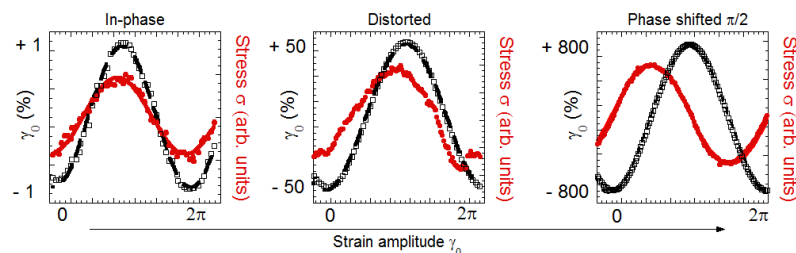
This change of signals with the deformation can be explained by the strain behaviour of the VE-moduli:

- At small strains the elastic modulus dominates - this is the pre-elastic regime. Stress/strain are in-phase.
- By increasing the strain the elastic modulus decreases significantly while the viscous modulus remains almost constant. Above γ_{crit} the signals are distorted. Stress/strain are distorted
- At large strain amplitudes the G' is no longer measurable, the dynamic behaviour is determined by G''. Stress/strain are phase shifted.
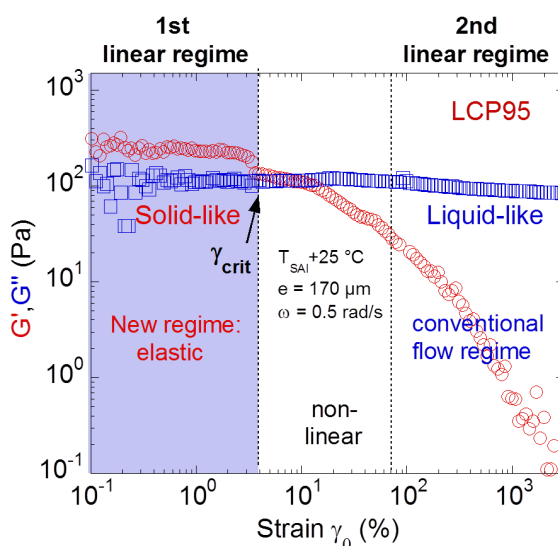
At large strain amplitudes the conventional behaviour of the liquid is recovered. A dynamic spectrum in this flow-regime shows an entirely viscous behaviour with G'' going with ω in the case of the 8CB and the LCP95. In the case of the PACN we observe a terminal visco-elastic behaviour where G' scales with ω^2 and G'' scales with ω.

At smaller strain amplitudes the perturbation is weaker and the systems closer to equilibrium. Therefore the **shear elastic regime must be considered as the fundamental response** of the isotropic phase. The conventional viscous behaviour corresponds to a sec-

ond linear domain occurring as a perturbative state in respect to the first linear solid-like domain.

No strong variation of the elastic moduli was found by crossing the nematic-isotropic transition (8CB, PACN). Also the magnitude of the shear elasticity decreases as the gap sizes increases, depending on the sample, and is no longer measurable at large sample thicknesses ($< 1.0 mm$). Under the same conditions (small strain amplitude, low frequency and small gap sizes), the conventional rheological measurement (on a glass substrate) shows a flow behaviour while the wetting improved (total wetting on α-alumina) experiment reveals an elastic behaviour. Finally, the shear elasticity does not have its origin in artefacts like the "poker chip" effect, nanocavitation or the low torque limit. It cannot be explained by the presence surface tension.

This important finding shows us that the, under conventional conditions "hidden", shear elasticity of the isotropic phase is revealed by using total wetting conditions. The results indicate that the isotropic phase is a fragile, long range, elastically correlated "self-assembly". The strength of the shear elasticity depends on the molecular architecture of the molecule (molecular mass, polymer or not) and likely on the nature of the intermolecular interactions (van der Waals, polar, H-bond) in agreement with the results for other liquids. Importantly we observed a shear elasticity in the isotropic phase of the 8CB, a small molecule that crystallizes at low temperatures (as does the LCP95). This invalidates any interpretation in terms of glass transition or contribution of the polymeric chains (though it may influence the magnitude of the elastic modulus) to be at the origin of the shear elasticity [27, 110].

The analysis presented in this chapter and the fact that for other liquids a low frequency shear elasticity has been detected [36, 37, 39–41], supports the assumption that we are dealing with a generic property of the liquid state. We take into consideration that a similar solid-like behaviour was obtained at smaller length-scales by Derjaguin [25, 26] Isrealachvili [22–24] and Granick [14–20] who observed a terminal shear elastic plateau. These experiments share a controlled or improved wetting condition. We seize the argumentation of Derjaguin and favour an interpretation of the shear elasticity as a measurement of the strength of long-range intermolecular, collective interactions and that the shear elasticity is inherent to the bulk. It thus presents a property possessed by all liquids without exception independently of their viscosity and polarity.

In the following chapter we try to verify the here described results by transferring the experimental procedure to optical measurements. Here-fore we use the birefringent properties of the pretransitional fluctuations present and embedded in elastic network of the isotropic phase of liquid crystals.

Chapter 3

Prentransitional fluctuations as a tool to visualize terminal shear elasticity
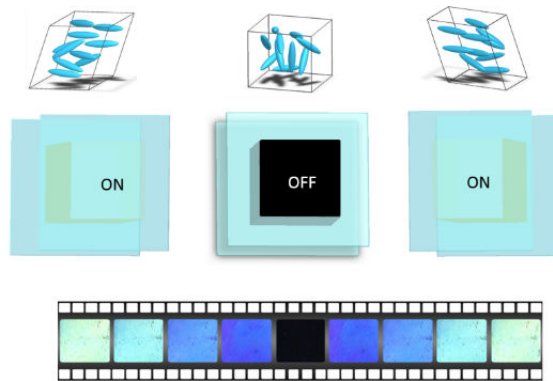
In the previous chapter we have demonstrated the existence of a terminal elasticity at the sub-millimeter scale that shows that the isotropic phase is a state correlated elastically at long distance [42, 43]. This property opposes the definition of a liquid state constituted by dynamically free molecules and introduces the concept of correlations.

Our further aim is to develop methods independent of the mechanical stress measurements to gain access to an elastic response in liquids. This is where the optical, birefringent properties of the liquid crystals come in handy. Above the liquid crystal to isotropic transition the long-range positional and orientational order is lost but pretransitonal fluctuations persist close to the clearing point. These clusters of pre-oriented molecules whose size depend

on the temperature should be embodied in the elastic medium observed at low frequencies. In 2001 Noirez et al. have observed a shear induced isotropic to nematic transition in the isotropic phase of SCLCPs [109]. They concluded that neither the usually addressed visco-elastic relaxation times nor the relaxation times of the pretransitional fluctuations measured by the Kerr-effect [44, 45] could account for the phase transition [32–34]. They were much too fast.

The observed presence of longer time-scales must have another origin - the shear elasticity observed at low frequencies.

In this chapter we develop a dynamic approach to visualize the low frequency shear elastic response by using birefringent properties of oriented pretransitional fluctuations as optical and dynamical tracers [43]. This is essentially done by transferring the principle of dynamic mechanical analysis to optical measurements applied to the samples from Chapter 2. Here, a trigger system (R&D Vision) permits us access to the raw input (strain) and output (birefringence) signals. We will show for the first time that, at the sub-milimeter scale, the pretransitonal orientational fluctuations are oriented in the strain field as soon as the lowest frequencies, synchronized with the strain signal and far from any reported relaxation time. At low frequencies the synchronized birefringence thus serves as a probe for the shear elasticity. The collapse of the signals at higher distortions, e.g. when the equilibrium condition is abandoned, approaches the well documented flow birefringence [109, 140–142]. In contrast to the direct measurement of the shear elasticity in the stress measurements the elasticity is here probed by using the pretransitional fluctuations as an optic probe. This usage is limited as the size of the swarms decreases with temperature while the shear elasticity itself is relatively indifferent to the temperature.

Finally the synchronized birefringence may serve a low energy consuming stimuli-responsive material presenting a true black state between crossed polarisers (see cover image of this chapter).

Contents

3.1   The liquid crystal to isotropic phase transition

In order to understand how it is even possible to orient pretransitional fluctuations we will recall the nature/ theoretical description of the smectic, nematic and isotropic phases and the transition between them at the isotropic transition temperature, the clearing point T_C. The vast majority of our experiments are carried out in the isotropic phase which is the phase of highest temperature in thermotropic liquid crystals.

The liquid crystal phases, director and order parameter

The microscopic nature of the isotropic phase of rod-like liquid crystals corresponds to a liquid in the usual sense where the gravity centres of the molecules present no positional order and their molecular axis no preferred long-range orientation. In the nematic phase (N) the molecules are positionally totally disordered, but arrange in a same preference direction, defined by the director vector, $\vec{n}$. A higher degree of positional order arises when molecules are distributed in layers. These are the smectic (Sm) phases. When molecules are perpendicular to the layers, the phase is called smectic A (SmA), but if the molecules are tilted relative to the layers, the phase is called smectic C (SmC)(not discussed here) phase (figure 3.1).
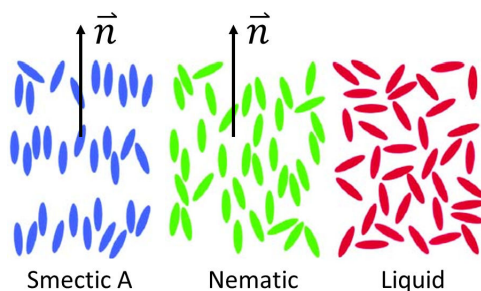
Figure 3.1: The smectic A, nematic and liquid (isotropic) phases. The director $\vec{n}$ is shown for the first two.

For the nematic phase we can easily define an order parameter S:

$$S = \langle \frac{3\cos^2 \vartheta - 1}{2} \rangle \tag{11}$$

The right side is the average of the second Legendre polynomial where the angle ϑ describes the orientation of a molecule relative to the preferential direction (the local director). The

brackets indicate spacial and thermal average. For a completely random isotropic sample $S = 0$ while for a perfectly aligned sample $S = 1$. The order parameter is strongly temperature dependent. It rapidly approaches zero when the isotropic transition temperature is reached.

Figure 3.2: The angle ϑ between the orientation of a molecule in respect to the director $\vec{n}$ defines the order parameter S.

Isotropic transiton in terms of Free Landau energy

We have already discussed in section 2.1.1 that the smectic-isotropic and nematic-isotropic transitions are of weak first order (small enthalpies involved). Due to this abrupt break in symmetry the Landau-de-Gennes theory permits to describe the transition [143, 144]. For geometrical reasons the NI transition (an analogous description can be given for the SmI transition) must be of first order. The argument is given by a mean-field approach, the Landau Free energy F, which can be extended to a power series of the order parameter and written in a simpler form:

$$F = F_0 + \frac{1}{2}A(T)S^2 + \frac{1}{3}B(T)S^3 + \frac{1}{4}C(T)S^4 + ...\tag{12}$$

where $A(T) = A_0(T - T^\star)$ with $T^\star$, the spinoidal temperature at which the transition would take place if it were of second order. F_0 presents the free energy associated to the isotropic phase. Figure 3.3 shows the Landau Free energy as a function of the order parameter.
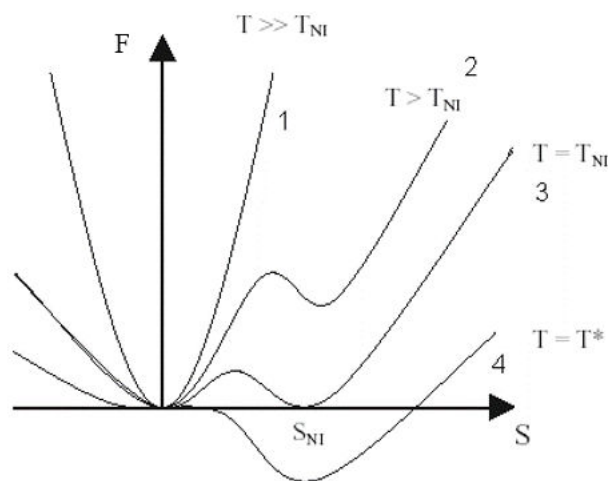
Figure 3.3: Free Landau energy as a function of the order parameter for various temperatures above (1), just above (2), right at (3) the transition temperature as well as right at the spinodal temperature (4). The minima of the curves give the equilibrium state for the given temperature. Reproduced from [118].

Solving the equation reveals two minima, one for $S = 0$ the other for $S \neq 0$, the latter is due to the factor C(T) in the Free Landau energy equation. Curve (1), above the transition shows one minim for $S = 0$, the isotropic phase. The second minimum appears when $A < \frac{B^2}{4C}$. When T approaches $T^\star$, A declines and the Free energy associated to $S \neq 0$ appears (Curve (2)). At $T = T_{NI}$ the two minima become equal in energy and the nematic phase coexists with the isotropic phase (curve (3)). We can write:

$$T_{NI} - T^\star = \frac{2B^2}{9A_0C} \text{ and } S(T = T_{NI}) = \frac{2B}{3C} \tag{13}$$

The minimum for $S = 0$, the isotropic phase, disappears for $T = T^\star$. $T^\star$ defines the limit of stability of the isotropic phase.

Pretransitional fluctuations

From the considerations above we can state that in the isotropic phase there is no long-range order in the direction of alignment of the molecules as the *order parameter vanishes on average*. However *locally*, molecules are still parallel to each other in order to minimize

the energy forming pretransitional clusters. This order persists over a certain characteristic distance $\zeta(T)$, the coherence length [118].

0.01 μm
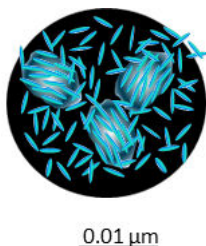
Figure 3.4: Orientational pretransitional fluctuations: Swarms of oriented molecules of size $\zeta = 0.01 \mu m$ co-existing in the isotropic phase.

Consequently in the isotropic phase, pretransitional orientational "swarms", i.e. small droplets of size $\zeta(T)$ co-exist in the isotropic phase (figure 3.4). Successive swarms are optically and orientationally uncorrelated [118]. The size and lifetimes of orientational pretransitional (also known as order parameter) fluctuations are strongly temperature dependant and may be oriented giving rise to a birefringence in the isotropic medium. This may be done by an external force e.g. a magnetic or electric force (Kerr effect, birefringence due to orientation of swarms) or a shear flow. We will show that it is also possible to orient the pretransitional fluctuations with a low frequency mechanical field.

3.2 Dynamics of the pretransitional fluctuations

While the nematic or smectic to isotropic transition is of first order type its magnitude (weak or strongly) varies firmly with the molecular architecture. We have seen in the DSC measurements (2.1.1) that the enthalpy of the NI transition for the 8CB is by ca. a factor 8 larger than for the isotropic transition of the LCP95, PACN respectively. In the case of the latter this is expressed by a smaller leading Landau coefficient $A(T)$ which leads to a higher (temperature) persistence and larger sizes of pretransitional fluctuations.

Different experimental methods access relaxation times of the pretransitional swarms. Among them we find Kerr effect measurements, dielectric relaxation, dynamic light scattering, NMR. However these techniques apply frequencies from the kHz to GHz range, none of them permits the access to low frequency phenomena. For small rod-like molecules, like the 8CB, dielectric relaxation measurements have shown relaxation times in the order of $10^{-9}s$ [44] which is comparable to the dielectric relaxation mode of small molecular liquids as liquid water which lies around $10^{-12}s$ [145].

For larger molecules as e.g. bent-core (banana shaped) LC light scattering [146] and NMR [147] experiments indicate slower relaxation times in the order of $10^{-7} - 10^{-5}s$.

Martinoty et al. have studied relaxation times of side-chain liquid crystal polymers using the Kerr effect [45]. Experimentally a rectangular electric pulse of 500 V (decay times less than $0.2s$) was applied to the isotropic phase between plate electrodes (Kerr cell) at macroscopic quantities. The relaxation of the electrically induced birefringence was measured between crossed polarisers as a function of the temperature above the isotropic transition(figure 3.5(a)).

(a) Kerr cell

(b) Kerr effect relaxtion time vs temperature for a side-chain liquid crystal polymer of degree of polymerization = 200.
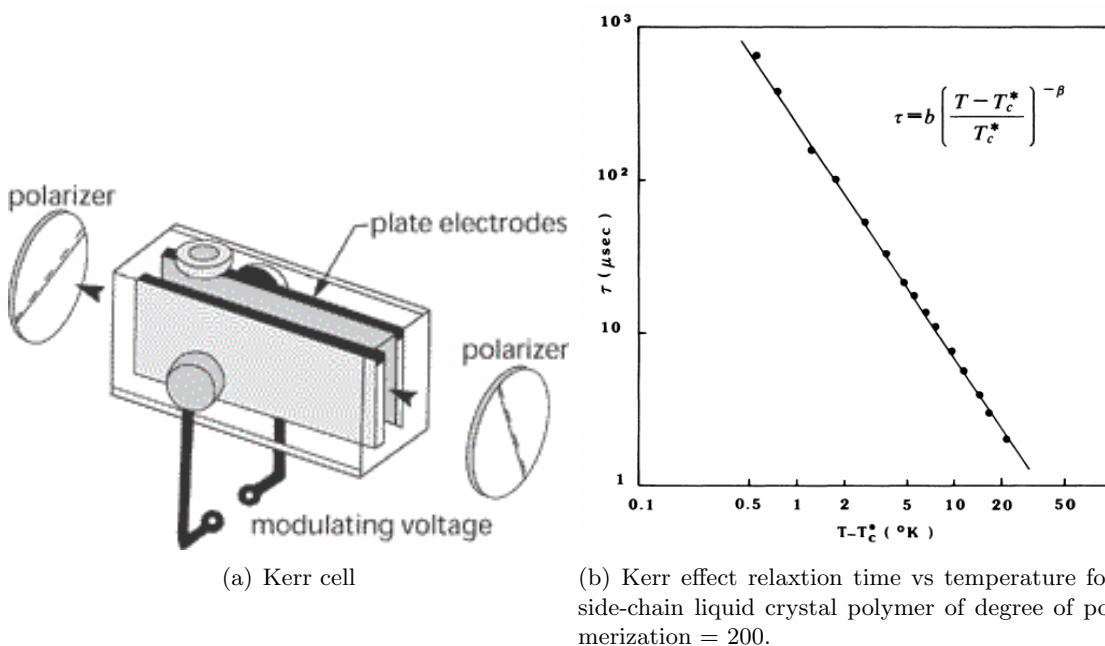
Figure 3.5: Kerr effect measurements of a SCLCP (degree of polymerization ≈ 200) in the isotropic phase. (a) Kerr effect measurement cell: The relaxation of the birefringence induced by a electric pulse is measured between crossed polarisers [148]. (b) Relaxation time vs the temperature, the fit line corresponds to a mean-field description giving the relaxation time τ. b and β represent fitting parameters. Reproduced from [45]

First, the clearing point T_C was found to be higher than $T_C^\star$; $T_C - T_C^\star = 0.6$ confirming the first order nature of the transition. Second, figure 3.5(b) shows that the pretransitional fluctuations are well described by the mean-field approach and yields relaxation times ranging from $10^{-6} - 10^{-3}s$ for temperatures from $0.1 - 20°C$ above the transition T_C. The characteristic times of the pretransitional fluctuations are shorter than the visco-elastic relaxtion times found in the isotropic phase of SCLCPs (2.1.2) that lie around $10^{-3} - 10^{-2}s$.

3.3   Inconsistency of the characteristic times

We have seen that the reported life-times of the pretransitioanl fluctuations in the isotropic phase are rather short and lie between $10^{-9} - 10^{-3}s$ depending on the molecular structure of the molecules. These relaxation times are obtained at frequencies above the kHz range. However in chapter 2 we have identified much longer (quasi infinite) relaxation times in the isotropic phase using the wetting protocol applied to low frequency (several Hz) dynamic relaxation measurements. Shouldn't there be a coupling between the instant reaction to stress (elastic behaviour) of the molecules in the isotropic phase and the orientation of the preoriented swarms dispersed in it?

Since 2001 Noirez et al. have observed a shear induced nematic to isotropic transition in the isotropic phase first of their home-made SCLCPs [109] and later for the molecule used in the Kerr effect measurements by Martinoty et al. [45]. They compared their applied shear rates to the usually addressed visco-elastic relaxation times and the relaxation times of the pretransitional fluctuations [32–34] and found a discrepancy:

According to the Deborah relation, a shear rate comparable to the inverse of the characteristic relaxation time (in this case the relaxation of the pretranstional fluctuations) must be applied to probe the event in a dynamic experiment (1.3.1). The authors observed the emergence of a flow birefringence in the isotropic phase at shear rates ranging form $\dot{\gamma} = 10 - 600s^{-1}$. According to the Deborah relation, this indicates that time-scales of at least $0.1s$ exist in the isotropic phase (figure 3.6). These long time-scale non-linear
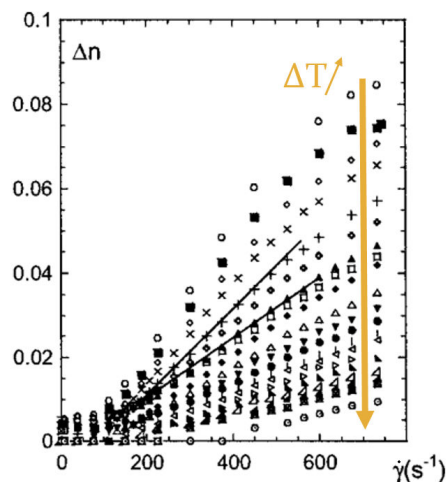
Figure 3.6: Shear induced birefringence Δn vs the shear rate $\dot{\gamma}$ at various temperatures $\Delta T = 0.5 - 18.5°C$ above the isotropic transition ($T_{NI} = 131.5°C$) for a side-chain liquid crystal polymer. Reproduced from [32].

phenomena were neither explained neither by a flow coupling with the conventional VE relaxation times [119] nor with phase pretransitional dynamics [149–151]. In fact the experiments indicated that relaxation times much longer than the ones usually reported or academically predicted might exist.

These findings are the very basis of what will follow. We will develop a dynamic approach to visualize the low frequency shear elastic response by using birefringent properties of oriented pretransitional fluctuations as optical and dynamical tracers [43]. The principle of dynamic mechanical analysis will be transferred to optical measurements of the isotropic phase. This way we get access to the lowest frequencies and strain amplitudes - the lowest possible excitations from a macroscopic mechanical point of view.

We will reveal that it is possible to mechanically induce a low frequency birefringence in the isotropic phase. This so far unknown property means that pretransitional swarms are essentially frozen in the liquid at the addressed time-scales.

3.4 Dynamic mechanical analysis combined with optical measurements

In the following we present the experimental setup of our optical measurements in the isotropic phase of the 8CB, LCP95 and PACN. The aim is to transfer the technical conditions of the dynamic mechanical analysis which implement the application of a low frequency, small strain amplitude to a device permitting to simultaneously analyse the birefringent signal and the applied strain.

Because a weak elastic regime has been discovered at sub-millimeter length-scale in the isotropic phase [42, 43] we examine the optical response under similar conditions. If the molecules in the liquid are elastically correlated the pretransitional fluctuations are embedded in a elastic network. The orientation or alignment of the swarms should lead to an anisotropy in the isotropic sample at the addressed time-scales leading to a birefringent signal. Figure 3.7 shows our apparatus. A more detailed description of the experimental setup and the measurement is found in the appendix A.
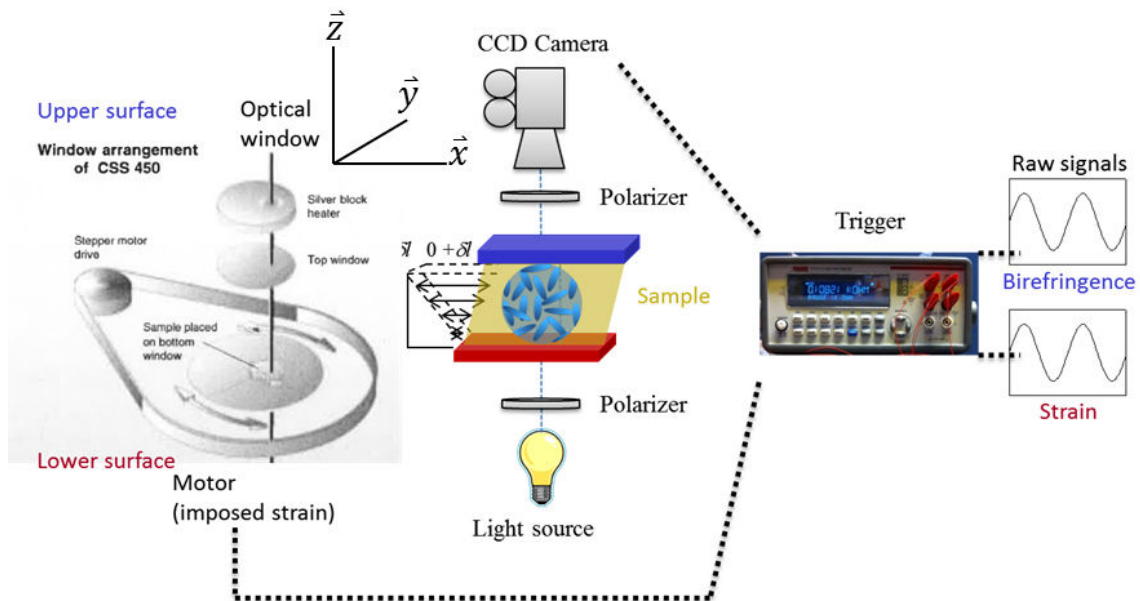
Figure 3.7: Scheme of the setup. The isotropic phase fills the gap between two Quartz discs of high optical quality. The oscillatory movement of the lower disk/surface provokes a stress in the sample that is measured between crossed polarizers by a sensitive CCD-camera. A trigger system (R&D Vision) permits to simultaneously access the mechanical input (strain) and optical output (birefringence) signals with a synchronization delay of $10^{-5}s$.

The optical experiments were performed in transmission mode under crossed polarized microscopy (Olympus BX60). Oscillatory shear motion was applied by a home-improved CSS450 Linkam cell (with a temperature gradient $< \pm 0.05°C$) equipped with quartz plate-plate fixtures. The customization by a torque reducer applied to the motor gave access to the low strain amplitudes. The used wavelengths were $\lambda = 420nm$ and $614nm$ respectively. The transmitted intensity I was measured with a CCD camera (Vision Technology) in the top-view plane $(\vec{x} - \vec{y})$(figure 3.7) and normalized to the uncrossed polariser intensity I_0. This professional CCD camera is characterized by a low level intensity detection. The averaged birefringence $\langle \Delta n \rangle$ is calculated using the formula:

$$\frac{I}{I_0} = \sin^2(\langle \Delta n \rangle \frac{e\pi}{\lambda}) \tag{14}$$

where e is the gap thickness. A trigger device (by R&D Vision) measures simultaneously the movement of the lower plate and the transmitted intensity with two individual cameras (ALLIED Vision Technology). The trigger synchronizes very accurately the recording of the position and the movement and the transmitted intensity with a synchronization delay $(\Delta \tau = 10^{-5}s)$. The input strain wave is sinusoidal:

$$\gamma = \gamma_0 \sin(\omega t) \tag{15}$$

Its amplitude is defined by the displacement length δl divided by the sample thickness:

$$\gamma_0 = \frac{\delta l}{e} \tag{16}$$

Typical displacements and strain amplitudes are of the order of $5\mu m$ to $250\mu m$ for $e = 250\mu m$ and γ_0 varying from $2 - 100\%$ respectively.

As surfaces we used silica 7980 from Corning glasses that guarantee a low reflection index and low birefringence (characteristic of stress birefringence $< 1nm/cm$).

3.5   Low frequency mechano-optic experiments in the isotropic phase of the 8CB

As our mechano-optical apparatus is partly customized to access the lowest light intensities, we had to assure the quality of the experiments. Before the liquid was placed in between the glass surfaces we measured the signal of the empty cell. Figure 3.8(a) shows the intensity of the empty cell at a gap size of $100\mu m$ at rest and for an applied oscillatory solicitation at constant strain amplitude of 100% at different frequencies $0.1 - 0.3 - 0.9Hz$. No variation of the intensity is observed which excludes any artefacts from the apparatus.

In a first attempt we tested the 8CB which is a well studied model liquid crystal molecule [114, 115]. Figure 3.8(b) shows the intensity of the 8CB heated into the isotropic phase $0.1°C$ above T_{NI} at rest for 20 minutes. The signal is also stable in respect to any possible temperature fluctuations.

(a) Frequency - Sweep in Empty Cell

(b) Static response of the isotropic phase of 8CB
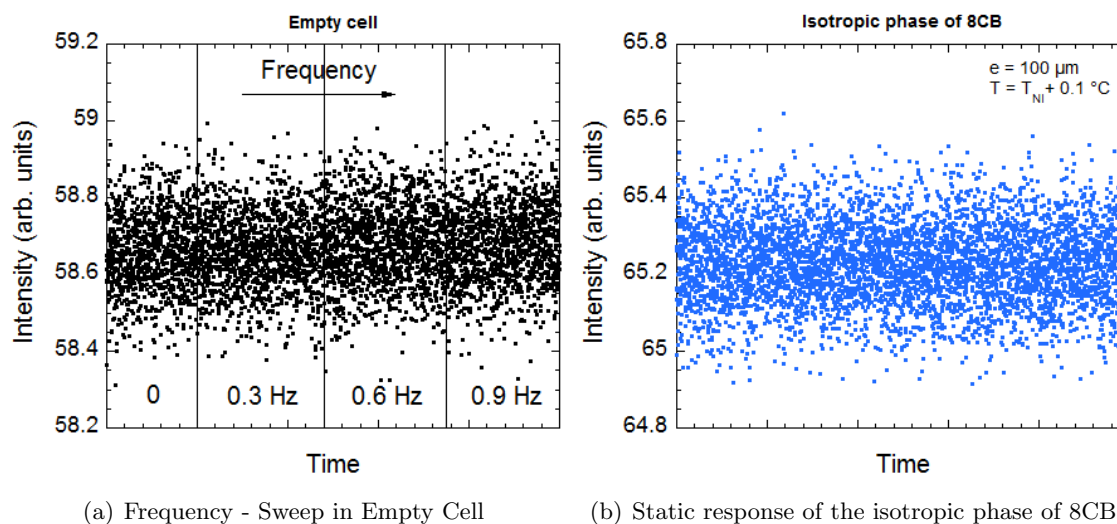
Figure 3.8: Verification experiments of our apparatus; measured intensity I vs time: (a) Different frequencies at a constant strain amplitude of 100% at cell gap of $100\mu m$ are applied to the empty cell. (b) The measured intensity of the isotropic phase of the 8CB at rest $0.1°C$ above the transition for $20min$.

Figure 3.9 shows the intensity as a function of the applied frequency in the isotropic phase. The liquid under the conditions as above was solicited by a constant strain amplitude of 100% at three different frequencies $(0.3, 0.6$ and $0.9Hz)$. The raw signal is given in the inserts of figure 3.9. From the intensities at rest we observe the emergence of weak

noisy oscillatory signals (too weak for the human eye to be detectable in the microscope) that show the same frequency as the applied mechanical strain. We extracted the signal amplitudes $I_{amplitude}$ by a sine fit:

$$I = I_{background} + I_{amplitude} \sin^2(\frac{2\pi t}{\omega} + \phi) \tag{17}$$

with t the time and ϕ the phase. The amplitude versus the frequency is presented in figure 3.9 and reveals a linear behaviour.
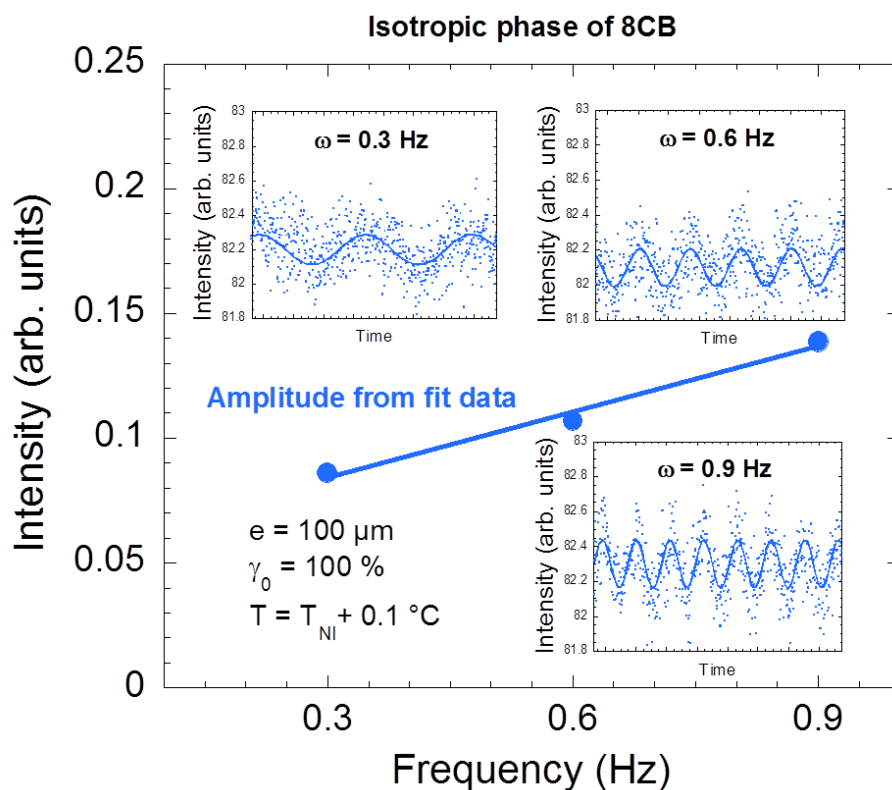
Figure 3.9: Intensity (amplitude) vs the frequency measured in the isotropic phase of the 8CB at $T = T_{NI} + 1°C$ at a constant strain amplitude of $\gamma_0 = 100\%$ between crossed polarizers. The insets present the measured intensity. The data has been fitted by a sine function.

What validity can we give to the strain induced signals?

In principle we expect that a strain induced orientation of the pretransitional fluctuations gives rise to an increase in intensity and thus a birefringent signal. In the logic of our philosophy it would be interesting to know the behaviour of the intensity as a function of the strain amplitude. However, concerning the isotropic phase of the 8CB, we are limited experimentally in this perspective in several ways which show that the results seen in figure 3.9 have to be questioned:

- As soon as we move the observation window, the background intensity is changed. This change is larger than the amplitude of the oscillatory signal.

- Small dust particles or air bubbles present in the sample may enter or leave the observation window and may contribute to an intensity change of the same frequency as the applied strain.

Though we observe the oscillatory signals as soon as the motor starts (insets in figure 3.9) which may rule out the second point, our observations still remain below the uncertainty and any interpretation in terms of birefringence or orientation of pretransitional swarms is precarious and not quantitatively exploitable. A rapid drop of the pretransitional fluctuations away from the transition and a low shear elasticity compared to the two other molecules LCP95 and PACN ($G'_{PACN} = G'_{8CB} \times 1000$) may be a reason why the signals are so weak.

In the following sections we will see that for the isotropic phases of the other samples, the LCP95 and the PACN it is indeed possible to induce a birefringent signal with the mentioned origin.

3.6 Low frequency synchronized birefringence in the isotropic phase of the LCP95

The situation is fairly different for the LCP95 that is a molecule with 12 repetitive units of cyanobiphenyl moieties. In this section we will show for the first time, that it is possible and by far easier than in the case of the 8CB, to orient pretransitional fluctuations in the isotropic phase of the LCP95 with a low frequency mechanical field. Similarly to optical trackers, we expect that the reorientation of the swarms along the stretching direction "visualizes" the strain field which is tested in equilibrium conditions where only the shear elastic properties are supposed to be solicited (the liquid is solicited at low frequency below its flow threshold).
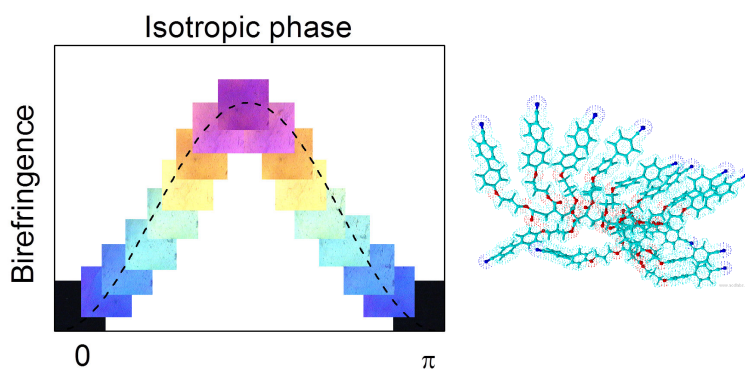
Figure 3.10: Exciting the isotropic liquid with a low frequency, low strain oscillatory force stretches elastic correlations so far neglected in the isotropic phase. As a result, the liquid transits synchronously with the solicitation revealing a bright state. The snaphsots were recorded in the top-view plane (the plane formed by the strain and the neutral axis, see figure 3.7) between crossed polarizers with a polychromatic light for one period of $0.5Hz$ and $\gamma_0 = 10\%$. The isotropic phase appears black at rest; $\gamma_0 = 0$.

The principal result is presented in figure 3.10 and presents photo snapshots of the transmittance of the isotropic liquid recorded while a small strain amplitude of $\gamma_0 = 10\%$ was applied at low frequency $\omega = 0.5Hz$. This section discusses in detail the emergence of a low frequency strain induced birefringent signal. We shall see that:

- At low frequencies the birefringent signal is synchronized to the strain rate or strain amplitude, depending on the magnitude of the latter.

- The signal analysis as a function of the strain amplitude points out a linear harmonic and a distorted signal regime. At large deformations the steady state flow birefringent state is approached.

- The evolution of the birefringence as a function of the strain amplitude resembles the phenomenological behaviour of the stress - strain relation - presenting an elastic behaviour.

- The induced birefringence as a function of the temperature can be described by a mean-field approach confirming the involvement of the pretransitional fluctuations.

- The birefringence can also be observed in the strain-thickness plane (side-view) indicating a bulk phenomenon and excluding surface induced effects like capillary forces as the origin of the signal.

- Finally, we describe the possibility to use the synchronized birefringence to design a stimuli-responsive material.

3.6.1 Low frequency synchronized birefringence

The experiments have been carried out with a wavelength of $\lambda = 614nm$ which permits the calculation of the birefringence Δn. The mechanical excitation is effected by applying a weak oscillatory strain stimulus γ_0 at low frequency (typically from $0.01Hz$ up to $2Hz$); i.e. close to equilibrium conditions. As for the 8CB, the input wave is a sinusoidal strain wave. For a sake of simplification, we consider here the module of γ in accordance with the transmittance (intensity) which is always positive, and a birefringence which is similar during the backward-forward motion:

$$\mid \gamma \mid = \mid \gamma_0 \sin(\omega t) \mid \tag{18}$$

Figure 3.11 shows an example of recorded images at rest and under oscillation between crossed polarizers (magnification $\times 100$). The birefringent image reveals a defect free texture indicating a homogeneous phase. At the lowest frequencies we observe an intense response without defects in contrast with Schlieren or conoscopic or polygonic textures as in the nematic, smectic phases respectively. The birefringence in the isotropic phase remains however weak about $0.1 - 1\%$ of the value reached by commercial nematic displays [152]. The response affects the whole sample. It is induced at low frequencies and relaxes instantly after the oscillation stops. The right side of figure 3.11 shows the signal as a function of time for the isotropic phase at rest and under an applied strain amplitude of $\gamma_0 = 10\%$ at frequency of $\omega = 0.5Hz$.
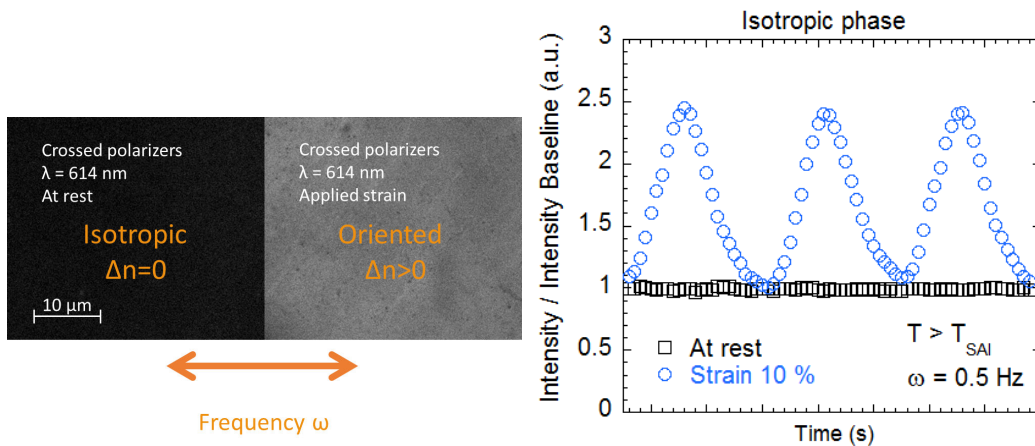
Figure 3.11: (left) Example of recorded images of the isotropic phase of LCP95 between crossed polarizers at a fixed wavelength at rest and excited by oscillatory strain. Magnification $\times 100$. (right) Corresponding intensity versus time.

The optical birefringence indicates that a long range orientation of the molecules establishes. The isotropic phase is thus optically active as soon as the lowest frequencies (down to $0.01Hz$), a property unknown of liquid crystals above the phase transitions. Since the shape of the input wave is kept (harmonic response), the analysis of the signal reveals that the optical birefringence wave is harmonic with the input signal and can therefore be modelled by a sine wave:

$$\Delta n = \Delta n_{max} \mid \sin(\omega t + \phi) \mid \tag{19}$$

with ϕ the phase-shift. Since the intensity is always positive, the birefringence will be taken as a positive value during the forward backward motion. We consider thus the absolute values of the quantities strain γ and birefringence Δn.

3.6.2   Strain dependence - from elastic harmonic signals to the onset of the flow birefringence

The synchronization of the birefringent signals and our claim of probing conditions close to equilibrium and shear elastic properties of the isotropic phase become clearer when we look at the signals as a function of the strain amplitude. Figure 3.12 shows the birefringence versus the strain amplitude at a sample thickness of $e = 250\mu m$ at $T = T_{SAI} + 1°C$ and a fixed frequency $\omega = 0.5Hz$.

The observed strain dependence curve is sigmoidal. An examination of the optical signal indicates three principal regimes. Two of them present a harmonic and one a distorted response:

- **(a)** At very low strain amplitudes $\gamma_0 < \gamma_{crit} = 4\%\pm1\%$, the optical signal is harmonic, weak and in-phase with the strain **(1)**; i.e. in-phase elastic behaviour.

- **(b)** Above this weak critical strain amplitude $4\% < \gamma_0 < 30\%$, the birefringence increases linearly with the strain amplitude. In this regime the optical signal is also harmonic but phase shifted up to $\frac{\pi}{2}$ in respect to the strain (it is in-phase with the strain rate) **(2)**.

- **(c)** At higher strains $\gamma_0 > 30\%$, the peak value of the birefringence does not evolve any more (plateau values) and the shape of the corresponding signal indicates that the system does not relax totally between two periods **(3)**. The signals become distorted and exhibit a frequency doubling. At even larger strains the oscillations become almost totally deteriorated, multiple harmonics flatten the signal to an asymptotic value corresponding to an approaching of a flow birefringent state. **(4)**.

In the following we will discuss these three regimes more in detail.
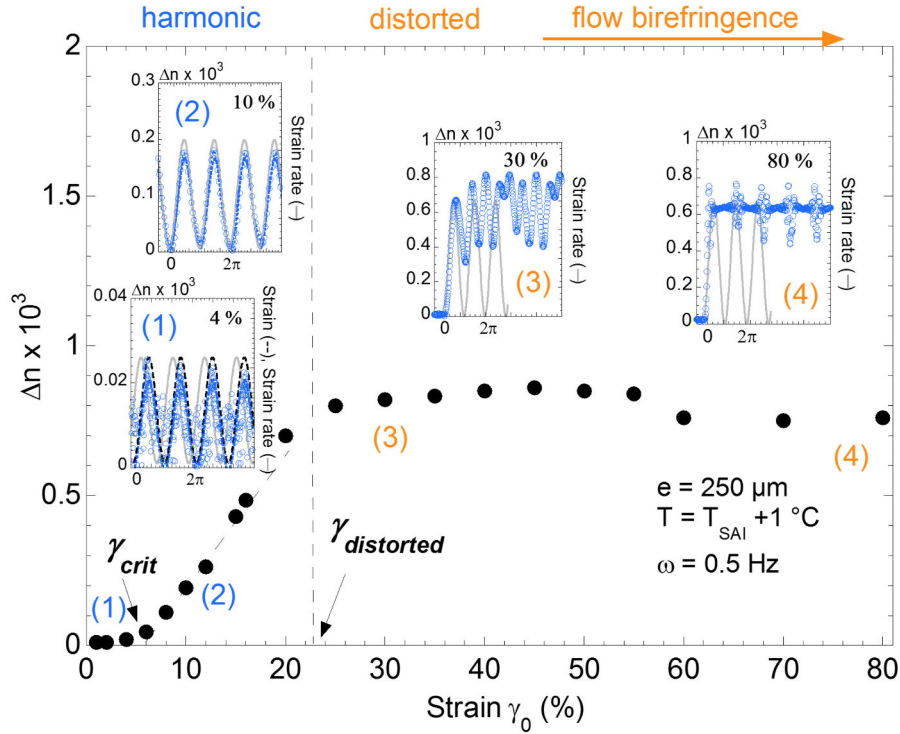
Figure 3.12: Strain dependence of the birefringent signal (peak values) in the isotropic phase of the LCP95. The corresponding oscillatory signals (along the strain/strain rate) are shown as inserts for $4\%(1), 10\%(2), 30\%(3)$ and 80% (4) strain amplitude. Experimental conditions: $(T = T_{SAI} + 1°C)$, $(\omega = 0.5Hz, e = 250\mu m)$.

(a) Fundamental elastic response at very small strains $\gamma_0 < \gamma_{crit}$

For very small strain amplitudes, smaller than a critical value $\gamma_0 < \gamma_{crit}$ the signals nearly superimpose with the strain as shown in figure 3.13 and in the insert (1) in figure 3.12. The harmonic signals in this regime are above the detection limit as they are visible to the eye and emerge from the background noise. While in the case of the 8CB, the observation of the birefringent signal could be attributed to the presence bubbles or dust particles we can exclude any such influence here. Being in-phase with the strain amplitude this regime is interpreted as the initial elastic optical response of the isotropic phase. Here an instant, in-phase collective response of the molecules, coherent with a stretching including pretransitional swarms, is at the origin of the birefringence.
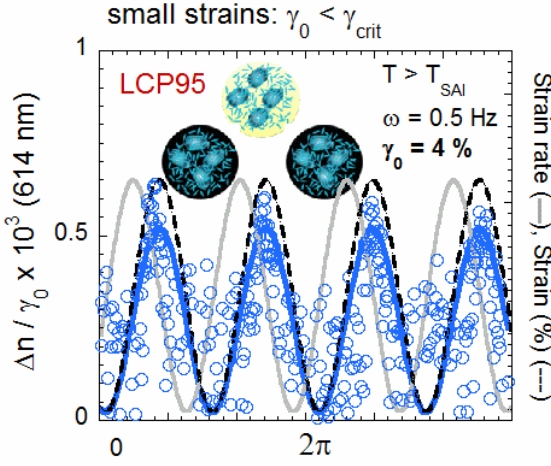
Figure 3.13: Harmonic birefringent signals at very small strain amplitudes of $\gamma_0 = 4\%$ (data: blue circles, sine fit: blue continuous line). The optical signal is weak and in-phase with the strain (black dashed line). Experimental conditions: $T = T_{SAI} + 1°C$, $\omega = 0.5Hz$, $e = 250\mu m$

(b) Linear regime at intermediate strains $\gamma_{crit} < \gamma_0 < \gamma_{distorted}$

At intermediate strain amplitudes $\gamma_{crit} < \gamma_0 < \gamma_{distorted}$, the signal is harmonic and increases linearly with the strain. This linear regime is interesting in several respects. Here the strain induced wave signals are strong and harmonic, the waves are $\frac{\pi}{2}$-phase shifted as shown in figure 3.14 and in the insert (2) in figure 3.12. The birefringent signals are in-phase with the strain rate that is defined by:

$$\mid \frac{d\gamma}{dt} \mid = \mid \gamma_0\omega \sin(\omega t + \frac{\pi}{2}) \mid \tag{20}$$

The strain rate is the rate of strain during the oscillatory motion. In the present experiments, the backward-forward displacement is small $4 - 250\mu m$ (depending on the temperature, see 3.6.3) in order to work in close equilibrium conditions (linear conditions with respect to the elastic property identified in stress measurements) and avoid the entrance in the flow regime. In a first analysis, we consider only the amplitude of the birefringence. In this regime we can define a birefringence renormalized by the strain value as a reduced dynamic birefringence:

$$\Delta n_{norm} = \frac{\Delta n}{\gamma_0 - \gamma_{crit}} \tag{21}$$

Plotted versus the strain amplitude in figure 3.15(a), (b) and for various temperatures in figure 3.19(a) we highlight a strain regime where the dynamic birefringence is independent of the applied strain amplitude. Being independent of the external stimuli, the linear regime defines a characteristic of the material; i.e. an intrinsic birefringence.
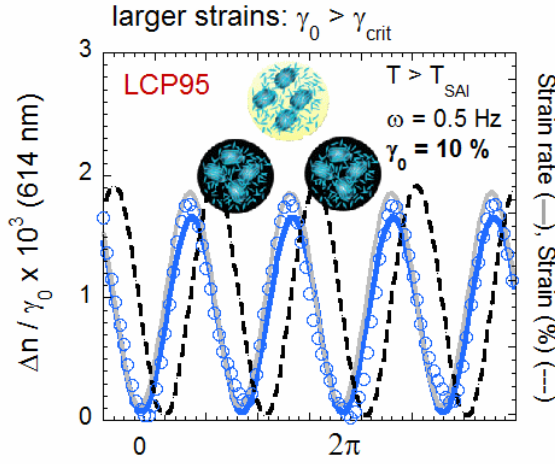
Figure 3.14: The birefringence increases strongly with the applied strain field (here shown for $\gamma_0 = 10\%$), becomes phase shifted by $\frac{\pi}{2}$ in respect to the strain and synchronizes with the strain rate (grey continuous line). Experimental conditions: $T = T_{SAI} + 1°C$, $\omega = 0.5Hz, e = 250\mu m$.
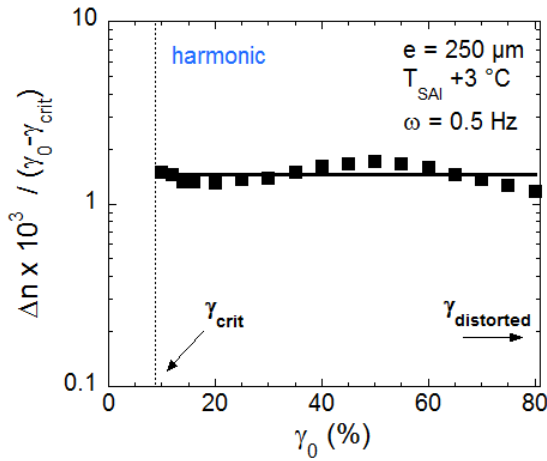
(a) Δn_{norm} for $\gamma_{crit} < \gamma_0 < \gamma_{dist}$ (b) Normalized wave signals in the linear regime
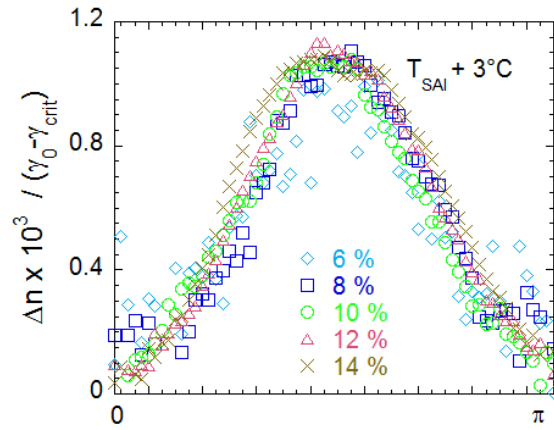
Figure 3.15: Normalized birefringence ($\Delta n_{norm} = \frac{\Delta n}{\gamma_0 - \gamma_{crit}}$) in the isotropic phase of the LCP95 at $T = T_{SAI} + 3°C$. (a) Plotted versus the strain amplitude the linear regime at small strains corresponds to a strain independent regime while the birefringent plateau at higher strains is here decreasing with the strain. The behaviour is similar to the stress - strain behaviour observed in solid mechanics (insert). (b) The superposing oscillatory signals of the reduced birefringence for various strain amplitudes.

This strain-independence is confirmed by the normalized oscillatory signals in the linear regime. The superposition of the curves as shown in figure 3.15(b) for $T = T_{SAI} + 3°C$ illustrates the conservation of the quantity Δn_{norm} with respect to the strain parameter.

We can thus write:

$$\frac{\Delta n}{\gamma_0 - \gamma_{crit}} = \Delta n_{norm} = constant \text{ for } \gamma_{crit} < \gamma_0 < \gamma_{distorted} \tag{22}$$

A strain dependent behaviour that resembles the strain-birefringence curve (figure 3.15(a)) is presented by the (normalized) stress-strain curve displaying a linear region at low strain. The relation between shear stress $(G_0 = (G'^2 + G''^2)^{\frac{1}{2}})$ and strain is written as followed:

$$\frac{\sigma}{\gamma_0} = constant = G_0 \tag{23}$$

Confrontation with lifetimes of the pretransitional fluctuations

Concerning the frequency and the corresponding timescales, the in-phase birefringence is substantial for frequencies as low as $+0.01Hz$ at $1°C$ above the transition temperature. Regarding the addressed timescales, the optical birefringence appears at much slower timescales than the lifetimes measured so far by Kerr effect [44, 45] (and other techniques [146, 147]) in the isotropic phase. These are of the order of $10^{-9} - 10^{-3}s$ for the orientational pretransitional fluctuations depending on the molecular structure of the molecules. An excitation of the swarms would demand frequencies of about $10^3 - 10^9 Hz$ to induce a coupling at these timescales. The present study explores a hundredth of Hz range (i.e. a factor of 10^6 with respect to the expected Kerr-effect lifetimes) via a mechanical action and reveals that the birefringence responds in phase at small strain amplitudes and in-phase with the strain rate at larger strain amplitude.

The synchronized signal under conditions similar as the stress experiments from chapter 2 indicates that the long range ordering is established in agreement with the assumption of an elastic deformation. We will see that this ordering rules out the condition of an isotropic liquid.

Origin of the phase shift at intermediate strains

Another important finding in the linear regime is the fact that the birefringent wave signal is phase shifted by $\frac{\pi}{2}$ in respect to the applied strain amplitude. In the dynamic relaxation experiments in chapter 2 we have attributed this $\frac{\pi}{2}$-phase shift to a viscous behaviour (e.g. figure 2.7(a)). Here a phase-shifted regime is entered above a critical strain value of $\gamma_{crit} = 4 \pm 1\%$ which is similar to the critical strain value found in the stress experiments $\gamma_{crit} = 6\%$. Above this value we observed a transition from an in-phase shear elastic to an out-of-phase viscous behaviour up to very high strain values $(10^3\%)$.

The $\frac{\pi}{2}$-phase shifted optical response observed at $\gamma_0 > \gamma_{crit}$ cannot describe an isotropic liquid but the establishment of a long range oriented state and thus a loss of entropy with

respect to the initial isotropic state. We have seen that the energy accumulated during the strain produces first an in-phase optical response (at $\gamma_0 < \gamma_{crit}$) that we attribute to an instant elastic stretching of the medium. Above at $\gamma_0 > \gamma_{crit}$, the birefringence increases linearly with the strain and is $\frac{\pi}{2}$-phase shifted. This indicates that a second mechanism succeeds to the first stretching phase. This second mechanism involves not only an elastic stretching but must involve a transition as a collective reorientation of pretransitionnal swarms (that will be established in the structural study in chapter 4). This two-steps mechanism contributes both to a rise of the birefringence; i.e. to a lowering of the entropy (with respect to the random isotropic state). The first one is instantaneous $\gamma_0 < \gamma_{crit}$), the second one is delayed ($\gamma_{crit} < \gamma_0 < \gamma_{distorted}$). The common point is that both steps increase the orientation and thus reduce the entropy. The reversibility is also another characteristic of an entropic process: the strain acts thus against an entropic system that relaxes once the strain is reduced. Therefore the isotropic phase exhibits an elastic response below γ_{crit} and a delayed elastic response above γ_{crit}, both alternating entropy loss and entropy recovery during the forward-backward motion. We interpret the delayed step as corresponding to a collective reorientation transition of the pretransitional swarms that appears above a critical strain value γ_{crit}. The $\frac{\pi}{2}$-phase shifted optical signal that succeeds to the first stretching step can be understood as the delayed product of the distortion (transformation) of the shear elasticity under strain. Similar processes with $\frac{\pi}{2}$-phase shifted responses are known in different physical or electronic systems called harmonic oscillators. There it corresponds to a RC oscillator [43].

We suppose that weak intermolecular interactions (of about several Pa) form a weakly linked elastic network up to a macroscopic scale. The interplaying forces are weak, fundamentally different from those governing LC-elastomer networks [153–155] but not negligible at the sub-millimeter scale. The free energy of the isotropic phase might be approximated by integrating a term coupling the orientational pretransitional fluctuations to the strain (at weak strain amplitudes). In analogy with a true elastic network as in LC-elastomers, we can write:

$$F = F_0 + \frac{1}{2}E_0\gamma_0^2 - \sigma\gamma_0 - kS(\gamma)\gamma_0 \tag{24}$$

where S is the order parameter assumed proportional to the birefringence for $\gamma_0 > \gamma_{crit}(S \simeq 0$ without strain), E_0 is the bulk modulus, which is related to the shear modulus G_0 (as identified in the isotropic phase [28, 29, 31, 42, 43]) via the Poisson equation, σ is the applied stress and k a constant coupling the order parameter to the strain γ_0. This expression does not contain the two-step process but indicates that the energy is lowered under strain via an increase of the order parameter (birefringence) and thus an entropy decrease. The stress release produces an entropy gain and a return to the isotropic state. This mechanism sets here the role of long range reversible (elastic) interactions as crucial in the liquid state above the isotropic transition.

(c) Asymptotic strain behaviour: Collapse of the harmonic response at larger strains towards the flow birefringence

At strain amplitudes $\gamma_0 > \gamma_{distorted}$ the initial wave form is not conserved (3.12). In the case of the isotropic phase of the LCP95 this regime is entered at strain amplitudes above $\gamma_0 = 25\%$ where we observe a saturation of the signals, a birefringence plateau. A further strain increase has no more effect in the accessible strain range. At large strain amplitudes as shown for $\gamma_0 = 30\%$ in figure 3.16(a) and in the insert of figure 3.12 a second harmonic is generated. The oriented pretransitional swarms do not have sufficient time to relax

(a) Large strain amplitudes $\gamma_0 = 30\%$. (b) Larger strain amplitudes $\gamma_0 = 80\%$.
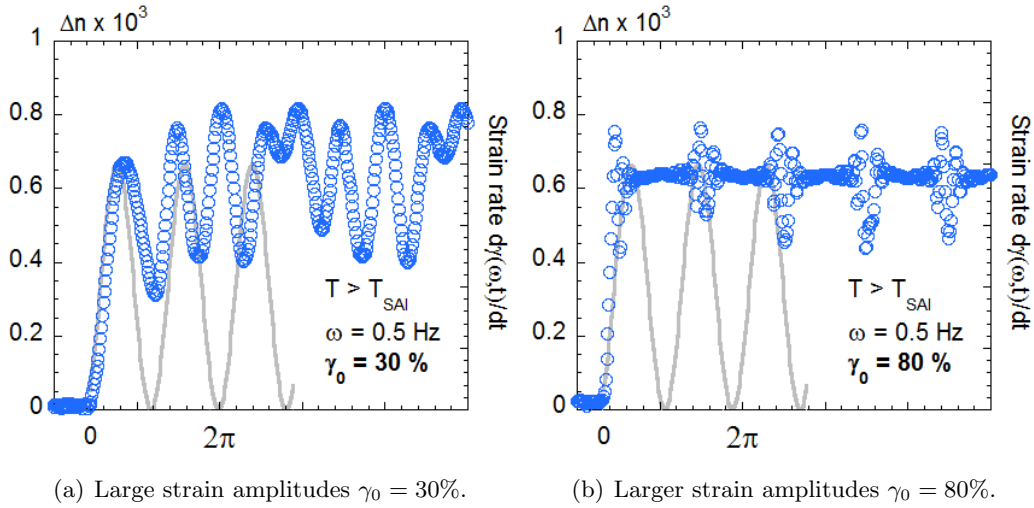
Figure 3.16: Asymptotic slope of the birefringent signals (blue circles) observed in the isotropic phase of the LCP95 at large strain amplitudes. (a) Above 30% strain amplitude, the optical signal exhibits a frequency doubling. (b) At 80% strain amplitude, the generation of multiple harmonics flattens the signal to an asymptotic value, to the flow birefringence. The grey continuous line represents the strain rate. Experimental conditions: $T = T_{SAI} + 1°C$, $\omega = 0.5Hz$, $e = 250\mu m$.

between two oscillations and the saturation of the signal can be explained by a "backflow effect". The further increase of the strain amplitude generates the superposition of multiple harmonics giving rise to an apparent continuous-like birefringent signal whose asymptotic value approaches the flow birefringence as seen in figure 3.16(b) and as an insert in 3.12. The conditions are thus approaching a steady state flow which produces the well-known flow birefringence. This strongly non-linear effect whose origin is still debated, has first been identified for simple liquids under very high shear rates by Sadron in 1936 [140] and later for the isotropic phase of liquid crystals by Zvetkov [141] and more recently for

micellar solutions by Decruppe [156]. In the case of the isotropic phase of liquid crystals a shear induced phase transition can be observed [109, 142]. Hess, Olmsted and Goldbart [149–151] reported on an attempt to theoretically describe this phenomenon by irreversible thermodynamics.

3.6.3 Temperature dependence of the low frequency birefringence

The strain induced birefringent signal can be observed far into the isotropic phase at temperatures up to $15°C$ above T_{SAI} (figure 3.17). For temperatures up to $5°C$ above the transition we observe the three regimes discussed in the previous section:

- A weak increase of the birefringence at very small strain amplitudes $\gamma_0 < \gamma_{crit}$, harmonic and in-phase with the strain.

- A linear regime with a strong increase of the birefringence and harmonic signals $\frac{\pi}{2}$-phase shifted in respect to the strain at intermediate strain amplitudes $\gamma_{crit} < \gamma_0 < \gamma_{distorted}$

- The saturation of the signals, a birefringent plateau at large strain amplitudes $\gamma_0 > \gamma_{distorted}$

Figure 3.17: Strain dependence of the birefringent signal (peak value) in the isotropic phase of the LCP95 for several temperatures above the isotropic transition at low frequency oscillatory excitation ($\omega = 0.5Hz$, sample thickness $e = 250\mu m$).
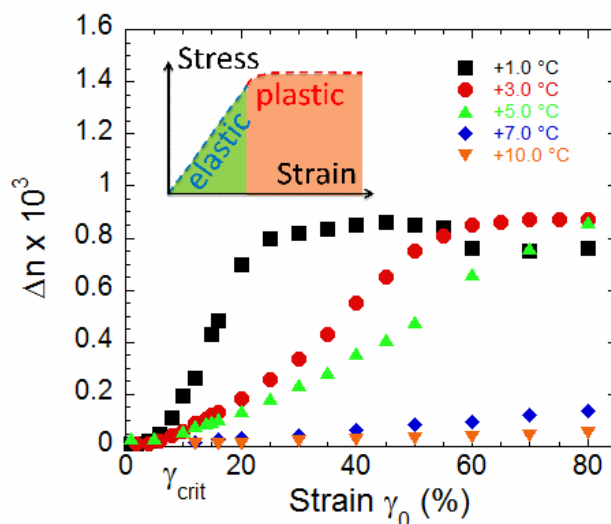
While the critical strain amplitude γ_{crit} weakly increases with the temperature the onset of the birefringent plateau above $\gamma_{distorted}$ is strongly shifted to higher strain amplitudes e.g. from 25% at $T = T_{SAI}+1°C$ to 60% at $T = T_{SAI}+3°C$. At temperatures above $+5°C$ above the transition the birefringent plateau is no longer observed in the accessible strain range. The size of the pretransitional swarms together with the birefringent signal decrease with

the temperature (figure 3.18). At higher temperatures above $T = T_{SAI} + 3°C$ we cannot no longer identify a elastic regime below γ_{crit}. Here we only observe signals $\frac{\pi}{2}$-phase shifted in respect to the strain and in-phase with the strain rate. The usage of the pretransitional swarms as optical probes is therefore limited by their size-temperature dependence which is most certainly a reason why we are not able to detect strong birefringent signals in the isotropic phase of small liquid crystal molecules as the 8CB. The normalized birefringent
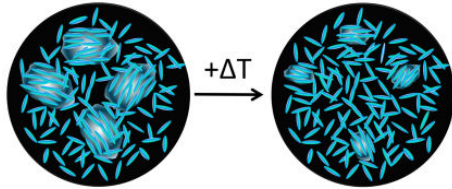
Figure 3.18: Decrease of the orientational pretransitional swarms with increasing temperature.

signal plotted versus the strain amplitude enables to highlight the regime independent of the strain amplitude for all tested temperatures (figure 3.19(a)). For $T = T_{SAI} + 1°C$
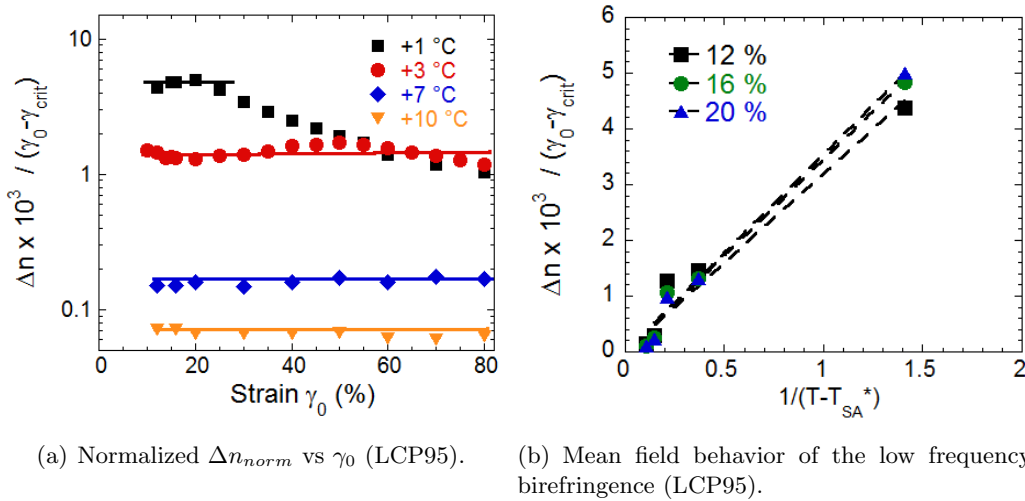
(a) Normalized Δn_{norm} vs γ_0 (LCP95).

(b) Mean field behavior of the low frequency birefringence (LCP95).

Figure 3.19: Reduced birefringence $\Delta n_{norm} = \frac{\Delta n}{\gamma_0 - \gamma_{crit}}$ of the isotropic phase of the LCP95 in the linear regime reveals a strain independent quantity: (a) Δn_{norm} versus the strain amplitude for various temperatures above T_{SAI}. The eye-guide lines present a strain independent regime. (b) A Mean field behaviour of the low frequency birefringence is observed at the approach of the isotropic transition which indicates independence of the applied strain (linear regime in figure 3.12 and 3.17). The normalized birefringence is shown for three strain amplitudes: 12% (black boxes), 16% (green dots) and 20% (blue triangles) as a function of $T - T_{SAI}^{\star}$ with $T_{SAI}^{\star} = T_{SAI} = 0.4°C$. The data points reveal a linear, pretransitional behaviour.

we observe again the decrease of Δn_{norm} above $\gamma_{distorted}$ while for higher temperatures this drop cannot be observed in the accessible strain range. The results show the strain-independent behaviour is observable in the probed temperature range despite the strong decrease of the size of the pretransitional swarms.

Finally the low frequency birefringence obeys at low strain a typical mean field behavior (figure 3.19(b)): $\Delta n_{norm} \propto \frac{1}{T - T^\star_{SAI}}$ where $T^\star_{SAI} - T_{SAI} = 0.4°C$ confirming that the measurements are carried out in nearly non-perturbative conditions e.g. the transition temperature is not affected by the application of the low frequency strain. A similar mean-field behaviour is observed for the isotropic phase in Kerr-effect measurements (see figure 3.5(b)).

3.7 Identification of a low frequency synchronized birefringence in the isotropic phase of the PACN
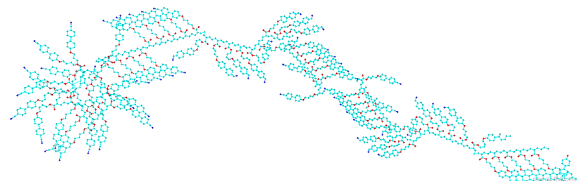
So far we have reported on the low frequency strain induced birefringence in the isotropic phase of the 12 repetitive units LCP95. Very similar observations can be made for the isotropic phase of the PACN. The study of this the molecule is useful as it presents several differences to the LCP95:

- The PACN has a polymeric nature (80 repetitive units): Does it have an influence on the persistence of the pretransitional fluctuations and on the strain induced signal?

- The PACN shows a nematic phase below the clearing point instead of a smecitc A phase.

- Higher shear elasticity at low frequencies: The shear elastic values of the isotropic phase exceed the ones of the LCP95 by almost a factor 5.

In the following we will shortly present the most important results obtained for the isotropic phase of the PACN and a comparison to the LCP95.

3.7.1 Low frequency synchronized birefringence

As for the LCP95 we can show for the PACN that it is possible to induce a birefringent signal in the isotropic phase by applying a low frequency oscillatory strain. Figure 3.20 presents birefringent signals: In the isotropic phase at $T = T_{NI} + 0.5°C$ at a sample thickness of $250\mu m$ we observe the emergence of harmonic signals. Similarly to the LCP95 the analysis reveals that the birefringence is in-phase with the applied strain at very low strain amplitudes $\gamma_0 < \gamma_{crit} = 5\%$ (figure 3.20(a)) and in-phase with the strain rate (figure 3.20(b)) at strains above a critical strain value $\gamma_0 > \gamma_{crit}$. In the microscope we observe a strong defect-free, perfectly homogeneous birefringence. The birefringence is thus not influenced by the phase below the clearing point.

The existence of an optical birefringence close to equilibrium conditions indicates that a long range orientation of the molecules establishes. The signal is accessible at low frequencies $\omega = 1.0Hz$. Kerr effect measurements have shown that the relaxation times of the

(a) Small strain amplitudes   (b) Larger strain amplitudes
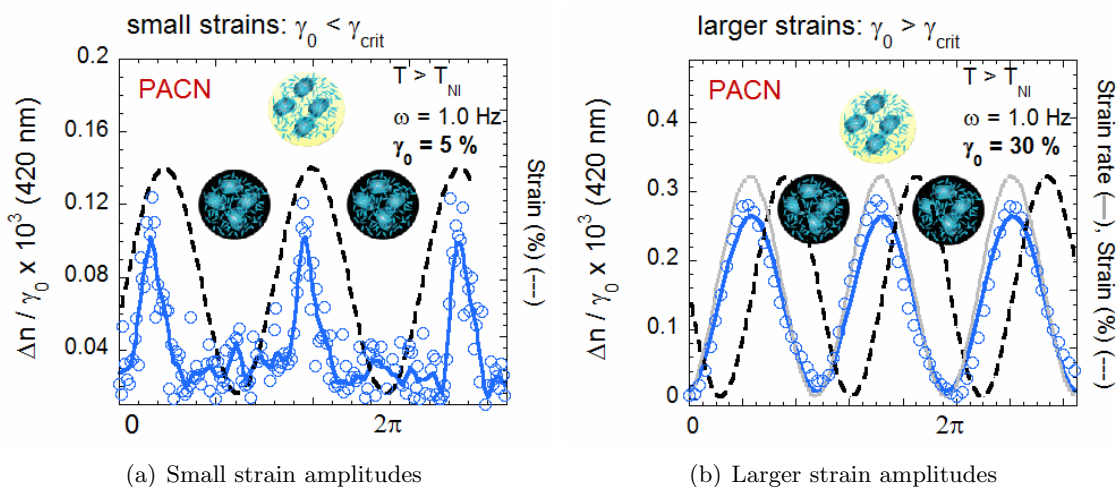
Figure 3.20: Harmonic birefringent signals induced in the isotropic phase of the PACN (data: blue circles, smoothing: blue continuous line): (a) For a very small strain amplitude of $\gamma_0 = 5\%$ the optical signal is weak and in-phase with the strain (black dashed line). (b) Above a critical strain (here shown for $\gamma_0 = 30\%$) the signal is in-phase with the strain rate (grey continuous line). Experimental conditions: $T = T_{NI}+0.5°C$, $\omega = 1.0Hz$, $e = 250\mu m$.

pretransitional fluctuations in the isotropic phase of SCLCPs like the PACN are slowed down. Relaxation times of up to $0.01s$ have been reported for liquid crystal molecules almost four times the mass of the PACN [45]. Here we explored frequencies of $1.0Hz$ and thus at time-scales of a factor 100 slower indicating much longer time-scales in the isotropic phase.

3.7.2   Strain and temperature dependence

Close to the isotropic transition we observe the same comportment of the low frequency birefringence as a function of the strain amplitude as for the LCP95 (figure 3.21). The birefringence can be observed at several degrees above the isotropic transition. Under the same conditions the signals show remarkably weaker signals as for the LCP95. The closer to the transition temperature, the more intense is the birefringence in agreement with the growth of the pretransitional fluctuations. We also find again a strain threshold γ_{crit} above which we observe a linear increase of the birefringence with the strain. At higher temperatures the onset of the birefringent plateau is not observable and probably shifted to higher strain values that are not accessible with our apparatus. The harmonic wave signals become distorted with the beginning of the birefringent plateau - as seen for the LCP95.
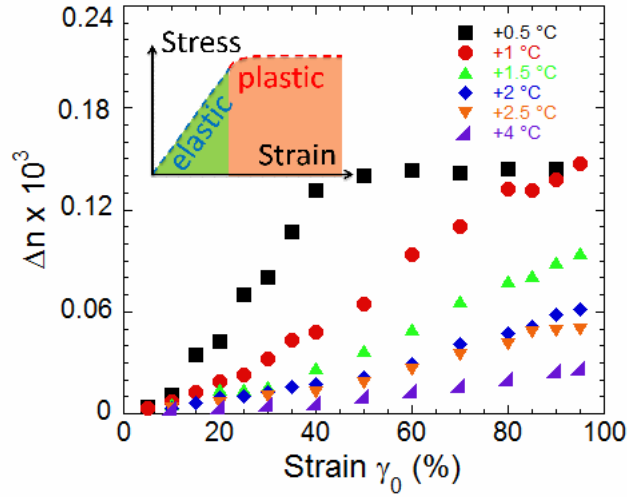
Figure 3.21: Strain dependence of the birefringent signal (peak value) in the isotropic phase of PACN for several temperatures above the isotropic transition at low frequency oscillatory excitation ($\omega = 1.0 Hz$, sample thickness $e = 250 \mu m$).

The introduction of a birefringence normalized by the strain (3.6.2) highlights the strain independent regime when plotted versus the applied strain amplitude (figure 3.22(a)). Close to the transition we observe a rapid decrease of Δn_{norm} at higher strains while for the higher temperatures the signal remains independent for all accessible strain values. Again we can argue that independent of the external stimuli, the linear regime defines a characteristic of the material resembling the strain-stress behaviour in solid-mechanics (insert in figure 3.21).

Concerning the role of the pretransitional fluctuations the intensity of the low frequency birefringent signal as a function of the temperature can be described by a mean-field behaviour (figure 3.22(b)): $\Delta n_{norm} \propto \frac{1}{T - T_{NI}^\star}$ where $T_{NI}^\star - T_{NI} = 0.4°C$ just as for the LCP95. Again this confirms that the measurements are carried out in close to equilibrium conditions.

(a) Normalized Δn_{norm} vs γ_0 (PACN).

(b) Mean field behavior of the low frequency birefringence (PACN).
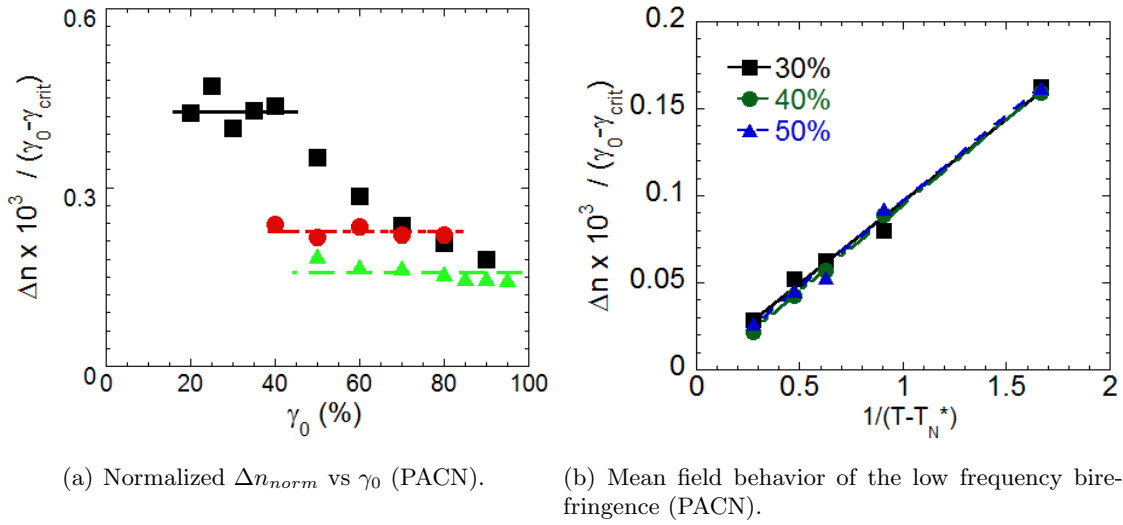
Figure 3.22: In the isotropic phase of the PACN, the reduced birefringence $\Delta n_{norm} = (\frac{\Delta n}{\gamma_0 - \gamma_{crit}})$ in the linear regime reveals a strain independent quantity: (a) Δn_{norm} versus the strain amplitude for various temperatures above T_{NI}. The eye-guide lines present a strain independent regime. (b) A Mean field behaviour of the low frequency birefringence is observed at the approach of the transition which indicates an independence of the applied strain (linear regime in figure 3.21). The normalized birefringence is shown for three strain amplitudes 30% (black boxes), 40% (green dots) and 50% (blue triangles) as a function of $T - T_{NI}^{\star}$ with $T_{NI}^{\star} = T_{NI} = 0.4°C$. The data points reveal a linear, pretransitional behaviour.

At comparable frequencies the optical signal of the LCP95 is about 100 times larger in the linear regime than for the PACN (3.23 insert). The difference might be explained by a stronger contribution of pretransitional fluctuations at the approach of the isotropic-smectic transition in comparison to the isotropic-nematic transition. Also, the clearing point lies at $T_{SAI} = 79.8°C$ in the case of the LCP95 and at $T_{NI} = 124°C$ in the case of the PACN. This temperature difference of $44°C$ is not negligible in terms of thermal energy which leads to a smaller size of pretransitional fluctuations in the case of the PACN and consequently to a weaker birefringence. A further parameter is the polarizability of the molecule. The LCP95 is used in liquid crystal displays because of its high birefringence. We can also observe that the entrance of the distorted regime (the birefringent plateau) is shifted to higher strain amplitudes for the PACN. Conclusively we can assume, that optimizing both chemical and physical parameters as the molecular structure or the anchoring are to have a large influence on the strain induced birefringence.
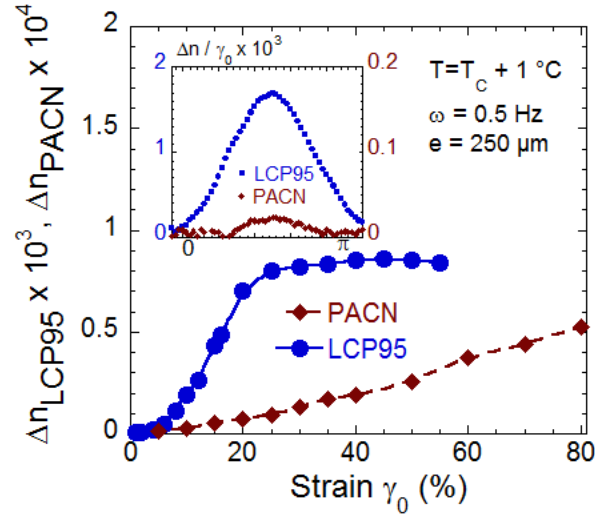
Figure 3.23: Comparative intensities of the low frequency birefringence (peak values) displayed in the isotropic phase of the LCP95 (blue dots, $\Delta n \times 10^3$) and the PACN (brown diamonds, $\Delta n \times 10^4$) under the same conditions ($0.5 Hz, 250 \mu m$, $T = T_C + 1°C$ above the isotropic transition) versus the strain amplitude. The lines serve as eye-guides. Insert: Comparison of the optical wave signals of the isotropic phase of LCP95 and PACN at $\gamma_0 = 10\%$ (the birefringence is normalized to the strain amplitude). Double scale.

3.8 Stimuli Response Material and aspects for application

Liquid crystals are exceptional tools to probe the condensed properties of liquids. Additionally the obtaining of a synchronized birefringence at low frequency is an interesting opto-mechanical effect that may be used as a stimuli responsive system. Such an On-Off-switch consumes little energy (the liquid is solicited close to its equilibrium state) is easily tunable by modifying chemical and physical parameters as the molecular structure or the anchoring and offers a reversible transition from a dark state to a bright birefringent state (figure 3.24). Concerning the available output signals we are able to easily produce oscillatory wave and square wave responses figure 3.24.

(a) Stimuli-Responsive, active material.   (b) Output signals
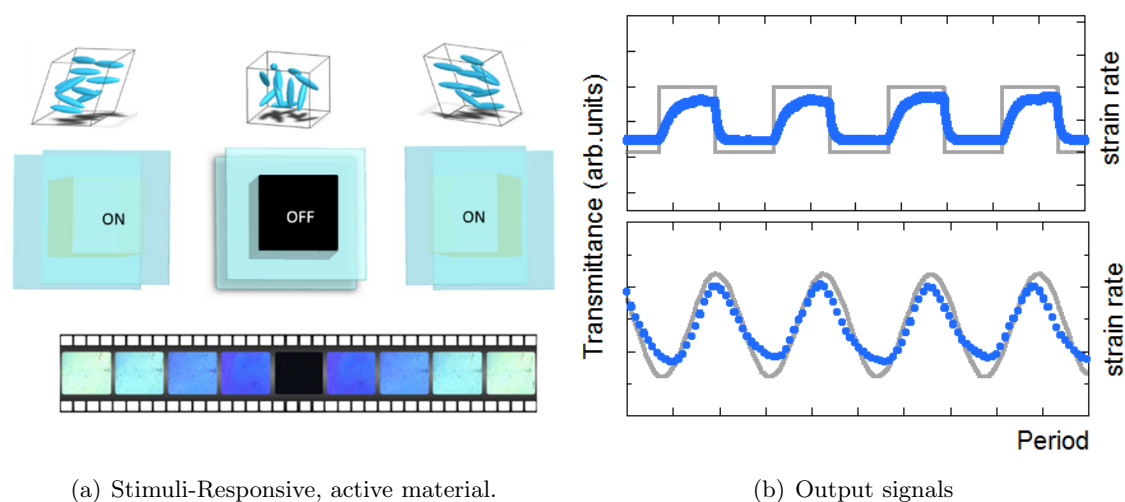
Figure 3.24: (a) The low frequency strain induced birefringence may serve as a stimuli responsive material presenting a mechanical On-Off-switch from a true black state to an bright birefringent state. The small images present photographs taken during the induction of the birefringence. (b) Different output signals are possible e.g. square and wave form.

3.9   Complementary experiments in the side-view plane

In addition to the microscopic measurements we established a second setup consisting in a home-made apparatus which we can use to observe qualitatively the plane of the gap or side-view plane $(\vec{x} - \vec{z})$ additionally to the so far studied top-view plane $(\vec{x} - \vec{y})$ (figure 3.25).
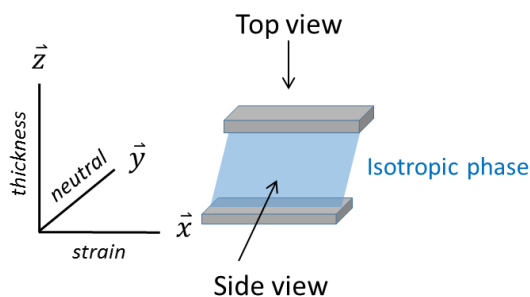
Figure 3.25: The isotropic phase between two surfaces: The side-view plane $(\vec{x} - \vec{z})$ is the plane formed by the strain $(\vec{x})$ and the thickness $(\vec{z})$ axis and is observed along the neutral axis $\vec{y}$. The top-view plane $(\vec{x} - \vec{y})$, observed in the microscope, is formed by the strain $(\vec{x})$ and neutral axis $(\vec{y})$ and is observed along the thickness axis $(\vec{z})$.

In this geometry the sample thickness and largeness are of the millimeter scale. The access to this plane of observation probes how the strain is transmitted to the sample in the whole thickness. This information is important to analyse the mechanism involved in terms of a macroscopic bulk process, and not in terms of interfacial effects. An additional goal of this setup is to carry out a structural analysis under strain by X-ray and neutron diffraction techniques under comparable conditions. The setup allows for the usage of non-transparent surfaces and we benefited from this advantage by using alumina substrates as in the stress measurements from chapter 2 in order to improve the wetting condition. In the following we examine the optical response between crossed polarizers in the side-view plane. A structural analysis by X-ray and neutron diffraction will be presented in chapter 4.

Optical measurements in the side-view plane

A scheme and a photograph of the apparatus are shown in figure 3.26. The light transmitted by the sample placed in between two polarizers is observed with a low level CMOS camera equipped with a $40\times$ magnification lens. The oscillatory movement is of square type in this geometry. The apparatus allows to apply the same frequencies and strain amplitudes as in the microscopic measurements. The observation of the side-view plane completes the

(a) Scheme of the side-view observation plane   (b) Photograph of the setup
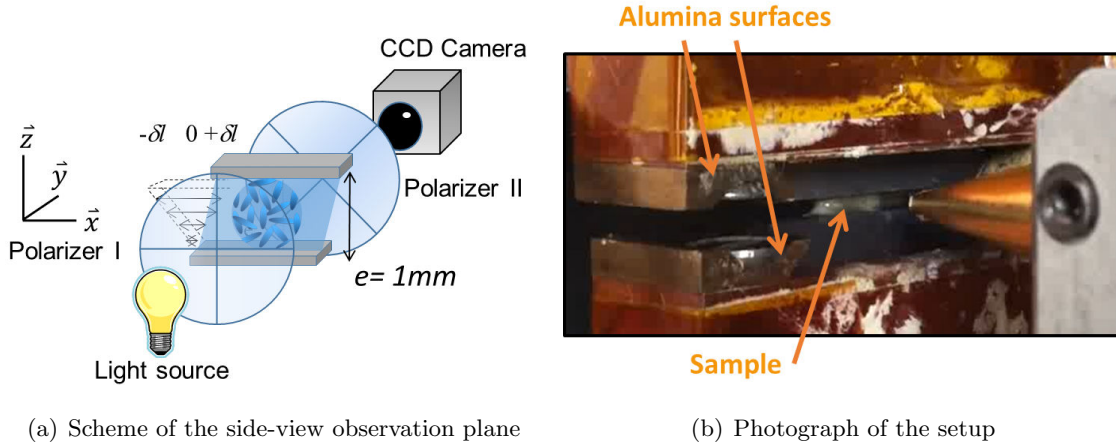
Figure 3.26: Observation of the optical signal generated within the gap of the two fixtures between crossed polarizers ($1mm$ gap thickness) and recorded from the gap side, the side-view plane ($\vec{x} - \vec{z}$).

analysis of the birefringence. In this geometry, the sample gap is directly observed. Figure 3.27(a) displays the photo snapshots recorded within a one millimeter gap over a strain period (the crossed polarizers are oriented at $45°$ with respect to the strain direction). The isotropic phase of the LCP95 was used as sample ($T = T_{SAI} + 1°C$, frequency $\omega = 0.5Hz$, strain amplitude $\gamma_0 = 80\%$. The birefringence is established within the whole sample volume indicating a macroscopic alignment effect of the pretransitional fluctuations. Its values are 10 times smaller than the ones found in the microscopic setup (top-view plane). The homogeneous birefringence is not induced by surface tension or interfacial tension related effect and also indicates that at low strain amplitude no non-linear effects as shear banding [150, 151, 157, 158] or shear induced transitions [109, 149–151, 157, 158] are observable.

The signal in the plane ($\vec{x} - \vec{z}$) is in phase with the strain rate in agreement with the observation of the top-view plane. The careful observation of the signal indicates an excess of intensity at the extreme positions (to the point of backward-forward return). A similar observation is done by rotating the crossed polarizers along the strain direction (parallel to the surface). This excess of intensity at the return might indicate that the rotation of the optical axis (of the pretransitional fluctuations) is achieved in the ($\vec{x} - \vec{z}$) plane (figure 3.27(b) and (c)). Figure 3.27(b) displays a weaker intensity at the return point than in Figure 3.27(c). The average strain induced intensity in figure 3.27(b) is also larger indicating a tilt of the birefringence axis (corresponding to the director of the pretransitional fluctuations) with respect to the strain axis which is coherent with the strain gradient within the gap (scheme at in figure 3.27(a)).
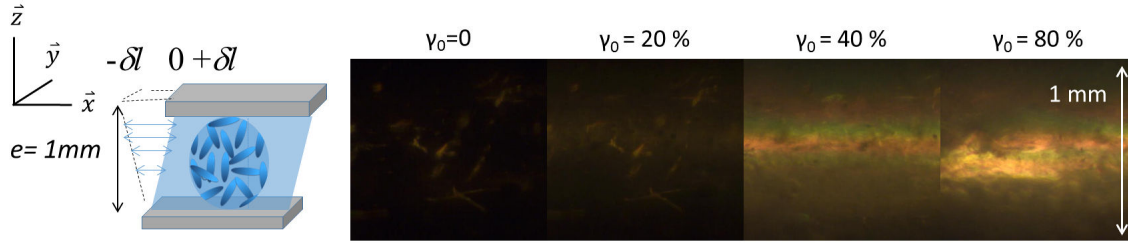
(a) Photographs taken in the side-view between crossed polarizers
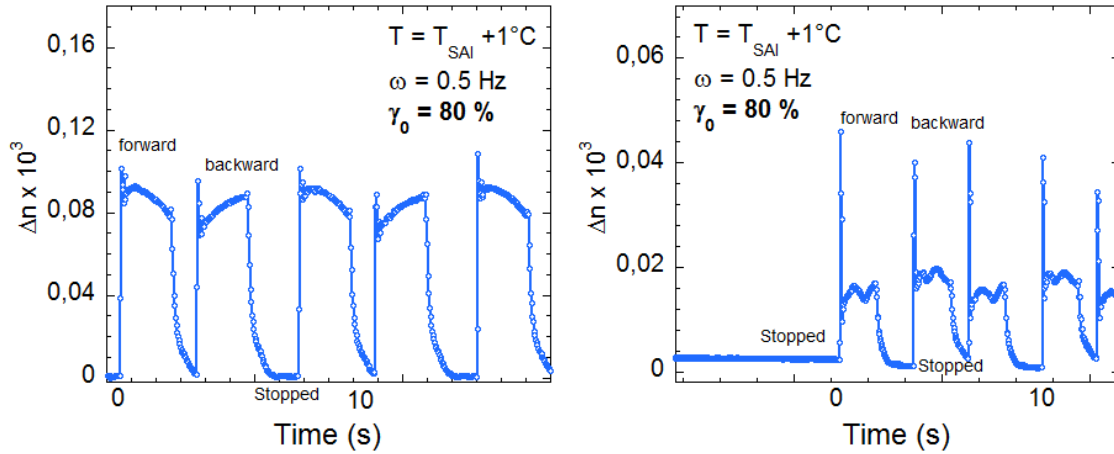
(b) Crossed polarizers oriented 45° in respect to $\vec{x}$

(c) Crossed polarizers oriented along $\vec{x}$

Figure 3.27: Observation of the optical signal within the side-view plane ($\vec{x} - \vec{z}$). The strain is applied by moving the top plate, the other plate is fixed. (a) Photo snapshots recorded between crossed polarizers during one square cycle period. (b) The crossed polarizers are oriented at 45° with respect to the strain direction $\vec{x}$ (80% strain amplitude, $0.5Hz$, data points collected every $1/30s$) visualizing the birefringence produced along the strain direction. (b) The crossed polarizers are oriented along the strain direction. Sample: LCP95, $T = T_{SAI} + 1°C$, gap thickness $e = 1mm$, frequency $\omega = 0.5Hz$, strain amplitude $\gamma_0 = 80\%$. Polychromatic light was used for irradiation and the birefringence was calculated using $520nm$ as an average wavelength.

In this plane of observation the isotropic phase of the PACN shows almost no birefringence at all. The fact that in the side-view plane the signal is weak in the case of the LCP95 and almost zero in the case of PACN coincides with the observation of a strong birefringence in the top-view plane. On a molecular scale this can be interpreted as a log-rolling orientation of the molecules under strain - a conformation which will be discussed more in detail by a structural analysis in chapter 4.

3.10 Summary and conclusions

On the basis of the identification of a terminal shear elasticity we have successfully transferred the experimental conditions of the dynamic mechanical analysis to optical measurements. This was done by synchronizing a microscope observation with an oscillatory shear cell which permitted to precisely control the temperature of the sample and apply a low frequency oscillatory strain amplitude. Our aim was to observe optically the response of the isotropic phase under similar conditions that led to the identification of a shear elastic response in the stress measurements of chapter 2. A trigger system (R&D Vision) granted access to both the optical signal between crossed polarizers, measured by a CCD camera, and the movement of the motor and thus to their phase behaviour.

Our premise was that the orientational pretransitional fluctuations that persist in the isotropic phase of liquid crystals are "feeling" the low frequency strain field.

This strategy was fruitful since for the first time, an optical birefringence is detected at low frequency in the isotropic phase. The obtained birefringent signal is harmonic (the input strain wave signal is conserved) strong, reversible and defect free. It is accessible at the lowest frequencies ($0.01Hz$), up to $15°C$ above the isotropic transition of the LCP95 and PACN and for millimeter sample sizes. This so far unknown low frequency phenomenon was identified in the top-view and side-view geometry and thus reveals a bulk-related property.

Concerning the harmonic optical response:

- At the lowest strain amplitudes below ($\gamma_0 < \gamma_{crit} \approx 4-5\%$), we observed a synchronization with the strain. This in-phase response is very weak and purely elastic.

- At intermediate strain amplitudes ($\gamma_0 > \gamma_{crit}$) the behaviour is also harmonic $\frac{\pi}{2}$-phase shifted (in-phase with the strain rate).
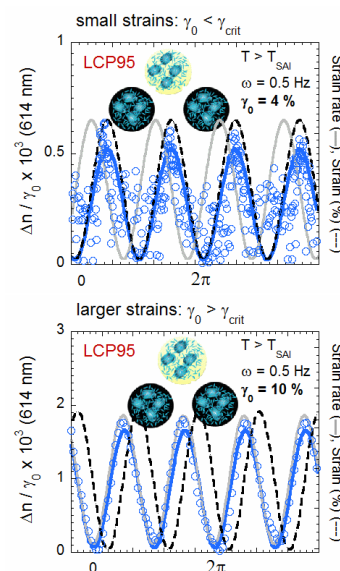
- At large strain amplitudes, the signal is distorted, due to the impossibility to relax

between two strain waves.

The characteristics of the low frequency birefringence can be gathered as following:

- The strain dependence of the low frequency Δn reveals a sigmoidal curve with a harmonic regime (sine signals in- or phase shifted by $\frac{\pi}{2}$) and a birefringent plateau at large strains above $\gamma_{distored}$. At large strains, the signals become distorted and eventually obtain a continuous signal - the onset of the flow birefringence [109, 140–142].
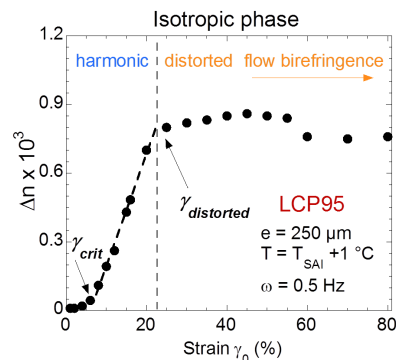
- The closer the transition temperature, the more intense is the birefringence in agreement with the growth of pretransitonal fluctuations and vice versa. This temperature dependence presents the limiting factor for using the pretransitional swarms as optical probes of the strain field.

- The birefringence normalized by the strain amplitude demonstrates that the linear harmonic regime is independent of the deformation. This important result indicates that the linear regime defines a characteristic property of the material. Interestingly the birefringence-strain behaviour is similar to the strain behaviour of the viscous modulus G'' demonstrated in chapter 2.
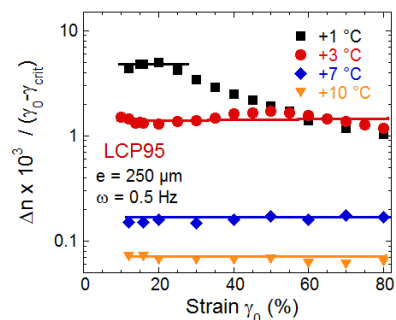
- Our claim to probe properties close to equilibrium is supported by a mean field behaviour of the strain induced Δn versus the temperature.
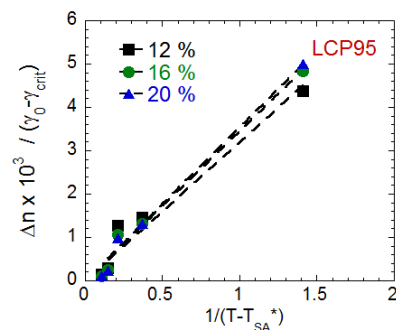
The origin of the birefringent signal

The origin of the dynamic birefringence is coupled to the orientation of the orientational pretransitional swarms coexisting in the isotropic phase. By mechanical excitation we have observed a strong signal at frequencies as low as $0.01Hz$, at least a factor 10^4 slower than reported by Kerr effect [44, 45], dynamic light scattering [146] and NMR measurements [147]. This evidences that much **slower time-scales should exist in the isotropic phase**.
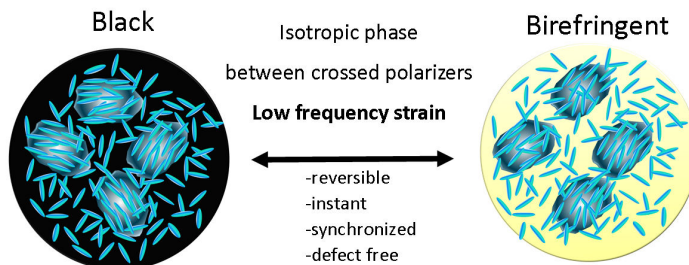
The birefringence which is due to the stretching and/or orientation of pretransitional swarms is obtained by a low frequency oscillation of the isotropic phase close to equilibrium. At lower strain amplitudes $\gamma_0 < \gamma_{distorted}$ the signal shape is conserved and the system can be viewed as a driven harmonic oscillator. This signifies that **the $\frac{\pi}{2}$-phase shift observed at intermediate strains $\gamma_{crit} < \gamma_0 < \gamma_{distorted}$ is not a signature of a dissipative event.** It rather corresponds to a process that transforms the initial stretching of the pretransitional clusters into a collective orientation (strong birefringence). Dissipative effects are observed at large strains $\gamma_0 > \gamma_{distorted}$ where we observe the apparition of anharmonics and a diminution of the signal (birefringent plateau). Increasing the amplitude of the oscillation will eventually, by a superposition of anharmonics, lead to continuous state, a flow birefringent regime [109, 140–142] where the energy is dissipated.

Concerning the flow birefringence, according to Olmsted [151] and de Gennes [48], a coupling of the terminal relaxation times to the flow is necessary in order to observe a nonlinear, dissipative birefringence. However neither conventional VE nor wetting improved stress measurements show any relaxation slow enough to account for the observation of a birefringence. Our results indicate that the origin of the flow birefringence and thus the viscosity related properties originate from intrinsic property at rest. This is supported by the observation of an in-phase (elastic) behaviour of the strain induced birefringence at the lowest strain amplitude (and thus closest to the equilibrium state).

Confrontation with the stress measurements

The spectacular **optical effect is neither explainable on the basis of the pretransitional lifetimes nor by visco-elastic relaxation time-scales**. It is approached by assuming an **opto-mechano coupling to the low frequency shear elasticity**. The dependence of the low frequency birefringence on the strain exhibits **similarities with the strain-stress behaviour**: both, the birefringence and the stress are in-phase with the strain at very low strain values and $\frac{\pi}{2}$-phase shift (in-phase with the strain rate) at higher strain values ($\gamma_0 > \gamma_{crit}$).
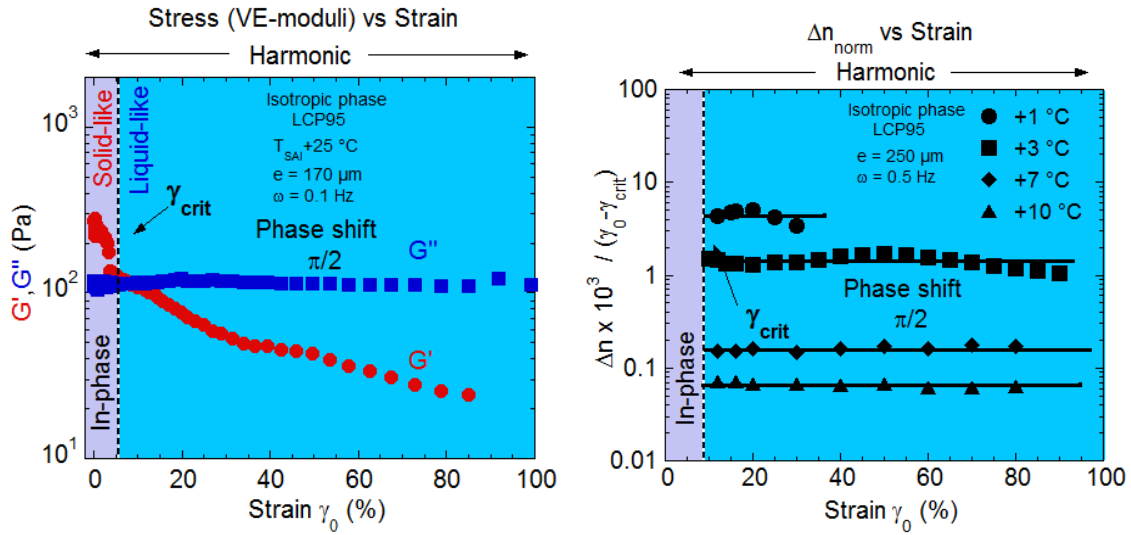
Figure 3.28: Comparison between the low frequency strain dependence of the viscoelastic moduli (left, for a better comparison the strain is not presented in log scale) and the reduced birefringence (right) for the isotropic phase of the LCP95. In both cases we observe signals in-phase with the strain below γ_{crit} and phase shifted signals above γ_{crit}. Since the birefringence shown represents the linear regime it is reduced by γ_{crit} and no points can be presented in-phase regime.

While in stress measurements the $\frac{\pi}{2}$-phase shifted regime indicates a liquid-like behaviour, the **low frequency birefringence indicates that a long range ordering is established**. Such an **ordering rules out the condition of an isotropic liquid**.

The $\frac{\pi}{2}$-phase shifted birefringence observed at intermediate strains ($\gamma_{crit} < \gamma_0 < \gamma_{dist}$ succeeds to the first in-phase response (simple stretching). It corresponds to a second mechanism occurring as a delayed process above γ_{crit} and is characterized by a linear increase of the birefringence with the strain. Both steps contribute to a rise of the birefringence;

i.e. to a lowering of the entropy (with respect to the random isotropic state) and explain the reversibility of the signal. The $\frac{\pi}{2}$-phase shifted optical signal is coherent with a reorientation process of the pretransitional swarms that is not instantaneous. Similar processes with $\frac{\pi}{2}$-phase shifted responses are found in different physical or electronic systems called harmonic oscillators [43].

The optical results seem to confirm that the isotropic phase is an elastically correlated "self-assembly" in agreement with stress measurements indicating a non-vanishing elastic modulus at low frequency. In the light of this, the birefringence indicates that the elastic correlations between molecules are not lost but directed.

Additionally, the strong birefringent signal at low frequencies in the isotropic liquid phase is obviously an attractive property for converting a mechanical action in an optical device based on a reversible transition from a true black state to a birefringent state.

Chapter 4

Structural analysis of the isotropic phase by 2D X-ray/Neutron scattering
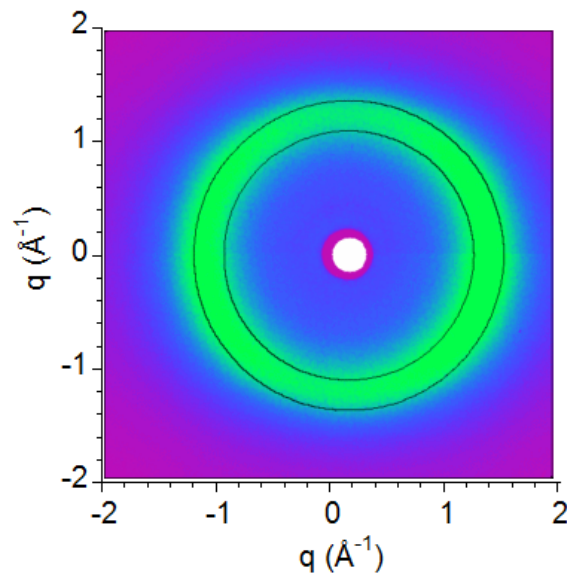
Since the observation of a macroscopic birefringent signal is the result of an anisotropy at the molecular level we should be able to deduce an anisotropic diffraction pattern under the same low frequency conditions using X-ray and neutron scattering techniques. These

techniques give average information over time and scattering volume for a sample thickness in the order of the millimeter which permits to reveal a bulk related property.

The structure of the isotropic phase is relatively easy since by definition, there is no structural order in this phase. Therefore, the study is focussed on the scattering produced by the intermolecular interactions ($q \approx 1.5 \mathring{A}^{-1}$).

Contents

4.1 Principles of the diffraction of liquid crystals

X-ray and neutron scattering are widely used to study structural properties of liquid crystals. Liquid crystal phases show intermediate diffraction patterns between those of a solid and a liquid depending on the mesophase. At large scattering vectors (q), where q is defined as:

$$| \vec{q} | = q = \frac{4\pi}{\lambda} \sin(\frac{\theta}{2}) \tag{25}$$

with θ the angle between incident and scattered beam and λ its wavelength, the scattering pattern can be schemed as following (figure 4.1).
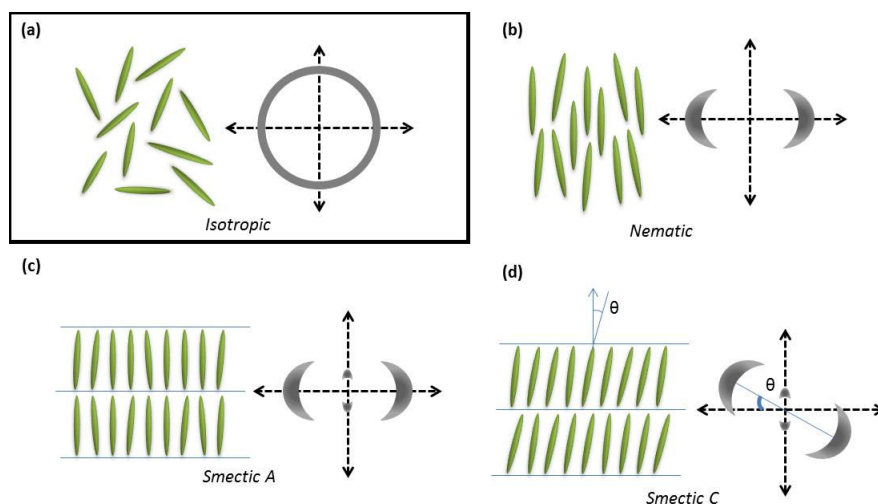
Figure 4.1: Schematic of 2D X-ray diffraction exhibited in conventional (calamitc, rod-like) liquid crystal phases: isotropic (a) and oriented (b) nematic (b), smectic A (c), and smectic C (d). Reproduced from [159].

At high temperatures above the isotropic transition, the liquid crystal is characterized by the absence of long-range positional or orientational correlations between the molecules. The 2D diffraction pattern consists of a diffuse ring due to a short-range excluded volume representing the molecular interactions (figure 4.1(a)). The ring at scattering vectors of around $1-3\mathring{A}^{-1}$ is known as the first correlation peak in liquids which defines approximately the distance between individual molecules [160, 161]. A more detailed discussion on the scattering of liquids is found in chapter 5 5.2.5.

At lower temperatures the nematic phase shows a long-range orientational order but no positional order. For an un-aligned sample we observe a liquid ring similar to the isotropic

phase but with a sharper distribution resulting in a smaller thickness of the ring. For an aligned sample (e.g. by a magnetic field) we observe diffuse arcs in reflection symmetry, their orientation depending on the alignment direction and the diamagnetic anisotropy of the molecule (figure 4.1(b). The corresponding scattering vector q represents the distance between molecules along their long axis. The intensity distribution of the scattering as a function of the azimuthal angle is related to the order parameter S (see 3.1).

$$S = \langle \frac{3\cos^2 \vartheta - 1}{2} \rangle \tag{26}$$

Where the angle ϑ describes the orientation of a molecule relative to the preferential direction (the local director).

An aligned smectic phase shows two sets of diffuse peaks in the 2D diffraction pattern. The arcs at large scattering vectors are similar to the ones in the nematic phase but the molecules arrange within the layers. Additionally at smaller scattering vectors, Bragg peaks are appearing which represent the distance between the smectic layers. The liquid crystalline molecules are tilted within the layers giving rise to a scattering at an angle corresponding to the average tilt of the molecules (Smectic A and C phases are presented in figure 4.1(c) and (d)) [118, 159].

In our experiments we observe the scattering in the side-view plane (strain, thickness) of the isotropic phase when a low frequency strain amplitude is applied. The experiments are thus complementary to the optical measurements (3.9).
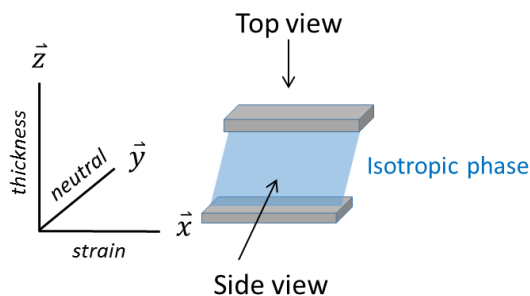
Figure 4.2: The liquid is supported by capillarity between two surfaces: The side-view plane ($\vec{x} - \vec{z}$) is the plane formed by the strain ($\vec{x}$) and the thickness ($\vec{z}$) axis and is observed along the neutral axis $\vec{y}$. The top-view plane ($\vec{x} - \vec{y}$), observed in the microscope in chapter 3, is formed by the strain ($\vec{x}$) and neutral axis ($\vec{y}$) and is observed along the thickness axis ($\vec{z}$).

4.2 Experimental setup

Our home-made device allows to probe the side-view plane of macroscopic sample sizes ($ca.1.0mm$) and to apply low frequencies ($0.5Hz$) and similar strain amplitudes ($10 - 150\%$)as in the microscope setup. We carried out the X-ray experiments at the University of Orsay in cooperation with P.-A. Albouy and D. Petermann. The liquid crystals (LCP95 and PACN) were heated to the isotropic phase at $+1°C$ above the isotropic transition (thermally controlled at $0.01°C$ using a Barras thermo-controller). Figure 4.3 shows the scheme (a) and a photograph (b) of the experimental setup.

(a) Scheme of the 2D X-ray diffraction setup   (b) Photograph of the setup
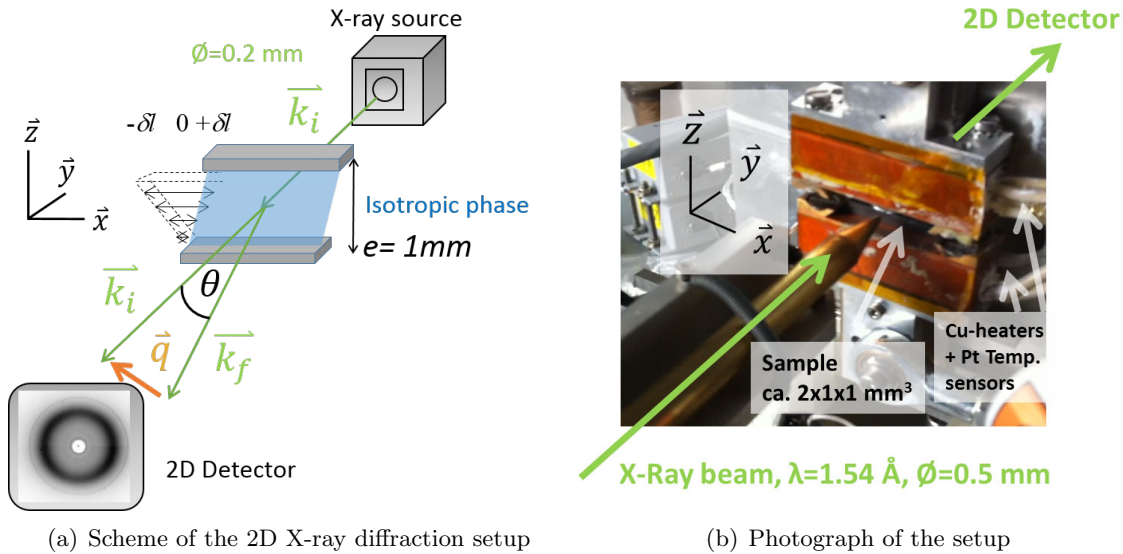
Figure 4.3: Scheme and photograph of the X-ray scattering setup. The incident X-ray beam (wave vector $\vec{k_i}$, wavelength $\lambda = 1.54\text{Å}$ and diameter $0.2mm$) is directed along the $\vec{y}$ direction. The scattered intensity (wave vector $\vec{k_f}$) is measured by a 2D Detector as a function of q. The observed plane is the side view-plane ($\vec{x} - \vec{z}$), at rest and under an applied strain amplitude $\gamma_0 = 10 - 150\%$ at a constant low frequency ($\omega = 0.5Hz$). Sample size ca. $\vec{x} = 1cm$, $\vec{y} = 1mm$ and $\vec{z} = 1mm$.

The scattered intensity was measured in the side-view plane by a 2D detector (Princeton Instr. Quad-RO: 4320). The primary beam was absorbed by a lead beamstop. The incident X-ray beam ($\lambda = 1.54\text{Å}$) was collimated to $0.2mm$ in order to reduce an absorption (and thus loss) of scattered intensity due to the heating surfaces that maintain the liquid. This effect of absorption leads to top and bottom "shadows" in the 2D diffraction pattern and is illustrated in figure 4.4. Unfortunately we could not completely get rid of these shadows

since the sample thickness was already large compared to the birefringence experiments. The recorded patterns show slightly less intensity in these areas (figure 4.4).
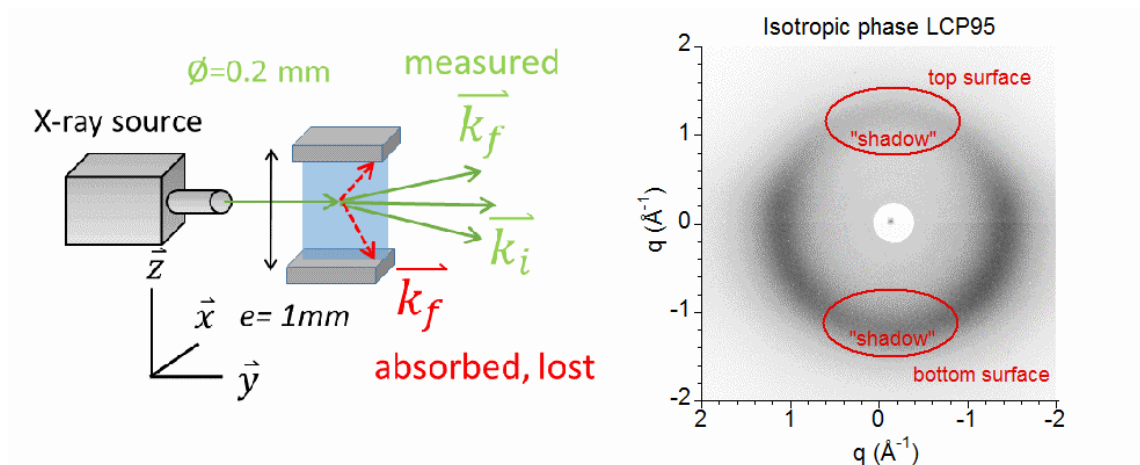
Figure 4.4: The absorption of scattered intensity by the top and bottom heating surfaces leads to a decrease in measured intensity in the $\vec{z}$ direction. In the 2D diffraction pattern this is expressed as "shadows", zones in the upper and lower image area that show a decreased intensity.

4.3   X-ray scattering results

4.3.1   X-ray scattering of the LCP95

Figure 4.5 shows the 2D diffraction pattern and the corresponding profile of the LCP95 as a function of the scattering vector q. The experiments were carried out in the isotropic phase ($T = T_{SAI} + 1°C$, verified optically and with crossed polarizers).
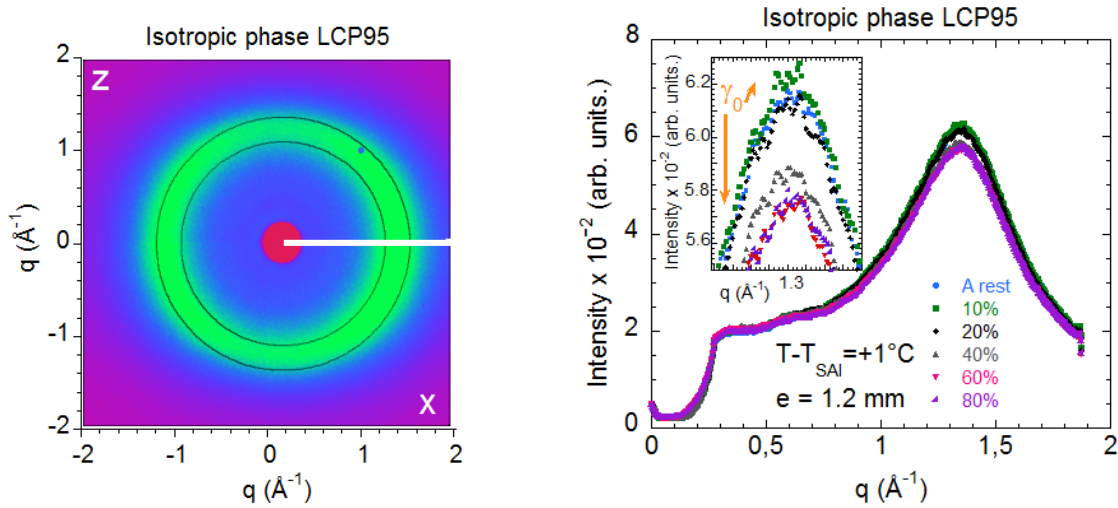
(a) 2D scattering pattern of the isotropic phase of LCP95 vs q

(b) Scattered intensity vs q (strain direction $\vec{x}$)

Figure 4.5: X-Ray scattering of the isotropic phase of the LCP95 at $T = T_{SAI} + 1°C$ (sample thickness $e = 1.2mm$). (a) 2D scattering pattern at rest. Absorption of scattered intensity by the lower and upper surfaces ("shadows") slightly reduces the intensity along the vertical direction. (b) Intensity versus the scattering vector q along the strain direction $\vec{x}$ (depicted as a white line in (a)) at rest and by increasing the strain amplitude at a fixed low frequency $\omega = 0.5Hz$. The insert is a zoom-in of the liquid peak at $q = 1.3Å^{-1}$

Upon increasing the strain amplitude we observe a decrease in intensity of the liquid ring. Figure 4.5(b) presents the scattered intensity versus q along the strain direction $\vec{x}$ (white line in figure 4.5(a)) of the isotropic phase at rest and for strain amplitudes ranging from $\gamma_0 = 10\%$ to $\gamma_0 = 80\%$ at a constant low frequency ($0.5Hz$). In the zoom-in of the liquid ring at $q = 1.3Å^{-1}$, the insert of figure 4.5(b), we observe a decrease in intensity of the liquid peak at strain amplitudes above $\gamma_0 = 20\%$ along the $\vec{x}$-direction. The scattering intensity is proportional to the number of scattering objects and so we can calculate that

for a strain amplitude of $\gamma_0 = 60\%$ around 7% of the scatterers are no longer in the plane of observation.

4.3.2 X-Ray scattering of the PACN

Analogous observations are made in the isotropic phase of the PACN. Figure 4.6(a) shows the 2D diffraction pattern of the PACN at $T = T_{NI} + 1°C$ as a function of the scattering vector q. Again the liquid ring at around $q = 1.3\AA^{-1}$ displays a lower intensity along the $\vec{z}$-direction for the same shadow reasons as above. In comparison with the LCP95 we observe a more pronounced decrease in intensity of the liquid ring upon increase of the strain amplitude. Figure 4.6(b) and (c) present the intensity of the liquid peak as a function of q along the strain ($\vec{x}$) and thickness direction ($\vec{z}$) at rest and for strain amplitudes from $\gamma_0 = 10\%$ to $\gamma_0 = 150\%$. In both directions a decrease in intensity of the liquid peak (inserts of 4.6(b) and (c)) is observed above a strain amplitude of $\gamma_0 = 40\%$. This is resulting from a reduction of scattering objects in the observation plane of 8% at a strain amplitude of $\gamma_0 = 80\%$ and of 13% at a strain amplitude of $\gamma_0 = 150\%$.

(a) 2D scattering pattern of the isotropic phase of PACN vs q

(b) Scattered intensity vs q(strain direction$\vec{x}$)

(c) Scattered intensity vs q (thickness direction$\vec{z}$)
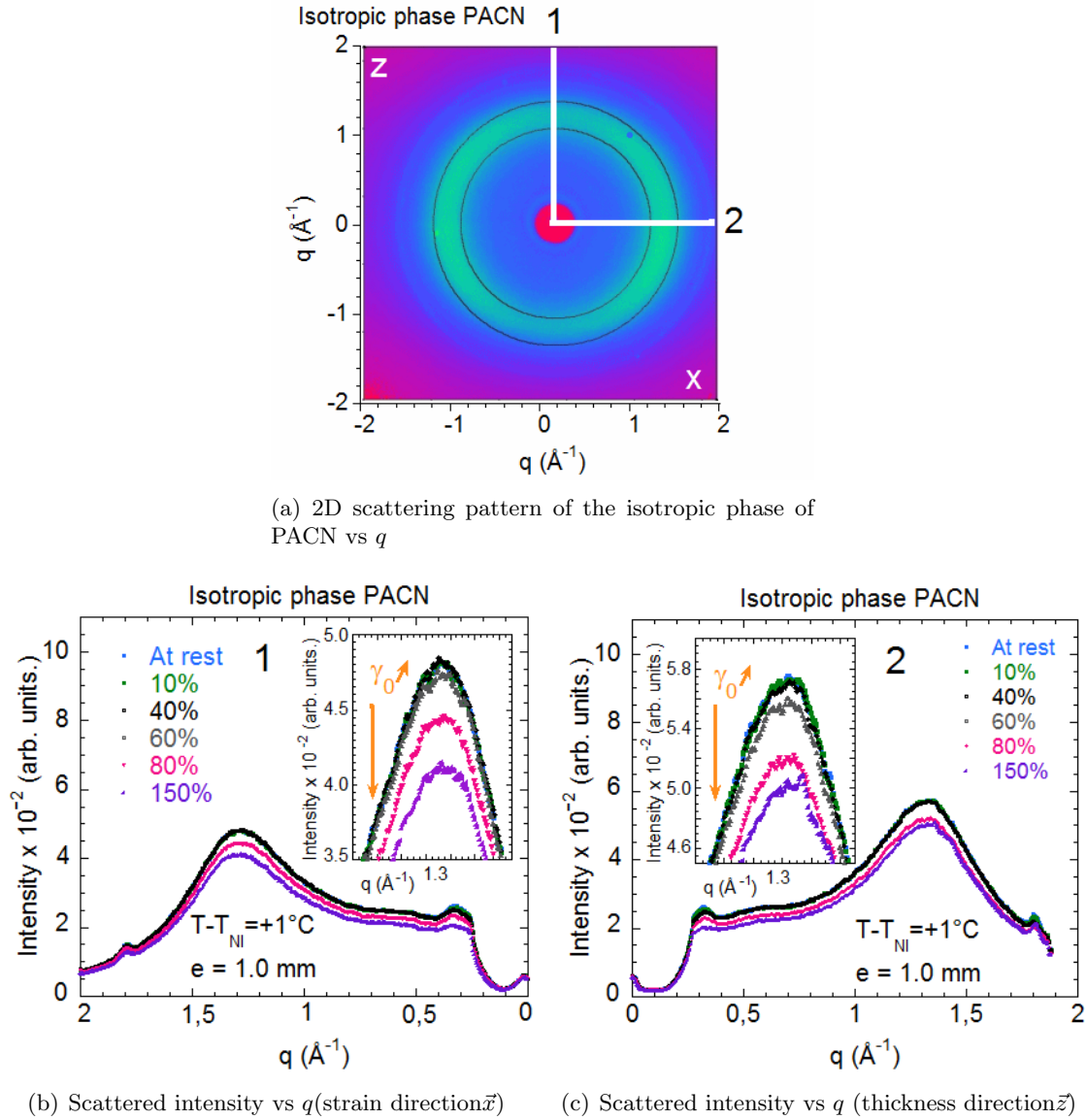
Figure 4.6: X-Ray scattering recorded in the isotropic phase of the PACN at $T = T_{NI} + 1°C$ (sample thickness of $e = 1.0mm$). (a) 2D scattering pattern (at rest). (b),(c) Intensity versus the scattering vector q along the strain direction $\vec{x}$ (white line (1) in(a)) and along the thickness direction $\vec{z}$ (white line (2) in(a)) at rest and at increasing strain amplitude at a fixed low frequency $\omega = 0.5Hz$. The inserts are zoom-ins of the liquid peak at $q = 1.3\overset{\circ}{A}^{-1}$. Similar variations are observed at different azimuthal angles.

4.4 Interpretation of the X-ray results: Strain induced log-rolling transition

For both the LCP95 and PACN we observe a decrease in the intensity of the liquid ring at $q = 1.3\mathring{A}^{-1}$ upon applying a strain amplitude above a threshold value γ_{crit}. The evolution of this decrease as a function of the strain amplitude is presented in figure 4.7 and resembles a sigmoidal curve.
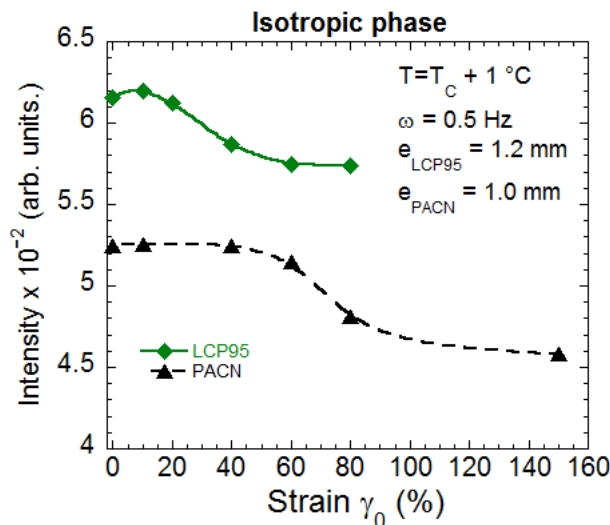
Figure 4.7: Intensity of the liquid ring as function of the strain amplitude for the LCP95 (horizontal) and the PACN (vertical and horizontal) in the isotropic phase at $T = T_C + 1°C$, $\omega = 0.5Hz$ and $e = 1.2mm, 1.0mm$ respectively. The lines serve as eye-guides.

As the volume of the scattering sample is considered to be constant, the decrease in intensity of the liquid peak must be due to a decreasing of scattering objects in the plane of observation. This may be explained by an orientation of molecules. Such an orientation is able to explain the establishment of the low frequency birefringence in the mechano-optic measurements in the top-view plane at the sub-milimeter scale on a molecular level. The reduction of scattering intensity can be interpreted as an orientation of the (rod-like) molecules in the pretransitional swarms along the beam/neutral direction ($\vec{y}$) in order to decrease the entropy by a rolling along their long axis in the strain direction ($\vec{x}$, figure 4.8(a)) similar to rolling of logs presenting the lowest state of energy 4.8(b). This log-rolling is known in the nematic phase under steady-state flow [162]. The rolling is able to explain the decrease in X-ray scattering intensity in the side-view plane (the molecules turn away form the X-ray beam) as well as an increase of anisotropy in the top-view plane.
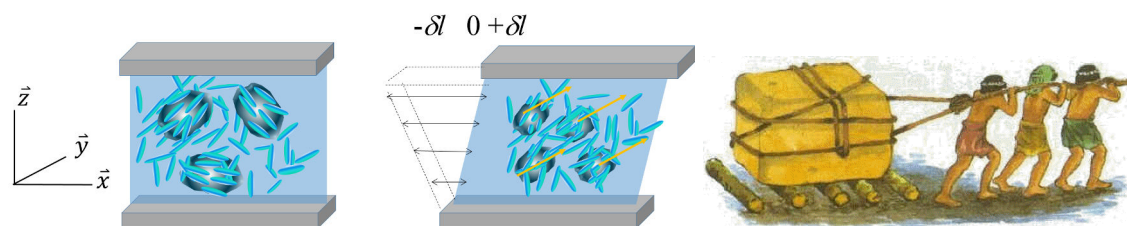
(a) Schematic model of molecular orientation along the roll axis   (b) The rolling of logs under load [163]

Figure 4.8: A model to explain the decrease in intensity (molecules out of plane) above a critical strain amplitude. (a) Orientation of molecules along their role axis in the shear direction. (b) Analogue situation of logs rolling under load.

4.5 Comparison of the structural approach to the mechano - optic results

So far we have seen a structural and optical response of the isotropic phase of the LCP95 and PACN when we apply a strain amplitude at low frequency. Are the two experimental approaches comparable? Figure 4.9 compares the results of the X-ray scattering in the side-view plane with the optical birefringence measurements in the top-view plane in the isotropic phase of the LCP95 and PACN both as a function of the (similar) strain amplitude and the same constant low frequency ($\omega = 0.5 Hz$) at $T = T_C + 1°C$.

(a) X-ray response LCP95 and PACN   (b) Optic response LCP95 and PACN
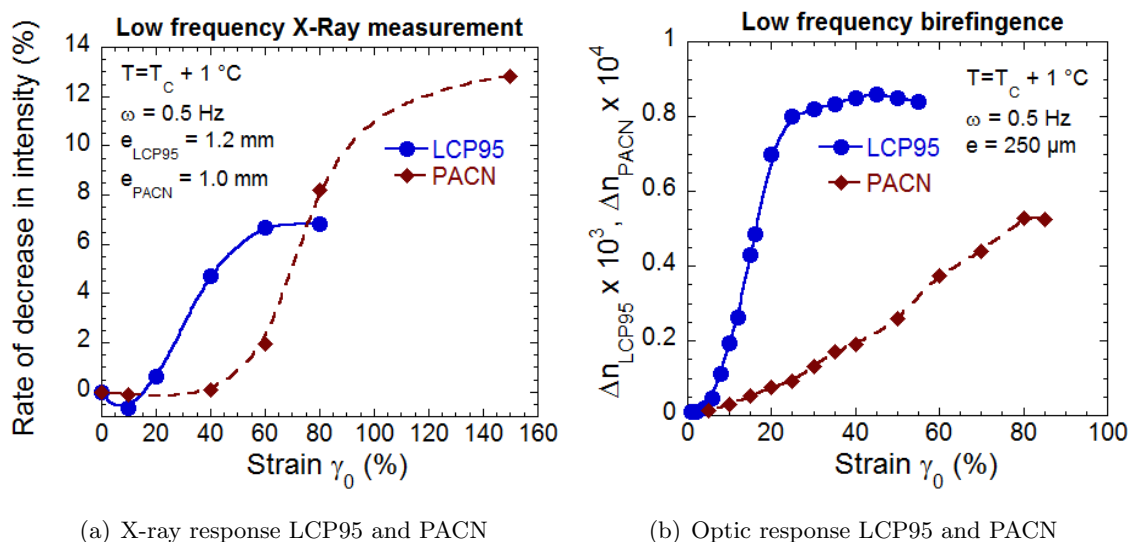
Figure 4.9: Comparison of the X-ray (a) and optical birefingence (b) responses obtained in the isotropic phase $T = T_C + 1°C$ of the LCP95 and PACN as a function of the applied strain amplitude at a constant low frequency ($\omega = 0.5 Hz$). (a) The ordinate presents the decrease in scattered X-ray intensity in the side-view plane ($\vec{x} - \vec{z}$) interpreted as the amount of molecules out of plane in percent. (b) The optical birefringence results obtained in the top-plane ($\vec{x} - \vec{y}$). The continuous and dotted lines serve as eye-guides.

If we interpret the decrease of intensity observed in the X-ray scattering pattern as the result of a partial orientation of molecules along the neutral axis $\vec{y}$, i.e. a decrease of the density of intermolecular interactions in this plane, is nearly proportional to the alignment of the molecules. Figure 4.9(a) presents the percentage of decreased intensity ($\equiv$percentage of oriented molecules) as a function of the strain amplitude. This represents the analogous interpretation of the optical birefringence as a measure of molecular alignment.

As a major result we observe in both experiments, X-ray scattering (figure 4.9(a)) and optical birefringence (figure 4.9(b)), a sigmoidal curve as a function of the strain amplitude. At small strains we see only a weak or no response at all. Above a critical strain value we have seen in chapter 3 that we can distinguish a linear regime before the signals saturate at high strain amplitudes. While the critical strain γ_{crit} lies around $\gamma_{crit} = 5\%$ for the LCP95 and the PACN in figure 4.9(b) we find larger values in the scattering experiments of $\gamma > 20\%$ in the case of the LCP95, $\gamma > 40\%$ in the case of the PACN (4.9(a)).

A noteworthy observation is that the molecules of the LCP95, which give a by a factor 100, stronger birefringent signal than in the case of the PACN, are seemingly less oriented in the X-ray scattering results.

This might be explained by first the comparison of two different planes of observation. Second we probe the birefringent properties of the pretransitional swarms in the optical experiments while we observe the intermolecular distances in the X-ray scattering. In the latter the effect of temperature plays a much weaker role than it is the case for the size of the pretransitional swarms. We note that the isotropic transition of the LCP95 lies at $T_{SAI} = 79.8°C$ and at $T_{NI} = 124°C$ for the PACN. This temperature difference of $44°C$ is not negligible in terms of thermal energy which leads to a smaller size of pretransitional fluctuations in the case of the PACN and consequently to a weaker birefringence. A further parameter is the polarizability of the molecule. The LCP95 is used in liquid crystal displays because of its high birefringence. Additionally the molecular size plays a role as the LCP95 in contrast to the PACN does not have a significant conformation entropy. Considering these parameters it is quite possible that the isotropic phase of the PACN shows a more intense X-ray scattering and a weaker birefringence than the isotropic phase of the LCP95.

4.6   Small angle Neutron scattering

To complete the structural study, Small Angle Neutron Scattering (SANS) experiments have been carried out to determine the form factor associated to the two molecules (PACN and LCP5) at rest and under low frequency and small strain amplitude. The same experimental setup as the one described in 3.9 and 4.2 is used. The observation plane is therefore the side-view plane $(\vec{x} - \vec{z})$.

To create a signal at a small angle in a melt or a liquid as the isotropic phase of a liquid crystal polymer (PACN) or an oligomer (LCP95), it is necessary to introduce density fluctuations. This contrast is created by mixing hydrogenated and deuterated homologues of a same chemical compound. In the case of an ideal mixture (without phase separation), the small angle signal corresponds to the form factor of the scattering object [164–167].

In the case of a mixture of hydrogenated and deuterated molecules, the scattering intensity is:

$$I_{HD}(\vec{q}) = a_H^2 \Phi_H N_{chain} P_H + a_H^2 \Phi_H^2 N_{chain}^2 Q_H + a_D^2 \Phi_D N_{chain} P_D$$
$$+ a_D^2 \Phi_D^2 N_{chain}^2 Q_D + 2 a_H a_D \Phi_H \Phi_D N_{chain}^2 Q_{HD} \quad (27)$$

where P corresponds to the intra-chain form factor and Q the inter-chain form factor; N_{chain} is the number of chains, Φ_H and Φ_D are the proportions, and a_H and a_D the sum of coherent scattering lengths on each monomer of hydrogenated and deuterated chains respectively.

Supposing H and D chains having the same polymerization degree, their conformation is similar, therefore : $P_H = P_D = P$ and $Q_H = Q_D = Q$. At small scattering vectors, we probe large fluctuations of scattering length and the atomic detail is not seen. Therefore, the intensity of a fully hydrogenated or a fully deuterated sample is totally incoherent and does not exhibit any coherent signal. One can write: $P = -N_{chain} Q$. Equation 27 can be simplified in:

$$I_{HD}(\vec{q}) = N_{chain} \Phi_H \Phi_D (a_H - a_D)^2 P(q) \quad (28)$$

with $K = a_H - a_D$ being the contrast.

The scattering intensity is maximum for a 1:1 hydrogenated/deuterated mixture ($\Phi_H = \Phi_D = \frac{1}{2}$). In the Guinier domain ($qR_g < 1$ where R_g is the radius of gyration), the form factor can be approximated:

$$P(q) \approx n^2(1 - \frac{q^2 R_g^2}{3}) \quad (29)$$

where R_g is defined by:

$$nR_g^2 = \sum_i \langle r_i^2 \rangle \tag{30}$$

with n the polymerization degree and r_i the distance to the mass center.

For these considerations the measured scattering intensity at small angles is thus proportional to the intra-chain form factor and in Guinier coordinates we can determine $P(q)$ and the radius of gyration. This is done by plotting $1/P(q)$ versus q^2:

$$\frac{1}{P(q)} \approx 1 + q^2 \frac{R_g^2}{3} \tag{31}$$

The use of a two-dimensional neutron detector is required to detect the anisotropy in systems submitted to an anisotropic force (here the strain field in the $\vec{x}$ direction). Indeed, the analysis of the 2D-scattering allows the determination of the components of the radius of gyration $R_g^2 = R_x^2 + R_y^2 + R_z^2$ following the strain axis (R_x) and along the vertical axis (R_z) which corresponds to the thickness axis.

4.6.1 Small angle neutron scattering of the PACN

The experiments have been realized using the 2D Neutron Diffractometer PAXY at the LLB/Orphée. The scheme of the spectrometer is presented in figure 4.10. The data treatment is partly achieved using the 2D software developed by G. Pépy [168].
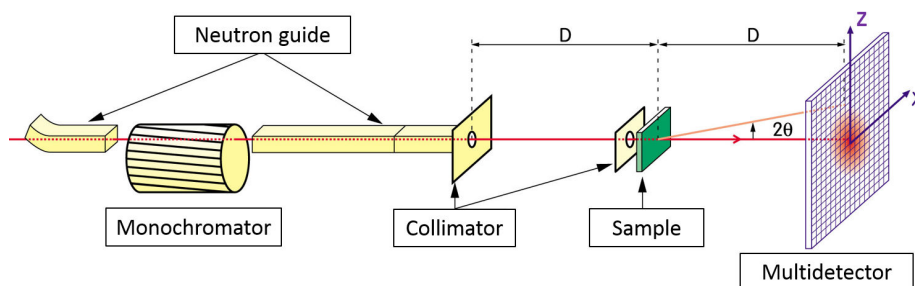
Figure 4.10: Scheme of a small angle Neutron spectrometer, PAXY.

Determination of the chain dimensions at rest

First we determine the form factor $P(q)$ of the PACN (1:1 mixture of hydrogenated and backbone deuterated (80 repetition units acrylate) in the isotropic phase ($T = T_{NI} + 1°C$)

at rest in a quartz cell. Figure 4.11(a) shows the small angle scattering intensity versus the scattering vector. In order to determine $P(q)$ the incoherent scattering has to be eliminated. Figure 4.11(b) presents the inverse of the inverse of $I(q)$ in Guinier coordinates. The form factor is observable in the Guinier region (at $q < 0.01\mathring{A}^{-1}$)). The slope of the straight line fit of the data points corresponds to the square of the radius of gyration and yields $R_g = 17 \pm 2\mathring{A}$.

(a) $I(q)$ vs q　　　　　　　(b) $\frac{1}{P(q)}$ vs q^2
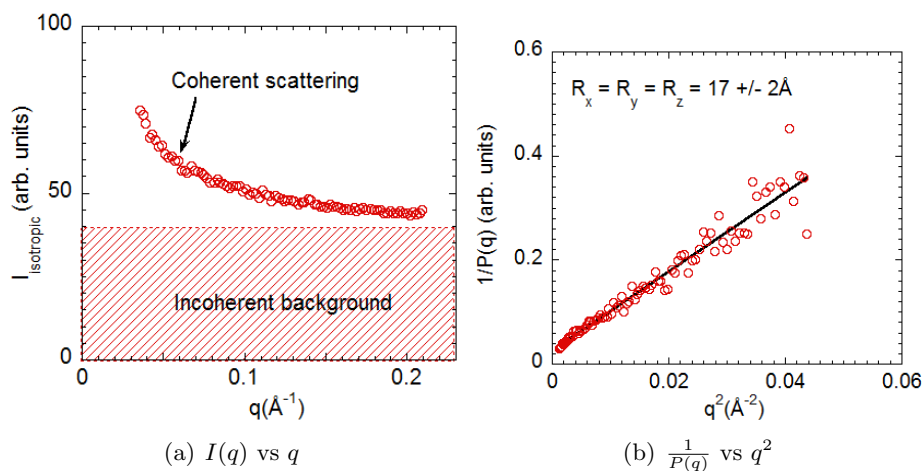
Figure 4.11: Small angle neutron scattering of the PACN at rest. (a) Scattering intensity displayed by a 1:1 mixture of hydrogenated and backbone deuterated PACN in the isotropic phase. (b) Fit of the inverse of the scattered intensity (the incoherent signal has been subtracted) in the Zimm representation. PAXY detector, $\lambda = 6\mathring{A}$, $d = 1.5m$.

Determination of the chain dimensions under external strain-field

Under an external strain field, a two-dimensional analysis is required. Figure 4.12 displays the small angle scattering produced by the 1:1 PACN mixture. In the dynamic experiments the isotropic phase ($T = T_{NI} + 1°C$) is suspended between the two heating surfaces of the setup presented in figure 4.3 (separation of $1.0mm$) and submitted to a strain amplitude of $\gamma_0 = 100\%$ in the $\vec{x}$ direction at a frequency of $\omega = 1.0Hz$. In the scattering pattern (figure 4.12(a)) and in the two-dimensional fits of the data along the strain and thickness axis (figure 4.12(b)) we observe an additional signal at large scattering vectors. This signal which is due to the scattering of the heating surfaces superposes to the chain form factor and gives rise to an apparent strong anisotropic form factor. A careful subtraction of the background scattering intensity is thus demanded. The radii of gyration can be either extracted from the two-dimensional fit in figure 4.12(b) or by a plot in Zimm representation. The Guinier region in figure 4.13 is fairly reduced in contrast to the sample at rest due

(a) 2D scattering pattern

(b) 2D fit along $\vec{x}$ and $\vec{z}$
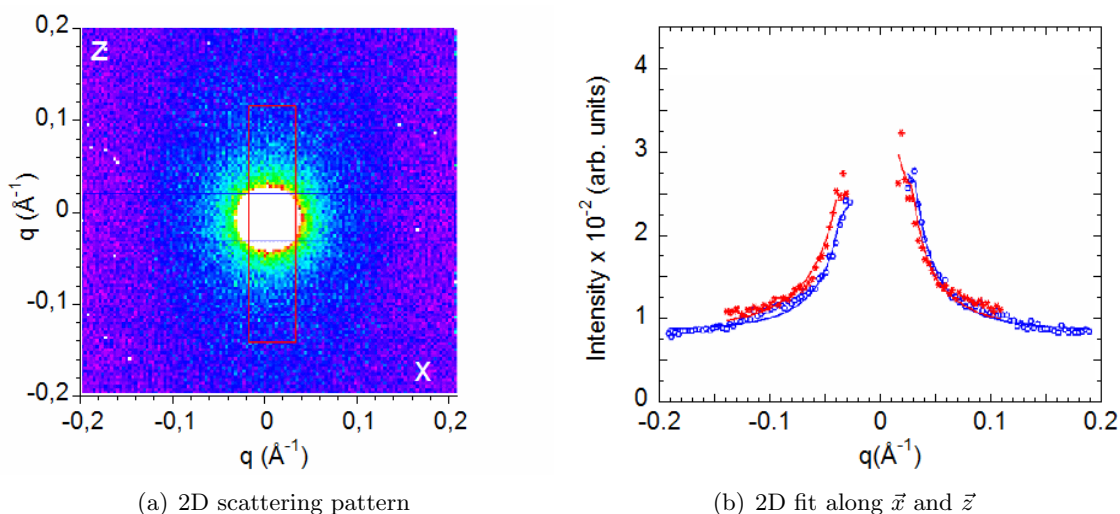
Figure 4.12: Small angle neutron scattering of the PACN at under external strain field.(a) 2D scattering pattern. (b) The two-dimensional fit might indicate a very slight elongation of the PACN chain along the strain axis. PAXY detector, $\lambda = 6\mathring{A}$, $d = 1.5m$

to the additional scattering of the heating surfaces that are not totally masked by boron nitride. In the narrow Guinier region, the two-dimensional treatment might indicate a very slight elongation of the chain $R_z/R_x = 0.84$ along the strain axis $\vec{x}$ with error bars of 20%. No significant change is observed by increasing the frequency or the strain amplitude (from 10% to 100%). Due to the low neutron flux, the acquisition times required are around $\frac{1}{2}$ hour or an hour. Therefore the measurements integrate several backward-forward strain motions. The orientation of the chain is averaged and does not correspond to its maximum extension. Experimental modifications as a trigger coupling would be needed to decouple the acquisition and the motion.

Figure 4.13: Inverse of the form factor in Guinier coordinates along the strain ($\vec{x}$, blue diamonds) and vertical ($\vec{z}$, black circles) direction. Sample thickness $1.0mm$, strain amplitude $\gamma_0 = 100\%$, frequency $\omega = 1.0Hz$).
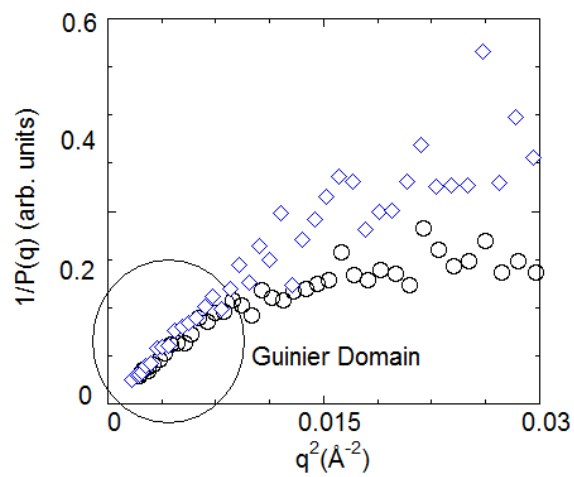
4.6.2   Small angle neutron scattering of the LCP95

Determination of the chain dimensions under external strain-field

The same treatment is achieved for the LCP95. Figure 4.14(a) displays the small angle scattering produced by the 1:1 LCP95 mixture in the isotropic phase ($T = T_{SAI} + 1°C$). Here, in order to create a signal at small angles, we had to use higher polymerization degree of the polymeric chain of ca. 60 (mol. mass $= 38475 g/mol$). The experimental conditions are otherwise similar to the PACN ($\gamma_0 = 100\%, \omega = 1.0 Hz$). Although the two-dimensional fit in figure 4.14(b) produces systematically a value of the radius of gyration slightly larger along the strain axis ($R_x = 14 \pm 5 \mathring{A}$ against $R_z = 12 \pm 5 \mathring{A}$) along the strain axis, the difference between the two components parallel and perpendicular remains within the error bars.

(a) 2D scattering pattern

(b) 2D fit along $\vec{x}$ and $\vec{z}$
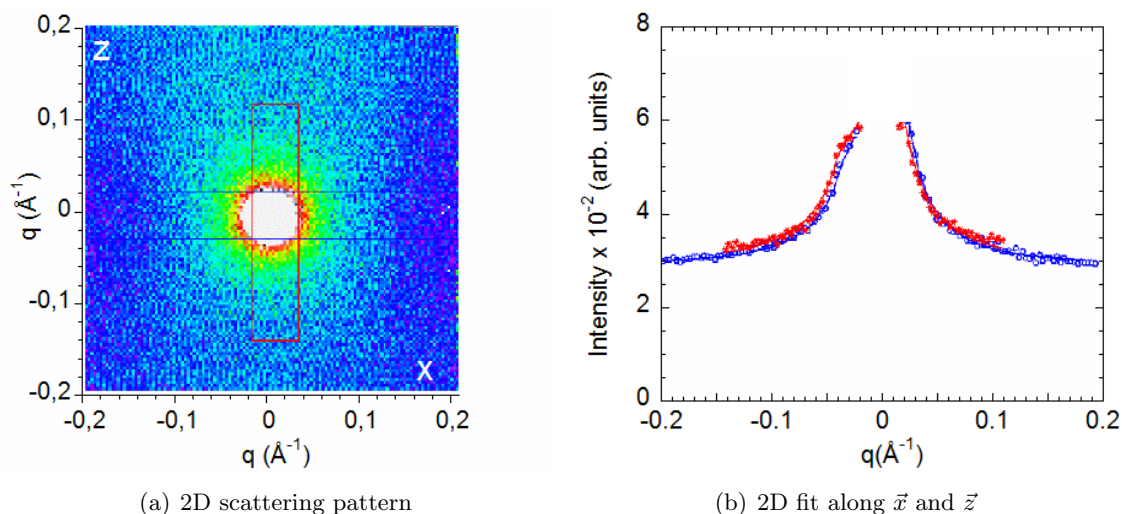
Figure 4.14: Small angle neutron scattering of the LCP95 at under external strain field.(a) 2D scattering pattern. (b) The two-dimensional fit indicates a very slight elongation of the LCP95 chain along the strain axis that remains within the error. PAXY detector, $\lambda = 6\mathring{A}$, $d = 1.5m$.

Conclusions: The present SANS experiment is technically difficult and is certainly not optimized but it tells that the strain field does not drastically change the chain conformation in the observation side-view plane ($\vec{x} - \vec{z}$) (In contrast, an elongation is reported under steady-state conditions in Couette-geometry for the flow birefringence observed in the isotropic phase in the top-view plane ($\vec{x} - \vec{y}$) [109], figure 4.15). The here presented result is in agreement with the change observed at wide angles by X-Rays, coherent with the log-

rolling geometry (reorientation of the liquid crystals perpendicular to the strain axis) and also in agreement with the assumption of an experiment carried out close to equilibrium conditions.
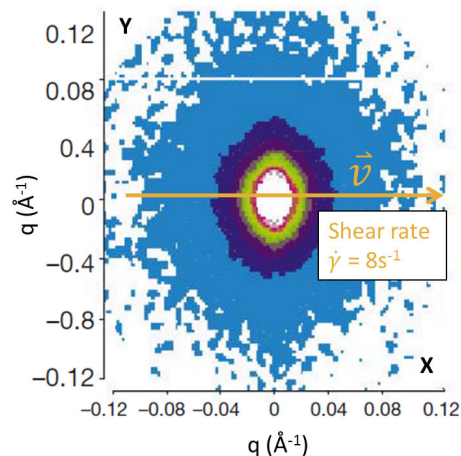
Figure 4.15: In the top-view plane $(\vec{x} - \vec{y})$, Rheo-SANS experiments have shown an elongation of the chains of side-chain liquid crystal polymers in the isotropic phase at $T = T_{NI} + 1°C$ in Couette-geometry under an applied shear rate along the velocity direction $\vec{v}$. Reproduced from [109].

4.7   Summary and conclusions

In this chapter we carried out a structural analysis of the isotropic phase of the LCP95 and the PACN upon a low frequency mechanical excitation using wide angle X-ray scattering and small angle neutron scattering techniques.

Experimentally:

- we developed an apparatus that allows to apply a low frequency (square type) strain to macroscopic sample thicknesses of $1mm$.

- we observed the plane formed by the strain axis and the thickness axis (side-view plane). The scattering techniques give average information over time and scattering volume for a sample thickness of the order of the mm^3 which permits to reveal a bulk related property.

- we probed the scattering intensity of the isotropic phase at rest and under increasing strain amplitude ranging from $\gamma_0 = 10 - 150\%$ at a constant frequency of $\omega = 0.5Hz$, $+1°C$ above the isotropic transition.

As a result, the X-ray scattering experiments identify a strain induced structural change at low frequencies of the isotropic phase in the case of both LCP95 and PACN. At large scattering angles, we observed a weak decrease in intensity of the liquid ring at scattering

vectors $q \approx 1.3 \mathring{A}^{-1}$ above a critical strain amplitude. For the liquid crystal molecules we observed quantitatively:

- for LCP95 a decrease in scattering intensity of about 7% above a critical strain amplitude γ_{crit} above 20%.

- for PACN a decrease in scattering intensity of about 12% above a critical strain amplitude γ_{crit} above 40%.

The diminution in intensity corresponds to a decrease in density of scattering objects e.g. intermolecular interactions in the plane of observation. It can be interpreted as the preferred orientation of molecules with their long axis in the X-ray beam direction adopting a geometry comparable to the geometry of the rolling of logs. Such an orientation under strain which has been observed under steady-state flow conditions in the nematic phase [162] gives rise to the emergence of a birefringence in the top-view plane as observed optically in chapter 3.

The X-ray intensity of the liquid ring displays a sigmoidal curve similar to the birefringence-strain curves described in chapter 3:

- Only a weak or no response at all at small strains.

- Above a critical strain value we enter an intermediate strain region where we distinguish a linear regime before the signals saturate at high strain amplitudes.

These observations indicate that the scattering experiments probe the same phenomenon as the optical experiments - an orientation of molecules. It can be however concluded that the optical birefringent measurements are by far more sensible towards low frequency, small strain amplitudes than the X-ray scattering technique.

Finally small angle neutron scattering experiments probed the conformation (radius of gyration) of the polymeric/oligomeric backbone chain of 1:1 mixtures of deuterated PACN, LCP95 respectively under low frequency mechanical strain. The strain coupled SANS experiments are technically difficult and certainly not optimized. At a strain amplitude of $\gamma_0 = 100\%$ the following radii of gyration were determined:

- for the LCP95 a $R_x = 14 \pm 5 \mathring{A}$ against $R_z = 12 \pm 5 \mathring{A}$ may indicate a stretching of the molecule of $14\% \pm 20\%$ along the strain axis.

- for the PACN a $R_x = 20 \pm 5 \mathring{A}$ against $R_z = 17 \pm 5 \mathring{A}$ may indicate a stretching of the molecule of $16\% \pm 20\%$ along the strain axis.

The strain field does not drastically change the chain conformation in the side-view plane. This result is compatible with the log rolling reorientation of the liquid crystals perpendicular to the strain axis. In this geometry, the side-view plane is a plane of symmetry.

The observation of a the plane containing the strain and the neutral axis (top-view plane, $\vec{x} - \vec{y}$) would have been certainly more appropriate.

Chapter 5

Role of the liquid / surface boundary condition
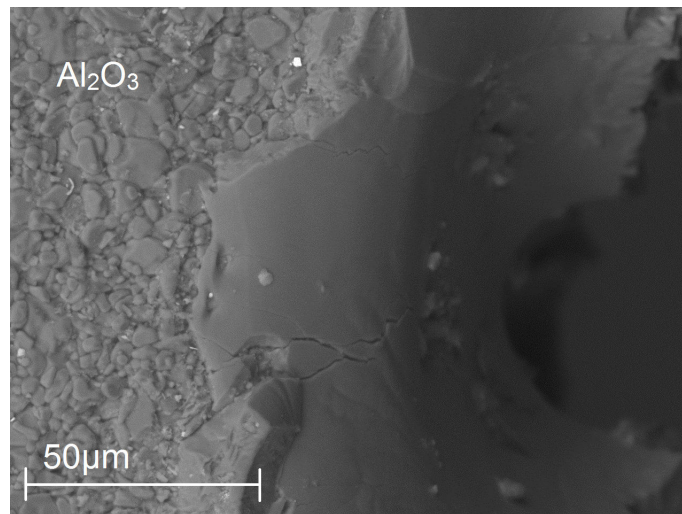
So far we have seen low frequency shear elastic properties of liquids evidenced by dynamic mechanical analysis and optical birefringence. In these techniques the applied stress is transmitted by the substrate. In the stress measurements we exploited the total wetting behaviour of the α-alumina fixtures while in optical birefringence experiments wetting was achieved by transparent quartz surfaces. In this final chapter we will try to get a deeper insight in the role of the interactions between the liquid and the substrate.

This chapter is divided into two sections.

Influence of the surface condition on the strain induced birefringence: In the first section we discuss the role of surface treatment of the quartz surfaces used in the mechano-optic experiments from chapter 3. The principal question is: does the mechanically induced birefringent signal in the isotropic phase of liquid crystals change when the liquid surface interaction is changed by a surface treatment.

Surface properties and liquid substrate interactions of the alumina: In the second section we take a closer look at the α-alumina. The strong liquid-surface interaction of the substrate permits to access a terminal shear elasticity at the sub-millimeter scale. Its extraordinary wetting performance is evidenced macroscopically by a contact angle of zero which for the case of an ideal surface favours microscopically a zero slip length boundary condition in the frame of the Tolstoi theory [125]. What is at the origin of this strong liquid substrate interaction? We will try to get to the bottom of this question by addressing the wetting behaviour using atomic force microscopy, zeta-potential and neutron scattering measurements.

Contents

5.1   Influence of the surface properties on the strain induced birefringence

The reinforcement of the substrate-liquid interaction using total wetting conditions in stress measurements leads to the identification of a terminal shear elasticity. Can we also see an influence on the optical birefringent signal as we play with the wetting parameter by using different surfaces or surface modifications?

Liquid crystals are known for their pronounced anchoring properties [118]. The contact between a liquid crystal molecule and a surface causes the director $\vec{n}$ to orient in a specific direction near the surface resulting in a planar, homeotropic or tilted alignment (for rod-like molecules). In the nematic phase, the molecules alignment may propagate over macroscopic distances [118] which is the basis of twisted LC-displays. In the isotropic phase, liquid crystalline molecules are still strongly oriented at the surface but the effect is rapidly lost above several molecular lengths (the coherence length is typically up to $10nm$) [118, 130, 131]. The anchoring is generally strong (though weak anchoring exists [169]) which guarantees a good wetting behaviour on many surfaces which may be modified chemically or by a physical deposition of (in)organic thin layers. Both methods come in handy as our optical experiments require highly transparent surfaces.

5.1.1   Surface modification

In our mechano-optic experiments we have used high quality quartz discs, silica 7980, provided by Corning glasses. The discs guarantee a low stress birefringence (permissible optical path difference per cm glass path of $< 1nm/cm$). In order to change the surface properties we carried out three modifications:

- Deposition of a thin layer of titanium dioxide (TiO_2)

- Chemical modification via a coupling agent by octadecyldimethyl-(3-trimethoxysilylpropyl) ammonium chloride ($DMOAP$)

- and by Octadecyltrichlorosilane (OTS).

The experimental procedures and protocols are found in the appendix. The latter is used to lower the surface energy and thus the adhesion performance, TiO_2 and $DMOAP$ layers are known to improve the liquid crystal wetting [170–173].

Deposition of titanium dioxide - wetting improvement

TiO_2 layers are widely used for optical and electrical applications presenting low-cost materials with high refractive index and a high dielectric constant. [170, 171, 174]. A most common method to orient liquid crystals on a surface consists in using rubbed polymer surfaces which leads to a planar orientation of molecules [175]. More recently it has been shown that on thin TiO_2 films the anchor condition of the liquid crystal molecules is modifiable. The pretilt angle (alignment angle of the liquid crystal molecules in respect to the surface) can be controlled by the procedure of the film deposition and by an ion beam treatment [170, 171]. This may result in a uniform planar or homeotropic alignment. While this property is particularly interesting for liquid crystal display devices the thin TiO_2 film is used here (without a particularly controlled orientation) to see the influence of the surface treatment on the induced birefringence in the isotropic phase at a macroscopic scale.

The deposition was carried out at the IMMM, Université du Maine by sputtering deposition. The quartz surfaces were coated with a $17nm$ (lower surface) and a $11nm$ (upper surface) thin layer of TiO_2 resulting in decrease of the surface roughness (RMS $5 \times 5\mu m^2$ from $1nm$ to $0.6nm$.

Chemical modification with a surface coupling agent: DMOAP - wetting improvement

Silane surface coupling agents are used to generate chemically stable surfaces on a wide variety of conducting and insulating substrates. The interfaces can be simply and reproducibly deposited. They show strong liquid crystal orienting interactions and due to their chemical stability, these surface treatments are expected to have the performance required for long device lifetimes [172]. Such a coupling agent produces of a bonding group which reacts chemically with the substrate to form a chemically stable bond, and an orienting group which interacts with the liquid crystal molecules in such a way as to produce the desired orientation. In the case of the $DMOAP$ the silane group acts as the bonding group (after activation by hydrolyzation) by reacting with the hydroxy groups of the quartz surface forming a mono-layer (figure 5.1). The 18 units long alkyl chains of the $DMOAP$ extend away form the surface forming a two-dimensional lattice. The alkyl chains are not densely packed leaving empty space between them. Here the (small, e.g. 8CB) liquid crystal molecules penetrate between the alkyl chains and orient parallel to them (right side in figure 5.1). On the glass, interfacial layers are formed. The first layer of liquid crystal molecules is tilted and oriented almost parallel to the surface. As cyanobiphenyl liquid crystal molecules have a strong tendency to form dimers, the molecules of the second layer orient almost perpendicularly to the surface. This forms the anisotropic base for the orientation of the following liquid crystals [173].
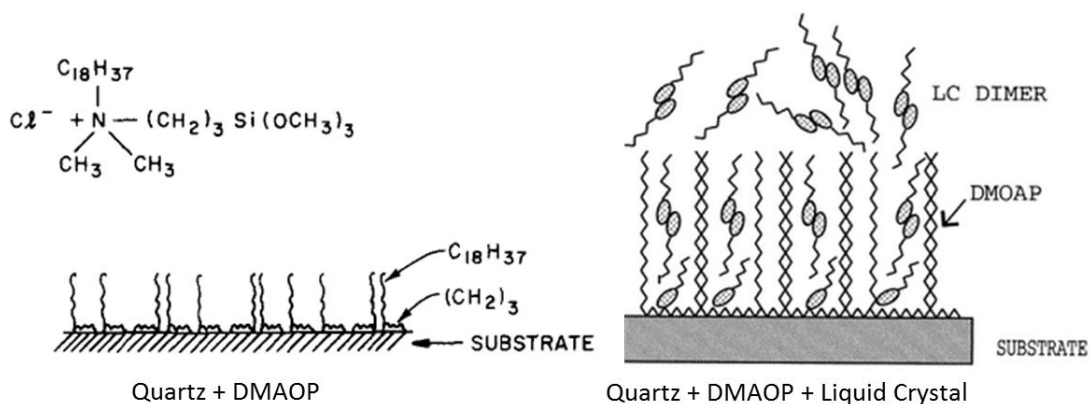
Figure 5.1: The activated coupling agent $DMOAP$ reacts with the hydroxy groups of the quartz surface and forms a mono-layer (left). Liquid crystals molecules (dimers) penetrate between the alkyl chains of the $DMOAP$ and orient parallel (homeotropic orientation) to them. Reproduced from 5.1 and [173]

Chemical modification with a surface coupling agent: OTS - dewetting

A similar chemical reaction is used to favour a dewetting behaviour using Octadecyl-trichlorosilane (OTS or $ODTS$). The siloxane coupling agent forms a well defined mono-layer on silica surfaces [176]. In contrast to the $DMOAP$ the coating is more complete leaving less empty spaces between the alkyl chains. This treatment is used to create a apolar, hydrophobic layer which servers as a anti-stick coating. It is supposed to hinder a favourable interaction with the polar groups of the liquid crystals. An interaction of the liquid crystal alkyl chains is however still possible.

5.1.2 Contact angle measurements

The study of the contact angle is the simplest way to address the interaction of a liquid on a surface. In order to facilitate the measurements of the contact angle we tested the isotropic phase of the 8CB. Its chemical formula is close to the LCP95 and PACN but the isotropic phase shows a fairly low viscosity (faster establishment of the equilibrium contact angle) and a low transition temperature of $T_{NI} = 40.5°C$ (against $T_{SAI} = 79.8°C$ and $T_{NI} = 124°C$ for the liquid crystal molecules used in the mechano-optic experiments).

Figure 5.2 presents the contact angles of the isotropic phase of the 8CB ($T = 45°C$) on various (treated) surfaces. The surfaces were cleansed in a ultrasonic bath and with ethanol before usage and heated to $T = 45°C$ during the experiment to avoid any phase transition of the 8CB. They yield the following contact angle values:

- Quartz: $\theta = 24°$

- Quartz $+ TiO_2$: $\theta = 19°$

- Quartz $+ DMOAP$: $\theta = 20°$

- Quartz $+ OTS$: $\theta = 57°$

- α-Al_2O_3, $Sapphire$: $\theta = 10°$

- α-Al_2O_3 (heat-cleaned, non-transparent surface): $\theta = 0°$, total wetting
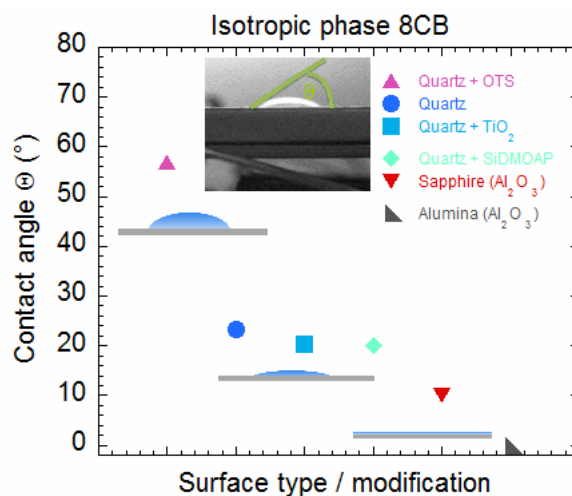
Figure 5.2: Contact angles formed by a drop of 8CB in the isotropic phase ($T = T_{NI} + 5°C$) on pure Quartz and chemically and physically modified Quartz surfaces as a well as on sapphire and non-transparent alumina surfaces.

The untreated quartz surface gives a contact angle of 24°. The wetting is slightly improved by the deposition of the thin TiO_2 film and the $DMOAP$ surface treatment. The treated quartz surfaces yield contact angles of 19° and 20° respectively.

The poorest wetting behaviour is found for the quartz treated with the OTS coating which shows a contact angle of 57°. In comparison to water contact angles of up to 110° on OTS coated surfaces [176] this value is relatively low which indicates an interaction of the alkyl chain of the 8CB with the surface. In comparison to the untreated quartz the OTS treatment still presents a dewetting performance though.

None of these surfaces provides total wetting which is only presented by the non-transparent α-Al_2O_3 substrate. The plates used consist of pressed α-Al_2O_3 powder and it presentes the surface we used in the stress relaxation measurement (wetting improved dynamic relaxation). Its contact angle with the 8CB reaches 0° when the surface is heat cleaned

at $450°C$ before the deposition (a discussion on the alumina properties is given in the upcoming section).

A transparent structural analogous of the pressed alumina surfaces is given by the Sapphire, a mono-crystalline α-Al_2O_3. Among the tested transparent surfaces it achieves the best wetting performance with contact angles of $10°$.

In general contact angle measurements are not easy to interpret since different cleaning and preparation methods of the surfaces give a broad range of results on the same surface [177] depending on the protocol used. It gives however a fast qualitative estimation of the liquid substrate interaction.

5.1.3   Birefringence vs strain amplitude on different surfaces

Now we determine the influence of the different surface treatments on the low frequency strain induced birefringence described in chapter 3. Figure 5.3(a) presents the transmittance $\frac{I}{I_0}$ as a function of the strain amplitude for the different surfaces at constant low frequency ($\omega = 0.5 Hz$) in the isotropic phase of the LCP95 ($T = T_{SAI} + 1°C$) and a sample thickness of $250\mu m$. In figure 5.3(a) we observe behaviour previously described. Namely a sigmoidal curve presenting three regimes (weak elastic at small strains, linear harmonic at intermediate strains and distorted saturated at large strains). We see that in the linear regime the curves obtained on the quartz treated with TiO_2 and quartz treated with $DMOAP$ surfaces roughly superpose while the values obtained for the pure quartz and quartz treated with OTS surface are shifted to higher strain amplitudes.

(a) $I/I0$ vs γ_0 on different surfaces   (b) $I/I0$ normalized by $\gamma_0 - \gamma_{crit}$
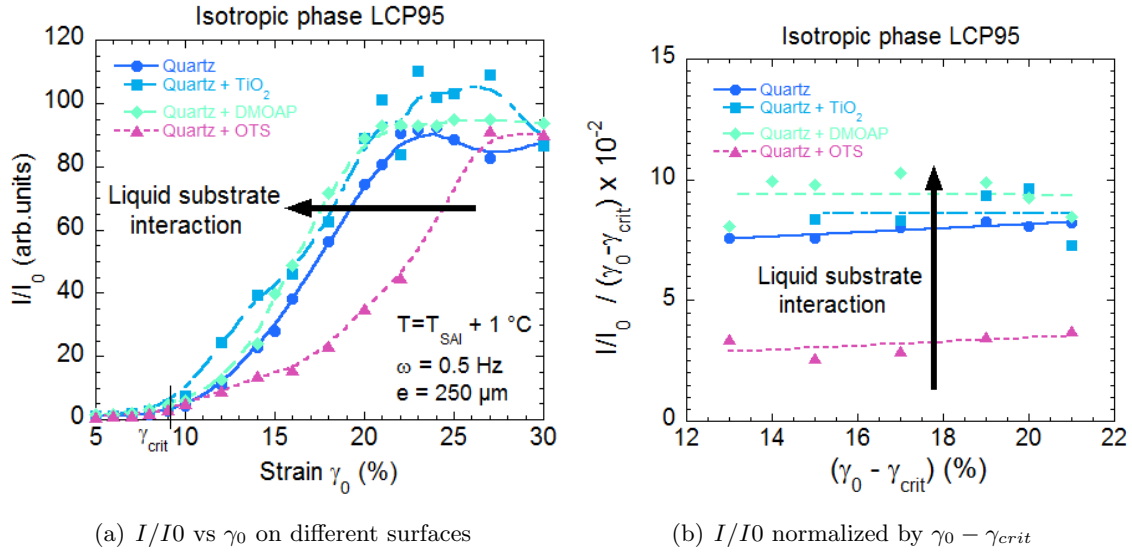
Figure 5.3: (a) Influence of the surface treatment on the strain dependence of the low frequency birefringence ($\omega = 0.5 Hz$) of the LCP95 at $T = T_{SAI} + 1°C$ and a sample thickness of $250\mu m$. (b) Intensities normalized by the strain amplitude (only the linear regime of (a) is presented). The fits of the data points highlight the strain independent regime.

The surface effect is better highlighted in figure by displaying the intensity (in the linear regime) normalized by the strain amplitude (figure 5.3(b)) . In this plot, the intensity is roughly independent of the applied strain (see chapter 3), pointing out more clearly the influence of the different surface treatments:

The quartz surface coated with $DMOAP$ gives the highest intensity followed by the quartz

treated with TiO_2 (-11% intensity) and the quartz itself (-16% intensity). The lowest intensity is measured on the surface coated with OTS (-66% intensity). The strain induced intensity decreases as the wetting performance decreases confirming our premise. In the case of weaker interacting surfaces we need to apply a larger strain to obtain the same birefringence (and smaller strains on stronger interacting surfaces).

Finally figure 5.4 shows the strain induced birefringence from Figure 5.3(a) at small strain amplitudes plus the empty cell at rest ($\gamma_0 = 0$). We see that the isotropic phase shows (nearly at rest) a lower birefringence on the pure quartz and quartz treated with OTS than on the quartz treated with TiO_2 and quartz treated with $DMOAP$ surfaces. As the latter are widely used to induce an orientation of liquid crystals (usually in the nematic phase) at the surface we may here observe the effect of a surface-induced orientation.
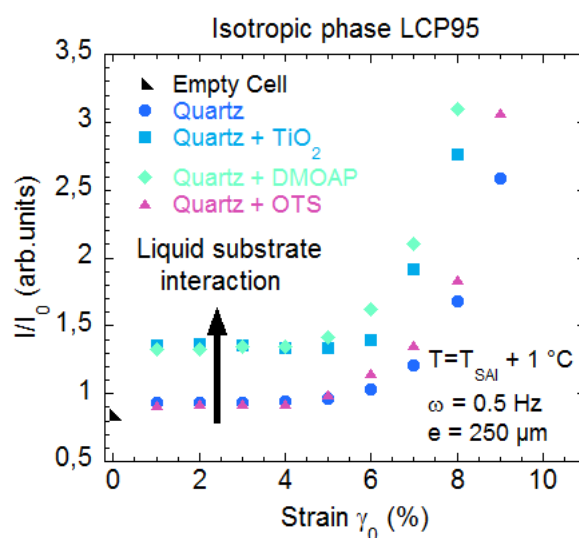
Figure 5.4: A zoom-in of at small strain amplitudes of the data form figure 5.3(a).

5.1.4   Conclusions

If the pretranstional swarms are "trapped" in an elastic network this elastic network is more easily probed using strong interacting surfaces. This is an important result that shows that enhancing the surface-liquid condition of interaction plays a major role. The surface treatment can reinforce the strong anchoring property of the liquid crystal molecules. Optimized surfaces may however give or improve access to a low frequency strain-induced birefringence in smaller molecules as the 8CB. Unfortunately experiments with the promising sapphire were unsuccessful as the surface shows an intrinsic birefringence and thus itself creates a birefringent signal.

5.2 Surface properties and liquid substrate interactions of the alumina

Throughout this manuscript we have pointed out the efficiency of a strong anchoring (total wetting condition) to access the identification of low frequency shear elasticity. In this final section we will try to gain a deeper insight into the interactions and properties that govern the interfacial region between liquid and substrate. This question is discussed by taking a closer look at the wetting behaviour of surfaces in general and the alumina in particular: What kind of interfacial forces lead to strong molecular anchoring on surfaces. Contact angle measurements, atomic force microscopy, zeta-potential and neutron scattering measurements are used to explore the wetting behaviour.

5.2.1 The alumina
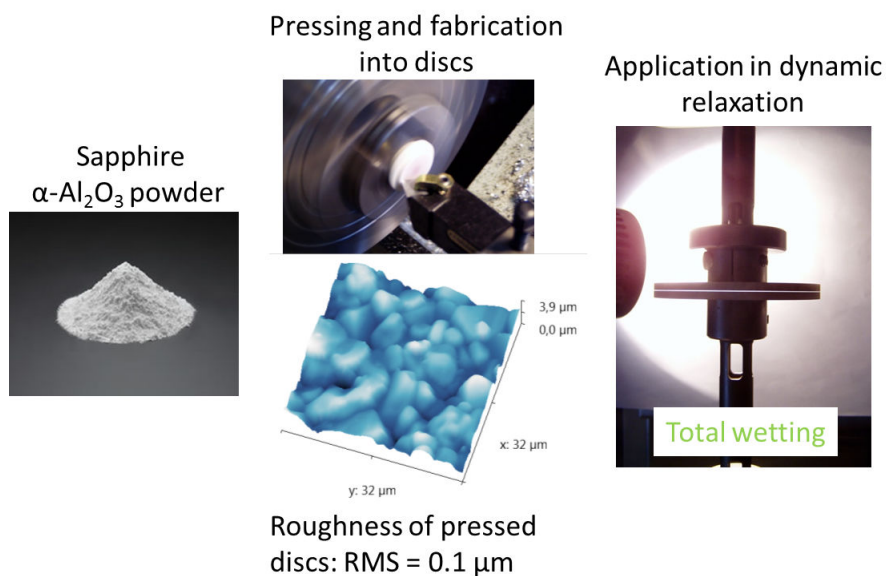
Figure 5.5: From the α-alumina powder to wetting improved dynamic relaxation. The powder is pressed and shaped into discs adapted to the rheometer (fixtures) with a defined low surface roughness of less than $0.1\mu m$. After cleaning by heat treatment the fixtures serve as wetting improved substrates in dynamic relaxation experiments.

Our wetting improved dynamic relaxation measurements (Chapter 2) have been carried out on aluminium oxide (alumina) fixtures (figure 5.5). This material is industrially prepared

from crystallites of α-Al_2O_3 (mono-crystalline powder) under high pressure and temperature. It present a convenient compromise between performance (wettability and durability) and prize in comparison to e.g. titanium oxide TiO_2 or silicon carbide SiC. The polished surfaces show a roughness (RMS) of $0.1\mu m$ and zero porosity. A profile of the alumina obtained by atomic force microscopy is shown in figure 5.6
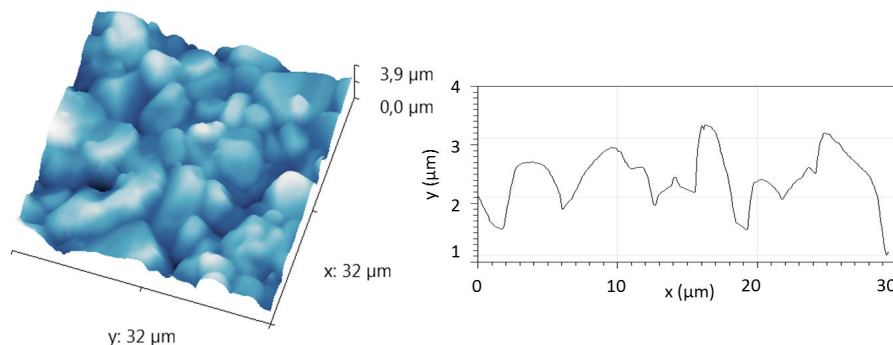
Figure 5.6: AFM photograph and surface profile of the zero-porosity alumina showing a RMS roughness of $0.1\mu m$ (J.F. Bardeau, Scientec AFM).

While there is a vast literature dealing with the behaviour of liquids on metal oxides like the Al_2O_3 [178, 179] only few studies deal with the interaction between heat-treated α-Al_2O_3 and liquids [180, 181].

Before we discuss the properties of the strong interacting and the influence of cleaning the surface we demonstrate how we can predict a good wetting condition and why metal oxides are a good choice in substrates for probing the properties of liquids.

5.2.2 Thermodynamics of the wetting behaviour, surface forces and surface condition

Young's equation and spreading parameter

We have seen in chapter 1 that a high wettability (low contact angles) leads to a strong anchoring of the liquid molecules on the solid surface and following the Tolstoi equation, a zero slip length [125]. The simplest way to describe the liquid substrate interaction is by analysing the macroscopic contact angle. The contact angle of liquid drop on a solid surface can be described by the thermodynamics of the system solid (s) - liquid (l) - gas (g) and the involved interfacial energies γ:

$$\gamma_{sg} = \gamma_{sl} + \gamma_{lg}\cos(\theta) \qquad (32)$$

The Young's equation relates the involved surface energies between the phases to the contact angle for a perfectly flat surface and planar geometry of the drop (figure 5.7). The surface energy (surface tension is the preferred term for liquids) is the amount of energy needed to increase its surface area. However often the solid surface energies are not known and a simpler description is sufficient to predict the wetting behaviour.
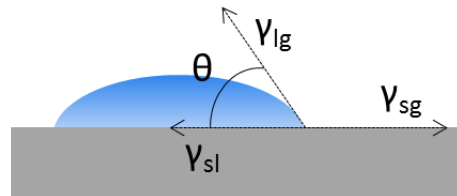
Figure 5.7: Contact angle θ of a drop on a perfect rigid surface.

A useful quantity to estimate the wetting behaviour is the spreading parameter S_{CA}:

$$S_{CA} = \gamma_{sg} - (\gamma_{sl} + \gamma_{lg}) \tag{33}$$

The spreading parameter is the negative difference in free Gibbs energy when bringing a liquid into contact with a surface. For $S_{CA} > 0$ the liquid will spread completely (total wetting) and for $S_{CA} < 0$ partial wetting occurs (figure 5.8)
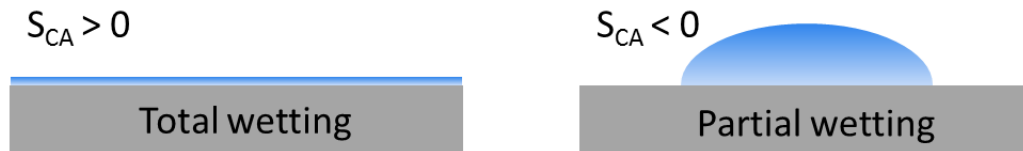
Figure 5.8: A negative spreading parameter leads to a total wetting while a positive one results in a partial wetting.

This presentation of the contact angle serves as a brief introduction. The contact angle may be increased by a pronounced roughness and chemical heterogeneities (Wenzel model) or the inclination of trapped air on the surface (Cassie-Baxter models). These models all describe the appearance of partial wetting. Surfaces as the cleaned alumina show no macroscopic contact angles - the wetting regime is total which indicates much stronger forces between surface and liquid.

High and low energy surfaces

Though strongly simplified the equations above are useful as they express the tendency of the strength of the liquid substrate interaction. The higher the difference between the surface energy of the solid γ_{sg} and the liquid γ_{lg} the higher is the resulting attraction between the liquid and the substrate and the lower the contact angle.

Table 3 shows the surface energies of various substances. The values for metals and metal oxides are much larger than those of organic polymeric substances as polycarbonate or polystyrene. This leads to the classification of high and low energy surfaces. Surface energies are related to their bulk energy which is determined by the types interatomic or -molecular forces that hold the substrate together. High energy substrates as metals and metal oxides are held together by stronger bonds (in the order of eV, $500 - 5000 mJ/m^2$) as low energy substrates like organic polymers (in the order of kT, $10 - 50 mJ/m^2$). Generally covalent, ionic, and metallic bonds are much stronger than van-der-Waals and hydrogen bonding. The latter are the dominating interactions in liquids and thus show comparable surface tensions to low energy surfaces (Table 3). The small difference between the surface tension of liquids and low energy surfaces result in weaker adhesion and bad wetting behaviour. In the case of water this property has a main application in hydrophobic surface coatings.

Concerning the wettability we can claim for most cases that *"as a rule of thumb, the higher the surface energy, the greater the strength of adhesion."*

Surface type	Substrate	Surface energy γ_{sg} (mJ/m^2)
High energy surface	Aluminium	840
	$\alpha-$Alumina (Sapphire)	638
	Alumina (anodized)	169
	Copper	1360
	Silica	250-500
	Stainless steel	700-1100
Low energy surface	Polycarbonate	42
	Polyethylene	32.4
	Polystyrene	40.6
Liquids	Water $(20°C)$	72
	Alkanes $(20°C)$	ca. 18-28

Table 3: Surface energies of various substances. The surface energy comprises all intermolecular forces on the surface of a material. Values from [182].

In principle many metals and most metal oxides should provide total wetting. The atomic structure of the solid has a strong influence on the wettability and in principle the mentioned substrates are supposed to show total wetting. However due to their high surface energy some metal oxidise on the surface and metal oxides as the alumina and glass are covered with hydroxy groups whose presence, type and density largely determine the surface properties. While the high surface energy makes the surface highly wetting (for most liquids), the presence of the hydroxy groups renders the surface hydrophilic and less attractive for organic liquids. Both properties massively attract impurities like organic compounds or dust by adsorption which increases the contact angle and lowers the wetting capacity.

Surface condition: Thermal cleaning results in high wettability

In the case of metal oxides, the presence of hydroxy groups and adsorbed impurities can be overcome by cleaning the surface via thermal (e.g. for TiO_2, Al_2O_3, SiO_2), sometimes UV (TiO_2) and by plasma torch treatment [180, 181, 183].

Organic and other adsorbed impurities are roughly removed from at temperatures above ca. $100°C$. The elimination of the metal-hydroxy groups (M-OH) is observed at higher temperatures and involves chemical reactions. Figure 5.9 proposes a model scheme of the chemical events on the surface by thermal treatment. Upon heating two neighbouring (vicinal) M-OH groups react to form a metal-oxane (M-O-M) group by expelling molecular water. M-OH groups without neighbours (single) are not affected. This dehydroxylation leads to a substantial decrease in the number of surface M-OH groups [180]. In the case of TiO_2 the dehydroxylation becomes irreversible above $400°C$ reducing the density of M-OH groups from 8 OH/nm^2 at room temperature to 3 OH/nm^2 at $200°C$ and virtually 0 OH/nm^2 above $500°C$ [181].
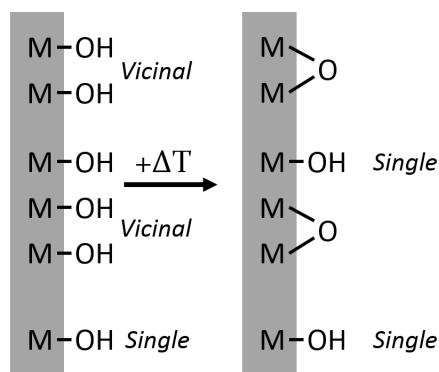
Figure 5.9: Simplified scheme of surface dehydroxylation (M=Si,Ti). A similar model can be proposed for Al_2O_3. Reproduced from [181]

The reduction of the M-OH groups happens by the following reactions in the case of the alumina. Two vicinal $-AlOH$ groups form a bridged hydroxy group $-Al_2OH$ by expelling molecular water [180]:

$$2x - AlOH \rightleftharpoons -Al_2OH + H_2O \tag{34}$$
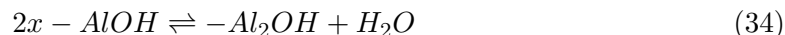
Once most hydroxy groups have disappeared, the surface can show its high surface energy. But what kind of interactions are still left to show an interaction with liquids?

- Polar liquids may interact with the surface via Lewis acid/base type reactions. The remaining aluminium species on the surface react as strong Lewis acids. In the case of water this is basically the back-reaction from above resulting in a strong anchoring of the liquid molecules. The surface is super hydrophilic as the molecules dissociatively adsorb on the Al_2O_3 surface [178]. Not all metal oxide surfaces cleaned of hydroxy groups may show this behaviour e.g. a heat-treated silica surface shows a weak hydrophobicity.

- Any liquid (apolar, polar, with OH-groups or not) may also show a strong interaction with the surface due to van-der-Waals forces (dipole-dipole, dipole induced dipole and dispersion forces). A surface cleaned of hydroxy groups shows a high surface energy (otherwise reduced by hydroxy groups, pollution etc.). Fowkes and Israelachvili have shown a relation between the surface energy and the Hamaker constant (a measure of the van-der-Waals interaction potential) of the surfaces [184, 185]. In this scenario clean solids are wetted mainly due to their high Hamaker constants.

The first point can be very nicely evidenced in wetting experiments with water: The water contact angle on mono-crystalline α-Al_2O_3 before any cleaning or heat treatment is approximately ($\theta = 55°$) [180]. Cleaning of the surfaces reduces the contact angle by removing organic contamination, i.e. the intrinsic hydrophilicity of aluminium oxide is recovered ($\theta = 10°$). Heating the samples reduces the contact angle further and the Al_2O_3 surface, after being heated to over $350°C$, becomes totally hydrophilic ($\theta = 0°$). This procedure also improves the wetting and may show total wetting for many less polar liquids than water. In this state, the initial high surface energy of the metal oxide is recovered. But not for long as recontamination after the heating process may take only minutes (TiO_2) to few hours (SiO_2) [181].

The second point is likely the reason why we observe total wetting even for polar and apolar liquids after thermal treatment on heat treated alumina.

Conclusion: With the heat-treatment the density of the Al-OH sites decreases significantly. The surface energy of the alumina increases leading to a strongly increased wettability for many liquids. In the case of water the surface becomes super hydrophilic. The clean alumina is thus intrinsically a strong wetting substrate.

We exploited the circumstance of total wetting on the cleansed surface by using them in the dynamic relaxation experiments in order to enhance the liquid substrate interactions. This granted access to the terminal shear elasticity. A discovery that is hardly (for strong anchoring liquids as liquid crystals) observable for uncleansed polluted, conventional metallic or glass surfaces.

In the following sections we will try to have a closer look at the interactions close to the alumina surface in contact with water. Here the surface is saturated with hydroxy groups and is highly hydrophilic. We will discuss atomic force microscopy results (forces close to the surface) and streaming potential experiments (zeta potential or surface charge measurements). We finish by verifying if there is any structural change of the bulk water in contact with the α-Al_2O_3.

5.2.3   Atomic Force Microscopy

The ability of the atomic force microscope (AFM) to create three-dimensional micrographs with resolution down to the nanometer and Ångstrom scales has made it an essential tool for imaging surfaces in applications ranging from semiconductor processing to cell biology [186] (The cover image of this chapter shows an AFM image of the alumina). It can also be used to measure force versus distance curves. Such curves, briefly called force curves, provide valuable information on local material properties such as elasticity, hardness, Hamaker constant, adhesion and surface charge densities [186, 187].

Our interest concerning the alumina lies in the determination of adhesive properties in contact with a liquid. Can we distinguish any information on the effective forces?

Introduction to force curves

In the AFM (figure 5.10) the sample is scanned by a tip, which is mounted to a cantilever spring. While scanning, the force between the tip and the sample is measured by monitoring the deflection of the cantilever. A topographic image of the sample is obtained by plotting the deflection of the cantilever versus its position on the sample.
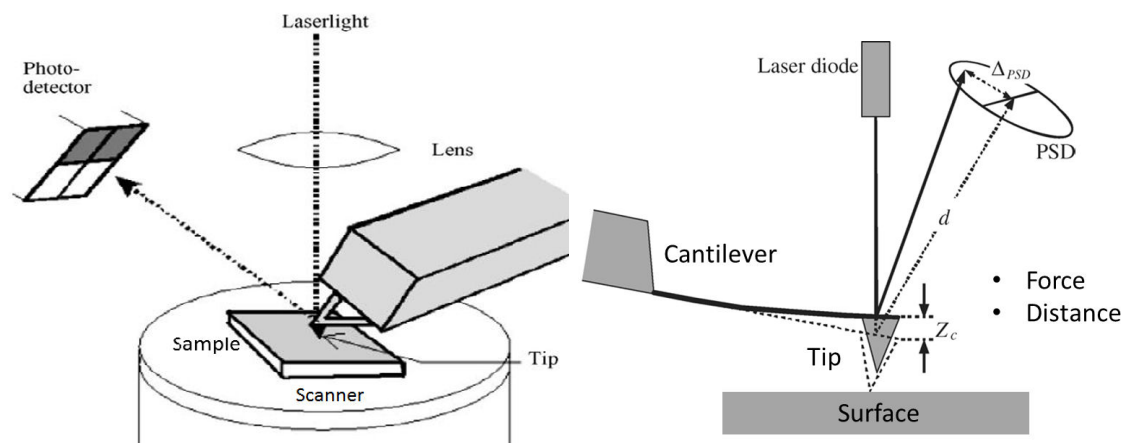
Figure 5.10: (left) Scheme of an AFM. (right) The detection of the deflection of the cantilever spring Z_c: A position sensitive Device (PSD) measures the position of the laser light reflected by the cantilever. Reproduced from [186].

Principle: In an AFM force curve measurement, the tip attached to a cantilever spring is moved towards the sample in the normal direction. Vertical position of the tip and

deflection of the cantilever are recorded and converted to force versus distance curves, the force curves.

In a force measurement the sample is moved up and down by applying a voltage to the piezoelectric translator, onto which the sample is mounted, while measuring the cantilever deflection resulting from the interaction between the tip and the sample surface. To reduce problems arising from the surface roughness the sample is has to be smooth on a scale comparable to the radius of curvature of the tip. The result of a force measurement is a measure of the cantilever deflection, Zc, versus position of the piezo (=tip-surface distance), normal to the surface. The force can be calculated when the spring constant of the cantilever is known. Figure 5.11 shows typical force curves for hard and deformable surfaces with and without repulsive and attractive surface forces.
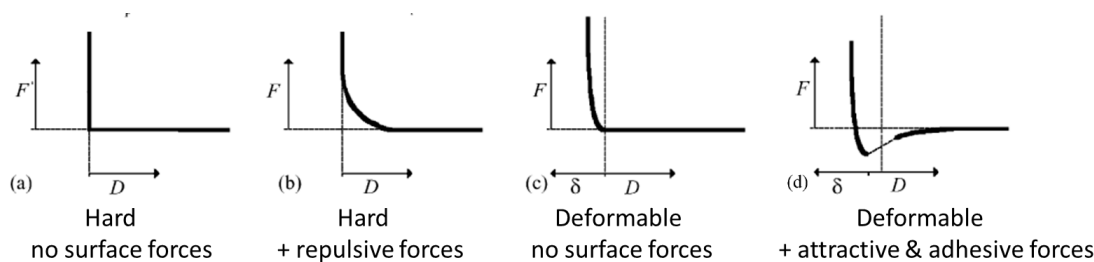
Figure 5.11: Typical force curves for: (a) infinitely hard tip and sample without surface forces (b) infinitely hard tip and sample with long range repulsion (c) Deformable materials without surface forces (d) Deformable materials with attraction and adhesion forces. δ is the "negative" distance when the tip is in contact and penetrates the surface. Reproduced from [186]

Force curves may show a pronounced hysteresis (due to dissipative effects). This means that the approaching and retraction of the tip do not show the same curve. A typical example curve is shown in figure 5.12 where we can identify three hysterysis zones: (A) in zero force line, (B) in the contact zone and (C) the adhesion. Upon approaching the surface the tip feels no force until close to the surface where an instant attractive force makes the tip jump onto the surface ("jump-in"). Here begins the contact zone. By further decreasing the distance the force becomes repulsive. The slope of the force is proportional to the Young modulus of the surface. It is reproduced when retreating the tip from the sample. The tip adhesion often keeps it in contact with the surface until the cantilever force overcomes the "pull-off" force (adhesion force) F_A. This even happens in purely elastic, non-dissipative situations.

The adhesive force measures the interaction of the tip and the surfac. We will see that this force gives us a first approach of the adhesive properties of the alumina.
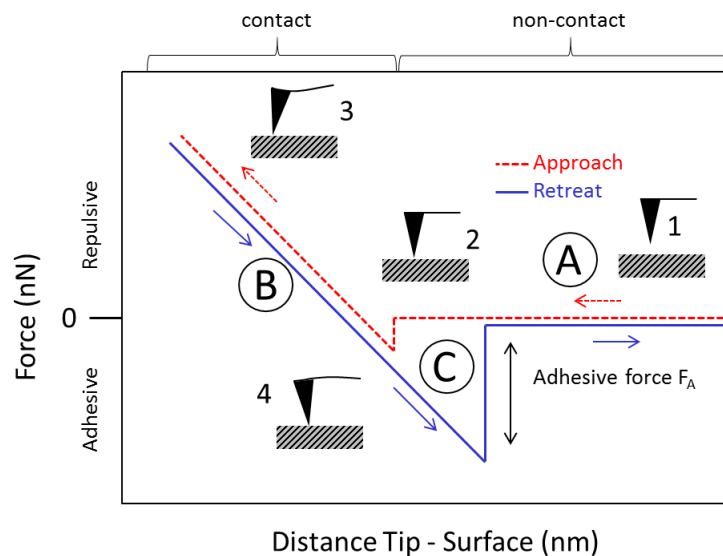
Figure 5.12: A typical approaching and retreating force curve showing hysteresis in the zero force line (A), the contact zone (B), the adhesion (C) and the corresponding position of the tip relative to the surface.

Force curve of the Alumina

Figure 5.13 shows the obtained forces of the approaching and retreating tip versus the distance. In the approaching curve we observe a weak attractive force between $12nm$ and $2.5nm$ tip - surface distance. At the contact zone the force increases linearly with a slope of $3N/m$, here we probe the stiffness of the sample. The retreating curve shows an adhesive zone up to $24nm$. The curve shows no abrupt break of adhesion but a continuous decrease in force with a maximum adhesion force of $F_A = 7nN$.
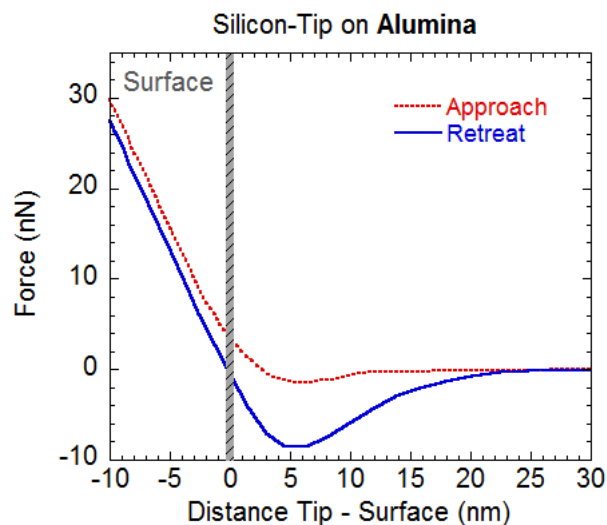
Figure 5.13: Distance - force curves of a silicon tip on the alumina surface under ambient conditions. The measurement was carried out with conventional silicon tip (spring constant of $5 N/m$). The sample was heated to assure optimal surface conditions and was contained under vacuum until shortly before the experiment.

How can we interpret this adhesion force? The adhesion force F_A is a combination of the electrostatic force F_{el}, the van-der-Waals force F_{vdW}, the meniscus or capillary force F_{cap} and forces due to chemical bonds or acid-base interactions F_{chem}:

$$F_A = F_{el} + F_{vdW} + F_{cap} + F_{chem} \tag{35}$$

We are probing the interaction between a silicon tip and an alumina surface. Electrostatic forces become relevant in aqueous solution or for insulators and we can exclude any chemical binding between the surface and the tip. Van-der-Waals interactions are always attractive and may contribute to the adhesion force. However the approaching force curve shows only a weak attraction. Due to the fact that the alumina is a high energy surface, a condensation of water from the ambient environment on the surface and the tip is likely. The formation of a meniscus between tip and surface leads to a contribution of capillary forces to the overall adhesive force. Humidity studies using a variety of tips have shown that meniscus forces are expected to give the largest contribution to F_A [188, 189]. They are large for hydrophilic (e.g. the alumina) and vanish for very hydrophobic surfaces.

Chemical force microscopy - comparison Alumina-Aluminium

The adsorption of humidity on high energy solid surfaces can be overcome by carrying out the experiments in water. Here the forces decrease by ca. a magnitude. Additionally, the tip can be functionalized to vary the interacting force. This procedure is called chemical force microscopy as it is able to introduce a chemical force between sample and tip. We used silicon tips (NanoCraft, spring constant $0.3N/m$) coated with hydroxy groups to better simulate the interaction between the surface and a water/OH-group molecule.

(a) Forces OH-Tip - aluminium in Water
(b) Forces OH-Tip - α-alumina in Water
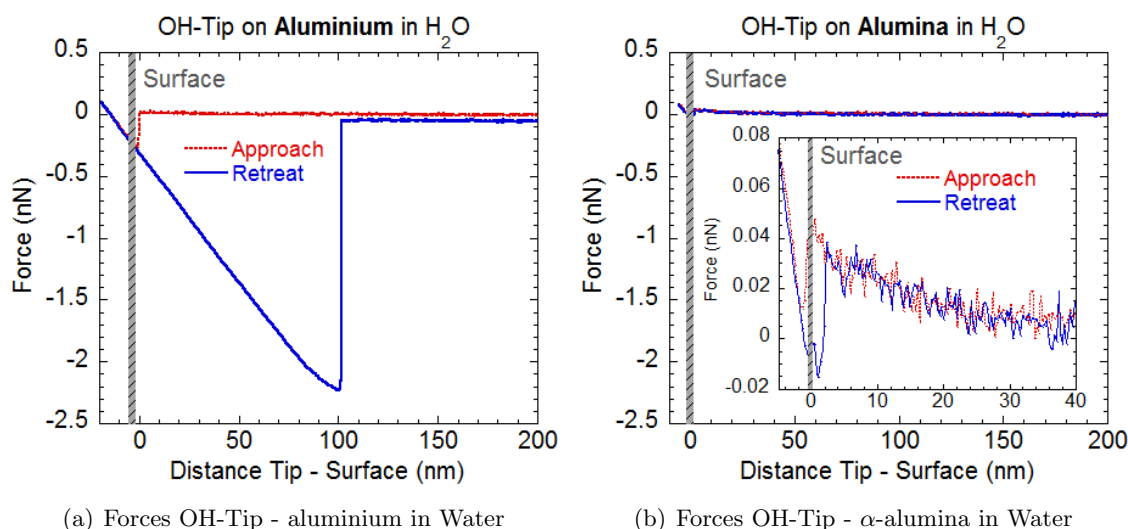
Figure 5.14: Distance - force curves (approach and retreat) of the OH-coated tip with aluminium and α-alumina surfaces in water. The experiments were carried out with a Bruker Multimode 8 NanoscopeV (Biophys) in force volume mode.

Figure 5.14 shows the obtained force curves of a OH-modified tip with the aluminium (figure 5.14(a)) and α-alumina surfaces (figure 5.14(b)). The curves have been obtained in the force volume mode. The AFM scans the sample as in the topographic mode and collects force curves on each position. The aluminium serves a comparing surface and shows adhesion forces of $2nN$. Both, the "jump in" and the "pull out" appear abruptly. The adhesive force is observed up to $100nm$ from the surface. The measured forces are similar to the ones observed for hydrophilic COOH-COOH interactions in ethanol [187, 190]. The relatively long-ranging adhesion curve of up to $100nm$ is probably due to the low spring constant of $0.3N/m$ of the tip which makes it quite extendible before the "pull out" event.

The force curve of the alumina presents a very different behaviour (figure 5.14(b)). At similar scales, almost no interaction is observed with the α-alumina. In detail we observe

a very weak repulsion up to $0.05nN$ of the modified tip close to the surface at a distance from $40nm$ to approximately $1nm$ before the jump-in. The latter distance coincides with the length of a OH-group. The repulsive curve resembles the model case of a infinitely hard surface with long range repulsive surface forces seen in figure 5.11(b). We also detect a weak adhesion of $0.015nN$ with a range of $2.5nm$ before rupture. Other (the far minority) zones on the surface have shown a somehow stronger adhesion but inferior to $1nN$. For both the aluminium and the alumina surface we find a slope of $0.2N/m$ in the contact zone indicating a comparable stiffness of the surfaces.

Repulsive forces - Electrostatic and hydration forces

Apparently the force curve with a short range repulsive interaction seems to contradict the strong adhesion properties of the alumina observed in the wetting experiments. However we have to consider that the experiments have been carried out in water. In the case of total wetting the surface is saturated with a thin film of water molecules of several Å[191]. In order to establish a surface contact the OH-coated tip first needs to pass already hydrated water molecules on the substrate. The approach of hydrated tip and surface at atomic/ Ångstrom distances leads to a weak repulsive force called hydration repulsion [186]. These repulsive forces are attributed to the energy required to remove hydrate water from the surface which is bound by strong charge-dipole, dipole-dipole and H-bond interactions [192–194].

The origin of the repulsive hydration force is still debated [195–197]. It is certainly related to the first layer of molecules strongly bound to the surface though the repulsion extends at larger distances. Importantly Israelachvili and Wennerström pointed out that the hydration force is caused by water-solid and not by water-water interactions [194]. Marcelja and Radic showed that a short-range repulsion can be explained by a modification of the water structure close to a hydrophilic surface [198]. Here the water molecules are more ordered than molecules in the bulk. These "ice-like water layers" have been observed via surface sum frequency generation spectroscopy on various substrates [199] and even on protein surfaces [200]. The mentioned authors conclude that the short-range repulsive forces between inorganic surfaces are probably not only due to structured water layers, but to the osmotic effect of hydrated ions which are electrostatically trapped between two approaching surfaces [201].

The hydration forces are supposed to decay exponentially:

$$U_A = A \times exp(\frac{-x}{\lambda_H}) \qquad (36)$$

where U_A is the potential energy between two hydrated surfaces, A the amplitude, x the distance and λ_H the hydration decay length [186]. The force is the negative gradient of

the potential and is thus proportional to the exponential decay of the potential. The decay of the force of our alumina is shown in figure 5.15 and gives a decay length of $25nm$ with a force amplitude of $0.05nN$. Reported values for silica, mica and clays give values of λ_H of $1-3nm$ and force amplitudes $0.07nN$ [186, 202]. The large decay length found for our alumina may indicate a thick strongly bound water layer on the substrate. Also the used tip shows a low spring constant of $0.3N/m$ making it fairly elastic and sensible to surface forces which could explain the observation of the long-range (weak) repulsive forces. However while the observed weak forces indicate the presence of hydration forces, the decay length is to long and other repulsive forces must be considered.
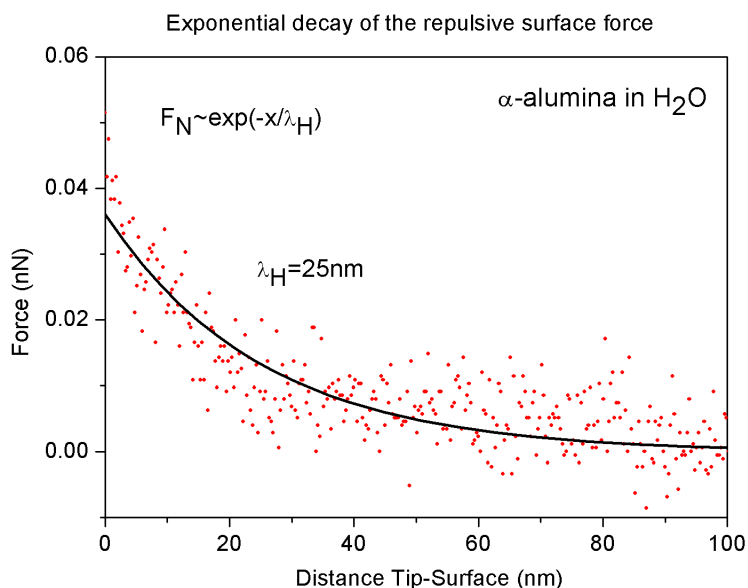
Figure 5.15: Decay of the surface force vs the tip-surface distance observed in figure 5.14(b). The experimental curve has been fitted by an exponential law yielding the decay length λ_H.

As mentioned before, in an aqueous medium the electrostatic force cannot be neglected [186]. In water many surfaces are charged. One can imagine this situation by a dissociation of protons from the OH-groups on the alumina. These surface charges cause an electric field which decreases exponentially with increasing distance from the surface. This is the origin of the electrochemical double-layer (EDL) [202, 203] which may act repulsive or attractive depending on the charge of the approaching tip (we will take a closer look at the surface charges in the following section). Concerning our AFM experiment the tip does not bear free electric charges but polarization charges at the tip/water interface caused by the surface charge of the substrate gives rise to an electrostatic interaction[202].

This electrostatic force is repulsive with force values around $10^{-12} - 10^{-10} N$ [202, 204]. Additionally the observed decay length lie around several tens of nano-meter coinciding with our results [202].

From the available data we cannot attribute the repulsive interaction between the OH-coated tip and the alumina in aqueous medium to hydration and or purely electrostatic forces. Such a distinction might be achieved by varying the ionic strength in the aqueous phase in order to suppress the electrochemical double layer forces. The latter can be examined by Zeta-potential measurements which will be presented in the following chapter.

Conclusions: We can summarize that the aluminium and the α-alumina have very different characteristics concerning the interactions of a OH-coated tip with the surface in water. The aluminium shows comparable adhesive properties as reported in literature for COOH-COOH interactions [187, 190]. The (heat cleaned) α-alumina shows very weak short-range repulsive forces in contact the with hydrophilic tip. These repulsive forces are likely due to a combination of hydration and electrostatic forces. Both imply a strong bound layer of molecules on the surface with an interaction potential that decays exponentially from the surface. The relative long decay length of $25 nm$ (relative to short decay lengths of the hydration forces of $1 - 3 nm$) indicates a significant participation of the electrostatic repulsion of the electrochemical double layer formed in the aqueous phase by the surface. Comparable force curves have been found for e.g. mica [186, 202], a substrate that is also known for total wetting properties.

Interestingly Israelachvili [22–24] and Granick [14–21] used cleaved mica surfaces in their surface force apparatus experiments. They exploited its strong adhesive (total wetting) properties to identify a solid-like behaviour of thin nanometric liquid films. It is indicated that the here examined heat cleaned α-alumina possesses similar properties as the mica.

However, the present AFM results cannot totally explain the role of total wetting or the zero slip length in the identification of a terminal shear elasticity in liquids at the sub-millimeter scale.

5.2.4   Zeta-potential

In the previous section we discussed the role of hydration and electrostatic forces of the α-alumina in water as the origin of the observed weak forces measured by AFM. the electrostatic forces have their origin in surface charges that result from a dissociation of water or hydroxy groups bound (chemically) on the surface. The question of surface charges can be addressed experimentally by zeta potential measurements. Apart from its major role in colloid sciences as a measure for the stability of particle dispersion and emulsion the Zeta-potential can be used as an indicator for solid surface charge providing information on the interfacial behaviour of solids, especially if water or an aqueous solution determine the material's surroundings [203].

The electrochemical double layer

All materials will spontaneously acquire a surface electrical charge when brought into contact with a polar medium like water. A material in deionized water is usually negatively charged (though few positively charged surfaces exist too). In the case of metal oxides, the ionization of the hydroxy groups bound on the surface is the main reason for the surface charges. The electrostatic situation at the interface between a solid and an aqueous phase is given by the electrochemical double layer (EDL) [203, 205]. Figure 5.16 presents a simplified model of the EDL. The electrical potential of a charged surface Ψ^S decreases in the bulk electrolyte solution with increasing distance from the surface. The charge formation arises either from the dissociation or protonation of surface functional groups in contact with the aqueous phase or from the adsorption of charged molecules or ions on the solid surface.

The molecules in layer close to the wall are strongly bound due to electrostatic interactions. Within this immobile (or solvated) layer the decay fo the electrical potential is linear but depends on the structure of this layer and thus on the complexity of the double layer model used. The immobile layer is further divided into the inner and outer Helmholtz layers which are not relevant for the understanding and use of the zeta potential. After passing the imaginary shear plane and entering the bulk aqueous phase the potential decays exponentially. The slope of the potential decrease depends on the surface potential and the number of charge compensating ions.
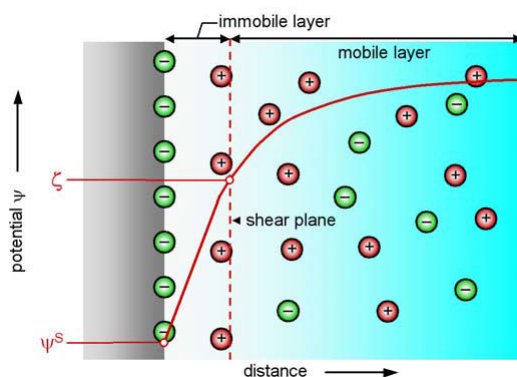
Figure 5.16: Model of the electrochemical double layer. The immobile layer of ions remains stagnant on the surface under liquid flow, and the mobile layer of (surface)-charge compensating ions move with the liquid relative to the solid surface during the Zeta-potential measurement.

The Zeta-potential as a measure for surface charges

As the surface potential is fundamentally not accessible [206], the Zeta-potential or the electrokinetic potential, is measured as a substitute. It presents the surface charge of the immobile layer and is proportional to the solid surface charge. For macroscopic solids, the Zeta-potential is measured by the electro-kinetic effects of streaming potential and streaming current. By applying an electric field, a shear flow is induced in the mobile layer. Under flow the Zeta-potential is proportional to the cell geometry and the electric conductivity (pH or ionic strength) in the mobile layer. The extrapolation of the Zeta-potential to infinite dilute solution yields the surface potential.

Principle: Streaming potential

A relative motion between the immobile and mobile layers of the EDL will result in the generation of an electrokinetic potential. This electrical response may be detected as a dc voltage (streaming potential): When an aqueous solution is streaming in a capillary between solid surfaces, shear forces act on the counterions compensating the surface charge and move the ions in the direction of the shear flow. A back-current of charges arises which compensates the flow of ions in the flow direction. The net charge separation leads to a electrical potential difference, the streaming potential U_{str}. It depends on several measuring conditions as the volume flow rate (which corresponds to a pressure difference Δp in a capillary geometry), the ionic strength (and or pH) and the size of the capillary. Knowing these parameters the zeta potential ζ can be calculated via the Helmholtz-Smoluchowski

equation [203, 205]:

$$\zeta = \frac{dU_{str}}{d\Delta p} \times \frac{\eta}{\epsilon\epsilon_0} \times const_{cell} \times \frac{1}{R} \tag{37}$$

where $const_{cell}$ is the cell constant, the length of the capillary in relation to its surface. η and $\epsilon\epsilon_0$ the viscosity and dielectric constants of the (electrolyte) solution and R the electrical resistance inside the channel.

Titration curve and isoelectric point

A most important origin of charge formation on metal oxides are acid - base reactions with the aqueous phase. The physical adsorption of water ions on the surface plays thus a major role in the establishment of the EDL. These processes are strongly pH dependent and affect the Zeta-potential.

Figure 5.17 shows the Zeta-potential as a function of the pH, the titration curve, for surfaces with acidic, basic, amphoteric groups (species), and for surfaces without dissociable (Brönsted) groups. The Zeta-potential is a measure for the effectiveness of the surface charge which is related to the dissociation constant of the surface groups at a given pH.
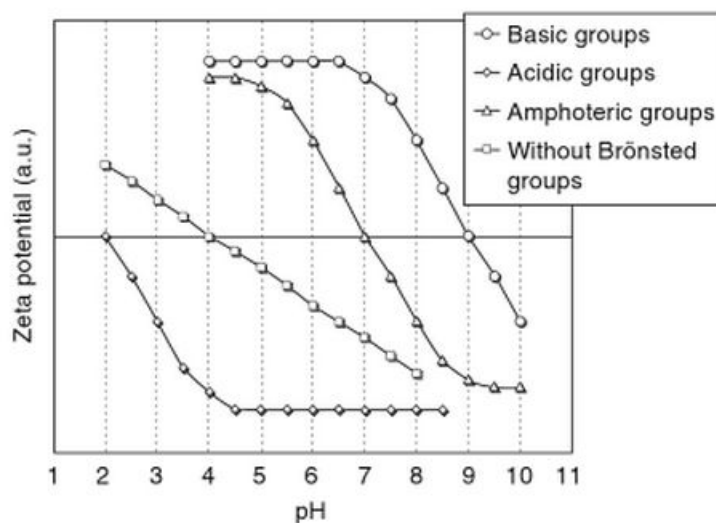
Figure 5.17: Dependence of the Zeta-potential on the pH for surfaces with acidic, basic, amphoteric groups, and for surfaces without dissociable (Brönsted) groups. The horizontal line indicates the zero value of the Zeta-potential and its intersection with the curves gives the isoelectric point IEP. Reproduced from [207].

Increasing the pH increases the concentration of protons (H^+) or protonated species in the aqueous solution.

Basic groups have low dissociation constants and are protonated at low pH (high concentration of protons) showing a positive Zeta-potential. By increasing the pH, ζ decreases, starting from a plateau value, and eventually reverses its sign at the isoelectric point IEP. IEP values of basic groups are always found at values higher than pH=7. More basic surface groups are shifted to higher IEP. At the IEP, the electrokinetic charge density becomes zero which means the surface charge is in average also zero. At high pH, the surface groups are deprotonated and the surface is charged negatively.

Acidic groups show the inverse behaviour. Their IEP are found at low pH ($pH < 7$). Upon increasing the pH, the groups become deprotonated easily as they have higher dissociation constants and thus show more negative values of ζ than basic groups. At high pH, the Zeta-potential reaches a plateau - here all groups are deprotonated.

Amphoteric groups can react as Brönsted bases and acids. Thus a combination of their titration curves produce a plateau at high and at low pH. The IEP depends on the dissociation constants of the titrated species.

The appearance of the plateaus in the titration curves is also a measure for the variety of species on the surface. The absence of a pronounced plateau indicates different species each showing individual dissociation constants.

The zeta potential of the alumina

Figure 5.18 shows the results of the Zeta-potential measurements for the α-alumina. Particles of size $500 \mu m$ have been used for the measurements (Anton-Paar). The alumina shows the titration curve of a substrate with acidic surface groups. Only at lowest pH values (pH=2.9) we find positive values for the Zeta-potential which decreases upon increasing the pH showing an IEP of 3.1. This indicates fairly acidic surface groups. The absence of a pronounced titration plateau at high pH indicates the presence of more than one surface species. Conclusively the tested alumina shows, for large range of pH (4-9), a negatively charged surface and hydrophilicity. These charges should thus contribute to the repulsive forces discussed in the previous section.
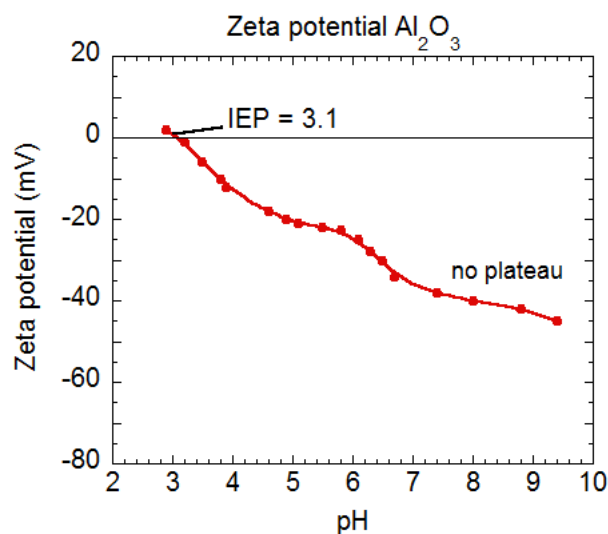
Figure 5.18: Zeta potential of α-alumina particles (size $500\mu m$, initialized by heating) as a function of the pH. Characterized by the streaming potential technique (Anton Paar).

The surface species at low pH, IEP and high pH are presented in figure 5.18.
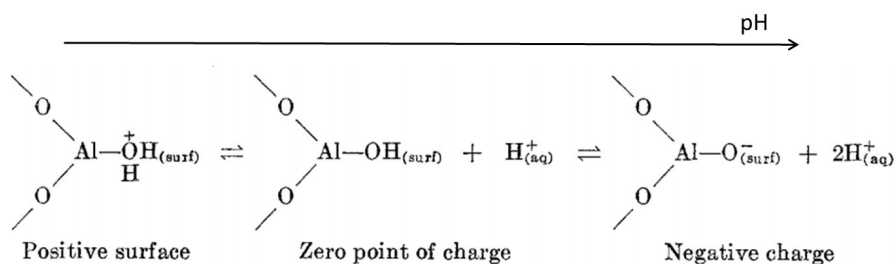
Figure 5.19: The principal species of the surface group of the alumina at low pH, the IEP and at high pH. Reproduced from [208].

It is interesting that the observed titration curve is of acidic type as the alumina is known to show amphoteric properties [208]. However the Zeta-potential depends on the surface condition, geometry (roughness, grains or plates, porosity) and history (heat treatment) [203]. This is the reason why we may find different curves for the same material composition and different morphologies ($\alpha, \beta, \gamma - Al_2O_3$). Concerning the α-alumina, IEP ranging from 3 to 9 have been reported [180, 208, 209].

In the case of our $\alpha - Al_2O_3$ and by using similar Zeta-potential experiments Ralston et al. [180] have even shown a marked decrease of the zeta potential after heat treatment

at $500°C$ for alumina plates while their alumina powder of grain size $150nm$ showed an amphoteric behaviour with an IEP of 8.5. Comparable observations were made for silica and titanium oxide [181]. This decrease was found consistent with the decrease in hydroxy groups at the surface due to the heat treatment.

Conclusions: Our $\alpha - Al_2O_3$ shows acidic properties in zeta-potential measurements and the surface is negatively charged a large range of pH values (4-9). This ensures a hydrophilic behaviour. The absence of a pronounced titration plateau at high pH indicates that probably more than one surface species is responsible for the acidic properties. The IEP (3.1) of our $\alpha - Al_2O_3$ particles (size $500\mu m$) is more acidic than for other reported alumina surfaces and particles (around 8-9) which show amphoteric behaviour [180, 208, 209]. However other authors have also shown acidic properties of $\alpha - Al_2O_3$ single crystals but not for polycrystalline particles (size ($150nm$) [180]. The linking element of their and our experiments is the observation of total wetting upon cleaning the surfaces by heat treatment. We can conclusively state that our alumina shows negative surface charges which is likely to improve the wetting condition of hydrophilic substances. The surface charges are directly linked to the surface hydroxy groups and are likely to be at the origin of the weak local repulsive forces observed in the AFM measurements. Certainly the thermal history of the alumina plays an important role in its surface state. It remains that the chemistry of water on alumina is poorly understood [179]

5.2.5 Structural analysis of water in contact with the alumina

So far we have studied the extraordinary wetting performance of α-alumina by examining the liquid substrate interaction. In this final section we examine the bulk related structural change (the first correlation peak) of the wetting liquid, water, in contact with the α-alumina. Additionally we want to rule out any chemical reaction involving water or the formation of other aluminium oxide species. We thus carried out a structural analysis of water in contact with α-alumina by neutron scattering. The experiments have been realized using the 3T-1 Thermal Neutron Two Axis Diffractometer at the LLB/Orphée.

Neutron scattering of liquids - the first correlation peak

Neutron scattering is well suited to study the structural properties of liquids [161]. The scattered intensity $I(q)$ of a specific particle is proportional to the structure factor $S(q)$:

$$\langle I(q) \rangle \sim N|f(q)|^2 S(q) \tag{38}$$

where $f(q)$ is the form factor and N the number of scatterers. $S(q)$ can then be expressed in terms of the radial distribution function $g(r)$:

$$S(q) = 1 + \rho \int_V dr \times exp(-iqr)g(r) \tag{39}$$

where ρ is the scatterer density, V the volume segment and r the distance. The radial distribution function describes how the density varies as a function of the distance from a scattering particle e.g. the distances to the most neighbouring scatterers. For a qualitative description we can equally discuss $I(q)$, $S(q)$ or $g(r)$.

Let us consider the structure factor: Figure 5.20 shows $S(q)$ for an atomic liquid. The first peak that appears at small q is called the "first correlation peak". It defines approximately the interatomic distance and the spacial extent of the short range order. For a molecular liquid the individual structure factors of different atoms add up and contribute to the total $S(q)$ depending on the stoichiometry their ability to scatter (cross section). The obtained diffraction spectra thus give an average response of the molecule and the first correlation peak the intermolecular distance at short range. At larger scattering vectors $S(q)$ shows modulations that are related to the intramolecular correlations before it converges to the average density of the liquid [160, 161].

Neutron scattering water in contact with the alumina

The first correlation peak of liquid water has been extensively studied in the literature [161]. It lies at scattering vectors of around $q = 2.0$Å(its inverse describes the intermolecular
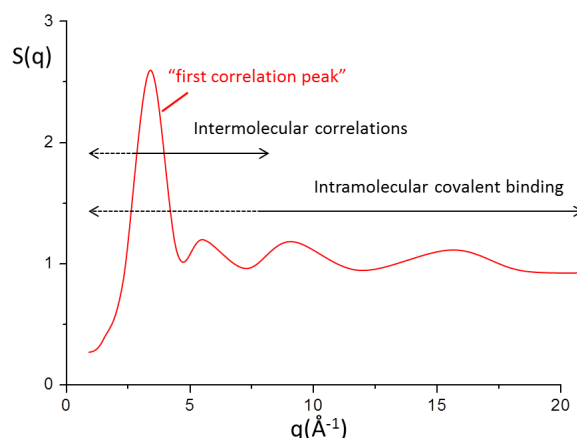
Figure 5.20: Structure factor $S(q)$ of a liquid versus scattering vector. The values of q determine the range of intermolecular correlations at smaller q. The "first correlation peak" serves as a measure of the local order.

distance between the individual molecule and its nearest neighbours, e.g. the short-range structure) and presents a rather a broad band rather than a peak due to the contribution of hydrogen and oxygen atoms and a statistical thermal distribution of the short range structure. Our aim is to determine if any structural change is induced by the metal oxide by e.g. strong interacting forces that exceed surface induced effects, a chemical reaction or a dissolution of the metal oxide. In particular we want to check that the α-alumina does not react with water into, or dissolve forming e.g. γ-alumina (γ-$AlOOH$, Boehmite). If any of this events affects the scattering volume, we should be able to see a change in scattering of the water.

Experimentally we substituted the water by heavy water, D_2O, which shows similar chemical properties but an increased (and positive) scattering cross section and a fairly lower neutron absorption coefficient. This reduces the incoherent scattering and results in a higher resolution of the diffraction pattern. We used the α-alumina in the form of a powder (grain size $60\mu m$) and plates (similar to the fixtures used in dynamic relaxation) that both have been heat cleaned at $450°C$. Heavy water and alumina were mixed in vanadium containers (volume=$4mL$, vanadium guarantees a low absorption of neutrons in the observed scattering vector range).

Figure 5.21 presents the scattered intensity $I(q)$ of D_2O alone and in contact with the α-alumina powder (figure 5.21(a)), the plates (figure 5.21(b)) respectively. We observe in both cases the first correlation peak of D_2O with a maximum at $q = 1.96$Åwhich is the reported value for bulk water [161]. The contributions of the α-alumina and vanadium to $I(q)$ in the concerned range of q have been separated out. The pattern of D_2O superpose in the presence of the alumina and we observe neither a broadening or narrowing of the

band nor the appearance of additional peaks.

(a) D_2O and α-alumina plates   (b) D_2O and α-alumina powder
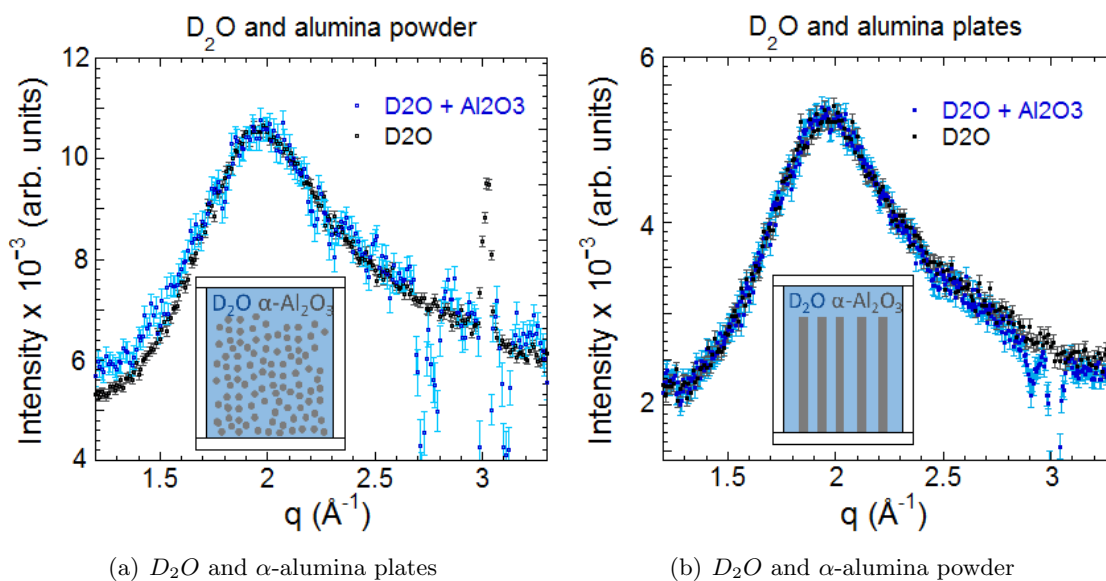
Figure 5.21: Neutron diffraction at large angles of liquid D_2O: Diffraction intensity versus the scattering vector: D_2O alone, in the presence of alumina plates (a) and powder (b) at room temperature.

Conclusions The first correlation peak of bulk phase D_2O does not change when in contact with the α-alumina (powder or plates). The bulk structure of D_2O is thus seemingly unaffected and as a major result we can exclude any chemical reaction in terms of the formation of aluminium oxide species as the Boehmite that would affect the bulk water.

5.2.6   Conclusions

The strong wetting properties of the α-alumina permits to access a terminal shear elasticity at the sub-millimeter scale. Its extraordinary wetting performance is evidenced macroscopically by a contact angle of zero which favours microscopically a zero slip length boundary condition [125].

In principle α-alumina shows high surface energy [182] but to achieve total wetting the surface conditions must be controlled. By heat cleaning the substrate above $450°C$ organic impurities are eliminated and the density of hydroxy groups on the surface is reduced [180, 181]. This procedure leads to a improvement of wettability for many liquids and a total wetting in most cases. The intrinsically strong wettability of the α-alumina is revealed. In this state interfacial interactions with liquids are likely due to Lewis-acid/base type interactions and the high Hamaker constants of the substrate e.g. van-der-Waals attraction.

Using atomic / chemical force microscopy we simulated the interaction between a water molecule and the α-alumina submersed in water. We did not observe a strong interaction e.g. adhesion between the OH-coated tip and the α-alumina but a weak repulsive force of a decay length of ca. $25\mu m$. This observation can be attributed to a combination of two repulsive forces : The resistance of the first strongly bound water layers on the surface, e.g. ice-like layers [198, 199], the hydration force and the electrostatic repulsion between the electrochemical double layers of tip and surface. The latter is evidenced by Zeta-potenial measurements. Immersed in water, hydroxy groups are formed by a Lewis acid/base reaction on the surface of the α-alumina. These groups are acidic and dissociate forming a highly negatively charged surface. Additionally, in neutron scattering experiments show no substantial change in the first correlation peak of water for aqueous dispersions of α-alumina particles (size$60 mum$).

Interestingly, Israelachvili [22–24] and Granick [14–21] used cleaved mica surfaces in their surface force apparatus measurements to identify a terminal shear elasticity in liquids at the nano-meter scale. Their mica surface shows comparable properties to the α-alumina, namely the repulsive forces in the AFM [186, 202], a negatively charged surface and total wetting [210].

Similarly, the wetting behaviour of the α-alumina is a key parameter in dynamic mechanical analysis of liquids at a macroscopical scale and its thermal history plays an important role for its surface state. It remains that the interaction of liquids on alumina is poorly understood [179].

General Conclusions and Perspectives

The aim of this thesis is to enlighten the terminal shear elasticity in liquids and related properties. This presents a very challenging task, since in the conventional macroscopic description, liquids are supposed to have no shear elasticity (or only at very high frequency [211]). Liquids are supposed to exhibit a flow behaviour at low frequency ($< 1Hz$). However, it seems to be more and more evident that the dynamic processes occurring at the nano-, micro, and even submillimeter scale are different from those at the macroscopic scale and rather demand a multi-scale approach. A terminal shear elasticity was identified at the nanometer scale by Granick et al. [22–24] and Isrealachvili et. al [14–21] and at the micrometer scale by Derjaguin et al. [25, 26, 212] and Martinoty et al. [27, 110]. More recently Noirez et al. [28–30, 32–34, 36, 38–41] evidenced a non-negligible shear elastic behaviour for various liquids at the sub-millimeter scale (typically $0.05 - 0.2mm$). The existence of a terminal shear elasticity at macroscopic sample sizes implies that molecules in the liquid state may not be dynamically free but weakly elastically correlated. The shear elasticity appears as the first linear regime prior to the well known viscous or VE behaviour that is recovered at larger strains. Experimentally, this terminal shear elasticity has been obtained by measuring the stress induced by a low frequency, small strain amplitude, mechanical excitation. The role the liquid-substrate boundary condition is crucial since both strain and stress are transmitted from the surfaces.

Motivated by the lack of alternative techniques that gain access to the shear elastic properties of liquids we transferred the principle of dynamic mechanical analysis to optical measurements. Our premise was that the pretransitional fluctuations that are present in the isotropic phase of liquid crystals should feel the strain field and thus serve as an optical probe. Their twist under strain should give rise to a birefringent signal.

Terminal shear elasticity

In a first step we have shown by stress measurements that we can identify a terminal shear elasticity in the isotropic phase of three representative liquid crystals: the 8CB (low molecular weight, $M_{8CB} = 292 g/mol$), the LCP95 ($12 \times M_{8CB}$), a "fat" molecule and the PACN ($80 \times M_{8CB}$), a non-entangled side-chain liquid crystal polymer. For the first time we demonstrated, at low thickness, the existence of a terminal shear elasticity in the isotropic phase of low molecular weight liquid crystals (8CB, LCP95) [42, 43] while conventional measurements display a viscous or VE behaviour.

The **stress measurements** of the elastic response can be summarized as follows:

- At low strains ($\gamma_0 < \gamma_{crit}$), in-phase strain/stress signals evidence an elastic response. The visco-elastic spectrum shows a terminal shear elastic plateau $G' > G'' \neq fct(\omega)$.
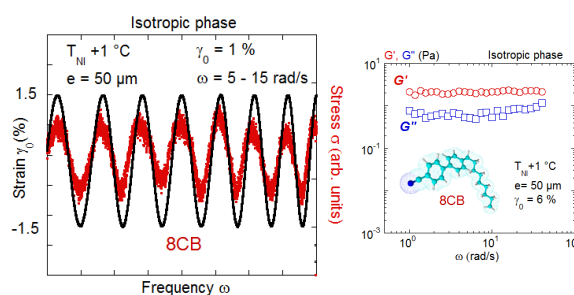
- The elastic regime found at small strain amplitudes ($\gamma_0 < \gamma_{crit}$) - the response is delicate and can be lost by increasing the strain. Above γ_{crit} the stress/strain signals become phase shifted by $\frac{\pi}{2}$. G' decreases while G'' stays relatively constant. At large strains the visco-elastic spectrum recovers the conventional viscous (8CB, LPC95) or visco-elastic (PACN) behaviour. The elastic regime is thus a first linear regime prior to the conventional linear VE regime.
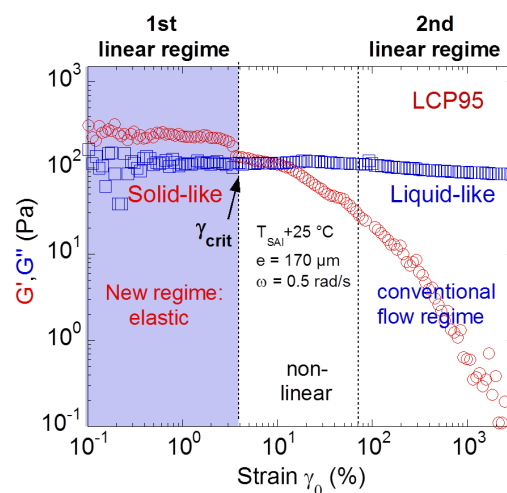
The terminal shear elasticity in the isotropic phase of the 8CB and LCP95 (they crystallize at low temperature) is measurable far away from the liquid crystal transition. It reveals a property due to intermolecular interactions and rules out any interpretation in terms of glass transition effects.

Visualization of shear elasticity

In a second step, we probed the optical birefringent properties of the isotropic phase of the liquid crystals under similar conditions to the stress measurements. We revealed that it is possible to induce dynamically a strong, defect free and reversible birefringence. The emergence of this harmonic optical signal at low frequency is not explainable by a coupling to the known relaxation times of pretransitional fluctuations. The results indicate a long-range correlation in the bulk [43]. The observation of a harmonic birefringent signal indicates that the liquid behaves as an optical oscillator, transforming reversibly the energy into an orientation of the pretransitional swarms (which is not a dissipative effect).

The **optical results** can be summarized as follows:

- At the lowest strain amplitudes ($\gamma_0 < \gamma_{crit}$) the harmonic strain/ birefringence signals are in-phase. At larger strains ($\gamma_0 > \gamma_{crit}$) they are $\frac{\pi}{2}$-phase shifted (in-phase with the strain-rate).
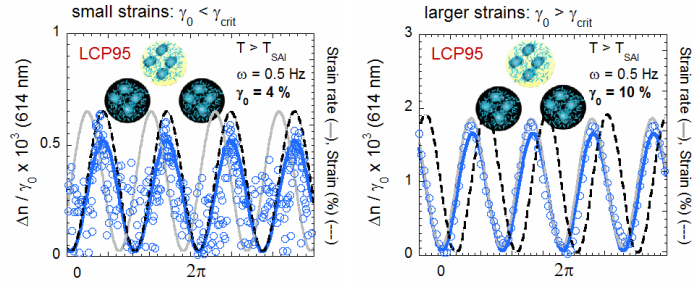
- The strain dependence describes a sigmoidal curve and reveals harmonic ($\gamma_0 < \gamma_{distorted}$) and distorted ($\gamma_0 > \gamma_{distorted}$) signals by increasing the strain. In the linear regime the strain/birefringent signals are phase shifted by $\frac{\pi}{2}$.
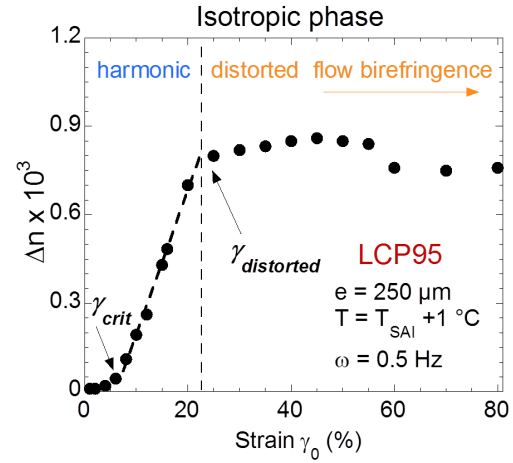
How can we interpret the optical results? At very low strain amplitudes the birefringent signal is in-phase with the strain - here the response must be considered to be elastic. As soon as we pass a critical strain amplitude, we observe a linear increase of the signal with the strain and a synchronization with the strain rate. The response is in-phase with

the strain rate, it succeeds the first elastic regime. It is obtained at similar conditions as the flow (liquid-like) regime of the stress measurements and exhibits similar characteristics (the signal is $\frac{\Pi}{2}$ shifted in respect to the strain) as the viscous response. However the observation of a birefringence indicates a long-range ordered phase and contradicts the state of an isotropic liquid. The isotropic phase behaves, above γ_{crit}, as a delayed elastic material alternating entropic loss and recovery during the backward-forward motion [213]. This mechanism transforms the accumulation of the energy into an ordering (entropy loss during the stretching phase) and its recovery to the initial state (entropy gain during the relaxing phase). This might explain the synchronization with the shear strain rate. This result is possible if the pretransitional swarms are embedded within the elastic net and respond reversibly to the stress field playing the role of a dynamic optical probe.

Further we can compare the results with the strain behaviour of the visco-elastic moduli. Above γ_{crit}, at the onset of a non-linear regime, G' decreases with the strain while G'' stays constant. The elastic properties are not completely lost during this process, the elastic character persists as demonstrated by the induction of a reversible ordered state. The viscous behaviour and the dynamic birefringence behaviour are gathered in the following table. It tells that the viscous behaviour might not be totally dissipative but can hide
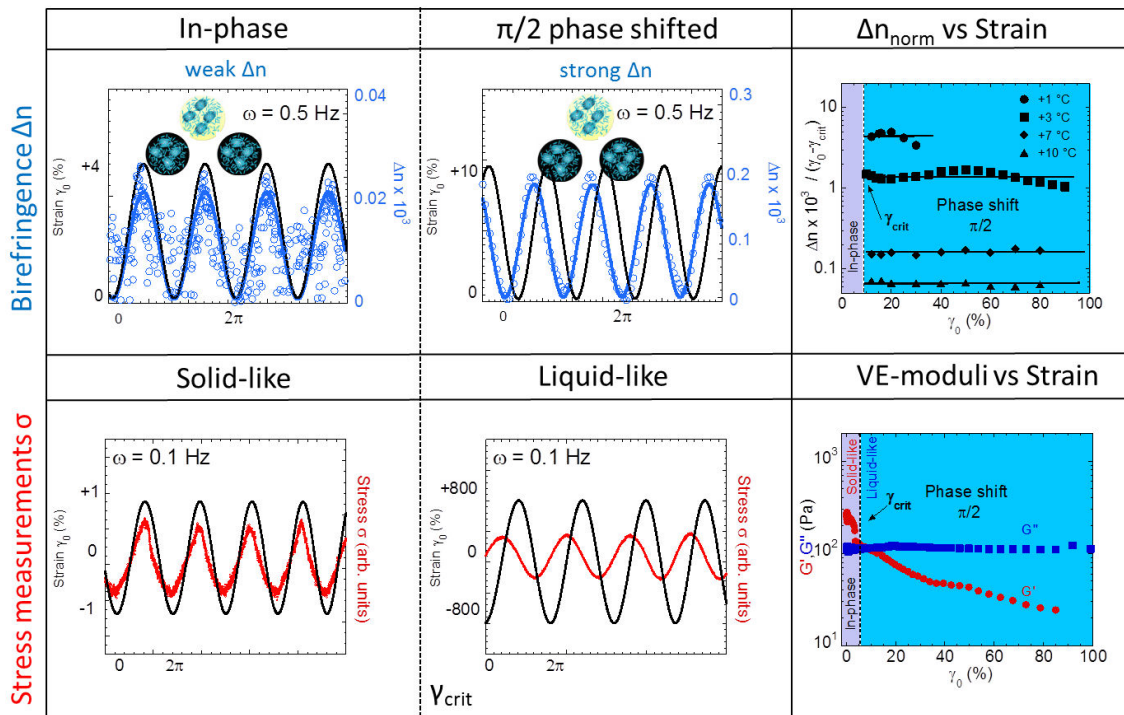
oriented states visible via the birefringence.

Structural analysis

We further carried out a structural analysis of the isotropic phase upon the event of the low frequency strain amplitude using X-ray and neutron scattering techniques. In the X-ray scattering experiments we observed, above a critical strain amplitude, a decrease in intensity of the first liquid correlation peak at a scattering vector $q \approx 1.3\overset{\circ}{A}$.

- The decrease in intensity versus the strain amplitude in the observed plane can be interpreted as a twist of molecules in the side-view $\vec{x} - \vec{z}$ plane and describes a sigmoidal curve.
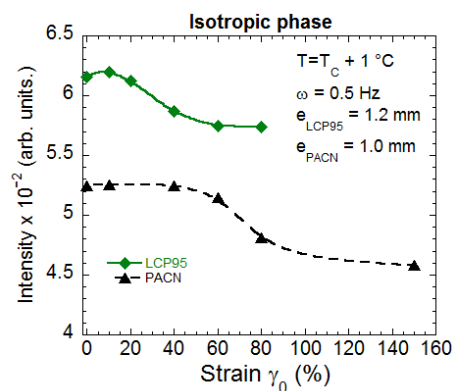
The orientation can be described as a twist of the rod-like molecules with their long axis oriented along the neutral direction $\vec{y}$. The log-rolling geometry is in agreement with the observed increase of birefringence in the plane of observation formed by the strain and neutral axis $(\vec{x} - \vec{z})$.

Role of the surface interaction

In a fourth step we aimed at determining the influence of the liquid-surface boundary condition (wetting behaviour) of both, the transparent surfaces used in the optical bire-fringent measurements and the total wetting fixtures (α-alumina) applied in the dynamic mechanical analysis.

- Several surface treatments were applied to the transparent quartz fixtures in order to play with the anchoring conditions of the liquid crystal. It is shown that an increase of the contact angle (de-wetting) between the isotropic liquid and the surface reduces the strain induced birefringent signal and vice versa.

Concerning the wetting performance of the α-alumina: The high energy of the ceramic permits to access a terminal shear elasticity at the sub-millimeter scale. The extraordinary wetting performance of the α-alumina with many liquids is evidenced macroscopically by a zero contact angle which is supposed to favour microscopically a zero slip length boundary condition in the frame of the Tolstoi relation [125, 126].

- The α-alumina reveals its strong wetting performance when the surface is cleaned from polluting (organic) substances by heating. A further reduction of surface bound hydroxy groups allows for a stronger interaction with less polar liquids. In this state the interactions are likely dominated by Lewis-acid/base type interactions and van der Waals interactions due to the high Hamaker constant of the ceramic.

- In aqueous medium, atomic force microscopy with chemically modified tips indicates a strongly bound first layer of (water) molecules on the surface. Zeta-potential measurements show a strongly negatively charged surface in an aqueous medium. Neutron scattering experiments show that the α-alumina does neither change the bulk structure of water in contact nor dissolve itself in it.

The origin of the total wetting behaviour remains however unclear [179]. It is an important factor to facilitate the access to the shear elasticity. Interestingly Israelachvili [22–24], Granick [14–21] and Derjaguin [25, 26] used similar surface properties in their surface force apparatus protocol to identify a terminal shear elasticity in liquids at the nano-meter scale.

Final conclusions and perspectives

Conclusively, we first assumed that liquids contain long range elastic correlations. This elastic regime, accessible at low strains and at the sub-millimeter length-scale (typically from nano to $0.2mm$ thickness), is prior to the conventional visco-elastic or viscous regime with respect to the strain amplitude and can be easily lost if the sample is not strongly interacting with the substrate or if it is containing nano, micro or macro bubbles. We have shown that it is also possible to access the low frequency shear elasticity in the liquid isotropic phase of three different liquid crystals mainly differing by their molecular weight and displaying different liquid crystal phases. The chosen liquid crystalline molecules (8CB, LCP95 and PACN) are ordinary cyanobiphenyl liquid crystal molecules, broadly studied in the literature (8CB) or used in LC-displays (LCP95). In all cases, we reveal that it is possible to identify a low frequency shear elasticity whose modulus increases with increasing molecular weight.

While a liquid behaviour deforms irreversibly under strain (flow behaviour), the solid-like behaviour is characterized by a linear, reversible response to small amplitude strains. On the basis of the existence of an elastic network, we predicted that the pretransitional swarms that coexist randomly in the isotropic phase of liquid crystals could be oriented by applying a small oscillatory strain. For this challenge, a specific setup was mounted to enable the synchronized measurement of the optical observation and of the strain.

The experimental results show that it is possible to induce dynamically a strong, defect free and reversible birefringence. The emergence of a harmonic optical signal at low frequency that is in-phase with the strain at low strains and $\frac{\pi}{2}$-phase shifted at larger strains is not

explainable by a coupling to the known relaxation times of pretransitional fluctuations (VE relaxation times are not relevant here). The results indicate long-range correlations in the bulk. The observation of a harmonic birefringent signal indicates that the liquid behaves as an optical oscillator, transforming reversibly the energy into an orientation of the pretransitional swarms.

Therefore, the pretransitional fluctuations can serve as an efficient probe to visualize the strain field in the liquid and identify its shear elastic properties. At low strain, the in-phase birefringence corresponds to the elastic regime identified in stress measurements. At larger strains the $\frac{\pi}{2}$-phase shifted birefringence observed reflects also an elastic property. Indeed, the birefringence corresponds to a long-range orientational order. The long range ordering and the harmonic response oppose a dissipative (viscous) state but indicate a loss of entropy with respect to the isotropic state. The shear elasticity (which decreases above the first linear regime) is thus not lost at larger strains but has undergone an entropy-driven transformation associated to an anisotropic state and gives rise to the viscous signal. Entropic elasticity is known in polymer physics. It is usually explained by the reversible stretching of the entangled chains along the strain direction (decreasing the number of conformations of the chains).

In the present case, the molecules 8CB and LCP95 are too short to present several configurations, it cannot stretch and does not exhibit any characteristic relaxation time (the conventional VE spectrum displays a Newtonian behaviour). We suggest that the entropy loss is produced by the stretching of the elastic network formed by the intermolecular interactions. In this process, X-ray measurements indicate in the case of the LCP95, that the pretransitional fluctuations twist (stretching and orientation) under stress to adopt the log-rolling geometry (which minimizes the energy) and relax back to the initial orientation once the dynamic stress field is released. Because of the similitude between the birefringence behaviour and the viscous modulus, we suggest that a similar transient entropic process might take place at least partly in the viscous regime. In the light of this, few theoretical developments introduce the role of intermolecular interactions as crucial in liquids (entangled and non-entangled polymers) [80–84]. Theoretical models describing the melting process in glass forming or amorphous solids [214, 215] may provide a helpful approach of the present results. To our knowledge the concept of entropic intermolecular elasticity is not seen as a relevant parameter in low molecular liquids. The entropic scheme is a scheme compatible with the assumption of a non-zero static shear elasticity in liquids firstly proposed by Volino [85]. Essentially, above a critical strain value, the strain produces a rheo-thinning of an initial elastic network giving rise to a viscous regime.

It turns out that while the elastic response is relatively simple, the viscous regime is complex and might hide entropic-driven processes related to a non-equilibrium state of the shear elasticity. Other illustrations of the manifestation of the shear elasticity is the recent observation of the co-existence of cool and warm shear bands visible at large strains or

under steady state flows in liquids [216]. These complex thermal effects contrast with the academic view that foresees a heating by friction of molecules and opens the route for further investigations. Mechanical analysis is a powerful method to access the condensed state properties. A coupling of the mechanical analysis with other probes (e.g. microscopically with the pretransitional fluctuations or fluorescent probes or at large scales with particle tracking [217] or thermal mapping [216]) is also certainly a very promising way to progress in the understanding of and foreseeing new effects at different scales in the liquid state. Concerning the pretransitional fluctuations, the strong birefringent signal at low frequencies in the isotropic liquid phase is obviously an attractive property for converting a mechanical action in an optical device based on a reversible transition from a true black state to a birefringent state and providing an alternative in the active field of liquid crystalline actuators [218].

Appendix A

Dynamic mechanical analysis combined with optical measurements

A major part of this thesis consisted in transferring the principle of dynamic mechanical analysis to optical measurements and exploiting the birefringent properties of the pretransitional fluctuations present in the isotropic phase of liquid crystals. From an instrumental point of view this is realized by combining polarization microscopy to a shear cell. A customized trigger system permits to analyse simultaneously the optical birefringence and applied strain. Figure A.1 shows the scheme of the experimental setup.
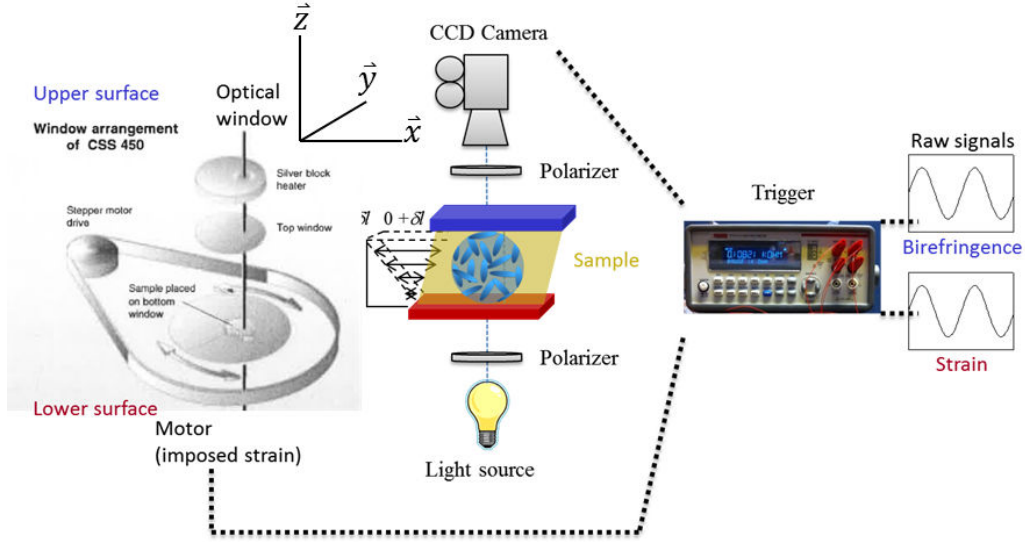
Figure A.1: Scheme of the setup. The isotropic phase fills the gap between two Quartz discs of high optical quality. The oscillatory movement of the lower disk/surface provokes a stress in the sample that is measured between crossed polarisers by a sensitive CCD-camera. A trigger system (R&D Vision) permits to simultaneously access the mechanical input (strain) and optical output (birefringence) signals with a synchronization delay of $10^{-5}s$.

The Optical part: Microscope and birefringence

The optical birefringence is observed under crossed polarizers using an Olympus BX60 microscope. The signal is measured by a CCD camera (Vision technology) that is characterized by a low level intensity detection. Polarization microscopy is a commonly used technique to examine birefringent samples like the mesophases of liquid crystals.

The strong interaction of polarized light with birefringent samples is due to the anisotropy of the refractive index. For an anisotropic sample e.g. an oriented nematic liquid crystal the refractive index along the $\vec{x}$ axis denoted n_1 is different from the refractive index in the perpendicular direction $\vec{z}$ denoted n_2. The intrinsic birefringence is the difference between these two indices:

$$\Delta n = \mid n_1 - n_2 \mid \tag{40}$$

This anisotropy of the refractive indices can be visualized by irradiating the sample placed between crossed polarizers with monochromatic light. The polarizer eliminates all planes of the electromagnetic wave but one depending on the orientation of transmission of the polarizer. When this linear polarized wave interacts with the anisotropic sample the plane

of the wave is rotated. The wave now possesses a component along the $\vec{x}$ and $\vec{y}$ axis, depending on the magnitude of the refractive indices n_1 and n_2 and thus on the strength of anisotropy (figure A.2). For the two wave components we can now write:
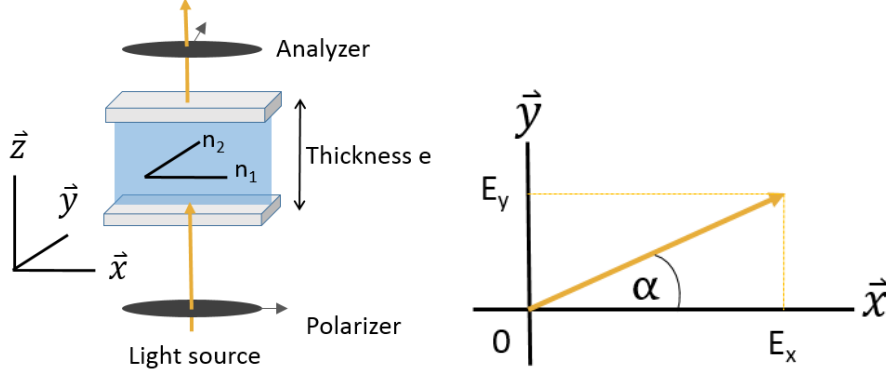
Figure A.2: Components of the linear polarized electromagnetic wave.

$$E_x = E_0 cos(\alpha)cos(\omega t) \tag{41}$$

$$E_y = E_0 sin(\alpha)cos(\omega t) \tag{42}$$

With the amplitude E_0. When the incident beam has passed the whole sample thickness e the components have covered an optical path-length of $n_1 e$, $n_2 e$ respectively. The components that leave the sample can thus be written as:

$$E'_x = E'_0 cos(\alpha)cos(\omega t - \frac{2\pi}{\lambda}n_1 e) \tag{43}$$

$$E'_y = E'_0 sin(\alpha)cos(\omega t - \frac{2\pi}{\lambda}n_2 e) \tag{44}$$

Where λ is the wavelength and E' is an amplitude different from the incident one presenting an energy loss due to reflections. If we change time of origin of wave we obtain:

$$E'_x = E' cos(\alpha)cos(\omega t - \frac{2\pi}{\lambda}\rho) \tag{45}$$

$$E'_y = E' sin(\alpha)cos(\omega t) \tag{46}$$

With $\rho = \Delta n \times e$ is the difference in the optical path-length and $\phi = \frac{2\pi}{\lambda}\rho$ the phase shift.

These two wave components pass the analyzer and only analogue to the polarizer only one plane is transmitted. The two wave components are now parallel (figure A.3):
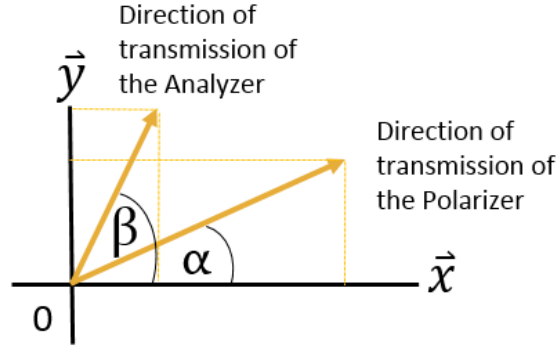
Figure A.3: Wave transmitted by the analyzer and polarizer.

$$E''_x = E' cos(\alpha) cos(\beta) cos(\omega t - \frac{2\pi}{\lambda}\rho) \tag{47}$$

$$E''_y = E' sin(\alpha) sin(\beta) cos(\omega t) \tag{48}$$

The two waves are coherent and interfere. The resulting intensity is given by:

$$I = \langle (E''_x + E''_y)^2 \rangle \tag{49}$$

which corresponds to

$$I = I_0[cos^2(\alpha + \beta) + sin(2\alpha)sin(2\beta)cos^2(\frac{\phi}{2})] \tag{50}$$

with I_0 the intensity transmitted by an empty cell between parallel polarizers.

When the directions of transmission of polarizer and analyzer are parallel,$\alpha = \beta$ and:

$$I_1 = I_0[1 - sin^2(2\alpha)sin^2(\frac{\phi}{2})] \tag{51}$$

$$I_2 = I_0 sin^2(2\alpha)sin^2(\frac{\phi}{2}) \tag{52}$$

When they are perpendicular (crossed polarizers), $\beta = \alpha + \frac{\pi}{2}$ and if additionally $alpha = \frac{\pi}{4}$ we obtain simple equations for the intensities:

$$I_1 = I_0 cos^2(\frac{\phi}{2}) \tag{53}$$

$$I_2 = I_0 sin^2(\frac{\phi}{2}) \tag{54}$$

In our measurements we fixed the angle at $alpha = \frac{\pi}{4}$ where the transmitted intensity has a maximum. The birefringence was calculated using equation 54. We used wavelengths of $\lambda = 420nm$ and $\lambda = 614nm$, respectively.

The Mechanic part: Linkam cell

The oscillatory strain was applied using a Linkam CSS450 shear cell equipped with quartz plate-plate fixtures. The liquid sample is placed between the two parallel transparent surfaces (figure A.4).
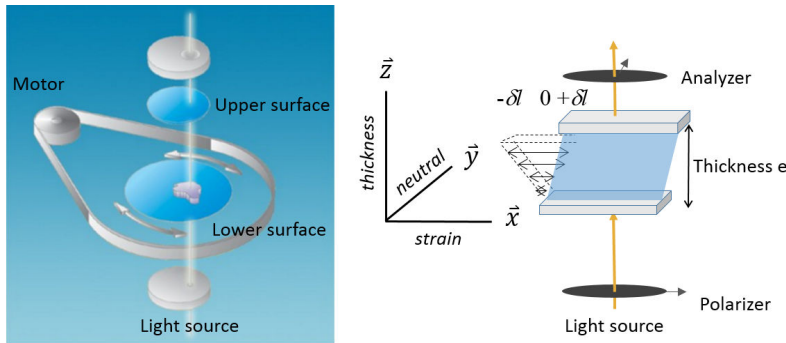
Figure A.4: Scheme of the Linkam shear cell CSS450.

The commercially available cell was improved in two ways: An external thermo-controller assures a temperature gradient of $< 0.05°$ and a torque reducer applied to the motor gives access to the lowest strain amplitudes. The sample thickness is controlled within $1.25\mu m$ and can be varied between $50\mu m$ and $1.0mm$. The observation window covers a surface of WODENN. The frequency of an oscillatory strain can be set from $0.01Hz$ to $2.0Hz$ the strain range depends on the sample thickness. At a sample thickness of $e = 250\mu m$ strain amplitudes between 0.1% and 95% are accessible.

The Synchronization: Trigger-system

The measurement of the optic signal (via a CCD camera) and the strain imposed by the motor are handled manually. In order compare the phase behaviour of input strain and

output optical response the start of the measurement must be synchronized. This was achieved by a trigger system (by R&D Vision technology) (figure A.5). The delay in synchronization of the measurements is less than $10^{-5}s$.
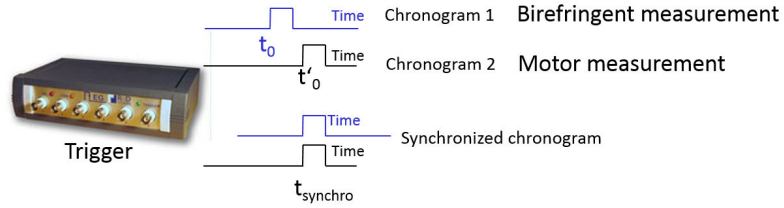
Figure A.5: Principle of the trigger synchronization.

Appendix B

Published articles

Hidden solidlike properties in the isotropic phase of the 8CB liquid crystal

P. Kahl, P. Baroni, and L. Noirez[*]

Laboratoire Léon Brillouin (CEA-CNRS), CE-Saclay, 91191 Gif-sur-Yvette, France
(Received 19 July 2013; published 6 November 2013)

Novel dynamic experiments have enabled the identification of a macroscopic solidlike response in the isotropic phase of a low molecular weight liquid crystal, 4,4'-*n*-octylcyanobiphenyl (8CB). This unknown property indicates that the low frequency shear elasticity identified in the isotropic phase of liquid crystal polymers is not reminiscent from the glass transition but reveals likely a generic property of the liquid state. The comparison to high molecular weight liquid crystals indicates, however, that the shear modulus is much enhanced when the liquid crystal moieties are attached to a polymer chain. The macroscopic length scales probed (0.050–0.100 mm) exclude wall-induced effects.

The knowledge of the timescales involved in liquid crystalline systems is of outmost importance to understand, control, and improve their characteristics. The submillimeter scales properties attract a tremendous research interest [1–4]. However, few studies concern the isotropic phase away from pretransitional effects. Assimilated to ordinary viscous liquids, the isotropic phase is not supposed to exhibit solidlike properties, or at very high frequency only (mega- or gigahertz) as ordinary liquids. For this reason, the low frequency behavior of the isotropic phase remains mistakenly unexplored.

Experimentally, the viscous or solidlike nature of a material is deduced from its response to a low frequency mechanical solicitation. A couple of years ago, careful dynamic experiments carried out in the isotropic phase of high molecular weight liquid crystals [side-chain liquid crystalline polymers (SCLCPs)] have revealed an as-yet unknown property: the isotropic melt does not flow but exhibits a finite shear elasticity of about several thousand Pascals at low frequency (0.1–10 Hz) [5–9]. The identification of low frequency shear elasticity in the isotropic phase of SCLCPs away from the isotropic-nematic transition opens numerous questions on the origin of this new property. It neither seems to result from the contribution of the liquid crystal moieties nor from surface anchoring effects, but likely from a generic property of the liquid state. Measurable in SCLCPs at macroscopic length scales as far as 100° away from the glass transition temperature [5,7,9], the shear elasticity of SCLCPs still raises the debated question of reminiscent glass transition effects.

In this Rapid Communication, we probe the dynamic properties of the low molecular counterpart: the 4,4'-*n*-octylcyanobiphenyl (8CB). The widely studied liquid crystal molecule can be considered as a representative liquid crystal molecule. 8CB exhibits a crystalline phase at low temperatures that enables one to rule on the question of pretransitional glass transition effects. We reveal a low frequency, solidlike response at several tens of micrometers sample thickness in the isotropic phase of 8CB, meaning that long range correlations are preserved when the orientational order is lost. This shear elasticity is detectable if special attention is paid to boundary conditions between the substrate and the sample. Under these conditions, the shear stress is optimally transmitted between the sample

and the substrate. The optimization of the boundary conditions is here achieved by improving the total wetting of the liquid to the substrate and by probing small gaps. Length scales up to 0.200 mm are probed, showing that the low frequency shear elasticity measured in the isotropic phase cannot be interpreted as a surface-induced effect but might indicate a bulk property.

Mechanical oscillatory shear is used in solid mechanics as well as in fluids to probe their dynamic properties at low frequency. This method gives access to long relaxation times. It consists in applying an as weak as possible oscillatory strain to the sample to probe equilibrium properties (at rest). The equilibrium state properties are described as a function of the frequency (ω), typically from 0.1 to 100 rad s^{-1}. The transfer of the motion to the liquid is here achieved by ensuring total wetting boundary conditions between the liquid and the substrate (alumina plates of 40 mm diameter) and by probing small gaps. The oscillatory motion and the shear stress measurement are provided using a dynamic force apparatus (ARES2). A seven-digit voltmeter (Keitley, rate 300 data/s) measures the voltage of the motor imposing the oscillation (input wave), while another seven-digit voltmeter measures the voltage associated to the sensor (output wave). This setup enables simultaneous access to the strain/stress signals and to the dynamic profile versus frequency and versus strain amplitude. The analysis of the signals defines the strain range for which the conventional formalism in terms of elastic G' and viscous G'' moduli can be applied, i.e., as long as the stress wave keeps the shape of the imposed strain wave (sinusoidal-like). Under these conditions, the shear stress and the shear strain are related by $\sigma(\omega) = G_0\gamma_0\sin(\omega t + \Delta\phi)$, with G_0 the viscoelastic modulus, t the time, ω the frequency and $\Delta\phi$ the phase shift between the input and the output waves, or in terms of shear elastic (G') and viscous (G'') moduli: $\sigma(\omega) = \gamma_0[G'(\omega)\sin(\omega t) + G''(\omega)\cos(\omega t)]$, with G' the component in phase with the strain, and G'' the out-of-phase component.

A liquidlike character is identifiable by a vanishing response at long time scale, whereas a solidlike behavior (elastic) exhibits a finite response independent of the frequency (Fig. 1, right). A perfect solidlike response exhibits no phase shift. Experimentally, solidlike materials always exhibit a short delay due to internal freedom degrees and thus exhibit a nonzero G''. When the phase shift is lower than $\Delta\phi < \pi/4$, the elastic component G' dominates the viscous component G'' (Fig. 1, right). If the output response of the material presents

[*]Corresponding author: laurence.noirez@cea.fr
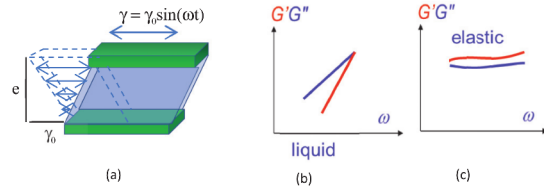
P. KAHL, P. BARONI, AND L. NOIREZ

FIG. 1. (Color online) Scheme of an oscillatory shear (a) and of typical dynamic relaxation spectra. (b) Flow behavior ($G' < G''$, with G' and G'' vanishing with the frequency). (c) Solidlike behavior ($G' > G''$, with G' and G'' weakly dependent on the frequency).

a phase shift larger than $\pi/4$, then the viscous component G'' dominates the elastic component G' (Fig. 1, left). The sample behaves liquidlike. If the phase shift reaches $\pi/2$ (G' vanishes), the sample is defined as purely viscous. A (Maxwell) liquidlike behavior typically displays a vanishing response characterized by a ω scaling of the viscous modulus and a ω^2 scaling dependence of the elastic modulus.

8CB (4,4'-n-octylcyanobiphenyl) was purchased from Aldrich and used as received. It shows crystalline ($T < 21\,°C$), smectic A ($T < 33\,°C$), nematic ($T < 40.5\,°C$), and isotropic phases. The phases and the transition temperatures were verified optically using a polarization microscope in accordance with the literature data [10,11].

Figure 2 illustrates the input sinusoidal strain wave and the output shear stress wave transmitted by a layer of 0.050 mm in the isotropic phase of 8CB for low, intermediate, and large strain amplitudes. The liquid crystal is solicited at $T = 42.5\,°C$ ($\pm 0.05\,°C$), i.e., at $T = T_{NI} + 2\,°C$ above the N-I transition temperature (*in situ* optically verified).

At low strain amplitude [$\gamma_0 = 6\%$, (a)] the input and output waves show almost superposition with a phase shift $\Delta\varphi$ of $12°$. This indicates a nearly instantaneous sample response, i.e., a solidlike response. A similar in-phase signal is observed for a wide range of frequencies from 1 up to 40 rad s^{-1}. Since the low frequency output shear stress is sinusoidal (linear regime), it can be described in terms of elastic G' and viscous G'' moduli. On the right side of Fig. 2(a) the evolution of G' and G'' is presented as a function of the frequency at low strain amplitude. Being at least three times as large as G'', the elastic shear modulus G' dominates the viscous contribution. The elastic modulus G' shows no apparent dependencies on the frequency. The viscous modulus G'' is also nearly constant at low frequency and does not obey a ω scale, as it would be expected for liquid behavior. Therefore both moduli indicate a nonflowing state.

For intermediate strain amplitudes [$\gamma_0 = 100\%$, Fig. 2(b)], the output signal becomes slightly distorted and its phase is shifted with respect to the input signal. The insets in the strain-stress diagrams in Fig. 2 show the discrepancy ($\Delta\sigma$) between the sine function model and the experimental points. For small ($\gamma_0 = 6\%$) and for large ($\gamma_0 = 8000\%$) deformations a straight line is obtained, indicating a convenient fit, while for intermediate ($\gamma_0 = 100\%$) strain amplitude $\Delta\sigma$ yields a pronounced periodical deviation. The latter displays two harmonics over one period. The appearance of these harmonics can be interpreted as the entrance into the nonlinear regime,
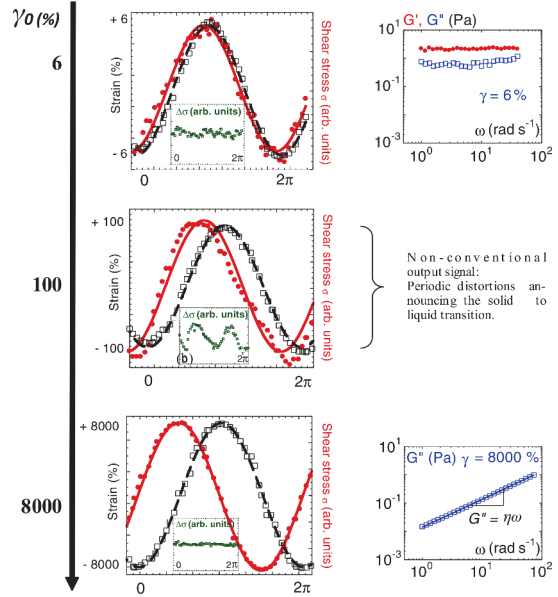
FIG. 2. (Color online) Input shear strain sine wave (open black squares, □) and output shear stress wave (red circles, ●) of 8CB in the isotropic phase at 0.050 mm gap thickness for low [$\gamma_0 = 6\%$, (a)], intermediate [$\gamma_0 = 100\%$, (b)], and high [$\gamma_0 = 8000\%$, (c)] strain amplitudes. The black and red lines correspond to a sine modeling of the input ($--$) and the output waves ($—$) of the data points. Insets: Data resulting from the subtraction of the model sine function from the data points ($\sigma_{experimental} - \sigma_0 = \Delta\sigma$, green squares, ■). Dynamic relaxation spectra (G': red circles, ●; G'' open blue squares, □) are shown for (a) and (c).

where the moduli G' and G'' become strongly strain and frequency dependent. A modeling of the signals in terms of G' and G'' is questionable. The occurrence of a slip mechanism might be addressed to illustrate the sin wave distortion in this regime.

At large strain amplitudes [Fig. 2(c)] i.e., away from equilibrium conditions, the distorsion is no more visible and the output wave recovers a sinusoidal shape, enabling a modeling in terms of G'' and G'. The phase shift is nearly $\pi/2$, in agreement with a viscous behavior. The corresponding dynamic relaxation spectrum displayed on the right side of Fig. 2(c) confirms the liquidlike response; G'' obeys a ω scaling with a slope of 14 mPa s, yielding a dynamic viscosity according to the literature data [12].

We have seen that the in-phase (solidlike) response is easily lost upon increasing the perturbation of the sample, being progressively replaced by a completely out-of-phase (viscous) response.

Figure 3 presents the evolution of the dynamic moduli in the isotropic phase on increasing the strain amplitude from 0.3% up to $10^4\%$. The experiment was carried out at a given frequency of $\omega = 5$ rad s^{-1} and a gap thickness of 0.050 mm.

At low strain amplitude, the elastic modulus G' dominates the viscous modulus G'', which contributes in average only about 4% of the total modulus [$G = \sqrt{(G'^2 + G''^2)}$].
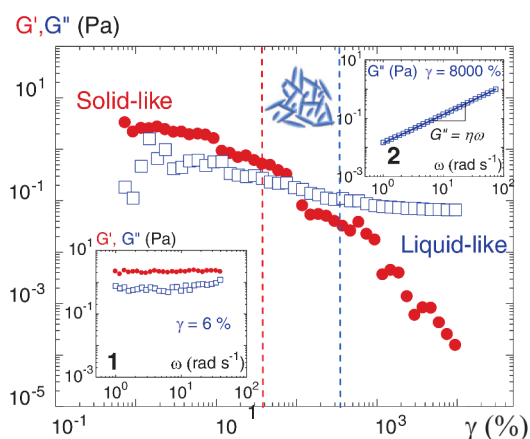
FIG. 3. (Color online) Strain dependence of the viscoelastic moduli (G': red circles, •; G'' open blue squares, □) of 8CB in the isotropic phase ($T = 42.5\,°C$) at 0.050 mm gap thickness at a frequency of $\omega = 5\,\mathrm{rad\,s^{-1}}$ (γ_0 evolves from 2.8 up to 10^4%). The vertical dashed bars delimit the zone where the output signal exhibits periodic distortions. Insets: Details of the frequency dependence at weak (1) and at large (2) strain amplitudes ($\gamma_0 = 6$% and at $\gamma_0 = 8000$%, respectively). The straight blue line in (2) shows the ω scale of G'', indicating a dynamic viscosity, in agreement with conventional experiments [12].

Upon increasing the strain amplitude, both the elastic and viscous moduli decrease with a more pronounced fall of G', leading to a transition from solidlike to liquidlike behavior. At high strain amplitude, the viscous modulus dominates the elastic modulus, the latter becoming negligible with respect to the total modulus (less than 1%).

The usual and generally expected viscous behavior of the liquid crystal in the isotropic phase is recovered by applying high strain amplitudes, thus away from mechanical equilibrium conditions. As a major result, a linear solidlike regime is found to precede the conventional flow regime. The solidlike response collapses upon entering the viscous regime.
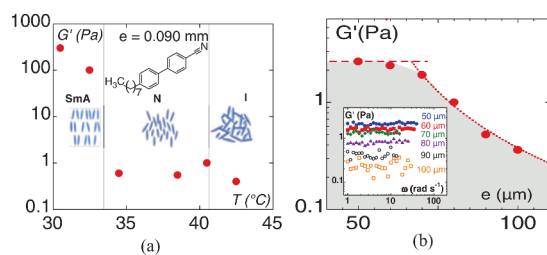
FIG. 4. (Color online) (a) Shear modulus G' (logarithmic scale) of 8CB versus temperature at 0.090-mm gap thickness. The vertical lines indicate the transition temperatures of the smectic (SmA)-nematic transition (N) and the nematic-isotropic (I) transition. (b) Shear modulus G' (logarithmic scale) of 8CB versus gap thickness at T (42.5 °C) $> T_{NI}$. Above 70 μm, the values lower rapidly following an exponential decrease (small dashed points). The inset displays the shear modulus from 1 up to 40 rad s^{-1} at different gap thicknesses.

For a better understanding of the origin of the elastic response, the experiments were also carried out for $T < T_{NI}$ in the nematic and smectic phases. Figure 4(a) shows the values of the shear elasticity measured at low thickness versus temperature. Both nematic and isotropic phases exhibit values of G' of around 0.8–1 Pa with no significant temperature dependency upon crossing the N-I transition temperature. This result indicates that neither pretransitional dynamics nor the nematic phase have an influence on the elastic response. Similar observations were reported for liquid crystal polymers [5,7]. The situation is different regarding below the SmA-N transition. Due to the positional order of the smectic phase, the values of the shear elasticity obtained in this phase exceed at least by 2 decades the ones found for the nematic and isotropic phases.

The thickness of the sample has also a significant influence on the elastic response. Figure 4(b) presents the evolution of the elastic modulus of 8CB in the isotropic phase as a function of the gap thickness. The average values of G' increase upon decreasing the gap thickness from 0.100 to 0.050 mm following an exponential law:

$$G' = (G'_0 - G'_\infty)\exp -\left(\frac{e - e_{\mathrm{crossover}}}{e_0}\right)^{\frac{1}{2}} + G'_\infty,$$

up to around $e_{\mathrm{crossover}} = 70\,\mu$m, the thickness value at the onset of the saturation, with $G'_0 = 1.7$ Pa the saturated shear modulus, $e_0 = 7.3\,\mu$m a constant length scale, and $G'_\infty = 0.12$ Pa the shear modulus at infinite thickness, which is negligible. The rapid lowering of the shear modulus might result from multiple effects such as increased voids, degree of freedom, loss of the shear stress transmission from and to the surfaces or dimensional character of the elastic property. In contrast, wall or capillary effects cannot explain the reinforcement of the moduli at low thickness. The probed gap distances far exceed coherence lengths that lie in the order of several nanometers by at least a factor of 1000 [13–16]. An interpretation in terms of surface effects or in terms of Frank's elasticity [13] might be an explanation for the viscoelastic properties found in the nematic phase [17,18], but this would be irrelevant in the present case since the elasticity is transmitted in the isotropic phase. The nematic and isotropic phases yield similar shear moduli, indicating that neither pretransitional dynamics nor the symmetry of the phase have an influence on the elastic response.

Shear elasticity was found but of stronger moduli for a series of liquid crystal polymers in the isotropic phase. To our knowledge, the low frequency elastic response of a liquid crystal polymer was firstly identified at low thickness by Gallani *et al.* [5] using a piezoelectric rheometer. Their interpretation was based on pretransitional dynamics related to the glass transition. In comparison to the low molecular weight liquid crystal 8CB, the presence of polymeric chains yields 10^3–10^4 times higher values for the elastic modulus, i.e., elastic moduli of the order of 10^3–10^4 Pa in the isotropic phase [8]. Also, a similar dependence of the elastic modulus on the gap thickness is observed [5,7]. The identification of finite macroscopic, low frequency shear elasticity in both small molecular weight and high molecular weight liquid crystals indicates that it originates neither from polymer chains, mesomorphic properties, nor pretransitional effects. Similarly, glass transition effects previously discussed to explain the low frequency elasticity of liquid crystal polymers are excluded.

We interpret the results in favor of long range intermolecular effects leading to the conclusion that the isotropic phase is a fragile, long range, elastically correlated "self-assembly." The strength of the solidlike response depends on the architecture of the molecule (polymer or not) and likely on the nature of the intermolecular interactions (van der Waals, H-bond, polar), in agreement with results obtained on other materials [19,20].

In conclusion, careful dynamic relaxation measurements have revealed a delicate solidlike response at macroscopic scale in the isotropic phase of 8CB, i.e., the liquid does not flow below a shear elastic threshold. This finite, low frequency shear elasticity is accessible by applying a weak mechanical stress to a submillimeter thickness sample. The solidlike character is established by the nearly instantaneous (in-phase) response to the input shear strain. The conversion of these mechanical waves in conventional terms of elastic G' (in phase) and viscous moduli G'' (out of phase) indicates that G' dominates G'' with no apparent (G') or very weak (G'') dependence on the frequency, indicating a major solidlike response over a wide frequency range (10^{-1} to 10^2 rad s^{-1}).

An indispensable condition for measuring this low frequency shear elasticity is a strong anchoring of the liquid crystal on the substrate, i.e., total wetting conditions. This solidlike regime is found for small strains prior to the usual viscous regime which is in apparence recovered at high strain amplitudes. These two linear regimes (solidlike and viscouslike regimes) are however not equivalent. Since the weaker strain amplitudes guarantee a weaker perturbation of the material, the elastic response needs to be considered as the fundamental response of the sample (at equilibrium). The usual viscous behavior (which is generally obtained when no special attention is paid to the wetting properties) corresponds to a second linear domain occuring as a highly perturbative state with respect to the solidlike regime.

The comparison to results obtained for high molecular weight liquid crystal polymers shows that the shear elasticity is neither related to pretransitional effects, mesomorphic properties, glass transition, the contribution of polymeric chains, nor anchoring effects, as predicted in recent theoretical works pointing out a significant enhancement of the shear modulus in the nematic phase of SCLCPs [21]. Figure 5 compares the shear moduli displayed in the liquid phase, by a low molecular weight liquid crystal (8CB), a side-chain liquid crystal polyacrylate, and a low molecular weight polybutylacrylate chain. It shows that
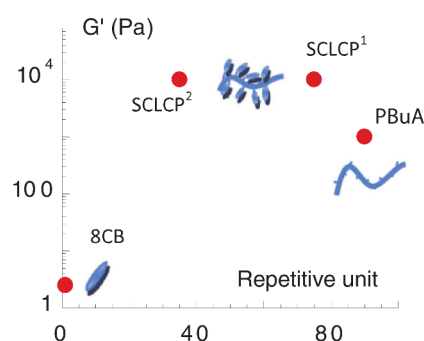
FIG. 5. (Color online) Comparison of the shear moduli G' measured in the liquid phase classified versus degree of polymerization (repetitive unit): 8CB, a polybutylacrylate chain (PBuA), a liquid crystal polyacrylate with a phenyl benzoate moiety (SCLCP[1]), and another liquid crystal polymer with a cyanobiphenyl moiety (SCLCP[2]). The three polymers are described in Ref. [7] and Eur. Phys. J. E **19**, 87 (2006).

the regular grafting of liquid crystal moieties on a polymer chain reinforces strongly the elastic character with respect to the low molecular weight liquid crystal but also with respect to the chain alone, pointing out the key role of the intermolecular interactions.

This analysis and the fact that for other liquids, a low frequency shear elasticity was detected [19,20], support the assumption that we deal with a generic property of the liquid state. We therefore interpret the low frequency shear elasticity as a measurement of the strength of long range intermolecular interactions. To our knowledge, very few theoretical developments set the role of the latter as crucial. In molecular liquids, noteworthy approaches consider a solidlike continuum [22] and even predict a low frequency shear elasticity, the strength of which depends on the network size [23]. Long range elastic correlations could be the origin of the shear-induced birefringence observed in the isotropic phase of high birefringence liquid crystals [24], of high molecular weight liquid crystals [25], or wormlike micellar solutions [26,27]. Predicted to result from a coupling with the lifetime of the pretransitional orientational fluctuations [28–30], these shear-induced behaviors are in fact observed for very much longer time scales.

[1] J. G. Cuennet, A. E. Vasdekis, L. De Sio, and D. Psaltis, Nat. Photonics **5**, 234 (2011).

[2] J.-C. Géminard, R. Hołyst, and P. Oswald, Phys. Rev. Lett. **78**, 1924 (1997).

[3] M. Vilfan, T. Apih, A. Gregorovic, B. Zalar, G. Lahajnar, S. Zumer, G. Hinze, R. Böhmer, and G. Althoff, Magn. Reson. Imaging **19**, 433 (2001).

[4] D. Porter, J. R. Savage, I. Cohen, P. Spicer, and M. Caggioni, Phys. Rev. E **85**, 041701 (2012).

[5] J. L. Gallani, L. Hilliou, P. Martinoty, and P. Keller, Phys. Rev. Lett. **72**, 2109 (1994).

[6] P. Martinoty, L. Hilliou, M. Mauzac, L. Benguigui, and D. Collin, Macromolecules **32**, 1746 (1999).

[7] H. Mendil, P. Baroni, and L. Noirez, Eur. Phys. J. E **19**, 77 (2006).

[8] H. Mendil, P. Baroni, and L. Noirez, Europhys. Lett. **72**, 983 (2005).

[9] L. Noirez, Phys. Rev. E **72**, 051701 (2005).

[10] B. Struth, K. Hyun, E. Kats, T. Meins, M. Walther, M. Wilhelm, and G. Grübel, Langmuir **27**, 2880 (2011).

[11] G. S. Iannacchione and D. Finotello, Phys. Rev. Lett. **69**, 2094 (1992).

[12] J. Jadzyn, R. Dabrwoski, T. Lech, and G. Czechowski, J. Chem. Eng. Data **46**, 110 (2001).

[13] P. G. de Gennes and J. Prost, *The Physics of Liquid Crystals*, 2nd ed. (Oxford University Press, Oxford, UK, 1993).

[14] B. Chu, C. S. Bak, and F. L. Lin, Phys. Rev. Lett. **28**, 1111 (1972).

[15] P. Sheng, Phys. Rev. A **26**, 1610 (1982).

[16] B. Jerôme, A. Bosseboeuf, and P. Pieranski, Phys. Rev. A **42**, 6032 (1990).

[17] W. R. Burghardt, J. Rheol. **35**, 49 (1991).

[18] P. Oswald and A. Dequidt, Europhys. Lett. **103**, 26002 (2013).

[19] L. Noirez, P. Baroni, and H. Cao, J. Mol. Liq. **176**, 71 (2012).

[20] L. Noirez and P. Baroni, J. Phys.: Condens. Matter **24**, 372101 (2012).

[21] E. P. Choate, M. G. Forest, and L. Ju, Rheol. Acta **49**, 335 (2010).

[22] A. V. Granato, Mater. Sci. Eng. A **521-522**, 6 (2009).

[23] F. Volino, Annales de Physique **22**, 142 (1997).

[24] C. Bailey, K. Fodor-Csorba, R. Verduzco, J. T. Gleeson, S. Sprunt, and A. Jákli, Phys. Rev. Lett. **103**, 237803 (2009).

[25] C. Pujolle-Robic, and L. Noirez, Nature (London) **409**, 167 (2001).

[26] F. Lequeux, V. Schmitt, A. Pousse, and D. Roux, Langmuir **10**, 955 (1994).

[27] D. C. Roux, J. F. Berret, G. Porte, and P. Lindner, Europhys. Lett. **25**, 521 (1994).

[28] P. D. Olmsted and P. Goldbart, Phys. Rev. A **46**, 4966 (1992).

[29] S. Hess, Z. Naturforsch. **31a**, 1507 (1976).

[30] S. Hess and P. Ilg, Rheol. Acta **44**, 465 (2005).

Harmonic strain-optical response revealed in the isotropic (liquid) phase of liquid crystals

P. Kahl, P. Baroni, and L. Noirez[a]
Laboratoire Léon Brillouin (CEA-CNRS), CE-Saclay, Paris-Saclay University, 91191 Gif-sur-Yvette, France

A strong optical birefringence is observed when applying a small amplitude oscillatory strain to the liquid phase of a liquid crystal. This unpredicted birefringence is found to oscillate at the same frequency as the driving frequency, with frequencies down to 0.01 Hz. This birefringence is visible up to 15 °C above the liquid crystal transition. This opto-dynamic property is interpreted as a result of a coupling of the orientational pretransitional fluctuations existing in the isotropic phase and long range elastic interactions recently identified in liquids. The conversion of the mechanical wave in an optical response is shapeable. Two examples of synchronized periodic signals are shown: the sine and the square waves. The optimization of the signal is analyzed using a Heaviside-step shear test. This optical property is immediately exploitable to design low energy on/off switching materials. © 2015 AIP Publishing LLC. [http://dx.doi.org/10.1063/1.4929321]

In liquid crystal (LC) displays, the tunable optical properties originate exclusively from the reorientation of the liquid crystalline domains. This is usually achieved by applying external fields as electric, magnetic, or mechanical fields.[1] No tunable properties were found at temperatures above the liquid crystal phases, i.e., in the isotropic phase. This phase is considered as an ordinary liquid.[2,3] Here, we reveal that the isotropic liquid is also convertible into an optically active material when it is stimulated at the sub-millimeter scale with a low frequency mechanical strain. These experiments suppose that a dynamic coupling exists between the pretransitional fluctuations (clusters of molecules with identical directions coexisting within the isotropic phase) and elastic properties uncovered at low frequency (typically below the Hz) in various liquids.[4–9] This strategy is efficient since a strong and reversible optical response is highlighted in the isotropic phase upon a low frequency low strain mechanical solicitation. This strain-induced optical birefringence is visible up to 15 °C above the isotropic transition and has the advantage of producing a true black phase between crossed polarizers in its inactivated state. This effect is synchronized with the excitation. Identified in the isotropic phase of several liquid crystalline fluids, this unknown effect is likely generic property. We illustrate the emergence of optical birefringence in the isotropic phase on the non-exhaustive basis of a low molecular weight liquid crystal polymer (LCP95) in use for LC-displays in its liquid crystal phase.[10] This molecule exhibits a particularly strong optical signal in the isotropic phase. We first present optical signals displayed at different strain amplitudes and different temperatures in the isotropic phase. Three different birefringence regimes are identified by increasing the strain amplitude: in-phase with the strain, in-phase with the strain-rate, and anharmonic optical signals. A Heaviside-step shear test completes the analysis and enables to define the experimental conditions for which this elastic optical response is dynamically stable and robust. Two examples

of periodic signals (sine and square) illustrate the optical response to low frequency mechanical stimuli.

The sample (LCP95) is a 12 repetitive units acrylate backbone crafted with cyanobiphenyl ended side chains linked by a propyl spacer presenting an isotropic-smectic transition at $T_{SAI} = 79.8 \pm 0.05$ °C. Its hydrodynamic radius determined by Light scattering is 1.4 nm. The isotropic phase exhibits the thermodynamic (Fig. 1(a)), conventional rheological (Fig. 1(b)), and symmetry characteristics of a simple liquid. This first order transition is resolved within ±0.05 °C with an order parameter vanishing at the transition. The optical measurements are performed in transmission mode under crossed polarized microscopy (Olympus BX60). Oscillatory and step shear motion were applied using a home-improved CSS450 Linkam cell (temperature gradient $< \pm 0.05$ °C) equipped with quartz plate-plate fixtures. The incident wavelength was $\lambda = 614$ nm. The transmitted intensity I was normalized to the uncrossed polarizer intensity I_0 and the averaged birefringence Δn is calculated using the transmittance: $\frac{I}{I_0} = \sin^2(\langle \Delta n \rangle \frac{e\pi}{\lambda})$, where e is the gap thickness. A trigger device (by R&D Vision, 10^{-9} s synchronization delay) measures simultaneously the strain amplitude and the transmitted intensity by using two individual CCD cameras (80 fps, Vision Technology) (Fig. 1(c)).

In a first series of experiments, the mechanical excitation is effected by applying a weak oscillatory strain stimulus at low frequency (typically from 0.01 Hz up to 2 Hz), i.e., close to equilibrium conditions. The input wave is a sinusoidal strain wave: $\gamma(t) = \gamma_0 \sin(\omega t)$ of angular frequency ω and strain amplitude γ_0 defined as the ratio of the displacement length Δl to the sample thickness: $\gamma_0 = \frac{\Delta l}{e}$. Fig. 2 illustrates the optical response of the isotropic phase to a 0.5 Hz oscillatory excitation at +1 °C above the S_{AI} transition. The photo snapshots at the top of Fig. 2 correspond to the true colors emerging from the isotropic phase during the periodic solicitation. The optical birefringence indicates that a long range orientation of the molecules establishes. The isotropic phase is thus optically active as soon as the lowest frequencies, a property unknown in physics of liquid crystals above the phase
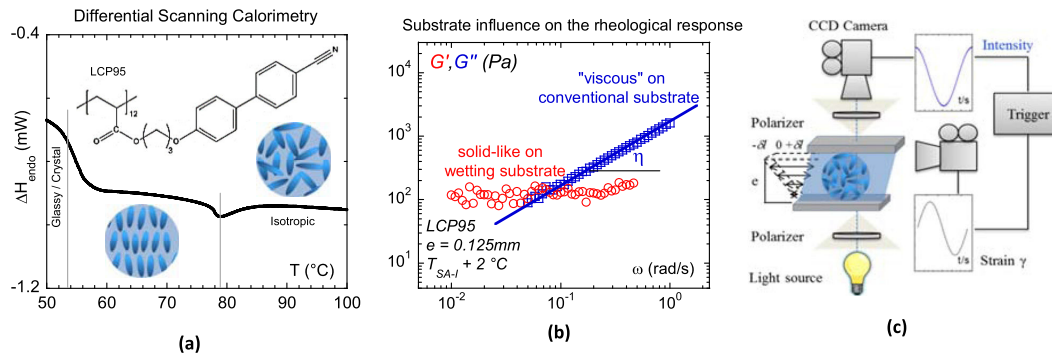
---

[a]Email: laurence.noirez@cea.fr

FIG. 1. (a) Differential scanning calorimetry on LCP95 indicates a first order smectic A to isotropic transition at 79.8 °C (data recorded at +10 °C/min). (b) Comparison of dynamic relaxation data of the LCP95 in the isotropic phase ($T_{SAI} + 2$ °C, e = 120 μm, 1% strain amplitude, ARES2 rheometer): On conventional substrate (glass): The shear modulus is not measurable and loss modulus G″ scales with ω^2 depicting a Newtonian behavior (blue squares (□): conventional glass substrate) and on wetting substrate (red circles (○): alumina substrate): the shear modulus (elastic response) G′ dominates at low frequency.[7] The storage modulus G′ dominates indicating a low frequency elastic behavior. (c) Optical setup: The isotropic phase fills the gap between two fixtures and is observed between crossed polarizers with a microscope (magnification lens: ×100). The upper fixture moves backward-forward with a tens microns scale oscillatory amplitude. A trigger device enables the simultaneous measurement of the optical signal and the movement by 2 individual CCD cameras.

transitions. The analysis of the signal reveals that the optical birefringence wave is harmonic with the input signal and can therefore be modeled by a sine wave: $\Delta n(\omega) = n_{max} \sin(\omega t + \varphi)$ with φ the phase-shift. For the applied shear frequency and a strain amplitude of $\gamma_0 = 10\%$, the signals almost superimpose with the strain rate $\frac{\partial \gamma(t)}{\partial t} = \gamma(t)\omega$. Similar optical signals are obtained for various low strain amplitudes and different temperatures up to 15 °C above the transition. The closer to the transition temperature, the more intense is the birefringence confirming the coupling to pretransitional fluctuations that melt by increasing the temperature. Fig. 3(a) displays the evolution of the birefringence (peak values) versus strain amplitude at +1 °C above the S_A-I transition. The examination of the strain dependence of the optical signal indicates three regimes. At very low strain amplitudes ($\gamma_0 \leq \gamma_{crit} \approx 4 \pm 1\%$), the optical signal is hardly detectable and is in-phase with the

strain (inset (1) of Fig. 3(a)), i.e., in-phase elastic behavior. Above this weak critical strain amplitude (4% < γ_0 < 30%), the birefringence increases linearly with strain amplitude. This linearity with the strain parameter is observed on all probed temperatures (Fig. 3(b)) confirming the direct dependence on the strain parameter. In this regime, the optical signal is nearly in-phase with the strain rate (inset (2) of Fig. 3(a)) with a phase shift close to 10°. At higher strains (γ_0 > 30% at +1 °C), the peak value of the birefringence does not evolve anymore (plateau values). The optical signal does not relax to the baseline between two successive periods (inset (3)), and the shape of the wave is splitted indicating the generation of a second harmonic and possibly a third harmonic of half period. The further increase of the strain amplitude generates the superposition of multiple harmonics giving rise to an apparent continuous-like birefringent signal whose asymptotic value is the flow birefringence (inset (4)). The conditions are equivalent to a steady state flow whose effects are already known.[11–14] In contrast to these far out-of-equilibrium conditions, at low frequency and low strain amplitude, the isotropic phase is close to an equilibrium state where no mechanical coupling is expected (the lifetimes τ of the pretransitional fluctuations determined by Kerr effects are of the order of $\tau \approx 10^{-9}$ s for rod-like liquid crystals[15] down to $\tau \approx 10^{-4}$ s for liquid crystal polymers[16]). In the low frequency harmonic regime (where the sine wave is conserved), a reduced dynamic birefringence $\Delta n^* = \frac{\Delta n}{\gamma_0 - \gamma_{crit}}$, can be defined by renormalizing the birefringence by the reduced strain value $\gamma_0 - \gamma_{crit}$. γ_{crit} defines the frontier separating the very low strain regime where the birefringent signal is weak and in phase with the applied strain wave from the strain regime where the optical signal is in phase with the strain rate and increases rapidly with the strain. In the second regime (above γ_{crit}), the evolution of the reduced birefringence Δn^* highlights a strain regime where the dynamic birefringence is independent of the applied strain amplitude (Figs. 3(b) and 3(c)). Being independent of the external stimuli (the strain), this quantity is linked to an elastic character of the material.
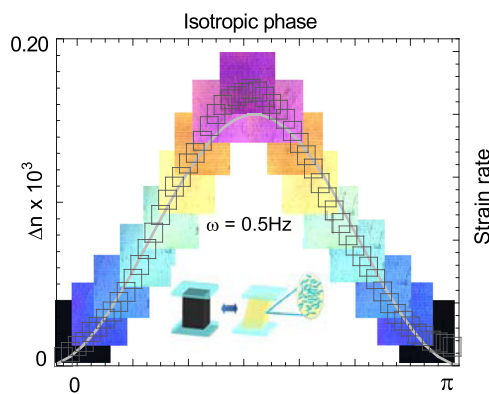
FIG. 2. Photo snapshots of the transmittance and corresponding birefringence (at $\lambda = 614$ nm) emerging upon a low frequency mechanical oscillation ($\omega = 0.5$ Hz) in the isotropic phase at $T - T_{SAI} = +1$ °C (sample thickness e = 250 μm and $\gamma_0 = 10\%$, the photographs are recorded between crossed polarizers). Corresponding input strain rate (grey continuous sine line ____) and induced birefringence (data points: black squares, □, sine model fit). The birefringence is in-phase with the strain rate (phase shift about $\varphi = 7°$).
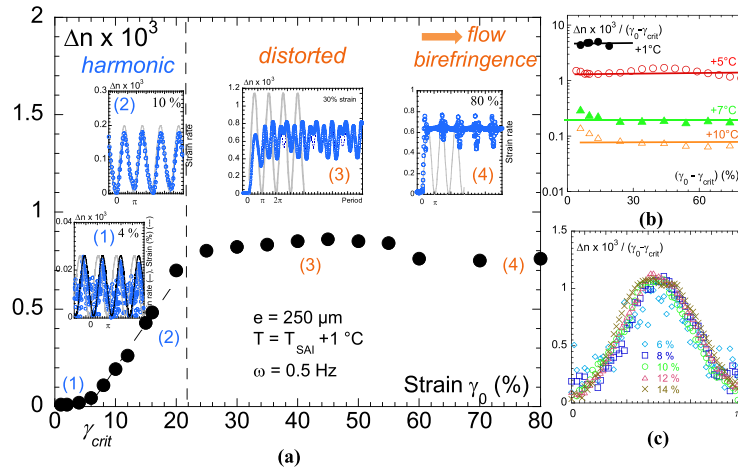
FIG. 3. (a) Strain dependence of the birefringent signal (peak value) in the isotropic phase (T − T$_{SAI}$ = +1 °C) at low frequency oscillatory excitation (ω = 0.5 Hz, sample thickness e = 250 μm) The corresponding oscillatory signals are shown as insets for 4% (1), 10% (2), 30% (3), and 80% (4) strain amplitude. The applied frequency is the same for all insets (ω = 0.5 Hz) and is represented by the continuous grey curve. γ_{crit} defines the frontier separating the very low strain regime where the birefringent signal is in phase with the applied strain wave from the strain regime where the optical signal is in phase with the strain rate and increases linearly up to 30% strain amplitude. Above 30% strain amplitude (inset (3)), the optical signal does not relax and is splitted indicating the generation of a second harmonic and possibly a third harmonic of half period (fitted by a dashed line), and at higher strains, the generation of multiple harmonics (4) flatten the signal to an asymptotic value corresponding to the flow birefringence. (b) Invariance of the reduced birefringence $\Delta n/(\gamma_0 - \gamma_{crit})$ with the strain amplitude observed at different temperatures: +1 °C (●), +5 °C (○), +7 °C (▲), and +10 °C (△). (c) The superposing oscillatory signals of the reduced birefringence at +3 °C above T$_{SAI}$ for various strain amplitudes.

A second series of mechanical measurements consists in probing the optical response of the isotropic phase to a Heaviside step excitation.[17] This step excitation allows the determination of the conditions of optimization of the transfer function from the mechanical motion to the optical response.[18] It gives a condensed overview of the expected dynamic behavior (even if the cutoff frequency is not experimentally accessible). This test is carried out experimentally by applying a sudden constant shear rate at t$_0$. A detailed illustration of the time-dependent evolution at a low shear rate of 3 s^{-1} is found together with the step function in Fig. 4(a). Different shear rates have been tested indicating a similar behavior (inset of Fig. 4). The highest birefringence (optimized gain) found before the development of instabilities is

obtained at around: $\dot{\gamma} = 30\,\text{s}^{-1}$. In terms of signal processing theory, the response to the Heaviside step function can be considered to be of first order and therefore modeled by $\Delta n(t) = K(1 - e^{-\frac{t}{\tau}})$, with τ_{off} the cutoff time and K the gain. As a response to the step function, the birefringence rises exponentially with corresponding cutoff times τ_{off} lower than 200 ms before saturating. The latter is the maximal intensity that can be obtained for a specific excitation. τ and K indicate how fast and how much the liquid is able to respond instantly to the sudden signal. The cutoff frequency is $\omega_{c.o.} = \frac{1}{\tau_{off}} \cong 20$ Hz. It is the maximum frequency value above which the signal starts to attenuate. In analogy with electronic filters, the birefringence behavior is similar to a capacitor and a resistor in series,[18] i.e., a low-pass filter. Below
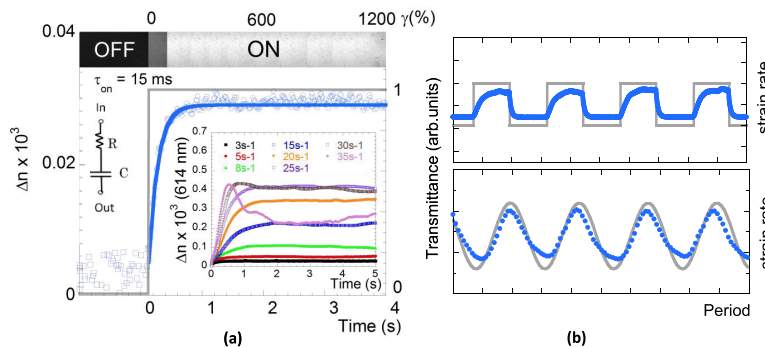
FIG. 4. (a) Input step function (grey continuous line, ___) and birefringent signal (data points: blue circles, ○, exponential model fit, blue continuous line, ___) in the isotropic phase at +1 °C above T$_{SAI}$ for a sample thickness e = 250 μm and shear rate $\frac{d\gamma}{dt}$ = 3 s^{-1}. Top of the figure: transmittance during the step function (photographs recorded between crossed polarizers with a monochromatic incident light). The isotropic phase behaves as a low pass filter with a resistor R and a capacity C. (b) Optical response (data points: blue filled circles, ●) synchronized to a sine and a square input strain rate waves (grey continuous line, ___).

this cut-off frequency, the output signal stays in-phase in respect to the solicitation. At low frequencies $\omega < \omega_{c.o.}$, the isotropic phase is therefore supposed to react elastically. This is confirmed by the harmonic behavior observed in the oscillatory experiments discussed above.

In conclusion, we have highlighted that, at the sub-millimeter scale, the isotropic phase of an ordinary liquid crystal behaves as a low frequency optical oscillator in response to a mechanical stimulation of frequencies as low as 0.01 Hz. The reversible synchronized birefringent response, whose intensity is directly linked to the strain amplitude, indicates an elastically driven behavior. The synchronized orientation of molecules, i.e., the strain field produces a long range organized material and its relaxation back to the isotropic liquid once the stress is removed indicate that the oscillatory strain produces a variation of entropy of the system (loss of entropy (during the orientation) and entropy gain (during relaxation)). This effect is possible if the pretransitional fluctuations are correlated at the scale of the sample in the isotropic liquid. In other words, the isotropic phase behaves dynamically as an elastic medium.[19] This synchronized birefringence is coherent with the stress results observed at low strain amplitudes on various liquids indicating an elastic pre-regime existing at the sub-millimeter scale prior to the conventional flow or viscous behavior.[4–9] This low frequency elastic plateau is also identified in the isotropic phase of LCP95 as illustrated in the stress measurements carried out at 0.200 mm on wetting substrate (Fig. 1(b)) and in agreement with previous results.[4–9] Finally, the birefringence induced in the isotropic phase cannot be interpreted as a surface induced property. Wall or capillary effects rule out since the probed gap distances far exceed coherence lengths of the order of several nanometers.[3,20–22] The birefringence instantly relaxes to its initial state (which appears black between crossed polarizers) demonstrating that no preorientation exists but that it has its origin in the reorientation of pretransitional fluctuations that are correlated in an elastic bulk. In the literature, orientational pretransitional fluctuations of rod-like liquid crystals exhibit lifetimes in the isotropic phase are of the order of $\tau \approx 10^{-9}$ s for the rod-like liquid crystals,[15] necessitating frequencies of the order of 10^9 Hz to induce a coupling with these timescales. In LCPs, the orientational pretransitional fluctuations announce lifetimes lying around $\tau \approx 10^{-4}$ s (Ref. 16) which still demand MHz solicitation frequencies. The present study reveals that the isotropic phase responds to a mechanical stimulation down to the tenth of the Hertz. Therefore, the pretransitional fluctuations are not free but elastically correlated in the isotropic liquid. Correlatively, the pretransitional fluctuations serve as a dynamic optical probe to "visualize" long range elastic interactions in the liquid. Weak intermolecular interactions (of about several Pa) can thus form a delicate elastic network up to a macroscopic scale. The interplaying forces are weak, fundamentally different from those governing LC-elastomer networks[23–25] but not negligible at the sub-millimeter scale. The free energy of the isotropic phase might be approximated by integrating a term coupling the orientational pretransitional fluctuations to the strain (at weak strain amplitudes): $F = F_0 + \frac{1}{2}.G_0.\gamma^2 - \sigma.\gamma - k.S(\gamma).\gamma$, where S is the order parameter assumed proportional to the birefringence ($S \cong 0$

without strain), G_0 is the weak shear modulus identified in the isotropic phase[4–8] (linked to the Young modulus), σ is the applied stress, and k is a constant coupling the order parameter to the strain γ. This expression indicates that the energy is lowered under strain via an increase of the order parameter (birefringence) and thus an entropy decrease. The stress release produces an entropy gain and a return to the isotropic state. This mechanism sets the role of long range reversible (elastic) interactions as crucial in the liquid state. In molecular liquids, noteworthy theoretical approaches consider a solidlike continuum[26] and even predict the elasticity, at several molecular length scale[27] or even macroscopically, the strength of which depends on the network size,[28] in particular, on the interactions between molecules.[28–30] Finally, this low frequency property consumes little energy (the liquid is stimulated close to its equilibrium state) and can serve as an excellent basis for LC-displays exhibiting a mechano-induction from a true black state to a birefringent state between crossed polarizers.

[1]*Handbook of Liquid Crystals*, 2nd ed., edited by J. W. Goodby, P. J. Collings, T. Kato, C. Tschierske, H. Gleeson, and P. Raynes (John Wiley & Sons, 2014), Vol. 8.

[2]G. Marrucci and F. Greco, Adv. Chem. Phys. **86**, 331 (1993).

[3]*The Physics of Liquid Crystals*, 2nd ed., edited by P. G. de Gennes and J. Prost (Oxford University Press, Oxford, 1993).

[4]B. V. Derjaguin, U. B. Bazaron, K. T. Zandanova, and O. R. Budaev, Polymer **30**, 97–103 (1989).

[5]L. Noirez and P. Baroni, J. Phys.: Condens. Matter **24**, 372101 (2012).

[6]L. Noirez, Phys. Rev. E **72**, 51701 (2005).

[7]L. Noirez, H. Mendil-Jakani, P. Baroni, and J. H. Wendorff, Polymers **4**, 1109 (2012).

[8]H. Mendil, P. Baroni, and L. Noirez, Eur. Phys. J. E **19**, 77 (2006).

[9]P. Kahl, P. Baroni, and L. Noirez, Phys. Rev. E **88**, 50501 (2013).

[10]L. D. Farrand, J. Patrick, and S. A. Marden, "Mesogenic compounds, liquid crystal medium and liquid crystal display," Merck Patent GmbH EP1690917 B1, 8 0ct. 2008.

[11]V. Zvetkov, Acta Phys. Chim. **19**, 86 (1944).

[12]C. Pujolle-Robic and L. Noirez, Nature **409**, 167 (2001).

[13]C. Bailey, K. Fodor-Csorba, R. Verduzco, J. T. Gleeson, S. Sprunt, and A. Jákli, Phys. Rev. Lett. **103**, 237803 (2009).

[14]C. Sadron, J. Phys. Radium **8**, 481 (1937).

[15]S. J. Rzoska, A. Drozd-Rzoska, P. K. Mukherjee, D. O. Lopez, and J. C. Martinez-Garcia, J. Phys.: Condens. Matter **25**, 245105 (2013).

[16]V. Reys, Y. Dormoy, J. L. Gallani, P. Martinoty, P. Le Barny, and J. C. Dubois, Phys. Rev. Lett. **61**, 2340 (1988).

[17]G. L. Anderson, J. Sound Vib. **34**, 425 (1974).

[18]B. Brogliato, R. Lozano, B. Maschke, and O. Egeland, *Dissipative Systems Analysis and Control*, 2nd ed. (Springer Verlag, London, 2007).

[19]G. Astarita, Polym. Eng. Sci. **14**, 730 (1974).

[20]B. Chu, C. S. Bak, and F. L. Lin, Phys. Rev. Lett. **28**, 1111 (1972).

[21]G. S. Iannacchione and D. Finotello, Phys. Rev. Lett. **69**, 2094 (1992).

[22]B. Jerôme, A. Bosseboeuf, and P. Pieranski, Phys. Rev. A **42**, 6032 (1990).

[23]P. G. de Gennes, C. R. Acad. Sci. Paris **281**, 101 (1975).

[24]E. M. Terentjev and M. Warner, Eur. Phys. J. E **4**, 343 (2001).

[25]S. Nikolov, C.-S. Han, and D. Raabe, Int. J. Solids Struct. **44**, 1582 (2007).

[26]A. V. Granato, Mater. Sci. Eng., A **521–522**, 6 (2009).

[27]M. Schoen, S. Hess, and D. J. Diestler, Phys. Rev. E **52**, 2587 (1995).

[28]F. Volino, Ann. Phys. **22**, 18 (1997).

[29]J. P. Ibar, Z. Zhang, Z. M. Li, and A. Santamaria, J. Macromol. Sci., Part B: Phys. **54**, 649 (2015).

[30]S. Droulias, A. G. Vanakaras, and D. J. Photinos, Liq. Cryst. **37**, 969 (2010).

Bibliography

[1] J. Goyon, A.Colin, G. Ovarlez, A. Ajdari, and L. Bocquet. Spatial cooperativity in soft glassy flows. *Nature*, 454(7200):84, 2008.

[2] F. H. Stillinger. A topographic view of supercooled liquids and glass formation. *Science*, 268(5206):1935, 1995.

[3] E. Agliari, A. Barra, R. Burioni, A. Di Biasio, and G.Uguzzoni. Collective behaviours: From biochemical kinetics to electronic circuits. *Sci Rep*, 3(3458):1, 2013.

[4] A. Baskaran and M.C. Marchetti. Statistical mechanics and hydrodynamics of bacterial suspensions. *PNAS*, 106(37):15567, 2009.

[5] R. A. Simha and S. Ramaswamy. Hydrodynamic fluctuations and instabilities in ordered suspensions of self-propelled particles. *Phys. Rev. Lett.*, 89(5):058101, 2002.

[6] L. Gheber and Z. Priel. Synchronization between beating cilia. *Biophys. J.*, 55(1):183, 1989.

[7] A. Bricard, J-B. Caussin, N. Desreumaux, O. Dauchot, and D. Bartolo. Emergence of macroscopic directed motion in populations of motile colloids. *Nature*, 503(7474):95, 2013.

[8] K. H. Nagai, Y. Sumino, R. Montagne, I. S. Aranson, and H. Chat. Collective motion of self-propelled particles with memory. *Phys. Rev. Lett.*, 114(16):168001, 2015.

[9] Gilroy Harrison. *The Dynamic Properties of Supercooled Liquids*. Academic Press, 1976.

[10] K. Falk, B. Coasne, R. Pellenq, F. Ulm, and L. Bocquet. Subcontinuum mass transport of condensed hydrocarbons in nanoporous media. *Nature Communications*, 6(6949):1, 2015.

[11] P. Levitz, M. Zinsmeister, P. Davidson, D. Constantin, and O. Poncelet. Intermittent brownian dynamics over a rigid strand: Heavily tailed relocation statistics in a simple geometry. *Phys. Rev. E*, 78(3):030102, 2008.

[12] M. Majumder, N. Chopra, R. Andrews, and B. J. Hinds. Nanoscale hydrodynamics: Enhanced flow in carbon nanotubes. *Nature*, 438(3):44, 2005.

[13] G. Manukyan, J. M. Oh, D. van den Ende, R. G. H. Lammertink, and F. Mugele. Electrical switching of wetting states on superhydrophobic surfaces: A route towards reversible Cassie-to-Wenzel transitions. *Phys. Rev. Lett.*, 106(1):014501, 2011.

[14] H.-W. Hu and S. Granick. Viscoelastic dynamics of confined polymer melts. *Science*, 258(5086):1339, 1992.

[15] J. Peachey, J. Van Alsten, and S. Granick. Design of an apparatus to measure the shear response of ultrathin liquid films. *Rev. Sci. Instr.*, 62(2):463, 1991.

[16] S. Granick, H.-W. Hu, and G. A. Carson. Nanorheology of confined polymer melts. II. Nonlinear shear response at strongly adsorbing surfaces. *Langmuir*, 10(10):3867, 1994.

[17] J. Peanasky, L. Cai, C. R. Kessel, , and S. Granick. Nanorheology of confined polymer melts. III. Weakly adsorbing surfaces. *Langmuir*, 10(10):3874, 1994.

[18] A.L. Demirel and S. Granick. Glasslike transition of a confined simple fluid. *Phys. Rev. Lett*, 77(11):2261, 1996.

[19] A.L. Demirel and S. Granick. Origins of solidification when a simple molecular fluid is confined between two plates. *J. Chem. Phys.*, 115(3):1498, 2001.

[20] A.L. Demirel and S. Granick. Friction fluctuations and friction memory in stick-slip motion. *Phys. Rev. Lett.*, 77(21):4330, 1996.

[21] G. Reiter, A. L. Demirel, J. Peanasky, L. L. Cai, and S. Granick. Stick to slip transition and adhesion of lubricated surfaces in moving contact. *J. Chem. Phys.*, 101(3):2606, 1994.

[22] M. L. Gee, P.M. McGuiggan, and J. N. Israelachvili. Liquid to solidlike transitions of molecularly thin films under shear. *J. Chem. Phys.*, 93(3):1895, 1990.

[23] B. Bhushan, J. N. Israelachvili, and U. Landman. Nanotribology: Friction, wear and lubrication at the atomic scale. *Nature*, 374:607, 1995.

[24] G. Luengo, F.J. Schmitt, R. Hill, and J. N. Israelachvili. Thin film rheology and tribology of confined polymer melts: Contrasts with bulk properties. *Macromolecules*, 30(8):2482, 1997.

[25] B. V. Derjaguin, U. B. Bazaron, K. T. Zandanova, and O. R. Budaev. The complex shear modulus of polymeric and small-molecule liquids. *Polymer*, 30:97, 1989.

[26] B. V. Derjaguin, U. B. Bazaron, Kh. D. Lamazhapova, and B. D. Tsidypov. Shear elasticity of low-viscosity liquids at low frequencies. *Phys. Rev. A*, 42(4):2255, 1990.

[27] D. Collin and P. Martinoty. Dynamic macroscopic heterogeneities in a flexible linear polymer melt. *Physica A*, 320:235, 2003.

[28] H. Mendil. *Indentification d'un comportement terminal élastique dans les fondus de polymères, de polymères cristaux liquides et analyse de transition de phase induite par cisaillement*. PhD thesis, Université Paris Sud - Orsay, U.F.R Scientifique d'Orsay, 2006.

[29] H. Mendil, P. Baroni, and L. Noirez. Unexpected giant elasticity in side-chain liquid-crystal polymer melts: A new approach for the understanding of shear-induced phase transitions. *Europhys. Lett.*, 72(6):983, 2005.

[30] H. Mendil, P. Baroni, and L. Noirez. Solid-like rheological response of non-entangled polymers in the molten state. *Eur. Phys. J. E Focus Point*, 19:77, 2006.

[31] H. Mendil, L. Noirez, P. Baroni, and I. Grillo. The frozen state in the liquid phase of side-chain liquid-crystal polymers. *Phys. Rev. Lett.*, 96(7):077801, 2006.

[32] L. Noirez. Origin of shear-induced phase transitions in melts of liquid-crystal polymers. *Phys. Rev. E*, 72(5):051701, 2005.

[33] H. Mendil-Jakani, P. Baroni, and L. Noirez. Shear-induced isotropic to nematic transition of liquid-crystal polymers: Identification of gap thickness and slipping effects. *Langmuir*, 25(9):5248, 2009.

[34] L. Noirez, H. Mendil-Jakani, P. Baroni, and J. H. Wendorff. Richness of side-chain liquid-crystal polymers: From isotropic phase towards the identification of neglected solid-like properties in liquids. *Polymers*, 4(2):1109, 2012.

[35] P. Baroni, H. Mendil, and L. Noirez. Method and device for determining at least one dynamic property of a deformable solid or fluid material. International patent publication number WO 2007/048890 A1, 2005.

[36] L. Noirez, P. Baroni, and H. Mendil-Jakani. The missing parameter in rheology: hidden solid-like correlations in viscous liquids, polymer melts and glass formers. *Polym. Int.*, 58(8):962, 2009.

[37] L. Noirez and P. Baroni. Revealing the solid-like nature of glycerol at ambient temperature. *J. Mol. Struct.*, 972:16, 2010.

[38] L. Noirez, H. Mendil-Jakani, and P. Baroni. Identification of finite shear-elasticity in the liquid state of molecular and polymeric glass-formers. *Philosophical Magazine*, 91(13):1977–1986, 2011.

[39] L. Noirez, P. Baroni, and H. Cao. Identification of low frequency shear elasticity in liquids n-heptadecane, liquid water and RT-ionic liquids [emim]5Tf2N]. *J. Mol. Liq.*, 116:18990, 2012.

[40] H. Mendil-Jakani, P. Baroni, L. Noirez, L. Chancelier, and G. Gebel. Highlighting a solid-like behavior in RTILs: Tri-octylmethylammonium bis(trifluoromethanesulfonyl)imide TOMA-TFSI. *J. Phys. Chem.*, 4(21):3775, 2013.

[41] L. Noirez and P. Baroni. Identification of a low-frequency elastic behaviour in liquid water. *J. Phys.: Condens. Matter*, 24:372101, 2012.

[42] P. Kahl, P. Baroni, and L. Noirez. Hidden solidlike properties in the isotropic phase of the 8CB liquid crystal. *Phys. Rev. E*, 88(5):050501, 2013.

[43] P. Kahl, P. Baroni, and L. Noirez. Harmonic strain-optical response revealed in the isotropic (liquid) phase of liquid crystals. *Appl. Phys. Lett*, 107(8):084101, 2015.

[44] S.J. Rzoska, A. Drozd-Rzoska, P.K. Mukherjee, D.O. Lopez, and J.C. Martinez-Garcia. Distortion-sensitive insight into the pretransitional behavior of 4-n-octyloxy-4'-cyanobiphenyl (8OCB). *J. Phys. Condens. Matter*, 25(24):245105, 2013.

[45] V. Reys, Y. Dormoy, J.L. Gallani, P. Martinoty, P.L. le Barny, and J.C. Dubois. Short-range-order effects in the isotropic phase of a side-chain polymeric liquid crystal. *Phys. Rev. Lett.*, 61(20):2340, 1988.

[46] P. E. Rouse. A theory of the linear viscoelastic properties of dilute solutions of coiling polymers. *The Journal of Chemical Physics*, 21(7):1272, 1953.

[47] B. H. Zimm. Dynamics of polymer molecules in dilute solution: Viscoelasticity, flow birefringence and dielectric loss. *J. of Chem. Phys.*, 24:269, 1956.

[48] P. D. de Gennes. Reptation of a polymer chain in the presence of fixed obstacles. *J. of Chem. Phys.*, 55:572, 1971.

[49] Masao Doi and Sam F. Edwards. *The Theory of Polymer Dynamics*. Clarendon Press, 1988.

[50] John D. Ferry. *Viscoelastic properties of polymers*. John Wiley & Sons, 1980.

[51] D. Rousseau. *Quelques proprietes inattendues des polymers cristaux liquides, des gels physique et des polymeres charges par des particules solides*. PhD thesis, Universite Louis Pasteur Strasbourg 1, 2002.

[52] W. F. Busse. The physical structure of elastic colloids. *J. Phys. Chem.*, 36(12):2862, 1932.

[53] L. R. G. Treloar. Elastic recovery and plastic flow in raw rubber. *Trans. Faraday Soc.*, 35:538, 1940.

[54] M.S. Green and A.V. Tobolsky. A new approach to the theory of relaxing polymeric media. *J. Chem. Phys.*, 14:80, 1946.

[55] A. S. Lodge. A network theory of flow birefringence and stress in concentrated polymer solutions. *Trans. Faraday Soc.*, 52:120, 1956.

[56] M. J. Yamamoto. The visco-elastic properties of network structure I. General formalism. *J. Phys. Soc. Jpn.*, 11:413, 1956.

[57] M. J. Yamamoto. The visco-elastic properties of network structure II. Structural viscosity. *J. Phys. Soc. Jpn.*, 12:1148, 1957.

[58] M. J. Yamamoto. The visco-elastic properties of network structure III. Normal stress effects (Weissenberg effect). *J. Phys. Soc. Jpn.*, 13:1200, 1958.

[59] F. Bueche. Viscosity, self-diffusion, and allied effects in solid polymers. *J. Chem. Phys.*, 20(12):1959, 1952.

[60] F. Tanaka and S. F. Edwards. Viscoelastic properties of physically crosslinked networks. Transient network theory. *Macromolecules*, 25(5):1516, 1992.

[61] A. N. Semenov, J.-F. Joanny, and A. R. Khokhlov. The rheology of solutions of associating polymers: Comparison of experimental behavior with transient network theory. *Macromolecules*, 28(4):1066, 1995.

[62] M. Doi and S. F. Edwards. Dynamics of concentrated polymer systems. Part 1. Brownian motion in the equilibrium state. *J. Chem. Soc., Faraday Trans. 2*, 74:1789, 1978.

[63] M. Doi and S. F. Edwards. Dynamics of concentrated polymer systems. Part 2. Molecular motion under flow. *J. Chem. Soc., Faraday Trans. 2*, 74:1802, 1978.

[64] M. Doi and S. F. Edwards. Dynamics of concentrated polymer systems. Part 3. The constitutive equation. *J. Chem. Soc., Faraday Trans. 2*, 74:1818, 1978.

[65] M. Zamponi, M. Monkenbusch, L. Willner, A. Wischnewski, B. Farago, and D. Richter. Contour length fluctuations in polymer melts: A direct molecular proof. *Europhys. Lett.*, 72(6):1039, 2005.

[66] T. P. Lodge. Reconciliation of the molecular weight dependence of diffusion and viscosity in entangled polymers. *Phys. Rev. Lett.*, 83(16):3218, 1999.

[67] M. Baumgaertel, A. Schausberger, and H. H. Winter. The relaxation of polymers with linear flexible chains of uniform length. *Rheologica Acta*, 29(5):400, 1990.

[68] T. C. B. McLeish. Tube theory of entangled polymer dynamics. *Advances in Physics*, 51(6):1379, 2002.

[69] W. W. Graessley. Some phenomenological consequences of the Doi-Edwards theory of viscoelasticity. *J. Polym. Sci., Polym. Phys. Ed.*, 18(1):27, 1980.

[70] M. Doi. Explanation for the 3.4-power law for viscosity of polymeric liquids on the basis of the tube model. *J. Polym. Sci., Polym. Phys. Ed.*, 21(5):667, 1983.

[71] N. P. T. O'Connor and R. C. Ball. Confirmation of the Doi-Edwards model. *Macromolecules*, 25(21):5677, 1992.

[72] M. Rubinstein. Discretized model of entangled-polymer dynamics. *Phys. Rev. Lett.*, 59(17):1946, 1987.

[73] M. Rubinstein, E. Helfand, and D. S. Pearson. Theory of polydispersity effects of polymer rheology: Binary distribution of molecular weights. *Macromolecules*, 20(4):822, 1987.

[74] J. Klein. The onset of entangled behavior in semidilute and concentrated polymer solutions. *Macromolecules*, 11(5):852, 1978.

[75] G. Marrucci and G. Ianniruberto. Open problems in tube models for concentrated polymers. *J. Non-Newtonian Fluid Mech.*, 82(2-3):275, 1999.

[76] G. Heinrich and E. Straube. A mean-field approach of the theory of topological constraints in polymer melts and networks. *Makromolekulare Chemie. Macromolecular Symposia*, 30(1):223, 1989.

[77] A. V. Granato. Mechanical properties of simple condensed matter. *Mater. Sci. Eng. A*, 6-11:521, 2009.

[78] A. V. Granato. The specific heat of simple liquids. *J. Non-Cryst. Solids*, 307-310:376, 2002.

[79] S. V. Khonik, A. V. Granato, D. M. Joncich, A. Pompe, and V. A. Khonik. Evidence of distributed interstitialcy-like relaxation of the shear modulus due to structural relaxation of metallic glasses. *Phys. Rev. Lett.*, 100(6):065501, 2008.

[80] M. Guenza. Cooperative dynamics in unentagled polymer fluids. *Phys. Rev. Lett.*, 88(2):025901, 2002.

[81] M. Guenza. Intermolecular effects in the center-of-mass dynamics of unentangled polymers. *Macromolecules*, 35:2714, 2002.

[82] M. Guenza. Cooperative dynamics in semiflexible unentangled polymer fluids. *J. Chem. Phys.*, 119(14):7568, 2003.

[83] J. P. Ibar. Do we need a new theory in polymer physics? *Journal of Macromolecular Science, Part C: Polymer Reviews*, 37(3):389, 1997.

[84] J. P. Ibar. The great myths of rheology part III: Elasticity of the network of entanglements. *Journal of Macromolecular Science, Part B: Physics*, 52:222, 2013.

[85] F. Volino. Theorie visco-elastique non-extensive. *Ann. Phys. Fr.*, 22:181, 1997.

[86] M. M. Cross. Rheology of non-Newtonian fluids: A new flow equation for pseudo-plastic systems. *Journal of Colloid Science*, 20(5):417, 1965.

[87] P. J. Carreau. Rheological equations from molecular network theories. *Trans. Soc. Rheol.*, 16:99, 1972.

[88] I. M. Krieger and T. J. Dougherty. A mechanism for nonnewtonian flow in suspensions of rigid spheres. *Trans. Soc. Rheol*, 3:137, 1959.

[89] W. P. Cox and E. H. Merz. Correlation of dynamic and steady flow viscosities. *J. Polym. Sci.*, 28:619, 1958.

[90] G. Marrucci. Dynamics of entanglements: A nonlinear model consistent with the cox-merz rule. *J. Non-Newtonian Fluid Mech.*, 62:279, 1996.

[91] D. W. Mead, R. G. Larson, and M. Doi. A molecular theory for fast flows of entangled polymers. *Macromolecules*, 31(22):7895, 1998.

[92] G. Ianniruberto and G. Marrucci. Convective orientational renewal in entangled polymers. *J. Non-Newtonian Fluid Mech.*, 95:363, 2000.

[93] Y. Lu, L. An, S. Q. Wang, and Z. G. Wang. Origin of stress overshoot during startup shear of entangled polymer melts. *ACS Marco Letters*, 3:569, 2014.

[94] T. Divoux, C. Barentin, and S. Manneville. Stress overshoot in a simple yield stress fluid: An extensive study combining rheology and velocimetry. *Soft Matter*, 7:9335, 2011.

[95] S.-Q.Wang, S. Ravindranath, P. Boukany, M. Olechnowicz, R. P. Quirk, A. Halasa, and J. Mays. Nonquiescent relaxation in entangled polymer liquids after step shear. *Phys. Rev. Lett.*, 97(18):187801, 2006.

[96] S. Q. Wang, Y. Y. Wang, S. W. Cheng, X. Li, X. Y. Zhu, and H. Sun. New experiments for improved theoretical description of nonlinear rheology of entangled polymers. *Macromolecules*, 46:3147, 2013.

[97] L. Noirez, H. Mendil-Jakani, and P. Baroni. New light on old wisdoms on molten polymers: Conformation, slippage and shear banding in sheared entangled and unentangled melts. *Macromolecular Journals*, 30(20):1709, 2009.

[98] H. Watanabe, T. Kanaya, and Y. Takahashi. Rheo-sans behavior of entangled polymer chains with local label under fast shear flow. *Activity Report on Neutron Scattering Research: Experimental Reports*, 14(146), 2007.

[99] F. Boue and P. Lindner. *Small Angle Neutron Scattering from Sheared Semidilute*

Solutions: Butterfly Effect, volume 597 of *ACS Symposium Series*, chapter 4, page 48. American Chemical Society, 2009.

[100] R. Oda, P. Panizzza, M. Schmutz, and F. Lequeux. Direct evidence of the shear-induced structure of wormlike micelles : Gemini 12-2-12. *Langmuir*, 13:6407, 1997.

[101] W. Paul, G. D. Smith, D. Y. Yoon, B. Farago, S. Rathgeber, A. Zirkel, L. Willner, and D. Richter. Chain motion in an unentangled polyethylene melt: A critical test of the rouse model by molecular dynamics simulations and neutron spin echo spectroscopy. *Phys. Rev. Lett.*, 80(11):2346, 1998.

[102] A. Kopf, B. Dunweg, and W. Paul. Dynamics of polymer "isotope" mixtures: Molecular dynamics simulation and rouse model analysis. *J. Chem. Phys.*, 107(17):6945, 1997.

[103] K. Kremer and G. S. Grest. Dynamics of entangled linear polymer melts: A molecular dynamics simulation. *J. Chem. Phys.*, 92(8):5057, 1990.

[104] A. Kolinski, J. Skolnick, and R. Yaris. Does reptation describe the dynamics of entangled, finite lenght polymer systems? A model simulation. *J. Chem. Phys.*, 86(3):1567, 1987.

[105] S. P. Obukhov, M. Rubinstein, and T. Duke. Dynamics of a ring polymer in a gel. *Phys. Rev. Lett.*, 73(9):1263, 1994.

[106] M. Kapnistos, M. Lang, D. Vlassopoulos, W. Pyckhout-Hintzen, D. Richter, D. Cho, T. Chang, and M. Rubinstein. Unexpected power-law stress relaxation of entangled ring polymers. *Nature Materials*, 7:997, 2008.

[107] X. Yang, S.-Q. Wang, A. Halasa, and H. Ishida. Fast flow behavior of highly entangled monodisperse polymer. *Rheol. Acta*, 37:415, 1998.

[108] J. A. Martins. Analysis of the adequacy of the representation of entanglement effects by chain loops. *Macromol. Theory and Simul.*, 19(6):360, 2010.

[109] C. Pujolle-Robic and L. Noirez. Observation of shear-induced nematic to isotropic transition in side-chain liquid crystal polymers. *Nature*, 409:167, 2001.

[110] J. L. Gallani, L. Hilliou, P. Martinoty, and P. Keller. Abnormal viscoelastic behavior of side-chain liquid-crystal polymers. *Phys. Rev. Lett.*, 72(13):2109, 1994.

[111] Y. Chushkin, C. Caronna, and A. Madsen. Low-frequency elastic behaviour of a supercooled liquid. *Europhys. Lett.*, 83:36001, 2008.

[112] S.-Q. Wang, S. Ravindranath, and P. Boukany Y. Wang. New theoretical considerations in polymer rheology: Elastic breakdown of chain entanglement network. *J. Chem. Phys.*, 127:064903, 2007.

[113] R. Zondervan, T. Xia, H. van der Meer, C. Storm, F. Kulzer, W. van Saarloos, and M. Orrit. Soft glassy rheology of supercooled molecular liquids. *PNAS*, 105(13):4993, 2008.

[114] J.W. Emsley, G.R. Luckhurst, G.N. Shilstone, and I. Sage. The preparation and properties of the alpha,omega-bis(4,4'-cyanobiphenyloxy) alkanes: nematogenic molecules with a flexible core. *Mol. Cryst. Liq. Cryst. Lett.*, 102:223, 1984.

[115] G. R. Luckhurst. Memories of George W. Gray. *Liquid Crystals*, 42(5-6):704, 2015.

[116] L. D. Farrand, J. Patrick, and S. A. Marden. Mesogenic compounds, liquid crystal medium and liquid crystal display, 2008.

[117] G. S. Iannacchione and D. Finotello. Calorimetric study of phase transitions in confined liquid crystals. *Phys. Rev. Lett.*, 69(14):2094, 1992.

[118] J. Prost and P.G. de Gennes. *The Physics of Liquid Crystals.* Oxford University Press, Walton Street, Oxford OX2 6DP, 2nd edition, 1993.

[119] R. H. Colby. Linear viscoelasticity of side chain liquid crystal polymers. *Liquid Crystals*, 13(2):233, 1993.

[120] G. Marrucci and F. Greco. *Advances in Chemical Physics, Volume 86: Flow Behavior of Liquid Crystalline Polymers.* John Wiley & Sons, Inc., 1993.

[121] M. R. Kannan, J. A. Kornfield, N. Schwenk, and C. Boeffel. Rheology of side-group liquid-crystalline polymers: Effect of isotropic-nematic transition and evidence of flow alignment. *Macromolecules*, 26:2050, 1993.

[122] V. Fourmaux-Demange, A. Brulet, J. P. Cotton, L. Hilliou, P. Martinoty, P. Keller, and F. Boue. Rheology of a comblike liquid crystalline polymer as a function of its molecular weight. *Macromolecules*, 31(21):7445, 1998.

[123] L. Prandtl. In A. Kratzer, editor, *Verhandlungen des dritten internationalen Mathematiker-Kongresses in Heidelberg 1904*, page 484. Teubner, Leipzig, Germany, 1905.

[124] P. Joseph. *Etude expérimentale du glissement liquide-solide sur surfaces lisses et texturées.* PhD thesis, Université Pierre et Marie Curie - Paris VI, 2005. ¡tel-00011075¿.

[125] D. M. Tolstoi. Molecular theory for slippage of liquids over solid surfaces (in russian). *Doklady Akad. Nauk SSSR*, 85:1089, 1952.

[126] T. D. Blake. Slip between a liquid and a solid: D.M. Tolstoi's (1952) theory reconsidered. *Colloids and Surfaces*, 47:135, 1990.

[127] S. Richardson. On the no-slip boundary condition. *J. Fluid Mech.*, 59(4):707, 1973.

[128] J. Koplik, J.R. Banavar, and J.F. Willemsen. Molecular dynamics of Poiseuille flow and moving contact lines. *Phys. Rev. Lett.*, 60(13):1282, 1988.

[129] J. Jadzyn, R. Dabrwoski, T. Lech, and G. Czechowski. Viscosity of the homologous series of n-alkylcyanobiphenyls. *J. Chem. Eng. Data*, 46(1):110, 2001.

[130] B. Chu, C. S. Bak, and F. L. Lin. Coherence length in the isotropic phase of a room-temperature nematic liquid crystal. *Phys. Rev. Lett*, 28(17):1111, 1972.

[131] B. Jerome. Surface effects and anchoring in liquid crystals. *Rep. Prog. Phys.*, 54:391, 1991.

[132] P. Attard. Thermodynamic stability of nanobubbles. *arXiv:1503.04365*, 2015.

[133] F. Y. Ushikubo, T. Furukawa, R. Nakagawa, M. Enari, Y. Makino, Y. Kawagoe, T. Shiina, and S. Oshita. Evidence of the existence and the stability of nano-bubbles in water. *Colloids Surf., A*, 361:31, 2010.

[134] J. R. T. Seddon, D. Lohse, W. A. Ducker, and V. S. J. Craig. A deliberation on nanobubbles at surfaces and in bulk. *ChemPhysChem*, 13:2179, 2012.

[135] M. Chaplin, nanobubbles. http://www1.lsbu.ac.uk/water/nanobubble.html. Accessed: 2015-10-01.

[136] B. V. Derjaguin and N. V. Churaev. Structure of water in thin layers. *Langmuir*, 3(5):607, 1987.

[137] K. Lum, D. Chandler, and J. D. Weeks. Hydrophobicity at small and large length scales. *J. Phys. Chem. B*, 103(22):4570, 1999.

[138] G. B. McKenna. Commentary on rheology of polymers in narrow gaps. *Eur. Phys. J. E Focus Point*, 19(1):101, 2006.

[139] A. M. Messner. Stress distributions in poker chip tensile specimes. *Aerojet General Technical Paper, 127 SRP*, 1963.

[140] C. Sadron. Dynamic double refraction of pure liquids. *J. Phys. Radium*, 7(6):263, 1936.

[141] V. Zvetkov. Magnetic and dynamic double refraction in the isotropic phase of substances capable of forming liquid crystals. *Acta Phys.-chim*, 19:86, 1944.

[142] C. Bailey, K. Fodor-Csorba, R. Verduzco, J. T. Gleeson, S. Sprunt, and A. Jakli. Large flow birefringence of nematogenic bent-core liquid crystals. *Phys. Rev. Lett.*, 103(23):237803, 2009.

[143] P. D. de Gennes. Short range order effects in the isotropic phase of nematics and cholesterics. *Mol. Cryst. Liq. Cryst.*, 12(3):193, 1971.

[144] L. D. Landau. *Collected Papers*. Gordon and Breach, New York, 1965.

[145] A. von Hippel. The dielectric relaxation spectra of water, ice, and aqueous solutions, and their interpretation. *IEEE Transactions on Electrical Insulation*, 23(5):801, 1988.

[146] S. Stojadinovic, A. Adorjan, S. Sprunt, H. Sawade, and A. Jakli. Dynamics of the nematic phase of a bent-core liquid crystal. *Phys. Rev. E*, 66(6):060701(R), 2002.

[147] V. Domenici, D. Frezzato, and C. A. Veracini. Slow dynamics of banana-shaped molecules: A theoretical approach to analyze 2H-NMR T2 relaxation times. *J. Chem. Phys. B*, 110(49):24884, 2006.

[148] Kerr-cell. `http://www.photonics.com/EDU/Term.aspx?TermID=4920`. Accessed: 2015-10-01.

[149] S. Hess. Pre- and post-transitional behavior of the flow alignment and flow-induced phase transition in liquid crystals. *Z. Naturforsch*, 31a, 1976.

[150] P. D. Olmsted and P. M. Goldbart. Theory of the nonequilibrium phase transition for nematic liquid crystals under shear flow. *Phys. Rev. A*, 41(8):4578, 1990.

[151] P. D. Olmsted and P. M. Goldbart. Isotropic-nematic transition in shear flow: State selection, coexistence, phase transitions, and critical behavior. *Phys. Rev. A*, 46(8):4966, 1992.

[152] J. Herman R. Dabrowski, P. Kula. High birefringence liquid crystals. *Crystals*, 3:3443, 2013.

[153] M. Camacho-Lopez, H. Finkelmann, P. Palffy-Muhoray, and M. Shelley. Fast liquid-crystal elastomer swims into the dark. *Nature Materials*, 3:307, 2004.

[154] M. Bispo, B. Donnio, and D. Guillon. Les élastomeres cristaux liquides: Comportement élastique. *Cincia e Tecnologia dos Materiais*, 19:2007, 2007.

[155] E.M. Terentjev and M. Warner. Linear hydrodynamics and viscoelasticity of nematic elastomers. *Eur. Phys. J. E*, 4:343, 2001.

[156] C. Humbert and J. P. Decruppe. Stress optical coefficient of viscoelastic solutions of CTAB and KBr. *Colloid. Polym. Sci.*, 276:160, 1998.

[157] P. D. Olmsted and C.-Y. David Lu. Phase separation of rigid-rod suspensions in shear flow. *Phys. Rev. E*, 60(4):4397, 1999.

[158] M. E. Cates and S. M. Fielding. Rheology of giant micelles. *Advances in Physics*, 55(7-8):799, 2006.

[159] Andrew R. Barron. *Physical Methods in Chemistry and Nano Science*. OpenStax-CNX, Available for free at Connexions http://cnx.org/content/col10699/1.20, 2009.

[160] F. Leclercq-Hugueux, M.-V. Coulet, J.-P. Gaspard, S. Pouget, and J.-M. Zanotti. Neutron probing the structure and dynamics of liquids. *C. R. Physique*, 8:884, 2007.

[161] P. A. Egelstaff. *An Introduction to the Liquid State.* Oxford series on neutron scattering in condensed matter 7. Oxford Science, second edition edition, 1994.

[162] C. R. Safinya, E. B. Sirota, and R. J. Plano. Nematic to smectic-a phase transition under shear flow: A nonequilibrium synchrotron x-ray study. *Phys. Rev. Lett.*, 66(15):1986, 1991.

[163] Log-rolling. `http://www.gsstoedtlen.homepage.t-online.de/rad/geschichte_rad3.htm`. Accessed: 2015-10-07.

[164] J. S. Higgins and H. C. Benot. *Polymers and Neutron Scattering.* Clarendon Press, 1994.

[165] J. P. Cotton. *Neutron, X-Ray and Light Scattering: Introduction to an Investigative Tool for Colloid and Polymeric Systems.* North-Holland, 1991.

[166] P. G. de Gennes. *Scaling concepts in Polymer Physics.* Cornwell Univ. Press, 1979.

[167] J. P. Cotton, D. Decker, H. Benoit, B. Farnoux, J. Higgins, G. Jannink, R. Ober, C. Picot, and J. des Cloizeaux. Conformation of polymer chain in the bulk. *Macromolecules*, 7:863, 1974.

[168] G. Pepy. New two-dimensional data treatment software for small-angle scattering. *Journal of Applied Crystallography*, 40:433, 2007.

[169] G. P. Bryan-Brown, E. L. Wood, and I. C. Sage. Weak surface anchoring of liquid crystals. *Nature*, 399:338, 1999.

[170] I.-G. Kim, H.-J. Na, H.-G. Park, Y.-H. Kim, B.-Y. Kim, J.-M. Han, T.-K.Park, D.-S. Seo, and H.-I. Yoon. Vertically aligned liquid crystal molecules on TiO_2- film treated by ion-beam irradiation. *Jap. J. App. Phys.*, 49:080220, 2010.

[171] J.-W. Lee, B.-M. Moon, K.-M. Lee, Y.-H. Kim, H. G. Park, J.-H. Lim, B.-Y. Oh, B.-Y. Kim, J.-Y. Hwang, C.-H. Ok, D.-S. Seo, and J.-M. Han. Homogeneous liquid crystal orientation on ion beam exposure TiO_2 surfaces depending on an anisotropic dipole field. *Liquid Crystals*, 37(3):279, 2010.

[172] F. J. Kahn. Orientation of liquid crystals by surface coupling agents. *Appl. Phys. Lett.*, 22:386, 1973.

[173] T. Rasing and I. Musevic. *Surfaces and Interfaces of Liquid Crystals.* Springer Berlin Heidelberg, 2004.

[174] H.-J. Na, H. J. Lee, I.-G. Kim, H.-G. Park, Y.-H. Kim, B.-Y. Kim, J.-Y. Hwang, J.-M. Han, T.-K. Park, and D.-S. Seo. Alignment characteristics of liquid crystal

molecules on titanium dioxide thin film. *Molecular Crystals and Liquid Crystals*, 550(1):45, 2011.

[175] J. Stöhr, M. G. Samant, A. Cossy-Favre, J. Diaz, Y. Momoi, S. Odahara, and T. Nagata. Microscopic origin of liquid crystal alignment on rubbed polymer surfaces. *Macromolecules*, 31:1942, 1998.

[176] M. E. McGovern, K. M. R. Kallury, and M. Thompson. Role of solvent on the silanization of glass with octadecyltrichlorosilane. *Langmuir*, 10:3607, 1994.

[177] D. Zhanga, Y. Wang, and Y.Gana. Characterization of critically cleaned sapphire single-crystal substrates by atomic force microscopy, XPS and contact angle measurements. *Appl. Surf. Sci.*, 274:405, 2013.

[178] J. W. Elam, C. E. Nelson, M. A. Cameron, M. A. Tolbert, and S. M. George. Adsorption of H_2O on a single-crystal alpha-Al_2O_3(0001) surface. *J. Phys. Chem. B*, 102:7008, 1998.

[179] K. C. Hass, W. F. Schneider, A. Curioni, and W. Andreoni. The chemistry of water on alumina surfaces: Reaction dynamics from first principles. *Science*, 282:265, 1998.

[180] D. Yang, M. Krasowska, R. Sedev, and J. Ralston. The unusual surface chemistry of alpha-Al_2O_3 (0001). *Phys. Chem. Chem. Phys.*, 12:13724, 2010.

[181] A. Kanta, R. Sedev, and J. Ralston. Thermally- and photoinduced changes in the water wettability of low-surface-area silica and titania. *Langmuir*, 21(6):2400, 2005.

[182] A. J. Kinloch. *Adhesion & Adhesives - Science & Technology.* Chapman & Hall, London, 1987.

[183] J. Abenojar, M.A. Martinez, N. Encinas, and F. Velasco. Modification of glass surfaces adhesion properties by atmospheric pressure plasma torch. *Int. J. Adhes.*, 44:1, 2013.

[184] F. M. Fowkes. Attractive forces at interfaces. *J. Ind. Eng. Chem.*, 56:40, 1964.

[185] J. N. Israelachvili. *Intermolecular and Surface Forces, Chapter 12.* Academic Press, London, 3rd edition, 1997.

[186] Hans-Jürgen Butt, Brunero Cappella, and Michael Kappl. Force measurements with the atomic force microscope: Technique, interpretation and applications. *Surface Science Reports*, 59:1, 2005.

[187] A. Noy, D. V. Vezenov, and C. M. Lieber. Chemical forcee microscopy. *Annu. Rev. Mater. Sci.*, 27:381, 1997.

[188] D. L. Sedin and K. L. Rowlen. Adhesion forces measured by atomic force microscopy in humid air. *Anal. Chem.*, 72:2183, 2000.

[189] Q. Ouyang, K. Ishida, and K. Okada. Investigation of micro-adhesion by atomic force microscopy. *Appl. Surf. Sci.*, 169:644, 2001.

[190] A. Noy, C. D. Frisbie, L. F. Rozsnyai, M. S. Wrighton, and C. M. Lieber. Chemical force microscopy: Exploiting chemically-modified tips to quantify adhesion, friction, and functional group distributions in molecular assemblies. *J. Am. Chem. SOC*, 117:7943, 1995.

[191] P.G. de Gennes, F. Bochard-Wyart, and D. Quere. *Gouttes, bulles, perles et ondes.* Edition Belin, Paris, 2005.

[192] G. Cevc. Hydration force and the interfacial structure of the polar surface. *J. Chem. Soc., Faraday Trans.*, 87:2733, 1991.

[193] S. Leikin, V. A. Parsegian, D. C. Rau, and R. P. Rand. Hydration forces. *Annu. Rev. Phys. Chem.*, 44:369, 1993.

[194] J.N. Israelachvili and H. Wennerstrom. Role of hydration and water structure in biological and colloidal interactions. *Nature*, 379:219, 1996.

[195] V.N. Paunov, R.I. Dimova, P.A. Kralchevsky, G. Broze, and A. Mehreteab. The hydration repulsion between charged surfaces as an interplay of volume exclusion and dielectric saturation effects. *J. Colloid Interf. Sci.*, 182:239, 1996.

[196] N. A. M. Besseling. Theory of hydration forces between surfaces. *Langmuir*, 13(7):2113, 1997.

[197] A. Trokhymchuk, D. Henderson, and D.T. Wasan. A molecular theory of the hydration force in an electrolyte solution. *J. Colloid Interf. Sci.*, 210:320, 1999.

[198] S. Marcelja and N. Radic. Repulsion of interfaces due to boundary water. *Chem. Phys. Lett.*, 42(1):1976, 1976.

[199] P. Huang, T. A. Pham, G. Galli, and E. Schwegler. Alumina(0001)/water interface: Structural properties and infrared spectra from first-principles molecular dynamics simulations. *J. Phys. Chem. C*, 118(7):8944, 2014.

[200] K. Meister, S. Strazdaite, A. L. DeVries, S. Lotze, L. L. Olijve, I.K. Voets, and H. J. Bakker. Observation of ice-like water layers at an aqueous protein surface. *PNAS*, 16:111, 2014.

[201] S. Marcelja, J.N. Israelachvili, and H. Wennerstrom. Hydration in electrical double layers. *Nature*, 385:689, 1997.

[202] H.-J. Butt. Measuring electrostatic, van der Waals, and hydration forces in electrolyte solutions with an atomic force microscope. *Biophys J.*, 60(6):1438, 1991.

[203] T. Luxbacher. *The Zeta Potential for Solid Surface Analysis: A practical guide to streaming potential measurement.* Anton Paar GmbH, Austria, 1st edition, 2014.

[204] T.J. Senden, C. J. Drummond, and P. Kekicheff. Atomic force microscopy: Imaging with electrical double layer interactions. *Langmuir*, 10:358, 1994.

[205] J. Lyklema and J.Th.G. Overbeek. On the interpretation of electrokinetic potentials. *J. Colloid Interface Sci.*, 16:501, 1961.

[206] E. A. Guggenheim. The conceptions of electrical potential difference between two phases and the individual activities of ions. *J. Phys. Chem.*, 33(6):842, 1929.

[207] R. M. Kozlowski. *Handbook of Natural Fibres: Processing and Applications.* Woodhead Publishing Limited, 2012.

[208] J.A. Yopps. The zero point of charge of alpha-alumina. *J. Colloid Sci.*, 19(1):61, 1964.

[209] R. J. Kershner, J. W. Bullard, and M. J. Cima. Zeta potential orientation dependence of sapphire substrates. *Langmuir*, 20:4101, 2004.

[210] R. F. Giese and C. J. van Oss. *Colloid And Surface Properties Of Clays And Related Minerals*, volume 105 of *Surfactant science*. Marcel Dekker, New York, 2002.

[211] W. P. Mason, W. O. Baker, H. J. Mcskimin, and J. H. Heiss. Measurement of shear elasticity and viscosity of liquids at ultrasonic frequencies. *Phys. Rev.*, 75:936, 1949.

[212] B.B. Badmaev, B.B. Damdinov, and T.S. Dembelova. Viscoelastic relaxation in fluids. *Bulletin of the Russian Academy of Sciences: Physics*, 79(10):1301, 2015.

[213] G. Astarita. Thermodynamics of dissipative materials with entropic elasticity. *Polymer Engineering and Science*, 14(10):730, 1974.

[214] A. Zaccone and E. M. Terentjev. Disorder-assisted melting and the glass transition in amorphous solids. *Phys. Rev. Lett.*, 110:178002, 2013.

[215] M. Schlegel, J. Brujic, E. M.Terentjev, and A. Zaccone. Local structure controls the nonaffine shear and bulk moduli of disordered solids. *Scientific Reports*, 6(18724), 2016.

[216] P. Baroni, P. Bouchet, and L. Noirez. Highlighting a cooling regime in liquids under submillimeter flows. *J. Phys. Chem. Lett.*, 4(12):2026, 2013.

[217] P. Jop, V. Mansard, P. Chaudhuri, L. Bocquet, and A. Colin. Microscale rheology of a soft glassy material close to yielding. *Phys. Rev. Lett.*, 108:148301, 2012.

[218] Z. Pei, Y. Yang, Q. Chen, E. M. Terentjev, Y. Wei, and Y. Ji. Mouldable liquid-

crystalline elastomer actuators with exchangeable covalent bonds. *Nature Materials*, 13:36, 2014.

Thèse de Doctorat

Philipp KAHL

Identification of long-range solid-like correlations in liquids and role of the fluid-substrate interactions

Identification des corrélations solides à longue portée dans les liquides et le rôle de l'interaction fluide-substrat

Résumé

Les liquides diffèrent des solides par une réponse retardée à la sollicitation en cisaillement; c'est-à-dire une absence d'élasticité de cisaillement et un comportement d'écoulement à basses fréquences (<1 Hz). Ce postulat pourrait ne pas être vrai à toutes échelles. A l'échelle submillimétrique, les mesures viscoélastiques (VE) réalisées en améliorant l'interaction entre le liquide et le substrat, montrent qu'une élasticité basses-fréquences existe dans des liquides aussi variés que les polymères, les surfondus, les liquides à liaison H, ioniques ou van der Waals. Ce résultat implique que les molécules à l'état liquide ne seraient pas dynamiquement libres, mais élastiquement corrélées.

En utilisant les propriétés biréfringentes des fluctuations prétransitionnelles qui coexistent dans la phase isotrope des cristaux liquides, nous montrons qu'il est possible de visualiser ces corrélations « cachées ». Dans des conditions similaires aux mesures VE, une biréfringence optique synchrone à la déformation est observée dans la phase isotrope à des fréquences aussi basses que 0.01 Hz et des températures éloignées de toute transition. Le comportement de la biréfringence basses-fréquences a des similitudes avec l'élasticité; elle est en phase avec la déformation à faibles amplitudes de déformation, puis en phase avec le taux de déformation à plus grandes amplitudes. La biréfringence basses-fréquences est forte, sans défaut et réversible. Elle indique un ordre à longue portée. La synchronisation de la réponse à la sollicitation en fréquence et l'état ordonné qu'elle produit ne sont pas compatibles avec un état liquide isotrope mais montrent qu'il s'agit d'un état élastique soumis à déformation (entropie élastique).

Mots clés

Etat liquide, élasticité de cisaillement, biréfringence basses-fréquences, phase isotrope des cristaux liquides, interaction liquide-substrat, diffraction des rayons X et diffusion des neutrons

Abstract

Liquids differ from solids by a delayed response to a shear mechanical solicitation; i.e. they have no shear elasticity and exhibit a flow behaviour at low frequency (<1 Hz). This postulate might be not verified at the sub-millimeter scale. By optimizing the measurement in particular by improving the liquid/substrate interactions (wetting), a low frequency shear elasticity has been found in liquids including molten polymers, glass-formers, H-bond polar, ionic or van der Waals liquids. This result implies that molecules in the liquid state may not be dynamically free but weakly elastically correlated.

Using the birefringent properties of the pretransitional fluctuations coexisting in the isotropic phase of liquid crystals, we show that it is possible to visualize these "hidden" shear-elastic correlations. We detect a synchronized birefringent optical response in the isotropic phase that is observable at frequencies as low as 0.01 Hz and at temperatures far away from any phase transition. The low-frequency birefringence exhibits a strain dependence similar to the low frequency elasticity: An optical signal that is in-phase with the strain at low strain amplitudes and in-phase with the strain-rate at larger strain amplitudes. The birefringent response is strong, defect-free, reversible and points out a collective response. This long-range ordering rules out the condition of an isotropic liquid and its synchronized response supports the existence of long-range elastic (solid-like) correlations. In the light of this, the strain dependence of the harmonic birefringent signal and the shear elasticity may correspond to an entropy-driven transition.

Key Words

Liquid state, shear elasticity, low frequency birefringence, isotropic phase of liquid crystals, interaction liquid-substrate, X-ray/neutron scattering